HUYGENS SUBGRIDDING FOR THE FREQUENCY-DEPENDENT– FINITE-DIFFERENCE TIME-DOMAIN METHOD

2011

By
Maksims Abaļenkovs
School of Electrical and Electronic Engineering
Microwave and Communication Systems Research Group

Contents

34669 words

List of Figures

List of Tables

List of Algorithms

14

List of Listings

Abstract

Computer simulation of electromagnetic behaviour of a device is a common practice in modern engineering. Maxwell's equations are solved on a computer with help of numerical methods. Contemporary devices constantly grow in size and complexity. Therefore, new numerical methods should be highly efficient. Many industrial and research applications of numerical methods need to account for the frequency dependent materials.

The Finite-Difference Time-Domain (FDTD) method is one of the most widely adopted algorithms for the numerical solution of Maxwell's equations. A major drawback of the FDTD method is the interdependence of the spatial and temporal discretisation steps, known as the Courant–Friedrichs–Lewy (CFL) stability criterion. Due to the CFL condition the simulation of a large object with delicate geometry will require a high spatio-temporal resolution everywhere in the FDTD grid.

Application of subgridding increases the efficiency of the FDTD method. Subgridding decomposes the simulation domain into several subdomains with different spatio-temporal resolutions.

The research project described in this dissertation uses the Huygens Subgridding (HSG) method. The frequency dependence is included with the Auxiliary Differential Equation (ADE) approach based on the one-pole Debye relaxation model. The main contributions of this work are (i) extension of the one-dimensional (1D) frequency-dependent HSG method to three dimensions (3D), (ii) implementation of the frequency-dependent HSG method, termed the dispersive HSG, in Fortran 90, (iii) implementation of the radio environment setting from the PGM-files, (iv) simulation of the electromagnetic wave propagating from the defibrillator through the human torso and (v) analysis of the computational requirements of the dispersive HSG program.

Declaration

No portion of the work referred to in this thesis has been submitted in support of an application for another degree or qualification of this or any other university or other institute of learning.

Copyright

i. The author of this thesis (including any appendices and/or schedules to this thesis) owns certain copyright or related rights in it (the "Copyright") and he has given the University of Manchester certain rights to use such Copyright, including for administrative purposes.

ii. Copies of this thesis, either in full or in extracts and whether in hard or electronic copy, may be made only in accordance with the Copyright, Designs and Patents Act 1988 (as amended) and regulations issued under it or, where appropriate, in accordance with licensing agreements which the University has from time to time. This page must form part of any such copies made.

iii. The ownership of certain Copyright, patents, designs, trade marks and other intellectual property (the "Intellectual Property") and any reproductions of copyright works in the thesis, for example graphs and tables ("Reproductions"), which may be described in this thesis, may not be owned by the author and may be owned by third parties. Such Intellectual Property and Reproductions cannot and must not be made available for use without the prior written permission of the owner(s) of the relevant Intellectual Property and/or Reproductions.

iv. Further information on the conditions under which disclosure, publication and commercialisation of this thesis, the Copyright and any Intellectual Property and/or Reproductions described in it may take place is available in the University IP Policy (see http://www.campus.manchester.ac.uk/medialibrary/policies/intellectual-property.pdf), in any relevant Thesis restriction declarations deposited in the University Library, the University Library's regulations (see http://www.manchester.ac.uk/library/aboutus/regulations) and in the University's policy on presentation of Theses.

to Reveka, Sergejs and Dmitrijs

Acknowledgements

<div align="right">

Manchester, UK

August 2011

</div>

About the Author

Maksims Abaļenkovs was born in Riga, Latvia in 1982. He attended the Riga Secondary School No. 72, where he studied in a Mathematics and Physics specialist class. He received a BSc degree in Computer Science (2006) from the Heinrich-Heine-Universität Düsseldorf, Germany and an MSc degree in Advanced Computer Science (2007) from the University of Manchester, UK. The last four years Maksims is working towards a PhD degree at the School of Electrical and Electronic Engineering in the University of Manchester, UK.

During his PhD time Maksims Abaļenkovs was a part-time teaching assistant in taught modules on Computation in Electromagnetics, Data Networking and Java Programming. Last year he initiated and currently helps to organise a PhD seminar series at the Microwave and Communication Systems (MACS) research group.

The main research interests of Maksims Abaļenkovs lie in the areas of the Finite-Difference Time-Domain (FDTD) methods, subgridding, dispersive materials modelling, Computational Electromagnetics (CEM), Bioelectromagnetics, computational methods in medicine, scientific computing and parallel programming languages.

Since 2007 Maksims Abaļenkovs has been a residential pastoral adviser in a University hall of residence. In the academic year of 2008/09 he was a secretary of the University of Manchester chess club. Maksims is also a volunteer trip leader for the International Society.

In his free-time Maksims plays badminton and learns to play an acoustic guitar. He speaks four European languages fluently: English, German, Russian and Latvian.

Chapter 1

Introduction

This chapter gives a brief introduction to the project described in the dissertation. It covers the motivation, problems and possible solutions to the specified problems. This chapter highlights the major and minor research aims. The last section describes the organisation of the dissertation in a chapter-by-chapter manner.

1.1 Motivation

Modern devices become increasingly complex. Prior to developing a physical prototype of a device, it is usually simulated on a computer with help of numerical methods. The efficient and accurate simulation of electromagnetic behaviour of these devices becomes an important research issue. Another vital topic in industry and academia is the ability to simulate the frequency dependent materials, materials that change their electromagnetic properties depending on the propagating wave frequency. A human body presents an excellent example of a collection of frequency dependent materials. Each human tissue changes its electromagnetic parameters depending on the illuminating wave frequency.

1.2 Problems

The Finite-Difference Time-Domain (FDTD) method is one of the most widely used techniques for the simulation of electromagnetic wave propagation. However, one limitation of the FDTD method is the interdependence of the spatial and temporal discretisation steps, known as the Courant–Friedrichs–Lewy (CFL) stability criterion. Therefore, high spatio-temporal resolution is required by the FDTD approach

in order to simulate an object with fine geometric features. But the high spatio-temporal resolution results in considerable use of computational resources and long execution times.

1.3 Solutions

Subgridding offers a way to increase the FDTD method efficiency. With a subgridding approach the simulation domain is decomposed into a number of subdomains with different spatio-temporal resolution. The main grid with coarse resolution contains the homogeneous object parts and the subgrid with fine resolution models the delicate features of an object. The CFL condition is maintained separately in each grid. Huygens Subgridding (HSG) applied in this work is a very promising subgridding technique operating by means of equivalent currents flowing from the main-to-sub and the sub-to-main grid at each FDTD time step.

1.4 Aims

The main aim of this work is extension of the one-dimensional (1D) frequency-dependent Huygens Subgridding method to three dimensions (3D). In the following dissertation the Frequency-Dependent Finite-Difference Time-Domain method with Huygens Subgridding developed during this project will be called a dispersive HSG method. Minor aims achieved within this project were (i) the development of radio environment setting from the digital human phantom data, (ii) proposal of an application framework for the dispersive HSG method to optimise defibrillators and (iii) testing of the CPU time and memory requirements of the dispersive HSG with the subgridding ratio of 5.

1.5 Organisation

This dissertation is organised in the following manner:

Chapter 2 introduces the most prominent Computational Electromagnetics (CEM) methods, provides the mathematical formulations of the classical FDTD and FD–FDTD methods in three dimensions (3D) and discusses the important properties of numerical algorithms.

Chapter 3 describes the key aspects of a subgridding algorithm and gives an in-depth review of modern subgridding techniques.

Chapter 4 is dedicated to the description of the HSG method. After a short introduction of the main principles the concept of the Total-Field/Scattered-Field technique is explained in Section 4.3. Section 4.4 follows with the discussion of equivalent currents on the Huygens Surfaces (HS). The HSG algorithm and the mathematical formulation are presented in detail in Sections 4.5 and 4.7. Section 4.6 briefly addresses the issue of native HSG instability.

Inclusion of the frequency dependency into the classical HSG method is explained in Chapter 5. Chapter 5 describes the changes necessary to the standard HSG algorithm in order to include the frequency dependency and provides the mathematical equations for the dispersive HSG formulation.

Chapter 6 reports on the numerical results obtained with the dispersive HSG implementation. Seven testing scenarios track the HSG behaviour in various environment settings. One scenario is dedicated to the observation of the HSG instability. Scenario human torso provides an example of wave propagation excited by two defibrillator pads and travelling inside the human torso. Chapter 6 also analyses the computational requirements of the dispersive HSG program.

Chapter 7 concludes this dissertation and Chapter 8 gives prospects for the future work.

Simulation of the wave propagation from the defibrillator through the human torso is a possible application of the dispersive HSG approach developed in this work. To better understand the specifics of this application case Appendix A explains the basics of cardiography and the defibrillation process. A special attention is paid to the numerical simulation of defibrillation.

Chapter 2

Computational Electromagnetics Methods

This chapter provides a brief overview of the Computational Electromagnetics (CEM) methods and introduces the important properties of numerical algorithms. Major sections of this work are dedicated to the formulations of the Finite-Difference Time-Domain (FDTD) and the Frequency-Dependent Finite-Difference Time-Domain (FD–FDTD) methods. Sections 2.3 and 2.4 give detailed theoretical explanations and mathematical equation derivations of both methods. Section 2.4.4 outlines the frequency dispersion models and presents the Auxiliary Differential Equation approach. Finally, Section 2.4.6 presents the implementation of the FD–FDTD method in a programming language.

2.1 Overview of Computational Electromagnetics Methods

Tables 2.1 and 2.2 adopted from [1] provide an introductory comparison of the major CEM methods widely used in academia and industry. The computational methods are evaluated along their common functionality as widely implemented and understood by the CEM community. No exceptional cases are covered by the data in Tables 2.1 and 2.2. Table 2.1 lists key performance features of the Method of Moments (MoM), the Finite Element Method (FEM) and the FDTD method for the open radiation and scattering problems. Radiation condition in Table 2.1 implements correct behaviour of the field far from the source, e.g. in free space the field

strength is inversely proportional to the distance [1]. Columns PEC only, Homogeneous Penetrable and Inhomogeneous Penetrable in Tables 2.1 and 2.2 compare the CEM methods suitability for solution of certain problems: perfectly or highly conducting materials versus homogeneous or inhomogeneous penetrable structures, e.g. dielectrics or human body. Table 2.2 lists the methods applicability for the solution of guided wave problems.

Method	Eq. Form	Calculation Domain	Radiation Condition	PEC only	Hom. Penetr.	Inhom. Penetr.
MoM	integral	frequency	yes	+	+	−
FEM	differential	frequency	no	−	+	+
FDTD	differential	time	no	−	+	+

Table 2.1: Computational electromagnetics methods for open region problems [1]. Symbols "+" and "−" signify good and not optimal methods performance. Abbreviations "Hom. Penetr." and "Inhom. Penetr." stand for homogeneous penetrable and inhomogeneous penetrable problems.

Method	Eq. Form	Calculation Domain	Wideband	PEC only	Hom. Penetr.	Inhom. Penetr.
MoM	integral	frequency	≈	+	+	−
FEM	differential	frequency	≈	+	+	+
FDTD	differential	time	+	+	+	+

Table 2.2: Computational electromagnetics methods for guided wave problems [1]. Symbols "+", "≈" and "−" denote good, satisfactory and not optimal methods performance.

2.1.1 Method of Moments

The MoM is most widely applied in the Radio Frequency (RF) CEM, especially in the area of antenna engineering [1]. In MoM the radiating or scattering structure is represented by a collection of equivalent currents, that are usually surface currents. Surface currents are discretised in wire segments in 1D or surface patches in 2D. Then a matrix equation, that represents the effect of every segment/patch onto every segment/patch, is derived. The inter-segment interaction is calculated by means of a problem-specific Green's function, e.g. free-space Green's function.

After the application of the relevant boundary condition, a system of linear equations is obtained. Solution of the linear equations system approximates the surface current value in each segment or patch. The resulting matrix, fully populated with complex valued entries, is factored or used in an iterative solver. Traditionally, MoM is formulated in the frequency domain. Commercial packages implementing the MoM include: FEKO [2], SuperNEC [3], IE3D [4] and GEMACS [5].

Strong Points

- MoM performs an efficient treatment of perfectly or highly conducting surfaces, whereas only the surface has to be meshed, no meshing of the wrapping "air region" is required.

- By design the MoM incorporates the correct behaviour of the field far from the source (also known as the radiating condition).

- Current density is a key operating variable, which enables straightforward derivation of other important antenna parameters.

- MoM allows to produce efficient formulations for the layered media, e.g. printed antennas, components and feed networks.

Weak Points

- MoM does not handle inhomogeneous materials as well as the other CEM methods formulated with differential equations.

- MoM does not scale well with frequency, where the scaling is $O\big((kd)^6\big)$ with kd denoting the size of a cubic grid structure.

- Some MoM formulations, e.g. based of magnetic field integral equation (MFIE), require the surface to be closed, which is usually impractical.

Summary

The MoM is recommended for the solution of radiating or scattering problems in frequency domain. The method handles perfectly or highly conducting wires and surfaces especially well.

2.1.2   Finite-Difference Time-Domain Method

The FDTD method is based on approximations of partial differential equations and does not require tailored Green's functions as the MoM [1]. The method solves Maxwell's equations directly on a grid staggered in time and in space. The electric and magnetic fields E, H are calculated with a marching-on-in-time algorithm on a regular grid. The FDTD is one of the most widely used schemes in time domain. The FDTD method can be either "explicit" or "implicit". In explicit FDTD method no simultaneous equations are set up and solved. The electromagnetic (EM) field values at the next time-step depend on the current and previous time-step values only. Explicit FDTD method is only conditionally stable (for details refer to Section 2.2.2). CST Microwave Studio®[1] [6] and Remcom XFDTD [7] are the commercial packages offering the FDTD method's implementation.

In implicit FDTD schemes (such as the Alternating-Direction Implicit–Finite-Difference Time-Domain [8] and Crank-Nicolson–Finite-Difference Time-Domain [9]) a set of simultaneous equations is used to calculate the unknowns. From a physics perspective the next time-step value depends on the previous, current and next time-step values of some or all points in the simulation domain [1].

Strong Points

- The FDTD method has an exceptionally simple formulation for a full-wave solver.

- The algorithm offers a straightforward treatment of material inhomogeneities.

- It has a fairly accurate geometric modelling ability, but less versatile than FEM's.

- Wideband solution is available after only one time domain run.

- The method offers a reasonable scaling behaviour in the order of $O\big((kd)^{5.5}\big)$.

- Very good Absorbing Boundary Condition (ABC) is offered by the Perfectly Matched Layer (PML) and its variations.

---

[1]CST Microwave Studio® is based on a more general Finite Integration Technique (FIT), which under certain conditions reduces to FDTD.

Weak Points

- Meshing is inflexible and can introduce "staircase" approximation errors.

- There is an uncertainty about the precise position of ABC, due to half space-step offsets between EM-fields.

- Implementation of dispersive materials requires considerable effort and complicates the initial algorithm.

- The method is less efficient than the MoM for modelling perfectly or highly conducting radiators or scatterers.

- Implementation of higher-order approaches is difficult, partially due to ambiguity of the exact ABC locations.

Summary

The FDTD scheme should be the method of choice for the solution of wideband systems. The algorithm is particularly useful, when quick solutions of any EM-radiation or scattering problems are required. The FDTD method can produce very accurate results, if sufficiently high spatio-temporal resolution is used.

2.1.3   Finite Element Method

The FEM usually formulated in frequency domain easily handles inhomogeneous materials and complex geometries [1]. Two major viewpoints for the derivation of the FEM include (i) variational analysis and (ii) weighted residuals.[2] Unknown field in the FEM is discretised with the mesh of finite elements: triangular elements in 2D and tetrahedrons in 3D. Triangles and tetrahedrons are the simplest forms to mesh the 2D and 3D regions. The Finite Element Analysis (FEA)[3] is aimed for eigenanalysis and deterministic analysis—source-free and driven types of problems respectively. The FEM has no radiating condition and requires an artificial absorbing region within the mesh or a hybridisation with the MoM to terminate the grid. Commercial distributions of the FEM are offered by Ansoft's HFSS [11] and COMSOL's Multiphysics® [12].

---

[2]A residual, also called an error, is a factor introduced into the Laplace equation [10].

[3]Finite Element Analysis (FEA) is a practical application of the Finite Element Method (FEM).

Strong Points

- The algorithm offers straightforward treatment of complex geometries and material inhomogeneities.

- FEM allows simple handling of dispersive materials and eigenvalue problems.

- Scales better in frequency than the MoM. Realistic scaling behaviour lays in between $O\big((kd)^5\big)$ and $O\big((kd)^6\big)$. It is problem-dependent and reflects the matrix sparsity pattern.

- Higher-order basis functions can be easily integrated into the core method.

- Curved geometries can be approximated with the use of conformal elements.

- The method's popularity and maturity in other fields of engineering gave rise to "multi-physics" solutions intertwining Maxwell's equations with the thermal or mechanics phenomena.

Weak Points

- The need for an additional "air region" between the radiator and the absorber results in FEM inferiority compared to the MoM in solving highly conductive radiation problems.

- Mesh generation for the FEM can become a very complex and time consuming process.

- The FEM implementation is more complicated than that of the FDTD, which also results in cumbersome parallelisation.

- Solutions involving higher-order elements require efficient preconditioned iterative solvers.

Summary

The FEM is better suited for the microwave device simulation and eigenvalue calculation. Hybrid FEM/MoM are preferred for the scattering problems simulation, that also involve dispersive media. The FEM can be efficiently applied for the specialised antenna problems.

2.1.4 Other Methods

Other less popular CEM methods include:

Transmission Line Matrix (TLM) method, that resembles the FDTD and discretises an array of short transmission lines equivalent to the original Maxwell's equations. Continuing research of the TLM is stipulated by the method's better suitability (compared with the FDTD) for the simulation of high-frequency circuits. Commercial package is offered by CST MICROSTRIPES™ [13].

Method of Lines (MoL) approximates Maxwell's equations by using semi-analytical solutions along a number of lines. The MoL is targeted for the accurate and memory-efficient simulation of wave guiding structures. No commercial product implementing the MoL is known of.

Generalised Multipole Technique (GMT) applies multipoles, special function-solutions of Maxwell's equations, as basis functions. Careful selection of initial multipole positions is expected from the user. Multipoles are arbitrary functions that exhibit most useful local behaviour. Local behaviour is the function property such that the corresponding field is concentrated around the multipole origin and turns into a singularity at the origin.

2.2 Numerical Algorithm Properties

2.2.1 Numerical Dispersion

Numerical dispersion is an undesirable non-physical characteristic of the FDTD method, when EM-waves propagate with different speeds along different directions.

In a dispersive medium the propagation velocities of EM-wave vary with frequency. In a non-dispersive medium, e.g. free-space, angular frequency ω and wavenumbers k_x, k_y, k_z relate as:

$$\left(\frac{\omega}{c}\right)^2 = k_x^2 + k_y^2 + k_z^2, \tag{2.1}$$

where k_x, k_y, k_z are propagation constants in x, y, z coordinate directions, and c is the speed of light in vacuum.

But even in a non-dispersive medium in the FDTD grid EM-waves travel with different speeds along different propagation directions. Numerical dispersion error

influencing the final result depends on the FDTD cell size and shape, as well as the finite-difference format used for discretisation of Maxwell's equations [14].

Equation (2.1) in 1D for a continuous case reduces to:

$$\left(\frac{\omega}{c}\right)^2 = k_x^2.$$ (2.2)

The phase velocity is defined as:

$$v_p = \frac{\omega}{k_x}.$$ (2.3)

Phase velocity determines the phase propagation speed of each frequency component in the given wave.

Wavelength and temporal period of a continuous case solution are:

$$\lambda_0 = cT, \quad T = \frac{2\pi}{\omega}.$$ (2.4)

In a discretised case a new notion of the spatial grid wavelength is defined as:

$$\lambda_g = \frac{2\pi}{k_x}.$$ (2.5)

Phase velocity and spatial grid wavelength are the two important measures of numerical dispersion, that are related as:

$$\frac{v_p}{c} = \frac{\lambda_g}{\lambda_0}.$$ (2.6)

To analyse numerical dispersion of the FDTD algorithm in Cartesian coordinates consider the plane wave function represented as:

$$P(x, y, z, t) = P_0 \exp\left[J\left(\omega t - k_x x - k_y y - k_z z\right)\right]$$ (2.7)

with $\omega = 2\pi f_w$. In (2.7) x, y, z, t stand for spatial and temporal coordinates, J is an imaginary unit, and f_w is a wave frequency. Using spatial and temporal increments Δx, Δy, Δz and Δt (2.7) can be rewritten as:

$$P^n\left(i, j, k\right) = P_0 \exp\left[J\left(\omega n\Delta t - k_x i\Delta x - k_y j\Delta y - k_z k\Delta z\right)\right],$$ (2.8)

where n, i, j, k are integer indices in time and space.

In free-space EM-wave satisfies the wave equation:

$$\left(\frac{\partial^2}{\partial x^2} + \frac{\partial^2}{\partial y^2} + \frac{\partial^2}{\partial z^2} - \frac{1}{c^2}\frac{\partial^2}{\partial t^2} \right) P = 0. \tag{2.9}$$

After discretising (2.9) with central-difference approximations in time and space it will turn into:

$$\frac{P^n\left(i+1, j, k\right) - 2P^n\left(i, j, k\right) + P^n\left(i-1, j, k\right)}{\Delta x^2} \tag{2.10}$$

$$+ \frac{P^n\left(i, j+1, k\right) - 2P^n\left(i, j, k\right) + P^n\left(i, j-1, k\right)}{\Delta y^2}$$

$$+ \frac{P^n\left(i, j, k+1\right) - 2P^n\left(i, j, k\right) + P^n\left(i, j, k-1\right)}{\Delta z^2}$$

$$= \frac{P^{n+1}\left(i, j, k\right) - 2P^n\left(i, j, k\right) + P^{n-1}\left(i, j, k\right)}{c^2\Delta t^2}.$$

The numerical dispersion relation is obtained by substituting discretised form of the plane wave function (2.8) into discretised form of the wave equation (2.10):

$$\left[\frac{1}{c\Delta t} \sin\left(\frac{\omega\Delta t}{2} \right) \right]^2 =$$

$$\left[\frac{1}{\Delta x} \sin\left(\frac{k_x\Delta x}{2} \right) \right]^2 + \left[\frac{1}{\Delta y} \sin\left(\frac{k_y\Delta y}{2} \right) \right]^2 + \left[\frac{1}{\Delta z} \sin\left(\frac{k_z\Delta y}{2} \right) \right]^2. \tag{2.11}$$

Numerical dispersion relation (2.11) reduces to (2.1) as $\Delta x, \Delta y, \Delta z \to 0$. Hence, numerical dispersion error decreases with the decrease of the FDTD cell size.

Consider an example from [14] presented in Figure 2.1 to verify that numerical dispersion is different along different propagation directions. Figure 2.1 shows the wave propagation in free-space in 2D modelled with the uniform FDTD mesh with $\Delta x = \Delta y$ and a line source oriented along the z-direction. First observation is that the numerical dispersion error is considerably smaller along the diagonals at $\varphi = 45°, 135°, 225°$ and $315°$. The dependency of phase velocity on the angle of propagation through the mesh is called grid anisotropy [15]. Grid anisotropy errors are

usually smaller than errors due to simple numerical dispersion. Second observation is that the numerical dispersion error decreases with the decrease of the spatial increment Δx (refer to Figures 2.1a to 2.1c), that follows from the numerical dispersion relation given by (2.11).

(a) $\Delta x = \Delta y = \dfrac{\lambda}{5}$ (b) $\Delta x = \Delta y = \dfrac{\lambda}{10}$ (c) $\Delta x = \Delta y = \dfrac{\lambda}{20}$
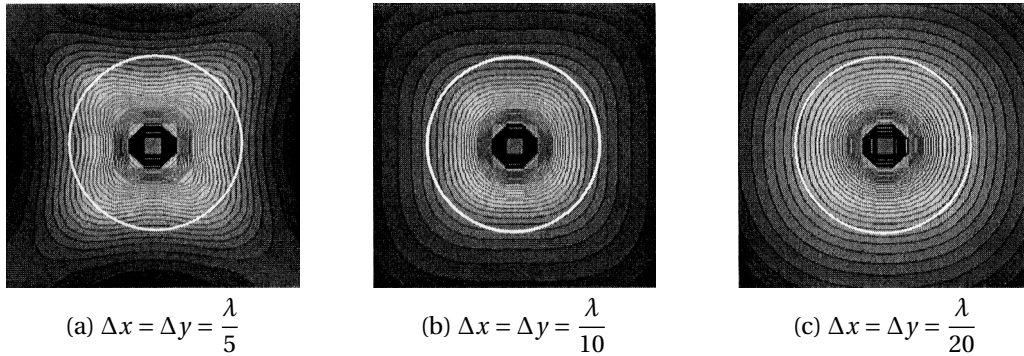
Figure 2.1: Numerical dispersion error [14]. Wave propagation in free-space in 2D from a line source oriented along z-direction. E_z field distribution in the xy-plane. White circle marks the ideal wave front without any numerical dispersion. Symbol λ denotes the numerical wavelength of the propagating wave.

2.2.2   Numerical Stability

Numerical instability is an undesirable property of the explicit differential equations solvers to spuriously increase computation results without limit. Stability of the FDTD technique depends on the nature of the physical model, differencing technique and the quality of the mesh structure [14].

There are two main approaches to analyse numerical stability: (i) the spectral technique of von Neumann and (ii) the complex-frequency analysis of the numerical dispersion relation [16].

These approaches account for two different instability sources of a numerical technique: the spectral (von Neumann) and the causal (Courant). The von Neumann's method deals with the instability arising from the inconsistency between the linear initial-value problem and the linear finite-difference approximation. Lax's equivalence theorem defines the concept of stability analysed by the von Neumann's method. The Lax's theorem states that stability is the necessary and sufficient condition for convergence, if the linear initial-value problem and the linear finite-difference approximation are consistent and well-posed[4] [1, 19]. On the other hand

---

[4]A well-posed problem according to Jacques Hadamard [17] is the problem for which (i) a solution

the Courant criterion analyses, whether a numerical model represents a physical problem sufficiently well.

Next sections provide a brief introduction into the essence of the von Neumann's method and explain the nature and the derivation of the Courant stability criterion.

Stability by the Fourier Series Method (von Neumann's Method)

Stability of a linear two time-level difference equation $u(x, t)$ specified in time interval $0 \le t \le T = Jk$, where T is finite and $\delta x = h \to 0$, $\delta t = k \to 0$, $J \to \infty$ can be analysed with the Fourier series method [20].

First, the initial values at mesh points along $t = 0$ are expressed in terms of a finite Fourier series. Second, the growth of a function, that reduces to this Fourier series, is examined for $t = 0$ using the method of separation of variables [19].

It is beneficial to express the Fourier series in terms of the complex exponential form in place of the sines and cosines:

$$\sum a_n \cos(n\pi x/l) \quad \text{or} \quad \sum b_n \sin(n\pi x/l) \quad \longrightarrow \quad \sum A_n e^{in\pi x/l}, \tag{2.12}$$

where $i = \sqrt{-1}$ and l is an x-interval where the function is defined. It is also helpful to alter the conventional notation of $u_{i,j}$ to $u(ph, qk) = u_{p,q}$.

Using the given notation terms of the Fourier series become:

$$A_n e^{in\pi x/l} = A_n e^{in\pi ph/Nh} = A_n e^{i\beta_n ph}, \tag{2.13}$$

where $\beta_n = n\pi/Nh$ and $Nh = l$.

The initial values of the pivotal points along $t = 0$ can be defined with $u(ph, 0) = u_{p,0}$, $p = 0(1)N$. The $N + 1$ equations are obtained in the following manner:

$$u_{p,0} = \sum_{n=0}^{N} A_n e^{i\beta_n ph}, \quad p = 0, 1, \cdots, N. \tag{2.14}$$

The $N + 1$ equations are sufficient to determine the $N + 1$ unknowns $A_0, A_1, \cdots, A_n$. Hence, the initial mesh values can be expressed in the complex exponential form .

The Fourier series method deals with the linear-difference equations, therefore

---

exists, (ii) the solution is unique and (iii) the solution depends continuously on the initial and/or boundary conditions [1, 18].

the propagation of only one initial value $e^{i\beta ph}$ should be investigated, since the separate solutions are additive. Coefficient A_n is constant and can be neglected.

Propagation of the given term is investigated as the time t grows:

$$u_{p,q} = e^{i\beta x} e^{\alpha t} = e^{i\beta ph} e^{\alpha qk} = e^{i\beta ph} \xi^q, \qquad (2.15)$$

where $\xi = e^{\alpha k}$, α is a complex constant and ξ is an amplification factor.

Finite-difference equations are Lax–Richtmyer stable [21], if $|u_{p,q}|$ is bounded for all $q \leq J$ as $h \to 0$ and $k \to 0$ for all values of β necessary to satisfy the initial conditions.

If exact solution of the difference equations doesn't grow exponentially with time t, the necessary and sufficient condition for stability is:

$$|\xi| \leq 1, \quad \text{i.e.} \quad -1 \leq \xi \leq 1. \qquad (2.16)$$

Else ($u_{p,q}$ increases exponentially with time), the necessary and sufficient condition for stability is:

$$|\xi| \leq 1 + Kk = 1 + O(k), \qquad (2.17)$$

where K is a positive number independent of h, k, β. Example applications of the Fourier series method can be found in [19]. Books of O'Brien et al [20] and Richtmyer and Morton [22] give a detailed explanation of the Fourier series approach.

Complex-Frequency Analysis Approach

Following the complex-frequency analysis approach the numerical dispersion relation (2.11) is solved for the angular frequency ω:

$$\omega = \frac{2}{\Delta t} \sin^{-1} \left(v \Delta t \sqrt{ \frac{1}{\Delta x^2} \sin^2 \left(\frac{k_x \Delta x}{2} \right) + \frac{1}{\Delta y^2} \sin^2 \left(\frac{k_y \Delta y}{2} \right) + \frac{1}{\Delta z^2} \sin^2 \left(\frac{k_z \Delta y}{2} \right) } \right). \qquad (2.18)$$

To consider a more general case the speed of light in vacuum c in (2.18) was changed to the speed of wave propagation in a given medium v:

$$v = \frac{1}{\sqrt{\varepsilon \mu}}, \qquad (2.19)$$

where ε, μ are electric permittivity and magnetic permeability of the medium.

According to the plane wave function relation (2.7), when ω is an imaginary number, the EM-waves will either (i) attenuate rapidly to zero, or (ii) grow exponentially and diverge. This wave behaviour depends on whether the imaginary part of ω is a positive or a negative term. In (2.11) the angular frequency ω is a real number when

$$\left|\sin\left(\frac{\omega\Delta t}{2}\right)\right| \leq 1. \tag{2.20}$$

Therefore, the argument of $\sin^{-1}$ expression in the round brackets of (2.18), must satisfy the following condition:

$$v\Delta t\sqrt{\frac{1}{\Delta x^2}\sin^2\left(\frac{k_x\Delta x}{2}\right) + \frac{1}{\Delta y^2}\sin^2\left(\frac{k_y\Delta y}{2}\right) + \frac{1}{\Delta z^2}\sin^2\left(\frac{k_z\Delta y}{2}\right)} \leq 1. \tag{2.21}$$

Note that in (2.21) the maximum possible value of a sine-squared term under the square root is 1. Then to obtain a stable FDTD solution the time-step Δt must obey:

$$\Delta t \leq \frac{1}{v\sqrt{\frac{1}{\Delta x^2} + \frac{1}{\Delta y^2} + \frac{1}{\Delta z^2}}}. \tag{2.22}$$

Equation (2.22) is called the Courant-Friedrichs-Lewy (CFL) stability condition or simply the Courant criterion. Courant criterion in (2.22) ensures that the time-step Δt is determined by spatial steps $\Delta x, \Delta y, \Delta z$ and the speed of wave propagation in a given medium v. When (2.22) is used as an equality, maximum time-step value Δt_{CFL} is obtained. However, in practice the maximum time-step is used rarely, because Δt_{CFL} at its theoretical limit might be error-prone. Usually the maximum time-step is scaled down by a factor of $N_{CFL} \in (0, 1]$, so that $\Delta t = N_{CFL} \cdot \Delta t_{CFL}$ and (2.22) for practical Δt setting becomes:

$$\Delta t = N_{CFL}\frac{1}{v\sqrt{\frac{1}{\Delta x^2} + \frac{1}{\Delta y^2} + \frac{1}{\Delta z^2}}}, \tag{2.23}$$

where the scaling factor N_{CFL} is called the Courant or the CFL number. Equations (2.24) and (2.25) specify the Courant criterion for 2D and 1D cases respectively:

$$\Delta t \le \frac{1}{v\sqrt{\dfrac{1}{\Delta x^2} + \dfrac{1}{\Delta y^2}}}, \tag{2.24}$$

$$\Delta t \le \frac{\Delta x}{v}. \tag{2.25}$$

It is interesting to note that the higher dimensional cases (2D and 3D) are more restrictive in terms of the Courant criterion. This phenomenon is exemplified in Figure 2.2.
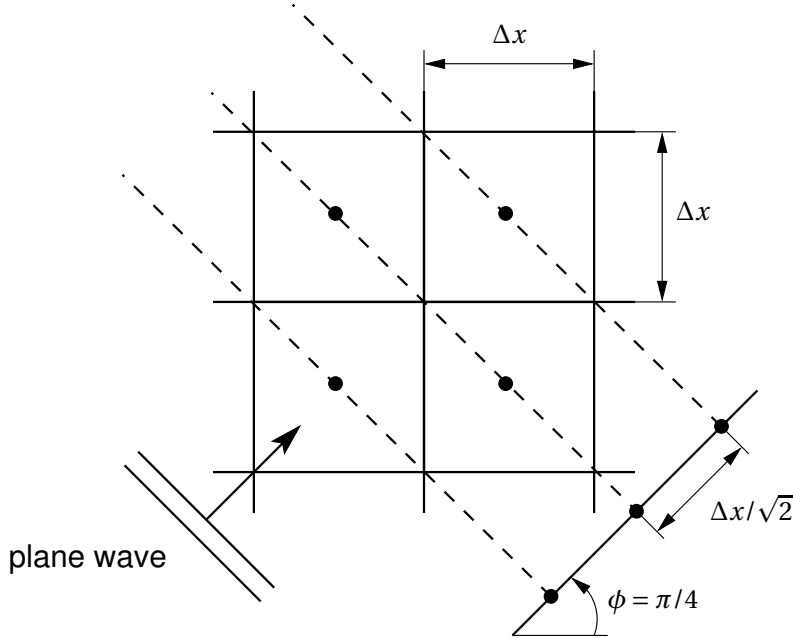
Figure 2.2: Courant criterion in 2D [15]. Plane wave propagates along the diagonals of the squared 2D FDTD mesh. Projections of lines with the constant phase result in a wave propagation along the 1D effective mesh with the cell size of $\Delta x/\sqrt{2}$. To account for such propagation scenarios the Courant criterion in 2D (2.27) should be more restrictive.

Examine (2.25) that defines the propagation time from nth to $(n+1)$th temporal FDTD node as $\Delta t = \Delta x/v$. The case of $\Delta t > \Delta x/v$ violates the causality and the FDTD method yields non-zero field value before reaching the $(n+1)$th node, which results in instability. In case of free-space, the speed of light c bounds the transmission rate across the mesh [15].

Figure 2.3 gives an example of the physical interpretation of the Courant criterion. For a stable solution the physical domain should be a part of the numerical domain. Consider the opposite case, when the physical domain contains the numerical domain. Grid points necessary for a correct approximation of the physical domain lie outside of the numerical domain. The lack of knowledge about the physical domain results in instability.

Solid lines bounding the numerical domain have the slopes of $\Delta t / \Delta z$, while dashed lines have the slopes of $1/v$, where v is the velocity of wave propagation on a line; $v = 1/\sqrt{LC}$ and L, C being the inductance and capacitance of an infinitesimal piece of a lossless transmission line. Physical domain will constitute a part of the numerical, when $1/u \geq \Delta t / \Delta z$, which is the Courant criterion.
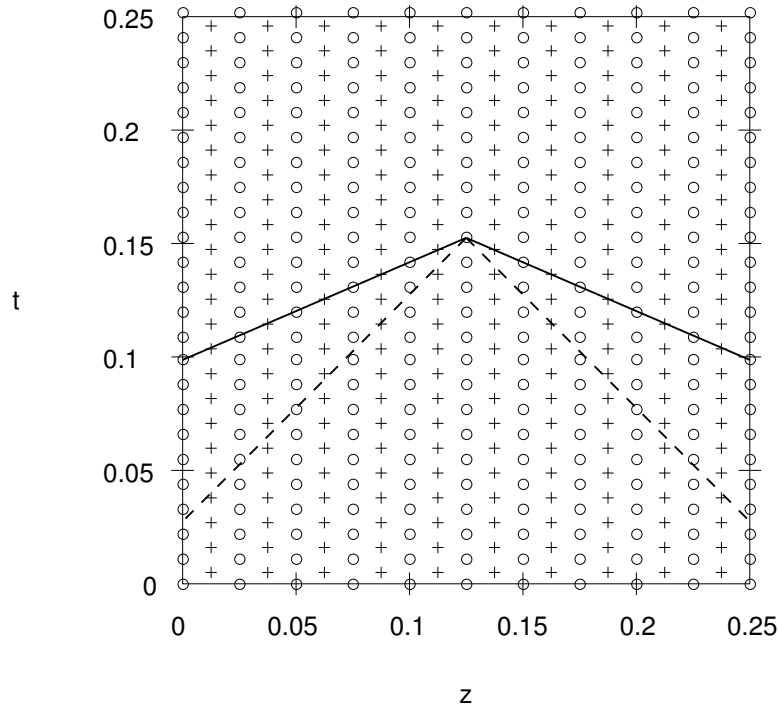
Figure 2.3: Physical interpretation of the Courant criterion [1]. Physical domain of dependence is marked with the solid and numerical domain of dependence—with the dashed lines.

When uniform 3D and 2D FDTD grids are used the inequalities (2.22) and (2.24) reduce to:

$$\Delta t \leq \frac{\Delta x}{v\sqrt{3}} \quad \longrightarrow \quad \Delta t \leq 0.577 \frac{\Delta x}{v}, \tag{2.26}$$

$$\Delta t \leq \frac{\Delta x}{v\sqrt{2}} \quad \longrightarrow \quad \Delta t \leq 0.707\frac{\Delta x}{v}. \tag{2.27}$$

For several media with different values of v, the overall Courant criterion remains valid when the maximum value of v is used.

For any Courant number $N_{CFL} > 1$ the FDTD algorithm will have an exponentially growing, rapidly oscillating sinusoidal numerical wave propagating within the computation grid. This exponentially growing wave is the origin of numerical instability. The selection of spatio-temporal resolution of the FDTD method is a two-step process. First, Electromagnetics expert selects a spatial increment Δx. Spatial step size mainly depends on the problem geometry and is chosen to adequately resolve a given structure. Also the spatial increment size is influenced by the principal components of the spectrum of signals propagating in the simulation space. Finally, the temporal step Δt is determined according to the CFL criterion for 1D, 2D or 3D space.

2.3 Finite-Difference Time-Domain Method

2.3.1 Historic Background

Historically numerical methods were developed for military applications. Since the World War II and during the Cold War numerical methods were used to improve the microwave radar technology. In those times numerical methods solved Maxwell's equations in integral form in frequency domain. Approximately in the 1970s and 1980s direct time domain Maxwell's equations solvers were developed. Direct time domain methods solved Maxwell's equations in differential form on spatial grids or lattices.

The early 1990s saw an expanded interest for the FDTD method. Multiple reasons served for the increased FDTD method popularity. Amongst them are such FDTD method's properties as no use of linear algebra, improved method's accuracy and robustness, natural treatment of impulsive and nonlinear behaviour, method's systematic approach to Maxwell's equations solution (that mostly depends on the structure's geometry) and rapid expansion of computer memory capacities and computer visualisation capabilities.

Since the 1990s there was a dramatic shift in the FDTD method's usage. Modern FDTD applications include global propagation of an Extremely Low Frequency (ELF)

EM-pulse generated by a lightning strike, Specific Absorption Rate (SAR) calculation generated by a mobile phone and absorbed by a human head, Ultrawide Band (UWB) microwave detection of malignant tumours, microwave pulse interaction with a missile radome, induced surface current calculation on the airplane surface, wireless digital interconnect design, photonic crystal microlaser operation and cross-waveguide switch simulation.

After the algorithm development by Kane S. Yee in 1966 [23], the FDTD method was continuously improved and adapted to different classes of problems. Developments important in the context of this work include the FDTD expansion for modelling of frequency-dependent dielectric permittivity by Kashiwa and Fukai [24], Luebbers et al. [25], and Joseph et al. [26] in 1990–1991, design of the Perfectly Matched Layer (PML), highly effective Absorbing Boundary Conditions (ABC), by Bérenger [27], PML extension to 3D by Katz et al. [28] in 1994 and the Convolutional PML (CPML) by Roden and Gedney [29] in 2000.

2.3.2 Maxwell's Equations in Three Dimensions

For a region of space without electric or magnetic currents and with EM-energy absorbing materials the time-dependent Maxwell's equations in differential form are:

Faraday's law:

$$\frac{\partial \boldsymbol{B}}{\partial t} = -\nabla \times \boldsymbol{E} - \boldsymbol{M}. \tag{2.28}$$

Ampère's law:

$$\frac{\partial \boldsymbol{D}}{\partial t} = \nabla \times \boldsymbol{H} - \boldsymbol{J}. \tag{2.29}$$

Gauss' law for electric field:

$$\nabla \cdot \boldsymbol{D} = 0. \tag{2.30}$$

Gauss' law for magnetic field:

$$\nabla \cdot \boldsymbol{B} = 0. \tag{2.31}$$

The following notation is used in the above formulation of the Maxwell's equations:

E electric field (V/m),

D electric flux density (C/m^2),

H magnetic field (A/m),

B magnetic flux density (Wb/m^2),

J electric current density (A/m^2),

M equivalent magnetic current density (V/m^2).

For linear (field-independent), isotropic (direction-independent) and non-dispersive (frequency-independent) materials the following constitutive relationships are true:

$$D = \varepsilon E = \varepsilon_r \varepsilon_0 E, \qquad (2.32)$$

$$B = \mu H = \mu_r \mu_0 H. \qquad (2.33)$$

Notation used in (2.32) and (2.33) is:

ε electrical permittivity (F/m),

ε_r relative permittivity (−),

ε_0 vacuum permittivity ($8.854 \cdot 10^{-12}$ F/m),

μ magnetic permeability (H/m),

μ_r relative permeability (−),

μ_0 vacuum permeability ($4\pi \times 10^{-7}$ H/m).

Let J, M act as independent electromagnetic field (EMF) energy sources J_{src}, M_{src} and allow materials with isotropic, non-dispersive electric and magnetic losses to attenuate EMF energy via conversion to heat energy:

$$J = J_{src} + \sigma E, \qquad (2.34)$$

$$M = M_{src} + \sigma^* H. \qquad (2.35)$$

where

σ electric conductivity (S/m),

σ^* equivalent magnetic loss (Ω/m).

Now substitute (2.32) to (2.35) into (2.28) and (2.29) to obtain Maxwell's curl equations for linear, isotropic, non-dispersive and lossy materials:

$$\frac{\partial \boldsymbol{H}}{\partial t} = -\frac{1}{\mu}\nabla \times \boldsymbol{E} - \frac{1}{\mu}\left(\boldsymbol{M}_{src} + \sigma^* \boldsymbol{H}\right), \tag{2.36}$$

$$\frac{\partial \boldsymbol{E}}{\partial t} = \frac{1}{\varepsilon}\nabla \times \boldsymbol{H} - \frac{1}{\varepsilon}\left(\boldsymbol{J}_{src} + \sigma \boldsymbol{E}\right). \tag{2.37}$$

Writing out vector components in Cartesian coordinates yields a system of six equations that shape foundation of the FDTD method:

$$\frac{\partial H_x}{\partial t} = \frac{1}{\mu}\left[\frac{\partial E_y}{\partial z} - \frac{\partial E_z}{\partial y} - \left(M_{src,x} + \sigma^* H_x\right)\right], \tag{2.38}$$

$$\frac{\partial H_y}{\partial t} = \frac{1}{\mu}\left[\frac{\partial E_z}{\partial x} - \frac{\partial E_x}{\partial z} - \left(M_{src,y} + \sigma^* H_y\right)\right], \tag{2.39}$$

$$\frac{\partial H_z}{\partial t} = \frac{1}{\mu}\left[\frac{\partial E_x}{\partial y} - \frac{\partial E_y}{\partial x} - \left(M_{src,z} + \sigma^* H_z\right)\right], \tag{2.40}$$

$$\frac{\partial E_x}{\partial t} = \frac{1}{\varepsilon}\left[\frac{\partial H_z}{\partial y} - \frac{\partial H_y}{\partial z} - \left(J_{src,x} + \sigma E_x\right)\right], \tag{2.41}$$

$$\frac{\partial E_y}{\partial t} = \frac{1}{\varepsilon}\left[\frac{\partial H_x}{\partial z} - \frac{\partial H_z}{\partial x} - \left(J_{src,y} + \sigma E_y\right)\right], \tag{2.42}$$

$$\frac{\partial E_z}{\partial t} = \frac{1}{\varepsilon}\left[\frac{\partial H_y}{\partial x} - \frac{\partial H_x}{\partial y} - \left(J_{src,z} + \sigma E_z\right)\right]. \tag{2.43}$$

2.3.3 Field Components Placement

Figure 2.4 presents the EMF components placement on the FDTD grid cell. A single FDTD grid cell shown in Figure 2.4 is also known as the Yee unit cell. Yee positioned the EMF components in such way, that every electric field (EF) component is surrounded by four circulating magnetic field (MF) components and also every MF is surrounded by four EF components. This components arrangement produces an

interlinked array of Faraday's and Ampère's laws contours that adheres to the original laws of Physics very well.
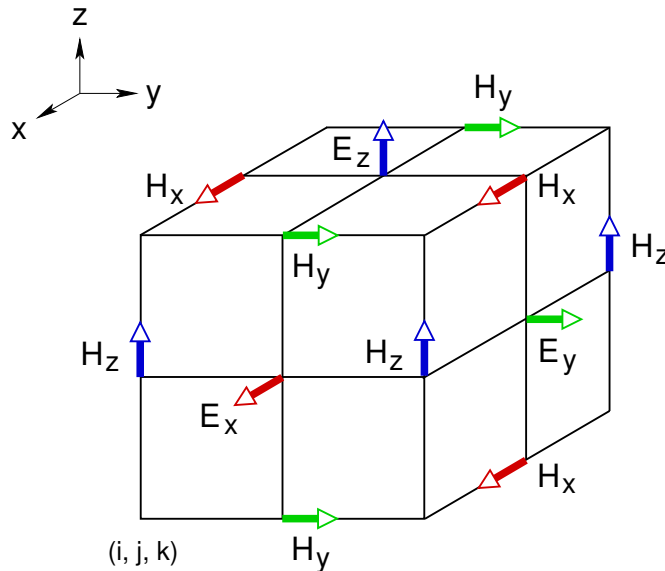
Figure 2.4: Yee unit cell [16]. Electric and magnetic field components placement on the FDTD grid cell. Red, green and blue arrows signify the x, y and z Cartesian coordinate directions. Coordinate origin marked with the indices (i, j, k) is located in the bottom left corner of the figure. Electric field components are placed in the middle of the cell faces, while magnetic field components are positioned in the middle of the cell edges.

According to the original Yee plan the $\boldsymbol{E}$ and $\boldsymbol{H}$ field components are also centred in time domain. Figure 2.5 depicts the "leap-frog" EMF components placement in time and Figure 2.6 illustrates the EMF components arrangement in space and time. Half time-step shifted components ensure that the time-marching FDTD algorithm is fully-explicit and requires no matrix inversion or simultaneous equations solution. Leap-frogging also makes the finite-difference expressions for time derivatives central-difference in nature and second-order accurate. However, the FDTD method is second-order accurate only on equidistant meshes, otherwise the accuracy order lies in between of the numbers 1 and 2.

2.3.4   Benefits of FDTD

The FDTD method possesses a number of benefits. First, it solves Maxwell's equations for both electric and magnetic fields in time and space using the coupled curl equations. This provides a more robust solution than either alone. Application of
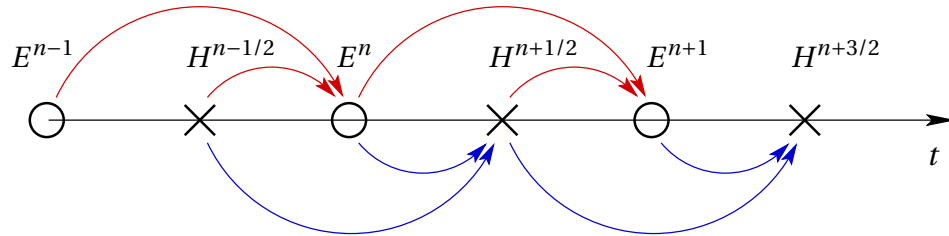
Figure 2.5: Leap-frog components placement in time [15]. Circles denote the electric and crosses the magnetic field components on a time axis t. Electric field calculation dependency is highlighted with red arrows and magnetic—with blue arrows. Half time-step offset of 1/2 between the electric and the magnetic field components makes the FDTD method explicit: electric field components at given time-step depend only on previous time-step values of the electric and magnetic field values, e.g. E^n depends on E^{n-1} and $H^{n-1/2}$. The same principle applies to the magnetic field calculation, e.g. $H^{n+1/2}$ depends on $H^{n-1/2}$ and E^n.
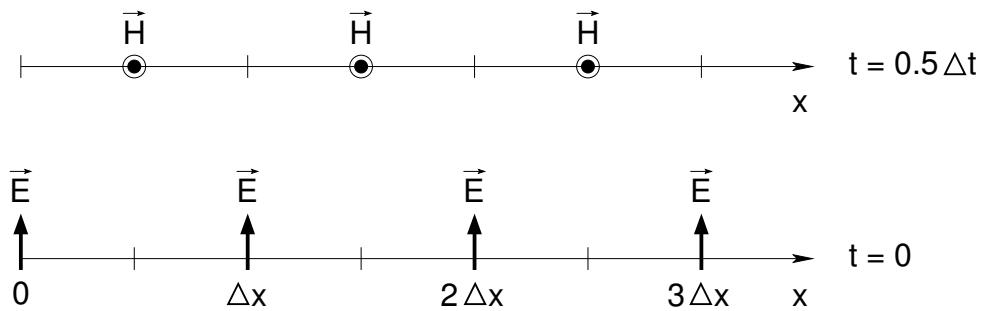
Figure 2.6: Leap-frog components arrangement in space and time domains [16]. Bottom: electric field components are shown in 1D at spatial locations with $x = 0, \Delta x, 2\Delta x, 3\Delta x$ and temporal location $t = 0$. Top: magnetic field components are depicted in 1D at shifted spatial locations of $x = \frac{1}{2}\Delta x, \frac{3}{2}\Delta x, \frac{5}{2}\Delta x$ and shifted temporal location $t = \frac{1}{2}\Delta t$.

interdependent Maxwell's equations also ensures the FDTD method is accurate for wider classes of structures. Another benefit of the FDTD scheme is the possibility to model unique electric or magnetic field features (E or H singularities) individually when both fields are available. These unique field features include tangential H singularities near edges and corners, azimuthal (looping) H singularities near thin wires and radial E singularities near points, edges and thin wires [16].

Staggered component placement, when each EF component is surrounded by four MF components and each MF component is surrounded by four EF components, yields an interlinked array of Faraday's law and Ampère's law contours. Therefore, the Yee algorithm simultaneously conforms to the pointwise differential and the macroscopic integral forms of the Maxwell's equations. Staggering of field components allows to maintain the continuity of tangential electric and magnetic fields naturally. For example, consider an interface of two different materials in the FDTD grid. Given the interface is parallel to one of the coordinate axes the discontinuity of tangential field components can be addressed by specifying the ε and μ at every point of the grid. This leads to a "staircase" approximation of the interface, where the quality of such approximation depends on the density of the FDTD mesh [16].

2.3.5   Yee Notation

Yee introduced a special notation for a single space point on a uniform rectangular lattice:

$$(i, j, k) = (i\Delta x, j\Delta y, k\Delta z), \tag{2.44}$$

where $\Delta x, \Delta y, \Delta z$ stand for the space increments in x, y, z coordinate directions, and i, j, k are integer numbers. Yee has also proposed a way to denote a function u of space and time:

$$u(i\Delta x, j\Delta y, k\Delta z, n\Delta t) = u^n\left(i, j, k\right), \tag{2.45}$$

with Δt being a time increment and n an integer number.

2.3.6   Central-Difference Approximations

Important for the derivation of the FDTD method are the definitions of the centred finite-difference (also called central-difference) approximations for space and time. First partial space derivative of function u in x-direction evaluated at time $t_n = n\Delta t$ is:

$$\frac{\partial u}{\partial x}\left(i\Delta x,\, j\Delta y,\, k\Delta z,\, n\Delta t\right) = \frac{u^n\left(i+\frac{1}{2},\, j,\, k\right) - u^n\left(i-\frac{1}{2},\, j,\, k\right)}{\Delta x} + O\left((\Delta x)^2\right). \quad (2.46)$$

Notice the $\pm\frac{1}{2}$ increment in x-coordinate (index i) that implements the space finite-difference over $\pm\frac{1}{2}\Delta x$.

By analogy the time partial derivative of u is approximated with (2.47):

$$\frac{\partial u}{\partial t}\left(i\Delta x,\, j\Delta y,\, k\Delta z,\, n\Delta t\right) = \frac{u^{n+\frac{1}{2}}\left(i,\, j,\, k\right) - u^{n-\frac{1}{2}}\left(i,\, j,\, k\right)}{\Delta t} + O\left((\Delta t)^2\right). \quad (2.47)$$

Here the $\pm\frac{1}{2}$ increment in time coordinate (exponent n) denotes the time finite-difference over $\pm\frac{1}{2}\Delta t$.

Another important concept used in the FDTD method's formulation is the semi-implicit (also known as the central-average) approximation:

$$u^n\left(i,\, j,\, k\right) = \frac{u^{n+\frac{1}{2}}\left(i,\, j,\, k\right) + u^{n-\frac{1}{2}}\left(i,\, j,\, k\right)}{2}. \quad (2.48)$$

Equation (2.48) means that any function u at the time moment of n can be derived as an average of this function half time-step back and half time-step forward in time.

2.3.7 Finite-Difference Formulation of Maxwell's Equations

Electric Field Components

Refer to Figure 2.4 to find the electric field component $E_x\left(i,\, j+\frac{1}{2},\, k+\frac{1}{2}\right)$, that is located at the front face of the Yee unit cell facing the reader. Take a note of the four surrounding magnetic field components $H_z\left(i,\, j,\, k+\frac{1}{2}\right)$, $H_z\left(i,\, j+1,\, k+\frac{1}{2}\right)$, $H_y\left(i,\, j+\frac{1}{2},\, k\right)$ and $H_y\left(i,\, j+\frac{1}{2},\, k+1\right)$. The finite-difference approximation of the scalar Maxwell's equations (2.41) for the $E_x^n\left(i,\, j+\frac{1}{2},\, k+\frac{1}{2}\right)$ component is:

$$\frac{E_x^{n+\frac{1}{2}}\left(i,\, j+\frac{1}{2},\, k+\frac{1}{2}\right) - E_x^{n-\frac{1}{2}}\left(i,\, j+\frac{1}{2},\, k+\frac{1}{2}\right)}{\Delta t} =$$

$$
\frac{1}{\varepsilon\left(i,\,j+\frac{1}{2},\,k+\frac{1}{2}\right)} \cdot \left(
\begin{array}{c}
\dfrac{H_z^n\left(i,\,j+1,\,k+\frac{1}{2}\right) - H_z^n\left(i,\,j,\,k+\frac{1}{2}\right)}{\Delta y} \\[2em]
-\dfrac{H_y^n\left(i,\,j+\frac{1}{2},\,k+1\right) - H_y^n\left(i,\,j+\frac{1}{2},\,k\right)}{\Delta z} \\[2em]
-J_{src,x}^n\left(i,\,j+\frac{1}{2},\,k+\frac{1}{2}\right) - \sigma\left(i,\,j+\frac{1}{2},\,k+\frac{1}{2}\right) E_x^n\left(i,\,j+\frac{1}{2},\,k+\frac{1}{2}\right)
\end{array}
\right).
$$

$$(2.49)$$

It is necessary to apply the semi-implicit approximation of (2.48) to convert the $E_x^n\left(i,\,j+\frac{1}{2},\,k+\frac{1}{2}\right)$ term to the half time-step locations. Equation (2.50) is obtained after using the semi-implicit approximation and moving the Δt to the right-hand side:

$$
E_x^{n+\frac{1}{2}}\left(i,\,j+\frac{1}{2},\,k+\frac{1}{2}\right) - E_x^{n-\frac{1}{2}}\left(i,\,j+\frac{1}{2},\,k+\frac{1}{2}\right) =
$$

$$
\frac{\Delta t}{\varepsilon\left(i,\,j+\frac{1}{2},\,k+\frac{1}{2}\right)} \cdot \left(
\begin{array}{c}
\dfrac{H_z^n\left(i,\,j+1,\,k+\frac{1}{2}\right) - H_z^n\left(i,\,j,\,k+\frac{1}{2}\right)}{\Delta y} \\[2em]
-\dfrac{H_y^n\left(i,\,j+\frac{1}{2},\,k+1\right) - H_y^n\left(i,\,j+\frac{1}{2},\,k\right)}{\Delta z} \\[2em]
-J_{src,x}^n\left(i,\,j+\frac{1}{2},\,k+\frac{1}{2}\right) \\[2em]
-\sigma\left(i,\,j+\frac{1}{2},\,k+\frac{1}{2}\right) \cdot \left(\dfrac{E_x^{n+\frac{1}{2}}\left(i,\,j+\frac{1}{2},\,k+\frac{1}{2}\right) + E_x^{n-\frac{1}{2}}\left(i,\,j+\frac{1}{2},\,k+\frac{1}{2}\right)}{2}\right)
\end{array}
\right).
$$

$$(2.50)$$

Collecting $E_x^{n+\frac{1}{2}}\left(i,\,j+\frac{1}{2},\,k+\frac{1}{2}\right)$ on the left-hand side yields (2.51):

$$
\left(1 + \frac{\sigma\left(i,\,j+\frac{1}{2},\,k+\frac{1}{2}\right)\Delta t}{2\varepsilon\left(i,\,j+\frac{1}{2},\,k+\frac{1}{2}\right)}\right) E_x^{n+\frac{1}{2}}\left(i,\,j+\frac{1}{2},\,k+\frac{1}{2}\right) =
$$

$$
\left(1 - \frac{\sigma\left(i,\,j+\frac{1}{2},\,k+\frac{1}{2}\right)\Delta t}{2\varepsilon\left(i,\,j+\frac{1}{2},\,k+\frac{1}{2}\right)}\right) E_x^{n-\frac{1}{2}}\left(i,\,j+\frac{1}{2},\,k+\frac{1}{2}\right)
$$

$$+ \frac{\Delta t}{\varepsilon\left(i, j+\frac{1}{2}, k+\frac{1}{2}\right)} \cdot \begin{pmatrix} \dfrac{H_z^n\left(i, j+1, k+\frac{1}{2}\right) - H_z^n\left(i, j, k+\frac{1}{2}\right)}{\Delta y} \\[2em] -\dfrac{H_y^n\left(i, j+\frac{1}{2}, k+1\right) - H_y^n\left(i, j+\frac{1}{2}, k\right)}{\Delta z} \\[2em] -J_{src,x}^n\left(i, j+\frac{1}{2}, k+\frac{1}{2}\right) \end{pmatrix}. \quad (2.51)$$

The final form of the explicit time-stepping relation for $E_x^{n+\frac{1}{2}}\left(i, j+\frac{1}{2}, k+\frac{1}{2}\right)$ is obtained by dividing both sides of (2.51) by $\left(1 + \dfrac{\sigma\left(i, j+\frac{1}{2}, k+\frac{1}{2}\right)\Delta t}{2\varepsilon\left(i, j+\frac{1}{2}, k+\frac{1}{2}\right)}\right)$:

$$E_x^{n+\frac{1}{2}}\left(i, j+\frac{1}{2}, k+\frac{1}{2}\right) = \left(\frac{1 - \dfrac{\sigma\left(i, j+\frac{1}{2}, k+\frac{1}{2}\right)\Delta t}{2\varepsilon\left(i, j+\frac{1}{2}, k+\frac{1}{2}\right)}}{1 + \dfrac{\sigma\left(i, j+\frac{1}{2}, k+\frac{1}{2}\right)\Delta t}{2\varepsilon\left(i, j+\frac{1}{2}, k+\frac{1}{2}\right)}}\right) E_x^{n-\frac{1}{2}}\left(i, j+\frac{1}{2}, k+\frac{1}{2}\right)$$

$$+ \left(\frac{\dfrac{\Delta t}{\varepsilon\left(i, j+\frac{1}{2}, k+\frac{1}{2}\right)}}{1 + \dfrac{\sigma\left(i, j+\frac{1}{2}, k+\frac{1}{2}\right)\Delta t}{2\varepsilon_{\left(i, j+\frac{1}{2}, k+\frac{1}{2}\right)}}}\right) \cdot \begin{pmatrix} \dfrac{H_z^n\left(i, j+1, k+\frac{1}{2}\right) - H_z^n\left(i, j, k+\frac{1}{2}\right)}{\Delta y} \\[2em] -\dfrac{H_y^n\left(i, j+\frac{1}{2}, k+1\right) - H_y^n\left(i, j+\frac{1}{2}, k\right)}{\Delta z} \\[2em] -J_{src,x}^n\left(i, j+\frac{1}{2}, k+\frac{1}{2}\right) \end{pmatrix}. \quad (2.52)$$

E_y and E_z components on the visible faces of the Yee unit cell $E_y^{n+\frac{1}{2}}\left(i-\frac{1}{2}, j+1, k+\frac{1}{2}\right)$ and $E_z^{n+\frac{1}{2}}\left(i-\frac{1}{2}, j+\frac{1}{2}, k+1\right)$ (Refer to Figure 2.4) are derived analogously:

$$E_y^{n+\frac{1}{2}}\left(i-\frac{1}{2}, j+1, k+\frac{1}{2}\right) = \left(\frac{1 - \dfrac{\sigma\left(i-\frac{1}{2}, j+1, k+\frac{1}{2}\right)\Delta t}{2\varepsilon\left(i-\frac{1}{2}, j+1, k+\frac{1}{2}\right)}}{1 + \dfrac{\sigma\left(i-\frac{1}{2}, j+1, k+\frac{1}{2}\right)\Delta t}{2\varepsilon\left(i-\frac{1}{2}, j+1, k+\frac{1}{2}\right)}}\right) E_y^{n-\frac{1}{2}}\left(i-\frac{1}{2}, j+1, k+\frac{1}{2}\right)$$

$$
+ \left(\frac{\dfrac{\Delta t}{\varepsilon\left(i-\frac{1}{2}, j+1, k+\frac{1}{2}\right)}}{1 + \dfrac{\sigma\left(i-\frac{1}{2}, j+1, k+\frac{1}{2}\right)\Delta t}{2\varepsilon\left(i-\frac{1}{2}, j+1, k+\frac{1}{2}\right)}} \right) \cdot \left(\begin{array}{c} \dfrac{H_x^n\left(i-\frac{1}{2}, j+1, k+1\right) - H_x^n\left(i-\frac{1}{2}, j+1, k\right)}{\Delta z} \\[2ex] -\dfrac{H_z^n\left(i, j+1, k+\frac{1}{2}\right) - H_z^n\left(i-1, j+1, k+\frac{1}{2}\right)}{\Delta x} \\[2ex] -J_{src,y}^n\left(i-\frac{1}{2}, j+1, k+\frac{1}{2}\right) \end{array} \right)
$$

$$(2.53)$$

and

$$
E_z^{n+\frac{1}{2}}\left(i-\tfrac{1}{2}, j+\tfrac{1}{2}, k+1\right) = \left(\frac{1 - \dfrac{\sigma\left(i-\frac{1}{2}, j+\frac{1}{2}, k+1\right)\Delta t}{2\varepsilon\left(i-\frac{1}{2}, j+\frac{1}{2}, k+1\right)}}{1 + \dfrac{\sigma\left(i-\frac{1}{2}, j+\frac{1}{2}, k+1\right)\Delta t}{2\varepsilon\left(i-\frac{1}{2}, j+\frac{1}{2}, k+1\right)}} \right) E_z^{n-\frac{1}{2}}\left(i-\tfrac{1}{2}, j+\tfrac{1}{2}, k+1\right)
$$

$$
+ \left(\frac{\dfrac{\Delta t}{\varepsilon\left(i-\frac{1}{2}, j+\frac{1}{2}, k+1\right)}}{1 + \dfrac{\sigma\left(i-\frac{1}{2}, j+\frac{1}{2}, k+1\right)\Delta t}{2\varepsilon\left(i-\frac{1}{2}, j+\frac{1}{2}, k+1\right)}} \right) \cdot \left(\begin{array}{c} \dfrac{H_y^n\left(i, j+\frac{1}{2}, k+1\right) - H_y^n\left(i-1, j+\frac{1}{2}, k+1\right)}{\Delta x} \\[2ex] -\dfrac{H_x^n\left(i-\frac{1}{2}, j+1, k+1\right) - H_x^n\left(i-\frac{1}{2}, j, k+1\right)}{\Delta y} \\[2ex] -J_{src,z}^n\left(i-\frac{1}{2}, j+\frac{1}{2}, k+1\right) \end{array} \right) .
$$

$$(2.54)$$

Magnetic Field Components

Time-stepping relations for magnetic field components are derived in a similar way. Figure 2.4 shows the magnetic field components locations in the Yee unit cell. H_x, H_y and H_z are calculated as follows:

$$
H_x^{n+1}\left(i-\tfrac{1}{2}, j+1, k+1\right) = \left(\frac{1 - \dfrac{\sigma^*\left(i-\frac{1}{2}, j+1, k+1\right)\Delta t}{2\mu\left(i-\frac{1}{2}, j+1, k+1\right)}}{1 + \dfrac{\sigma^*\left(i-\frac{1}{2}, j+1, k+1\right)\Delta t}{2\mu\left(i-\frac{1}{2}, j+1, k+1\right)}} \right) H_x^n\left(i-\tfrac{1}{2}, j+1, k+1\right)
$$

$$
+\left(\frac{\frac{\Delta t}{\mu\left(i-\frac{1}{2}, j+1, k+1\right)}}{1+\frac{\sigma^*\left(i-\frac{1}{2}, j+1, k+1\right)\Delta t}{2\mu\left(i-\frac{1}{2}, j+1, k+1\right)}}\right)\cdot\left(\begin{array}{c}\dfrac{E_y^{n+\frac{1}{2}}\left(i-\frac{1}{2}, j+1, k+\frac{3}{2}\right)-E_y^{n+\frac{1}{2}}\left(i-\frac{1}{2}, j+1, k+\frac{1}{2}\right)}{\Delta z}\\[4mm]-\dfrac{E_z^{n+\frac{1}{2}}\left(i-\frac{1}{2}, j+\frac{3}{2}, k+1\right)-E_z^{n+\frac{1}{2}}\left(i-\frac{1}{2}, j+\frac{1}{2}, k+1\right)}{\Delta y}\\[4mm]-M_{src,x}^{n+\frac{1}{2}}\left(i-\frac{1}{2}, j+1, k+1\right)\end{array}\right),
$$

$$(2.55)$$

$$
H_y^{n+1}\left(i, j+\frac{1}{2}, k+1\right)=\left(\frac{1-\frac{\sigma^*\left(i, j+\frac{1}{2}, k+1\right)\Delta t}{2\mu\left(i, j+\frac{1}{2}, k+1\right)}}{1+\frac{\sigma^*\left(i, j+\frac{1}{2}, k+1\right)\Delta t}{2\mu\left(i, j+\frac{1}{2}, k+1\right)}}\right)H_y^n\left(i, j+\frac{1}{2}, k+1\right)
$$

$$
+\left(\frac{\frac{\Delta t}{\mu\left(i, j+\frac{1}{2}, k+1\right)}}{1+\frac{\sigma^*\left(i, j+\frac{1}{2}, k+1\right)\Delta t}{2\mu\left(i, j+\frac{1}{2}, k+1\right)}}\right)\cdot\left(\begin{array}{c}\dfrac{E_z^{n+\frac{1}{2}}\left(i+\frac{1}{2}, j+\frac{1}{2}, k+1\right)-E_z^{n+\frac{1}{2}}\left(i-\frac{1}{2}, j+\frac{1}{2}, k+1\right)}{\Delta x}\\[4mm]-\dfrac{E_x^{n+\frac{1}{2}}\left(i, j+\frac{1}{2}, k+\frac{3}{2}\right)-E_x^{n+\frac{1}{2}}\left(i, j+\frac{1}{2}, k+\frac{1}{2}\right)}{\Delta z}\\[4mm]-M_{src,y}^{n+\frac{1}{2}}\left(i, j+\frac{1}{2}, k+1\right)\end{array}\right)
$$

$$(2.56)$$

and

$$
H_z^{n+1}\left(i, j+1, k+\frac{1}{2}\right)=\left(\frac{1-\frac{\sigma^*\left(i, j+1, k+\frac{1}{2}\right)\Delta t}{2\mu\left(i, j+1, k+\frac{1}{2}\right)}}{1+\frac{\sigma^*\left(i, j+1, k+\frac{1}{2}\right)\Delta t}{2\mu\left(i, j+1, k+\frac{1}{2}\right)}}\right)H_z^n\left(i, j+1, k+\frac{1}{2}\right)
$$

$$+ \left(\frac{\frac{\Delta t}{\mu\left(i, j+1, k+\frac{1}{2}\right)}}{1 + \frac{\sigma^*\left(i, j+1, k+\frac{1}{2}\right)\Delta t}{2\mu\left(i, j+1, k+\frac{1}{2}\right)}} \right) \cdot \left(\begin{array}{c} \dfrac{E_x^{n+\frac{1}{2}}\left(i, j+\frac{3}{2}, k+\frac{1}{2}\right) - E_x^{n+\frac{1}{2}}\left(i, j+\frac{1}{2}, k+\frac{1}{2}\right)}{\Delta y} \\[2em] -\dfrac{E_y^{n+\frac{1}{2}}\left(i+\frac{1}{2}, j+1, k+\frac{1}{2}\right) - E_y^{n+\frac{1}{2}}\left(i-\frac{1}{2}, j+1, k+\frac{1}{2}\right)}{\Delta x} \\[2em] -M_{src,z}^{n+\frac{1}{2}}\left(i, j+1, k+\frac{1}{2}\right) \end{array} \right) \cdot$$

$$(2.57)$$

2.3.8 Conclusion

Each EF or MF component in each time-stepping relation (2.52) to (2.57) depends on its own value at the previous time-step, values of four surrounding components and the values of electric or magnetic current sources. With the system of six time-stepping (2.52) to (2.57) the FDTD algorithm calculates the EMF values for all points of the space grid for the entire simulation time.

Section 2.3.7 presented the FDTD method formulation in Cartesian coordinates. However, depending on the problem geometry and the required wave–structure interaction accuracy, formulations for alternative grids are possible, e.g. polar grid, Cartesian grid with collocated EMF positions and hexagonal grid. Hexagonal grids have large potential in increasing the computation accuracy, because they reduce the numerical phase velocity well below that of Yee's Cartesian grid [16].

1: **for** each time-step $n \in [1, t_{max}]$ **do**
2:     **calc** H^n
3:     **calc** E^n
4:     **excite** $E^n\left(T_x\right)$
5:     **output** $E^n\left(R_x\right)$
6:     **term** $E^n\left(ABC\right)$
7: **end for**

Algorithm 1: FDTD pseudocode. Parameter t_{max} specifies the total number of simulation time-steps. Abbreviations "calc" and "term" stand for calculate and terminate.

Algorithm 1 shows the major steps of the FDTD method in pseudocode. A sequence of steps is repeated for each iteration of the time-step loop. First magnetic and then electric field values are calculated for the entire FDTD grid. Afterwards the electric field is excited at the excitation source location T_x.[5] Required electric field

values at the observation points R_x are printed out. The calculation of E values in the Absorbing Boundary Condition (ABC) region concludes the time-step loop iteration. Algorithm 1 illustrates the FDTD method in a special form. Additional steps for the excitation and output of magnetic field H might be added in case the user is interested in behaviour of the magnetic field. When PML is applied as the ABC, the magnetic field has to be terminated in the ABC region similarly to the electric field.

2.4 Frequency-Dependent Finite-Difference Time-Domain Method

2.4.1 Important Electromagnetic Properties

Research in the areas of aerial and ground-penetrating radars, high power microwaves, bio-electromagnetics, bio- and nanophotonics, and microlasers requires solutions of Maxwell's equations for materials exhibiting frequency-dispersive dielectric properties, non-linearity and gain [16].

Key characteristics of such materials to take into account during the computation are:

Linear dispersion: material's electric permittivity ε and magnetic permeability μ vary with frequency at low intensities of EM-fields.

Non-linear dispersion occurs when the strength of material's non-linearity varies with the sinusoidal frequency of the EM-wave. Non-linearity means that material's ε and μ change with intensity of the wave's local EM-field or Poynting power flux. Non-linearity is usually exhibited at high intensities.

Gain is the progressive amplitude increase of the EM-wave propagating in the material. Gain is usually exhibited by an active dielectric material that draws power from an external source, e.g. a laser drawing power from a pump. Gain can also be frequency-dependent and nonlinear.

---

[5]Symbols T_x and R_x denote the excitation and observation locations. This notation is common in the area of Electrical and Electronic Engineering (EEE). Letters "T" and "R" originated from the first letters of words "Transmitter" and "Receiver".

2.4.2 Practical Value of Frequency Dispersion

In 2002 the US Federal Communication Commission (FCC) applied a spectral mask for the operation of the UWB devices and declared an unlicensed UWB signal use [30]. UWB signal occupies 500 MHz or more in the frequency range of 3.1–10.6 GHz. The FCC recommendation stimulated an increased interest and a rapid development of UWB devices. This also had an effect on the CEM methods, which needed to properly represent the physical phenomena of the UWB waves. The UWB signal is characterised by very short pulses over a wide band of frequency. This UWB property allows to produce high resolution medical images and high throughput communication systems. The major UWB application ares are the radar and positioning systems, biomedical and through-wall imaging as well as remote monitoring [31].

2.4.3 Effect of Frequency Dispersion

The assumption of media parameters being constant is only valid for a narrow frequency band [32]. In a broadband pulse propagation the frequency-dependency of a medium should be taken into account. Figure 2.7 illustrates the change of ε and σ with the wave frequency in an human heart. Frequency dispersion is the variation of the dielectric properties with frequency. A medium where ε and μ are the functions of frequency $\varepsilon(f_w)$ and $\mu(f_w)$ is called a dispersive medium.

The dispersive medium reaction to frequency may be represented as a three-step superposition of (i) an instantaneous response (also known as the infinite frequency response), (ii) a retarded response, that comes from the energy initially absorbed and then returned by the medium and (iii) a time-delayed response that is caused by the material inertia and energy dispersion.

In a frequency-dispersive medium the electric permittivity ε becomes a complex number shown in (2.58). Complex form of ε reflects how the physical process in a medium affects the electric field:

$$\varepsilon = \varepsilon_{(Re)} - J\varepsilon_{(Im)}, \tag{2.58}$$

where the real part of complex permittivity $\varepsilon_{(Re)}$ is related to the amount of energy from an external field stored in a material and the imaginary part $\varepsilon_{(Im)}$ is related to the loss factor and the amount of energy dissipated or absorbed by the material.

The effect of frequency dispersion can be explained by the relaxation time—the time it takes dipoles to polarise, when the electric field is applied. Polar molecules
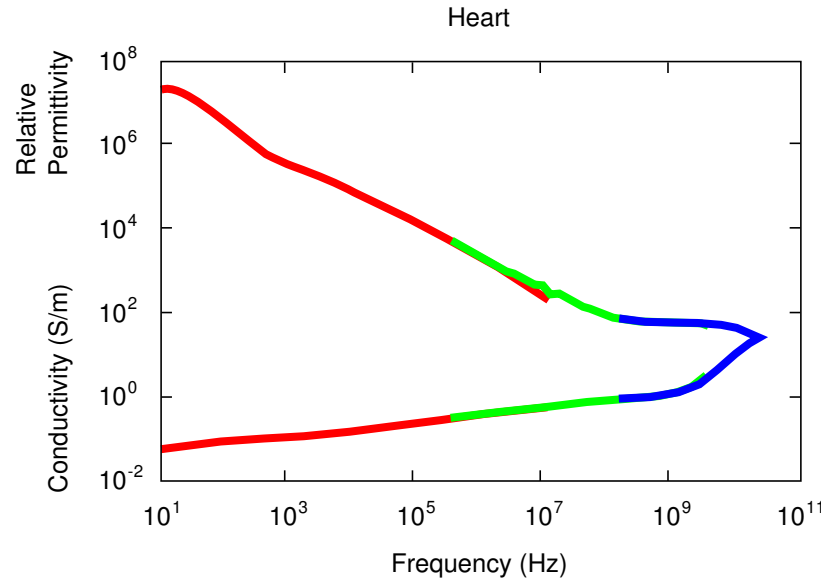
Figure 2.7: Conductivity and relative permittivity over wave frequency in human heart [33]. Experimental data measured in the frequency region of 10 Hz to 20 GHz. Colours red, green and blue illustrate the measurements in the low, medium and high frequency regimes.

of a dispersive medium rotate, as if they were in a damping frictional medium.

2.4.4 Models for Frequency Dispersion

Three main models exist to characterise the frequency-dependent properties of materials [31]:

Debye relaxation is the most widely used model. Approximately 60% of all FD–FDTD methods incorporate the Debye relaxation approach. Based on the rotational motion of molecules Debye model is also appropriate for the simulation of polar liquids in the microwave regime. One of the Debye model drawbacks is the inability to treat meta-materials (materials with negative ε and μ).

Debye medium is defined by a complex-valued, frequency-domain susceptibility function for a number of real poles P at distinct frequencies. The relative permittivity ε_r in Debye relaxation model is expressed as:

$$\varepsilon_r(\omega) = \varepsilon_\infty + \sum_{p=1}^{P} \frac{\Delta\varepsilon_p}{1 + J\omega\tau_p}, \tag{2.59}$$

where $\Delta\varepsilon_p = \varepsilon_{s,p} - \varepsilon_{\infty,p}$. Symbols ε_r, ε_s and ε_∞ denote relative, relative static and relative optical permittivities, $\Delta\varepsilon_p$ stands for the relative permittivity change due to the Debye pole p, J is an imaginary unit, ω is an angular frequency and τ is the pole relaxation time. Index p signifies a term in relation to a specific Debye pole [16].

Lorentz–Drude rests on the idea of bounded charge motion and proposes a system with a number of resonant frequencies. Approximately 35% of CEM methods use this model. Lorenz–Drude model is also capable of handling the metamaterials efficiently.

The complex-valued, frequency domain susceptibility function with a number of complex-conjugate pole pairs defines a Lorentz medium. The relative permittivity using a Lorentzian resonance model is expressed as:

$$\varepsilon_r(\omega) = \varepsilon_\infty + \sum_{p=1}^{P} \frac{\Delta\varepsilon_p \omega_p^2}{\omega_p^2 + 2J\omega\delta_p - \omega_p^2}, \tag{2.60}$$

where $\Delta\varepsilon_p = \varepsilon_{s,p} - \varepsilon_{\infty,p}$. Parameter $\Delta\varepsilon_p$ denotes the change in relative permittivity due to the Lorentz pole pair, ω_p signifies the frequency of the pole pair (undamped resonant frequency of the medium) and δ_p stands for a damping coefficient [16]. The rest of the notation is identical to Debye relaxation model defined in (2.59).

Drude model is usually applied at optical wavelengths to account for the physics of internal electron motion in the wave–metal interaction problems. Relative permittivity in Drude medium is:

$$\varepsilon_r(\omega) = \varepsilon_\infty - \sum_{p=1}^{P} \frac{\omega_p^2}{\omega^2 - J\omega\tau_p^{-1}}, \tag{2.61}$$

with ω_p denoting the Drude pole frequency [16].

Cole–Cole model resides on the Cole–Cole circular arc law [31]. Only 5% of commercial and academic CEM software implement frequency-dependency with the Cole–Cole approach. The relative permittivity in a Cole–Cole model is expressed as:

$$\varepsilon_r(\omega) = \varepsilon_\infty + \sum_{p=1}^{P} \frac{\Delta\varepsilon_p}{1 + (j\omega\tau_p)^\alpha}, \tag{2.62}$$

where $\Delta\varepsilon_p = \varepsilon_{s,p} - \varepsilon_{\infty,p}$. Value $\Delta\varepsilon_p$ denotes the relative permittivity change due to the pth Cole–Cole pole and the exponent α takes values in the region of $[0,1]$. Note that the Cole–Cole model reduces to Debye relaxation (2.59) in case $\alpha = 1$ [33, 34].

Debye relaxation model was chosen for implementation in the current project. The Debye model was preferred over other models because of its well-known and simple formulation. The intended application of the FD–FDTD method in this work is the simulation of wave propagation through a human body. The frequency-dependent characteristics of the human body tissues are well presented with the Debye model.

2.4.5 Auxiliary Differential Equation Method

Frequency dependency can be incorporated into the FDTD method by using either a direct or a convolutional approach [31]. In direct approach the EM-field data is saved to preserve the frequency information and then re-used at the next time-step. Convolutional approach saves the frequency information into an accumulator, similar to a mathematical series. Although the convolutional approach might outperform the direct in terms of computation speed, it also has a complex formulation and is more difficult to implement. Direct implementation scheme was selected for this project, due to its simplicity.

One pole Debye relaxation model represents the relative permittivity ε_r as a complex number:

$$\varepsilon_r = \varepsilon_\infty + \frac{\sigma}{j\omega\varepsilon_0} + \frac{\varepsilon_s - \varepsilon_\infty}{1 + j\omega\tau}. \tag{2.63}$$

Substituting (2.63) into the constitutive relationship for the electric flux density (2.32) leads to:

$$D = \varepsilon_0 \left(\varepsilon_\infty + \frac{\sigma}{J\omega\varepsilon_0} + \frac{\varepsilon_s - \varepsilon_\infty}{1 + J\omega\tau} \right) E,$$

$$\therefore \quad D = \left(\varepsilon_0\varepsilon_\infty + \frac{\sigma}{J\omega} + \frac{\varepsilon_0(\varepsilon_s - \varepsilon_\infty)}{1 + J\omega\tau} \right) E,$$

$$\therefore \quad D = \frac{J\omega(1 + J\omega\tau)\varepsilon_0\varepsilon_\infty + \sigma(1 + J\omega\tau) + \varepsilon_0(\varepsilon_s - \varepsilon_\infty)J\omega}{J\omega(1 + J\omega\tau)} E, \tag{2.64}$$

$$\therefore \quad D = \frac{(J\omega + J^2\omega^2\tau)\varepsilon_0\varepsilon_\infty + \sigma + J\omega\sigma\tau + J\omega(\varepsilon_0\varepsilon_s - \varepsilon_0\varepsilon_\infty)}{J\omega + J^2\omega^2\tau} E,$$

$$\therefore \quad D = \frac{J\omega\varepsilon_0\varepsilon_\infty + J^2\omega^2\tau\varepsilon_0\varepsilon_\infty + \sigma + J\omega\sigma\tau + J\omega(\varepsilon_0\varepsilon_s - \varepsilon_0\varepsilon_\infty)}{J\omega + J^2\omega^2\tau} E.$$

After grouping the $J\omega$ and $J^2\omega^2$ and eliminating $\varepsilon_0\varepsilon_\infty$ and $-\varepsilon_0\varepsilon_\infty$ terms (2.64) reduces to:

$$D = \frac{J^2\omega^2\tau\varepsilon_0\varepsilon_\infty + J\omega(\sigma\tau + \varepsilon_0\varepsilon_s) + \sigma}{J^2\omega^2\tau + J\omega} E. \tag{2.65}$$

Now extracting the D terms to the left-hand side and keeping the E terms at the right-hand side (2.66) is obtained:

$$J^2\omega^2\tau D + J\omega D = J^2\omega^2\tau\varepsilon_0\varepsilon_\infty E + J\omega(\sigma\tau + \varepsilon_0\varepsilon_s)E + \sigma E. \tag{2.66}$$

Taking into account the time dependence of $\exp(J\omega t)$ (2.66) is expressed in time domain as:

$$\frac{\partial^2(\tau D)}{\partial t^2} + \frac{\partial D}{\partial t} = \frac{\partial^2(\tau\varepsilon_0\varepsilon_\infty E)}{\partial t^2} + \frac{\partial((\sigma\tau + \varepsilon_0\varepsilon_s)E)}{\partial t} + \sigma E. \tag{2.67}$$

Equation (2.67) is the generic form of the Auxiliary Differential Equation (ADE), that will be used to extend the conventional FDTD method to frequency-dependent FDTD method. ADE is time dependent only, therefore no spatial discretisation is necessary. The discretised ADE (2.68) is the same for the electric field components in all coordinate directions E_x, E_y and E_z:

$$E^{n+\frac{1}{2}} = C_1 D^{n+\frac{1}{2}} - C_2 D^{n-\frac{1}{2}} + C_3 D^{n-\frac{3}{2}} + C_4 E^{n-\frac{1}{2}} - C_5 E^{n-\frac{3}{2}}, \tag{2.68}$$

where

$$C_1 = \frac{\tau + \Delta t}{\varphi}, \quad C_2 = \frac{2\tau + \Delta t}{\varphi}, \quad C_3 = \frac{\tau}{\varphi}, \quad C_4 = \frac{\chi}{\varphi}, \quad C_5 = \frac{\alpha}{\varphi}$$

with

$$\alpha = \varepsilon_0 \varepsilon_\infty \tau, \quad \beta = \varepsilon_0 \varepsilon_s + \sigma \tau, \quad \varphi = \alpha + \Delta t \beta + \frac{\Delta t^2 \sigma}{2}, \quad \chi = 2\alpha + \Delta t \beta - \frac{\Delta t^2 \sigma}{2}.$$

Since (2.67) is time-dependent only, the spatial coordinates for x-directed component $(i, j + \frac{1}{2}, k + \frac{1}{2})$ of E, D, τ, ε_∞, ε_s and σ are equal. This statement also holds for y and z-directed components. For the sake of clarity the indices denoting the spatial location of field components and Debye relaxation properties are not shown in (2.68).

In the FD–FDTD method the Faraday's law (2.28) remains the same as in the FDTD algorithm. The constitutive relationship for magnetic flux density (2.33) is substituted into (2.28) and both the differential (2.38) to (2.40) and discretised (2.55) to (2.57) for the magnetic field preserve their original FDTD form.

A minor change is done to the Ampere's law (2.29). In order to use the ADE approach, the constitutive relation for electric flux density (2.32) is not substituted into (2.29). In the FD–FDTD method the Ampere's law is solved for $\boldsymbol{D}$ instead of $\boldsymbol{E}$. Therefore, the Maxwell's curl equation for $\boldsymbol{D}$ becomes:

$$\frac{\partial \boldsymbol{D}}{\partial t} = \nabla \times \boldsymbol{H} - \boldsymbol{J}_{src}. \tag{2.69}$$

The $\sigma \boldsymbol{E}$ term responsible for EM-energy conversion to heat vanishes from (2.69), because it will be accounted for in the ADE (2.67). Equation (2.69) in scalar form for each Cartesian coordinate component becomes:

$$\frac{\partial D_x}{\partial t} = \frac{\partial H_z}{\partial y} - \frac{\partial H_y}{\partial z} - J_{src,x}, \tag{2.70}$$

$$\frac{\partial D_y}{\partial t} = \frac{\partial H_x}{\partial z} - \frac{\partial H_z}{\partial x} - J_{src,y}, \tag{2.71}$$

$$\frac{\partial D_z}{\partial t} = \frac{\partial H_y}{\partial x} - \frac{\partial H_x}{\partial y} - J_{src,z}. \tag{2.72}$$

In the FD–FDTD approach the electric flux density components D_x, D_y, D_z are

used in place of the electric field components E_x, E_y, E_z on the Yee unit cell in Figure 2.4. Discretising the scalar equations (2.70) to (2.72) on time and space with the central-difference approximations and applying algebraic transformations identical to (2.49) to (2.52) yield:

$$D_x^{n+\frac{1}{2}}\left(i,\, j+\tfrac{1}{2},\, k+\tfrac{1}{2}\right) =$$

$$D_x^{n-\frac{1}{2}}\left(i,\, j+\tfrac{1}{2},\, k+\tfrac{1}{2}\right) + \Delta t \cdot \left(\begin{array}{c} \dfrac{H_z^n\left(i,\, j+1,\, k+\frac{1}{2}\right) - H_z^n\left(i,\, j,\, k+\frac{1}{2}\right)}{\Delta y} \\[2ex] -\dfrac{H_y^n\left(i,\, j+\frac{1}{2},\, k+1\right) - H_y^n\left(i,\, j+\frac{1}{2},\, k\right)}{\Delta z} \\[2ex] -J_{src,x}^n\left(i,\, j+\tfrac{1}{2},\, k+\tfrac{1}{2}\right) \end{array} \right), \quad (2.73)$$

$$D_y^{n+\frac{1}{2}}\left(i-\tfrac{1}{2},\, j+1,\, k+\tfrac{1}{2}\right) =$$

$$D_y^{n-\frac{1}{2}}\left(i-\tfrac{1}{2},\, j+1,\, k+\tfrac{1}{2}\right) + \Delta t \cdot \left(\begin{array}{c} \dfrac{H_x^n\left(i-\frac{1}{2},\, j+1,\, k+1\right) - H_x^n\left(i-\frac{1}{2},\, j+1,\, k\right)}{\Delta z} \\[2ex] -\dfrac{H_z^n\left(i,\, j+1,\, k+\frac{1}{2}\right) - H_z^n\left(i-1,\, j+1,\, k+\frac{1}{2}\right)}{\Delta x} \\[2ex] -J_{src,y}^n\left(i-\tfrac{1}{2},\, j+1,\, k+\tfrac{1}{2}\right) \end{array} \right)$$

$$(2.74)$$

and

$$D_z^{n+\frac{1}{2}}\left(i-\tfrac{1}{2},\, j+\tfrac{1}{2},\, k+1\right) =$$

$$D_z^{n-\frac{1}{2}}\left(i-\tfrac{1}{2}, j+\tfrac{1}{2}, k+1\right) + \Delta t \cdot \left(\begin{array}{c} \dfrac{H_y^n\left(i, j+\tfrac{1}{2}, k+1\right) - H_y^n\left(i-1, j+\tfrac{1}{2}, k+1\right)}{\Delta x} \\[2ex] -\dfrac{H_x^n\left(i-\tfrac{1}{2}, j+1, k+1\right) - H_x^n\left(i-\tfrac{1}{2}, j, k+1\right)}{\Delta y} \\[2ex] -J_{src,z}^n\left(i-\tfrac{1}{2}, j+\tfrac{1}{2}, k+1\right) \end{array} \right).$$

$$(2.75)$$

2.4.6 Implementation in Programming Language

Minor alterations to (2.73) to (2.75) and (2.55) to (2.57) are necessary in order to implement the FD–FDTD method equations in a computer programming language. Electric flux density, electric field and magnetic field components on a computer are represented as 3D arrays in Cartesian space. For example a 3D array

$$\texttt{Dx(i\_min:i\_max, j\_min:j\_max, k\_min:k\_max)} \qquad (2.76)$$

keeps a scalar D_x component in the Cartesian coordinate space, with

$$i \in [i_{min}, i_{max}]; \quad j \in [j_{min}, j_{max}]; \quad k \in [k_{min}, k_{max}]. \qquad (2.77)$$

Indices i, j, k denote a spatial coordinate location in the x, y, z-coordinates. Computer programming languages do not allow real numbers to be used as array indices, i.e. i, j, k values in (2.76) have to be integer numbers. To achieve the spatial and temporal discretisation in integer steps the coordinate origins of D_x, D_y, D_z and H_x, H_y, H_z components are shifted in the following manner:

$$D_x^{n+\frac{1}{2}}\left(i, j+\tfrac{1}{2}, k+\tfrac{1}{2}\right) \longrightarrow D_x^n\left(i, j, k\right), \quad H_x^{n+1}\left(i-\tfrac{1}{2}, j+1, k+1\right) \longrightarrow H_x^n\left(i, j, k\right),$$

$$D_y^{n+\frac{1}{2}}\left(i-\tfrac{1}{2}, j+1, k+\tfrac{1}{2}\right) \longrightarrow D_y^n\left(i, j, k\right), \quad H_y^{n+1}\left(i, j+\tfrac{1}{2}, k+1\right) \longrightarrow H_y^n\left(i, j, k\right),$$

$$D_z^{n+\frac{1}{2}}\left(i-\tfrac{1}{2}, j+\tfrac{1}{2}, k+1\right) \longrightarrow D_z^n\left(i, j, k\right), \quad H_z^{n+1}\left(i, j+1, k+\tfrac{1}{2}\right) \longrightarrow H_z^n\left(i, j, k\right).$$

$$(2.78)$$

Since the ADE (2.67) is time-dependent only, origin shifts of the electric field

components E_x, E_y, E_z are identical to those of D_x, D_y, D_z defined in (2.78). Figure 2.8 illustrates the origin shifts for each component. The shifts defined in (2.78) reduce the separate origins of D_x, D_y, D_z, E_x, E_y, E_z, H_x, H_y, H_z components into a single coordinate origin. Therefore from a programming language point of view there exist no half space- and time-step offsets between the EM-components in the FD–FDTD method.
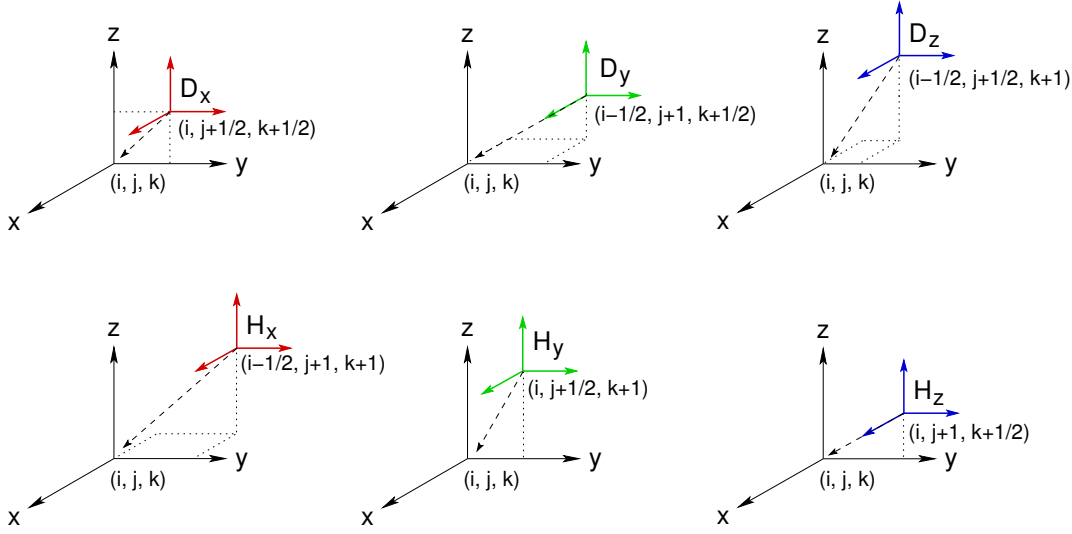
Figure 2.8: Coordinate origin shifts for electric flux density and magnetic field components. Smaller coordinate axes show original coordinates locations. Colours red, green and blue signify *x*, *y*, *z* coordinate directions.

Origin shifts (2.78) have to be applied onto original FD–FDTD update equations to obtain the method formulation suitable for implementation on a computer. Since the FD–FDTD method implementation for this project does not require to account for magnetic material properties the following assumptions were made:

$$\sigma^* = 0, \quad \mu = \mu_0, \quad M_{src} = 0. \tag{2.79}$$

Coordinate shifts (2.78) and assumptions of (2.79) transform the original half-step update (2.55) to (2.57) for magnetic field into:

$$H_x^n(i, j, k) = H_x^{n-1}(i, j, k)$$

$$+ \frac{\Delta t}{\mu_0} \cdot \left(\frac{E_y^n(i, j, k+1) - E_y^n(i, j, k)}{\Delta z} - \frac{E_z^n(i, j+1, k) - E_z^n(i, j, k)}{\Delta y} \right), \tag{2.80}$$

$$H_y^n(i, j, k) = H_y^{n-1}(i, j, k)$$

$$+ \frac{\Delta t}{\mu_0} \cdot \left(\frac{E_z^n(i+1, j, k) - E_z^n(i, j, k)}{\Delta x} - \frac{E_x^n(i, j, k+1) - E_x^n(i, j, k)}{\Delta z} \right) \quad (2.81)$$

and

$$H_z^n(i, j, k) = H_z^{n-1}(i, j, k)$$

$$+ \frac{\Delta t}{\mu_0} \cdot \left(\frac{E_x^n(i, j+1, k) - E_x^n(i, j, k)}{\Delta y} - \frac{E_y^n(i+1, j, k) - E_y^n(i, j, k)}{\Delta x} \right). \quad (2.82)$$

After the application of coordinate shifts (2.78) the FD–FDTD electric flux density update (2.73) to (2.75) become:

$$D_x^n(i, j, k) = D_x^{n-1}(i, j, k) + \Delta t \cdot \left(\begin{array}{c} \dfrac{H_z^n(i, j, k) - H_z^n(i, j-1, k)}{\Delta y} \\[2ex] -\dfrac{H_y^n(i, j, k) - H_y^n(i, j, k-1)}{\Delta z} \\[2ex] -J_{src,x}^n(i, j, k) \end{array} \right), \quad (2.83)$$

$$D_y^n(i, j, k) = D_y^{n-1}(i, j, k) + \Delta t \cdot \left(\begin{array}{c} \dfrac{H_x^n(i, j, k) - H_x^n(i, j, k-1)}{\Delta z} \\[2ex] -\dfrac{H_z^n(i, j, k) - H_z^n(i-1, j, k)}{\Delta x} \\[2ex] -J_{src,y}^n(i, j, k) \end{array} \right), \quad (2.84)$$

$$D_z^n(i, j, k) = D_z^{n-1}(i, j, k) + \Delta t \cdot \left(\begin{array}{c} \dfrac{H_y^n(i, j, k) - H_y^n(i-1, j, k)}{\Delta x} \\[2ex] -\dfrac{H_x^n(i, j, k) - H_x^n(i, j-1, k)}{\Delta y} \\[2ex] -J_{src,z}^n(i, j, k) \end{array} \right). \quad (2.85)$$

Finally, the origin shifts (2.78) enable implementation of the electric field update (2.68) in integer space- and time-steps:

$$E^n = C_1 D^n - C_2 D^{n-1} + C_3 D^{n-2} + C_4 E^{n-1} - C_5 E^{n-2}, \qquad (2.86)$$

where

$$C_1 = \frac{\tau + \Delta t}{\varphi}, \quad C_2 = \frac{2\tau + \Delta t}{\varphi}, \quad C_3 = \frac{\tau}{\varphi}, \quad C_4 = \frac{\chi}{\varphi}, \quad C_5 = \frac{\alpha}{\varphi}$$

with

$$\alpha = \varepsilon_0 \varepsilon_\infty \tau, \quad \beta = \varepsilon_0 \varepsilon_s + \sigma \tau, \quad \varphi = \alpha + \Delta t \beta + \frac{\Delta t^2 \sigma}{2}, \quad \chi = 2\alpha + \Delta t \beta - \frac{\Delta t^2 \sigma}{2}.$$

The FD–FDTD algorithm progresses in time by updating magnetic field values with (2.80) to (2.82), then calculating electric flux density values with (2.83) to (2.85) and finally using Auxiliary Differential (2.86) to advance the electric field values. The FD–FDTD method is very similar to the ordinary FDTD. The ADE introduces an additional intermediate step into the calculation routine. Instead of intertwined H and E updates the FD–FDTD approach has a mutually interdependent H, D and E updates.

```
 1: for each time-step n ∈ [1, t_max] do
 2:     save D^{n-1} → D^{n-2}, D^n → D^{n-1}
 3:     save E^{n-1} → E^{n-2}, E^n → D^{n-1}
 4:     calc H^n
 5:     calc D^n
 6:     calc E^n
 7:     excite E^n (T_x)
 8:     output E^n (R_x)
 9:     term D^n (ABC)
10:     term E^n (ABC)
11: end for
```

Algorithm 2: FD–FDTD pseudocode. Parameter t_{max} specifies the total number of simulation time-steps. Abbreviations "calc" and "term" stand for calculate and terminate.

Algorithm 2 lists the major steps of the FD–FDTD method in pseudocode. All EM-values are calculated in a global time-step loop. The algorithm steps repeat for each loop iteration. First the previously calculated values of D and E are saved into auxiliary data arrays. Previously calculated values at time-steps $n-2$ and $n-1$ are needed to update the current time-step values. Then H, D and E values are

advanced on time for all spatial locations. The calculation order can also be different. However, it is important to observe the circular dependency of the H, D and E components. After the general EM-value calculation is over the E component at the excitation location T_x is injected with a source signal, e.g. a Gaussian pulse. The source excitation is administered via the J_{src} component. It is also possible to excite the electric flux density components D_x, D_y or D_z. Then the EM-values at the observation locations R_x are printed into the files. Finally, the computation domain for electric flux density D and electric field E is terminated with the ABC calculation. The "true" ABC is calculated for the electric flux density components. The electric field values in the ABC region are just re-calculated using the new values of D.

Similarly to the FDTD method dissected in Algorithm 1, magnetic current M_{src} might be injected into magnetic field components H_x, H_y and H_z if the user is interested in the magnetic field behaviour. In case of PML all three EM-components H, D and E have to be terminated in the boundary region.

Chapter 3

Subgridding in Review

This chapter explains the aim of subgridding in the Finite-Difference Time-Domain method and highlights the key aspects of a subgridding scheme. A detailed review of modern subgridding techniques including classical, Huygens and hybrid subgridding is presented. This chapter also covers the limitations of a classical subgridding scheme and illustrates alternative subgridding methods as Domain Decomposition and Dielectric Subgrid Resolution. Finally, the material traverse ability and human body applications of subgridding are discussed in the concluding sections.

3.1 Computational Electromagnetics Methods

Numerous Computational Electromagnetics (CEM) methods exist to simulate an electromagnetic (EM) wave propagation. Selection of a method is problem-dependent. Each method is more suitable for a particular group of problems, usually described by a problem size in terms of wavelengths. The Finite-Difference Time-Domain (FDTD) method is applied to problems ranging from 0.01 to 10 wavelengths. Figure 3.1 shows examples of CEM methods with their example application areas [35].[1]

3.2 Numerical Dispersion in FDTD Method

In free space all plane waves propagate at the same speed, irrespective of frequency. But in the FDTD approach plane wave phase velocity depends on the spatial and

---

[1]Common CEM methods are abbreviated to the Method of Moments (MoM) and the Finite Element Method (FEM). The word "body" in the example application areas refers to human body.
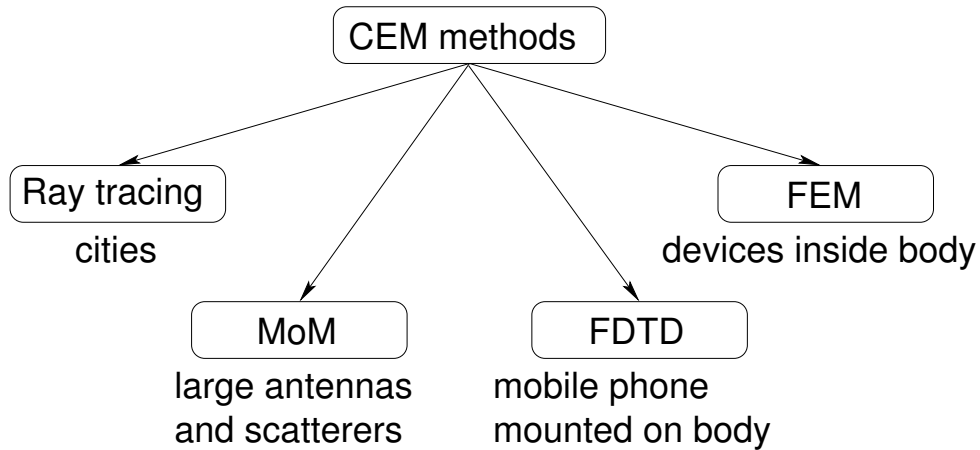
Figure 3.1: Computational Electromagnetics methods

temporal increments,[2] and the angle of propagation [36]. This effect is called *numerical dispersion*. However, angle of the wave propagation does not dramatically change the phase velocity. To avoid numerical dispersion sufficiently high spatio-temporal discretisation is necessary. With discretisations in the order of $\Delta s = \lambda/10$ the error on phase velocity is lower than 1.5% and with $\Delta s = \lambda/20$ the error reduces to 0.15%, where Δs is a spatial increment and λ is a wavelength.

3.3 Aim of Subgridding

Modern engineering problems require simulation of electrically large objects with fine geometric details. Due to Courant-Friedrichs-Lewy (CFL) stability criterion, also known as Courant criterion, the size of time-step in the FDTD method depends on the size of space-step. Common practice is to set the space-step Δs depending on the wavelength λ of the problem and then adjust the time-step Δt according to the CFL criterion [37]:

$$\Delta s \in \left[\frac{\lambda}{10}, \frac{\lambda}{20} \right], \quad \Delta t < \frac{\Delta s}{c\sqrt{3}}, \tag{3.1}$$

where

Δs space-step,
Δt time-step,
λ wavelength,
c speed of light.

---

[2]In this work the notions of spatial and temporal increments, spatial and temporal steps and space- and time-steps are used as synonyms.

To simulate an object with high precision, a uniform fine grid will be needed everywhere in space. Moreover, to preserve the algorithm stability, the simulation will have to advance in fine temporal steps. This approach of using fine spatio-temporal resolution throughout the entire space is computationally expensive. But usually only a part of the simulated structure has fine geometry. The rest of the features are smooth, homogeneous and contain little change. These regions could be simulated with the coarse spatio-temporal resolution.

The main idea of *subgridding* is the increase of simulation efficiency by dividing the computation domain into subdomains with independent spatial and temporal increments. Subgridding allows selective placing of a high resolution mesh, called *subgrid (SG),* around the delicate object structure. The rest of the object will be simulated with large spatio-temporal increments in the coarse grid, called the *main grid (MG).* In subgridding, the CFL criterion is maintained independently for each grid. Application of subgridding is always a compromise between the accuracy and efficiency. Although, the simulation results with subgridding will be obtained faster, than with the all fine FDTD grid, these results will be less precise.

3.4   Key Aspects of Subgridding

There are many aspects defining the quality of a subgridding scheme.

Subgridding interface is the cornerstone of a subgridding scheme. Subgridding interface specifies the way main and subgrid interact with each other during the simulation.

Rapid change in mesh size at the interface causes spurious reflections. Wave phase velocity changes when the wave enters from a low resolution coarse grid to a high resolution fine grid. Problems arise when that wave returns from the fine grid back into the coarse grid and starts interacting with the original coarse grid. To ensure precise results a good interpolation scheme and a small enough spatial step in the coarse grid should be chosen. Coarse grid spatial increment should be much smaller than the shortest wavelength under study [38].

Implementation of the interface contributes dramatically to the overall subgridding stability. Usually field components at the interface are interpolated and extrapolated at each time step [39]. Therefore selection of the spatial

and temporal inter- and extrapolation schemes is important. These schemes should be precise and efficient. Okoniewski et al. [40] provide a comparative analysis of tri-linear, cubical splines and shape preserving splines spatial interpolation. Tri-linear interpolation was found to be the fastest, whereas shape preserving splines is the most expensive and cubical splines may introduce local oscillations. Xiao et al. [41] incorporate special treatment of corner and edge elements at the subgridding interface with a modified interpolation pattern.

Also the choice of interpolation coefficients affects the algorithm stability. Wang et al. [42] designed a framework to derive interpolation coefficients at the subgridding interface. Three and five points linear interpolation coefficients were developed.

To achieve better stability the symmetry of the field components at the interface should be preserved [43]. The same coarse grid components, that influence fine grid, have to receive feedback from the fine grid components.

Quality of the interface defines the amount of field reflection. Artificial reflection from the interface occurs due to rapid change in numerical dispersion between the coarse and fine grids. Good subgridding interfaces produce low reflection.

Modern subgridding schemes use fields collocation to avoid extrapolation and reduce reflection. In this case locations of the coarse electric or magnetic field components at the interface coincide with the locations of some fine grid components. Celuch-Marcysiak and Rudnicki [44] developed a methodology to predict numerical reflection coefficients from a subgridding interface. Reflection is expressed as a function of angle or frequency. The authors conclude, that collocated schemes produce lower interface reflection, whereas full reflection starts at the cut-off and higher frequencies.

Subgridding ratio is the ratio between the space-steps in the main and subgrid. Usually it is the same for time-steps:

$$r = \frac{\Delta s_a}{\Delta s_b} = \frac{\Delta t_a}{\Delta t_b},$$

(3.2)

where

Δs_a space-step in main grid,

Δs_b space-step in subgrid,

Δt_a time-step in main grid,

Δt_b time-step in subgrid.

Relative to the all fine grid case, high subgridding ratio increases the total efficiency of the subgridding algorithm, but at the same time reduces the accuracy of numerical solution, especially in the main grid region.

Time advancement in a subgridding scheme can be divided into two main categories: synchronised unistep and synchronised multistep. In this context *synchronised* means that *r* fine grid time iterations are performed within one time-step of the coarse grid. Fine grid continuously synchronises with the coarse grid. Simulation for both grids runs simultaneously.

Unistep schemes use the same smallest time step Δt_b for both grids. This approach is easier to implement, but it is less efficient, since the coarse grid unnecessarily uses smaller temporal increments. Unistep approach naturally reduces to spatial subgridding only. On the contrary, multistep schemes provide the true merit of subgridding. Both spatial and temporal increments are different. Simulation in coarse grid is executed for larger spatial and temporal steps.

Grid geometry is the way of meshing the simulation space into smaller units, called cells. Commonly for FDTD methods the grid geometry bears a uniform and orthogonal character.

Grid recursion (also known as nesting or multilevel subgridding) is the possibility of allocating subgrids within subgrids recursively. Although more computationally expensive than one level subgridding, grid recursion allows finer tuning of the code to a given problem and reduces numerical dispersion by enabling a smoother change from Δs_a to Δs_b. Figure 3.2 gives an example of a grid recursion with two levels of subgridding in a two-dimensional (2D) space.

Number of subgrids is the amount of subgrids supported by the algorithm implementation. Normally variable number of subgrids is only the capability of a particular code, not an algorithm restriction. Support for multiple subgrids enables the simulation to concentrate on multiple volumes of higher precision.
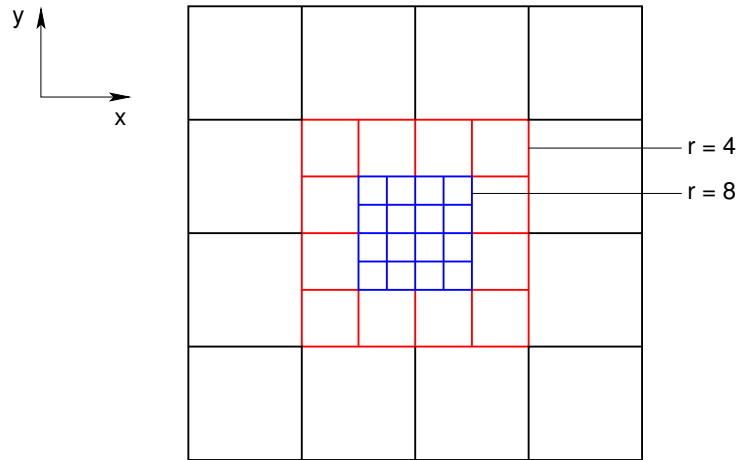
Figure 3.2: Grid recursion in 2D. Two grids are nested. First subgrid with $r = 4$ and second subgrid with $r = 8$. Subgridding ratios are given with respect to the main grid.

Stability is a crucial issue for all subgridding algorithms. In context of the FDTD method, algorithm stability means, that no numerical error introduced at certain time moment will accumulate [41]. Due to reflection from the interface many subgridding algorithms suffer from the late-time instabilities. Numerous remedies have been proposed to tackle the instability. Amongst them are the gradual change of mesh size, domain overriding, high order spatial interpolation and signal filtering. Thoma and Weiland [45] categorise the native FDTD method instabilities into dynamic and static. Dynamic instability can be of two origins: (i) model instability caused by the spatial derivatives approximation and (ii) Courant instability created by the time derivatives approximation. Static instability arises with the change of the FDTD grid topology. Usually two approaches are used to prove the stability of a subgridding scheme theoretically: the Matrix method and the Fourier method [41]. Along with the theoretical methods, stability of a subgridding algorithm can be proved numerically. In this case the simulation is run for various configurations for a large number of time steps, commonly in the order of 10^6.

Accuracy of a subgridding approach is the ability of numerical solution to converge to the actual solution [41]. Accuracy of a subgridding scheme should be comparable to that of the homogeneous fine grid solution in the critical simulation regions. Subgridding accuracy mostly depends on the interface implementation and the selection of the inter- and extrapolation methods.

Adaptability of the subgridding algorithm to a given physical problem is another highly desired feature. A good example might be a moving high resolution window that follows the wave propagation as in the Adaptive Mesh Refinement (AMR) algorithm.

Material traverse is the capability of a subgridding algorithm to allow dielectric media to reside in the fine grid and especially cross the subgridding interface. Material traverse functionality extends subgridding to account for material frequency response. This issue is vital in biomedical and electromagnetic compatibility (EMC) applications of subgridding.

Performance cost of subgridding includes the algorithm complexity and the programming complexity. Subgridding interface, field inter- and extrapolation and filtering schemes should be efficient. Programming complexity is mainly defined by the mathematical formulation of the algorithm. Algorithm implementation is a one time cost and is less important, compared to the algorithm complexity, that exhibits computational cost at every run time. As practice shows, good CEM algorithms are simple, elegant, adhere to the real world physics and are defined in a clean, straightforward manner.

Parallelisation of a subgridding algorithm might be considered another step towards the improvement of the overall simulation efficiency. Parallelisation will inevitably contribute to the programming complexity, but done in a right manner will dramatically increase subgridding performance. With the rise of Grid Computing, High Performance Computing (HPC) and Graphical Processing Unit (GPU) Computing parallelisation aspect of subgridding becomes an important and achievable goal in modern research.

3.5 Modern Subgridding Techniques

3.5.1 Classical Subgridding

Subgridding is usually applied to increase the efficiency of the FDTD method and enable the simulation of electrically large problems. Figure 3.3 highlights the main approaches for the solution of electrically large problems [46]. Domain decomposition methods highlighted in Figure 3.3 refer to the group of FDTD techniques that run two sequential simulations—one with the coarse and another with the fine

spatio-temporal resolution. Section 3.5.7 describes the domain decomposition approaches in greater detail. Higher-order schemes in Figure 3.3 refer to higher-order FDTD methods that achieve less numerical dispersion and permit coarser grid discretisation for a given error bound than the classical FDTD method. Higher-order FDTD schemes allow efficient simulation of electrically large objects or long distance of propagation [47]. Examples of such methods include the second-order in time and fourth-order in space FDTD (2,4) [47–49] or second-order in time and sixth-order in space FDTD (2,6) [47]. Another example of higher-order FDTD method is presented in [50]. Young et al. [50] use compact central-difference approximation for spatial derivatives in Maxwell's equations and four-stage Runge–Kutta integrator [51] for temporal derivatives.
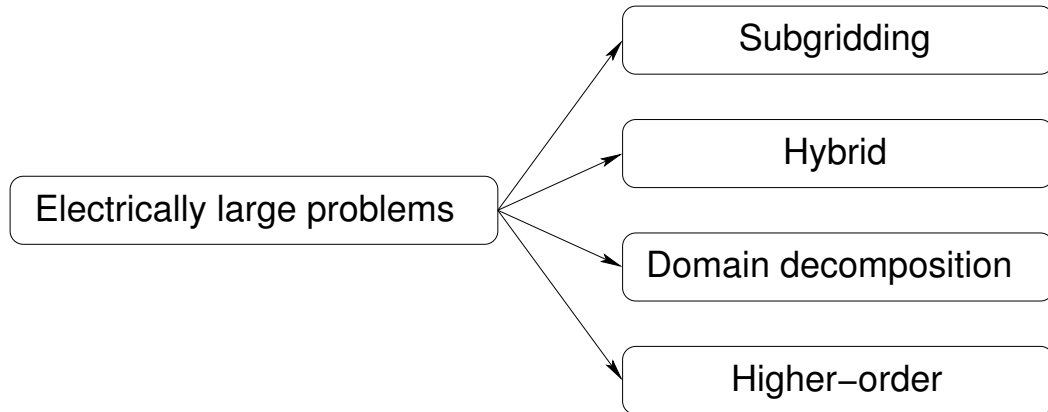
Figure 3.3: Methods for solution of electrically large problems

Classical subgridding methods are the most popular simulation schemes. Commonly subgridding is implemented by separating the main computation domain into subdomains with different spatial and temporal increments: $\Delta s_a, \Delta t_a$ and $\Delta s_b, \Delta t_b$. The interface area between the main and the subgrid can be viewed as a boundary condition for both grids. Coarse grid wave propagation terminates at the interface. The coarse grid values laying at the interface are interpolated and passed to the fine grid FDTD update equations. Similar action is taken in the fine grid. When the wave in subgrid reaches the interface, field components are extrapolated. These extrapolated values are subsequently used in normal FDTD update equations for the coarse grid interface values.

Apart from the small amount of works in spatial subgridding only [52, 53] and temporal subgridding only [54, 55] the majority of algorithms offer true spatio-temporal subgridding. Usually prototyping of new subgridding algorithms starts in 2D.

There is a minor corpus of research works presenting 2D approaches [38, 42, 52, 54, 56–58]. To avoid computationally expensive extrapolation new subgridding algorithms collocate the coarse and fine grid field components at the interface [40, 59–62].

Due to increased programming complexity a highly desirable feature of subgrid recursion is still scarcely presented in the modern approaches [57, 63–66]. Alternative to field interpolation at the interface, a few subgridding projects base the interface value calculation on the travelling wave equation [39, 67, 68], passive lumped circuits equivalent to Maxwell's equations (ME) [69, 70], Kirchhoff integral formula [71] and weighted current density passing through the cell [43, 72]. Remarkable is the work of Chow et al. [64], that split the subgrid region into blocks and solve ME inside the subgrid sequentially, block-by-block.

The most common ratios in subgridding approaches are two [40, 45, 52, 57, 65, 73], three [39, 41, 43, 46, 58, 62, 70, 72, 74–80] and four [38, 66, 67]. Less frequently subgridding techniques accommodate higher ratios: five [53, 81], seven [60, 82] and eight [83]. Ratios greater than 10 are very rare: 15 [84], 16 [85] and 17 [61].

3.5.2 Classical Subgridding Optimised

Two techniques [81, 83] reduce the Courant number N_{CFL} to 0.55 and 0.57 respectively to increase the algorithm stability and allow higher subgridding ratios. However, the reduced Courant number also results in the reduced subgridding efficiency. To further increase subgridding stability some approaches apply overlapped grids and domain overriding [83, 86, 87]. Rarely a special treatment for interface edge and corner elements is used [87].

Interesting is the work of Donderici and Teixeira [87], that explains the positive effect of overlapped grids to combat aliasing, high frequency cut-off and numerical impedance mismatch. *Aliasing* is the inexact correspondence between the fine and coarse grid medium field values. Apart from the overlapped grids, aliasing effect can be decreased using the Finite Impulse Response (FIR) filtering. *High frequency cut-off* occurs because the high frequency components in the subgrid cannot be present in the main grid due to the Nyquist limit. Also spurious reflections are produced when the high frequency signal exists in the subgrid. Finally, the *numerical impedance mismatch* is caused by different cell sizes in the fine and coarse grids. Here, in line with the grid overlapping, a phase compensation technique can be applied in the coarse grid to reduce the mismatch.

Unique to Donderici and Teixeira [86–88] is the method of domain overriding, when the auxiliary fine and coarse grids are created in the simulation domain and the one way field injection is used to prevent propagation return to the subgridding interface.

Only Vaccari et al. [84] use filtering in their work to delay the late-time instabilities. Typical accuracy–efficiency interdependency holds in filter application. Filters of 4th order slightly outperform the 2nd order filters for a higher computational cost. The authors also suggest increasing the filter order with the increase of the subgridding ratio r.

Another relatively novel approach to combat the instabilities is the decoupling of spatial and temporal interfaces [41,78,79,89,90]. In this case the temporal subgrid encloses the spatial subgrid with a minimum separation distance of $3\Delta s_a$. Figure 3.4 illustrates the decoupling of spatial and temporal interfaces for a subgridding ratio $r = 2$ [78]. Chow et al. [90] found the decoupled subgridding scheme stable for 10^7 iterations.
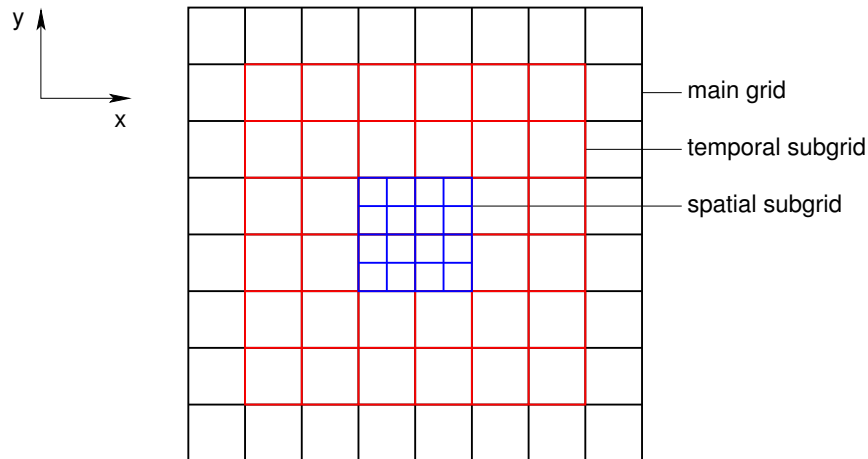
Figure 3.4: Decoupling of spatial and temporal interfaces in 2D. Minimum distance between the temporal and the spatial subgrids is $2\Delta s_a$. Spatial subgridding ratio is 4.

Wang et al. [78] have tested the accuracy of classical subgridding schemes by implementing various techniques into a commercial software package XFDTD. The authors suggest that subgridding accuracy mostly depends on the spatial interpolation rather than temporal. It was also confirmed that significant errors are caused by a material traversing the subgridding interface. To achieve better stability and accuracy White et al. [83] recommend at least $4\Delta s_a$ separation distance between the subgridding interface and the dielectric material boundary.

Another interesting approach is the application of 4th order spatial approxima-
tion in normal FDTD method. Georgakopoulos et al. [91] use 2nd order temporal
and 4th order spatial approximation (FDTD (2,4)) for the fine grid and conventional
FDTD (2,2) for the coarse grid. Use of FDTD (2,4) allowed Sun and Choi [85] to
achieve subgridding ratio of 16.

Inspired by the AMR algorithm, popular in the area of Computational Fluid Dy-
namics (CFD), Liu and Sarris [92, 93] and Gazave et al. [94] develop a creative idea of
an AMR–FDTD method. This method offers a high resolution parallelepiped, that
follows the wave propagation in a coarse grid.

Flexible interconnection of grids with various geometries is explored by Don-
derici and Teixeira [95].

Due to considerable programming efforts parallel subgridding approaches are
still uncommon. Only four works present parallelisation of their subgridding sche-
mes [57, 64, 96, 97].

3.5.3   Huygens Subgridding

Huygens Subgridding (HSG) is a promising subgridding technique consecutively
developed by Bérenger from 1D to 3D [98–102]. Main and subgrids are intercon-
nected via the Huygens Surfaces (HS) that transfer EM energy from coarse-to-fine
and fine-to-coarse grids through equivalent currents. Major advantages of the HSG
technique are (i) no theoretical limitation on the subgridding ratio and (ii) low re-
flection from the subgridding interface. But as many other subgridding schemes,
the HSG suffers from late-time instabilities.

Gradoni et al. [103] conducted the accuracy evaluation of the HSG using a rect-
angular TE_{10} waveguide and found the discrepancy of 2–3 dB between the HSG
and the reference codes negligible. Xie et al. [104] have successfully applied HSG
with $r = 3$ for the FDTD simulation of plasma problems. To combat the instabil-
ities Bérenger [99] proposed a cosine low-pass filter. Recently Zhou and Schnei-
der [105, 106] developed this approach further by offering a combination of a cosine
filter with an artificial constant loss and dispersive gain. Although more computa-
tionally expensive, the filter and artificial loss approach eliminated both the oscil-
lating and drift instabilities.

Recently the HSG–FDTD method was expanded to incorporate the Frequency
Dependency (FD). Material frequency response is implemented with the Auxiliary
Differential Equation (ADE) method using the one pole Debye relaxation model.

Costa et al. [107] tested the new HSG–FD–FDTD approach with metallic objects and $r = 3$ in 1D. This work was followed by Abaļenkovs et al. [108], and Costen and Bérenger [109] that applied the 1D HSG–FD–FDTD scheme with $r = 15$ to a problem of wave propagation in the human torso.

3.5.4 Limitations of Classical Subgridding Method

Higher precision in the classical FDTD method can be achieved by using non-uniform grids and subgridding. But along with efficiency non-uniform grids and subgrids may introduce the following problems:

- damage of second-order accuracy,

- non-physical reflection in wave propagation,

- possible increase of numerical dispersion,

- numerical instability,

- complexity of creating a non-uniform grid [36].

3.5.5 FDTD and FEM Suitability for Subgridding

Explicit FDTD method is very accurate when executed on a structured mesh. Application of a subgridding approach or a non-uniform FDTD mesh might be convenient for solving problems when only a small part of the problem requires higher precision. In this case the use of subgridding and non-uniform mesh is always a compromise between the spatio-temporal resolution and computational efficiency.

Contrary to the FDTD method the FEM discretises the space by elements of arbitrary size and shape. Field interpolation in FEM is governed by either a scalar trial function for nodal elements or by a vector trial function for Whitney elements. FEM is typically more efficient in frequency domain than the FDTD scheme. Programming of FEM in time domain is non-trivial and FEM based on implicit approaches is computationally expensive [36].

3.5.6 Hybrid Subgridding

Hybrid subgridding approaches are based on a combination of the conventional FDTD and the FEM. The aim of a hybrid scheme is to combine the strong points of

both the FDTD and FEM. Entire subgrid or only the subgridding interface is implemented via the Finite Elements (FE) approach. Courant criterion does not limit the FEM, therefore no temporal interpolation is necessary in hybrid subgridding schemes. Typically only spatial interpolation exists in a hybrid subgridding scheme. Also the FE region allows the usage of an unstructured mesh, e.g., tetrahedral and hexahedral. Grid geometry can be defined in other coordinate systems. Donderici and Teixeira [95] explain the way of interfacing the FE with the FDTD grids, where the adjacent grids are extended towards each other and two different representations of the same field coexist. Then scaling and rotation matrices are applied at the grid interface.

Similarly to conventional subgridding, new hybrid techniques are first tested in 2D [110, 111]. A multitude of methods are used to implement a hybrid subgridding algorithm: Discrete Wavelet Transform (DWT) [110, 112], Whitney forms [36, 113, 114], Lobatto Cell [115], Model Order Reduction (MOR) [111, 116, 117], Cell Method (CM) [118, 119] and hanging variables [120]. Minority of works present synchronised unistep hybrid methods [120, 121]. Hybrid methods host the standard subgridding ratios of two [110], three [118, 119, 122] and four [120, 123] as well as higher ratios of five [124], nine [116], 11 [121], and 15 [117].

A small group of research projects base their subgridding schemes on a mixture of the Alternating Direction Implicit–Finite-Difference Time-Domain (ADI–FDTD) and conventional FDTD methods [124–127]. Here, ADI–FDTD usually occupies the subgrid. ADI–FDTD is not bound by the Courant criterion and allows high resolution grid in space with coarse resolution grid in time.

Another branch of hybrid methods is the Finite Integration Technique (FIT) based subgridding approaches [96, 128–130]. FIT approach is matrix oriented and requires solution of high dimensional linear systems.

The benefits of using hybrid methods are the guaranteed stability,[3] ability to accommodate higher subgridding ratios and flexible subgrid geometry. On the other hand mathematical algorithm formulation is usually complex and implementation puts a heavy burden on computation resources. Computationally expensive block diagonal [96, 112–114], symmetric positive semi-definite [111, 118, 119, 121], positive definite [36], dense [116] or sparse [120] matrix inversion has to be calculated at every time step in the FE region.

---

[3]Although stability of the FEM itself is not always guaranteed, many of the hybrid subgridding approaches described in Section 3.5.6 are proven to be stable [113, 114, 118–120, 124, 126].

3.5.7 Domain Decomposition

Introduced by Kunz and Simpson [131] in 1981 the domain decomposition (DD) or the Dual Grid (DG) was a first technique to increase efficiency of the original FDTD method. In essence, the DG method runs two sequential FDTD simulations: one with coarse and another with fine grid resolution. While the object is simulated in a coarse grid, tangential electric field components at the boundary are stored at each iteration. After interpolation the stored coarse grid values are injected into the fine grid as the excitation source for the simulation [35]. High frequency noise caused by field interpolation can be filtered out. Alternatively, depending on the problem, the order of runs might be changed: fine grid simulation can be run first and its results injected into the consecutive coarse grid simulation [132].

The advantage of the DG–FDTD scheme is the flexibility it provides for testing an object in various environments: fine grid results have to be obtained only once and can be subsequently re-used for future tests [132]. For example, consider a surrounded antenna analysis case. At first the antenna is simulated without its environment in the fine grid. Antenna's radiation pattern is saved and injected as the excitation at the second simulation step in the coarse grid. The second simulation step contains the antenna's environment. Multiple environments of an antenna can be tested with the same radiation pattern obtained with the fine grid. Another benefit of using the DG–FDTD approach is the very small modification required to the original FDTD implementation. The DG–FDTD method is robust, while it only uses the basic FDTD scheme. The only serious drawback of the DG approach is the time consumption, because two independent FDTD simulations have to be run sequentially.

An interesting idea of a Switchable Grid–Finite-Difference Time-Domain (SWG–FDTD) was presented by Pascaud et al. [133]. An object and its environment are simulated in the fine grid until a certain switching time t_{sw}. At time t_{sw}, after most of the energy will have left the computation domain and lower simulation precision can be tolerated, the method switches into the coarse grid mode and runs until the observation time t_{obs}. Field components are interpolated and the high frequency noise is dealt with the correction step, when both fine and coarse grids co-exist. Finally, the computationally expensive Perfectly Matched Layer (PML) Absorbing Boundary Conditions (ABC) are replaced with less expensive Mur ABC. Compared to classical subgridding schemes the SWG–FDTD method is naturally more stable since the field interpolation is done only once.

3.5.8   Dielectric Subgrid Resolution

Sometimes subgridding approaches are used on a scale of a single FDTD cell to increase the material dielectric resolution [134]. This method is called the Dielectric Subgrid Resolution (DSR). DSR can be effectively applied instead of conformal FDTD method [135–137] to combat staircasing FDTD errors on curved shapes.

3.5.9   Material Traverse

Material traversing the subgridding interface remain one of the difficulties of conventional subgridding. Dielectric material crossing the interface may introduce additional reflection and stimulate earlier occurrence of instability. Chevalier et al. [37, 138] used collocated field components at the interface enforcing odd subgridding ratios. Only magnetic field components are interpolated at the interface. Electric fields are continuous at the interface, thus enabling non-magnetic material traverse. Donderici and Teixeira [88] in their FDTD subgridding with domain overriding decimate and extrude discretised dielectric materials traversing the interface. Pernice et al. [126] and Meglicki et al. [57] allow material traverse by expanding FDTD subgridding to Lorentz–Drude material model.

3.5.10   Human Body Applications of Subgridding

Application of subgridding techniques to modelling wave propagation in human body is scarce. Kopecký and Persson [82] used classical FDTD subgridding with ratios of 3, 5 and 7 to perform dosimetry in the inner ear. Twenty-four biological tissues in the head were specified by mass density and dielectric properties in the middle of the GSM frequency range 1710.2–1784.8 MHz. Xiaoli and Wenbing [68,80] applied conventional subgridding with $r = 3$ to examine wave propagation in interstitial applicators for bone cancer treatment. Human body tissues were characterised by relative electric permittivity ε_r and electric conductivity σ. Barchanski et al. [96] simulated current distribution from an electric hair dryer and an electric heating blanket inside the human torso. Dispersive materials were expressed with matrices of reluctivities, electric conductivities and permittivities.

Since subgridding offers dramatic improvements in simulation time, it is expected to see a wider use of subgridding in biomedical applications in the near future.

Chapter 4

Huygens Subgridding

This chapter describes the principles of the Huygens Subgridding (HSG) method (Section 4.2) including the concept of equivalent currents at the Inner and Outer Surfaces (Section 4.4) and the full HSG algorithm (Section 4.5). Instability of Huygens Subgridding is addressed briefly in Section 4.6. Section 4.7 concludes this chapter by presenting the mathematical formulation of the HSG method in 3D.

4.1 Introduction

A well-known drawback of the FDTD method is the inability to model geometric details smaller than the FDTD cell size. Subgridding methods offer approaches to overcome this problem. Subgridding replaces part of the FDTD grid with a finer grid [98].

Contemporary subgridding techniques are based on an inter-grid interface acting as a boundary condition. Due to numerical dispersion speed of wave propagation at the interface is different. Change of wave velocity at the interface results in spurious reflections and limited subgridding ratios. Also many subgridding algorithms suffer from the instability.

Huygens Subgridding (HSG) solves Maxwell's equations separately in main grid and subgrid. Instead of a direct connection between the grids the HSG algorithm uses Huygens Surfaces (HS) that transmit inter-grid influence via equivalent currents. Advantages of the HSG method include an arbitrary large subgridding ratio and no numerical reflection from the subgridding interface. HSG ratio is defined in (4.1):

$$r = \frac{\Delta s_a}{\Delta s_b} = \frac{\Delta t_a}{\Delta t_b}. \tag{4.1}$$

In order to achieve field collocation (and avoid field extrapolation on space), the HSG ratio r has to be an odd number. In contrary to the benefits, the HSG approach suffers from the instability.

4.2   Principles of Huygens Subgridding

The equivalence theorem plays an important role in the HSG method's formulation. According to the equivalence theorem field produced by outside sources in a given part of space can be reproduced impressing the EM current densities on the surface separating two parts of space [99]:

$$\boldsymbol{K}_{srf} = \quad \boldsymbol{n} \times \boldsymbol{H}_i, \tag{4.2}$$

$$\boldsymbol{L}_{srf} = -\boldsymbol{n} \times \boldsymbol{E}_i, \tag{4.3}$$

where

$\boldsymbol{K}_{srf}$ electric current density (A/m^2),

$\boldsymbol{L}_{srf}$ equivalent magnetic current density (V/m^2),

$\boldsymbol{E}_i$ electric field (V/m),

$\boldsymbol{H}_i$ magnetic field (A/m),

$\boldsymbol{n}$ unit vector ($-$).

Symbols $\boldsymbol{K}_{srf}$, $\boldsymbol{L}_{srf}$ denote the current densities injected onto the separating surface and $\boldsymbol{E}_i$, $\boldsymbol{H}_i$ are the fields that would exists on the surface, if the sources were present. Unit vector $\boldsymbol{n}$ is normal to the surface and is oriented in the direction opposite to the sources. Therefore, the Huygens surface is a surface with an equivalent current, that is used to impress an incident wave striking a given structure. The Anti-Huygens surface is the Huygens surface with a unit vector $\boldsymbol{n}$ oriented towards the sources.

Figure 4.1 explains the operation of the Huygens surface in 1D. Consider Figure 4.1a with the excitation source located in the main grid x_a. Huygens surface radiates from the main into the subgrid. Equivalent current (marked with red arrows) is taken at two points in the main grid and impressed at the corresponding

two points in the subgrid x_b.

Figure 4.1b presents a reversed situation with the source placed inside of the subgrid. Two points in the subgrid radiate to two points in the main grid via the Huygens surface. Points in the main grid are located at the same physical locations as the points in the subgrid. An equivalent current is shown with blue arrows.

(a) Radiation from main to subgrid

(b) Radiation from subgrid to main grid
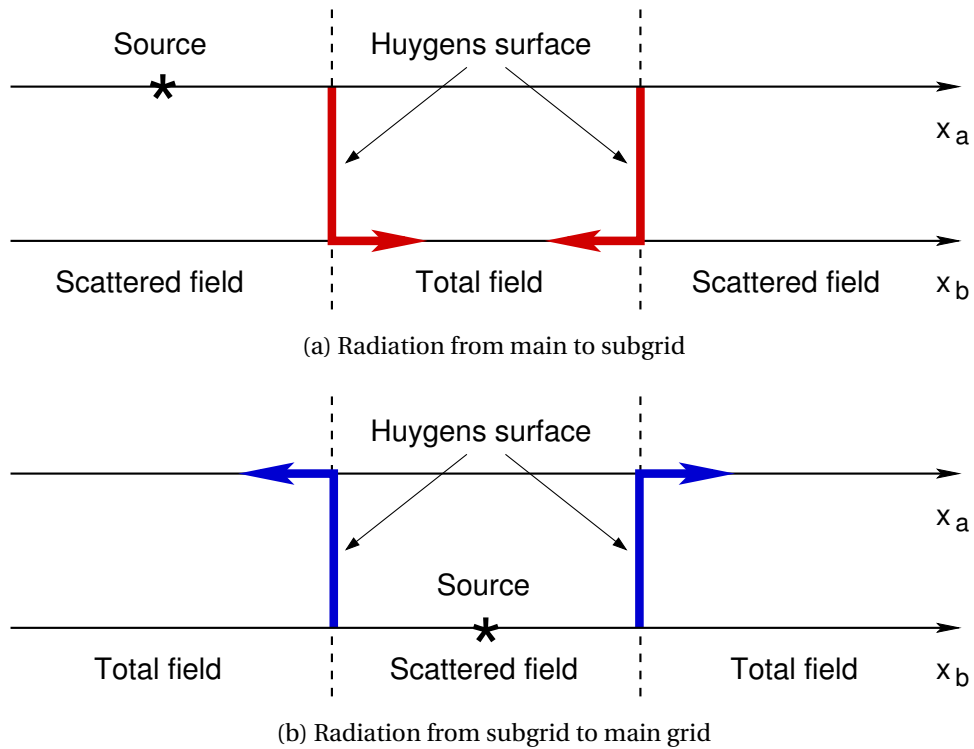
Figure 4.1: Huygens surface radiation [99]

Main principle of the HSG method is a combination of the two cases presented above—main and subgrid spaces interact via the Inner and Outer Huygens surfaces. Inner Surface (IS) radiates from the main grid into the subgrid and the Outer Surface (OS) radiates from the subgrid into the main grid.

The HSG method replaces the original physical problem with an equivalent problem that consists of two or more spaces. One space will become the main grid with coarse spatio-temporal resolution and another the subgrid with the fine spatio-temporal resolution. Figures 4.2a and 4.2b illustrate the original and equivalent problems as seen by the HSG method. Working and Non-working regions shown in Figure 4.2b are the regions outside of the OS–IS interface.

Bérenger has drawn and proven the following two propositions that constitute the main laws of the HSG operation [98]:

(a) HSG original problem
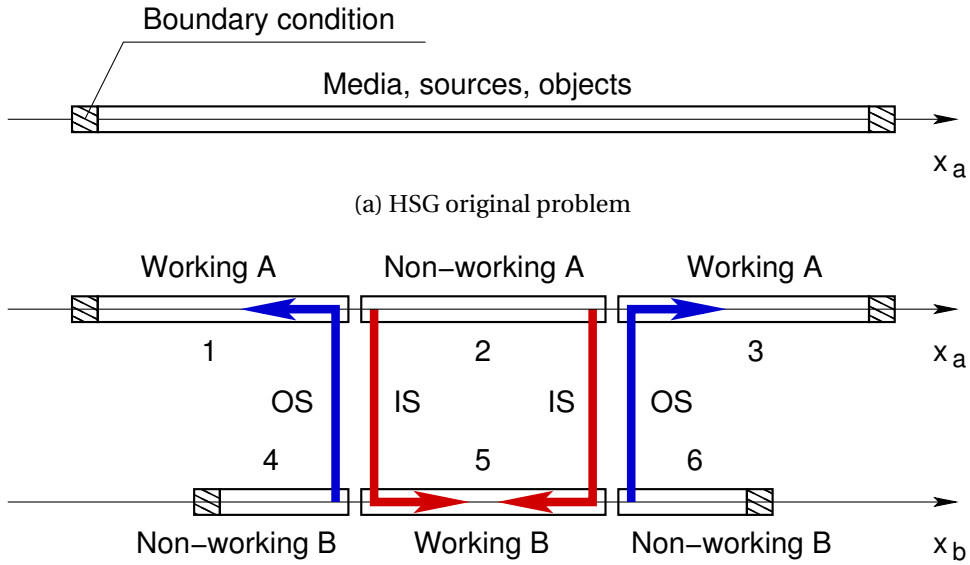
(b) HSG equivalent problem. Simulated wave propagates in the working regions 1, 5, 3. Regions 1 and 3 are located in the main and region 5 in the subgrid. For practical reasons the wave also travels via the non-working main grid region 2 and the non-working subgrid regions 4 and 6, but it has no influence onto the simulation result.

Figure 4.2: HSG principles [102]

Proposition 1. *Sources in non-working regions a or b radiate no field into working regions a or b.*

Proposition 2. *Field radiated into working regions a and b by sources in the working regions a and b is identical to the field, that would be radiated at the same location in a single space composed of media, sources in working regions a and b, and media inside the OS–IS interface.*

The above propositions describe the ideal state theory. However, there is a little discrepancy between the theory and practice. First, the objects in non-working regions can influence the computation results. Second, in theory any Absorbing Boundary Conditions (ABC) can terminate the subgrid region, but in practice it is recommended to use the Perfectly Matched Layer (PML) to achieve better instability suppression of the HSG method.

Figure 4.3 adopted from [98] shows a practical application case of the HSG scheme. Modelling a 1.01 mm slot with spatial increments of the coarse FDTD grid $\Delta s_a = 50$ mm would be impossible. But placing the slot and the surrounding region into the subgrid with fine spatial discretisation steps of $\Delta s_b = 0.505$ mm makes it a realistic task. In case of the HSG method with a subgridding ratio of $r = 99$ the thin slot would be modelled using two subgrid cells.
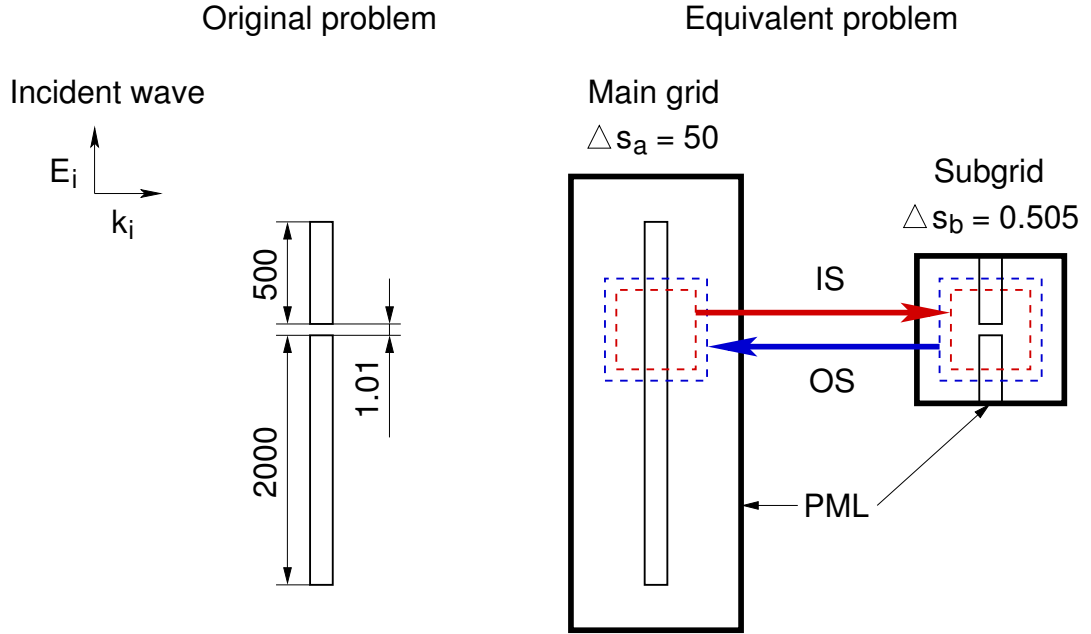
Figure 4.3: HSG space decomposition, 2D [98]. All distances are given in milli-metres (mm). Spatial increments of the main and subgrids are $\Delta s_a = 50$ mm and $\Delta s_b = 0.505$ mm. Subgridding ratio $r = 99$. Symbol k_i shows the direction of propagation of the incident wave.

4.3 Total-Field/Scattered-Field Technique

This section provides a brief introduction to the Total-Field/Scattered-Field (TF/SF) technique. It is important to understand the concept of the TF/SF scheme, since it plays a crucial role in the Huygens Subgridding approach. Mathematical formulation of the TF/SF algorithm is explained in 1D in Section 4.3.3.

4.3.1 Introduction

According to the Total-Field/Scattered-Field (TF/SF) theory [139, 140] the physical total field E_{tot}, H_{tot} can be decomposed into a sum of incident and scattered fields:

$$E_{tot} = E_{inc} + E_{sct}, \quad H_{tot} = H_{inc} + H_{sct}, \tag{4.4}$$

where E_{inc}, H_{inc} are the incident-wave fields assumed to be known at all spatial locations and all time moments of the FDTD space-time grid. Incident fields are the fields that would be present in vacuum, i.e. in the empty simulation domain with no materials of any kind. Scattered-wave fields E_{sct}, H_{sct}, assumed to be unknown

initially, are the result of an interaction between the incident wave and materials in the simulation domain [16].
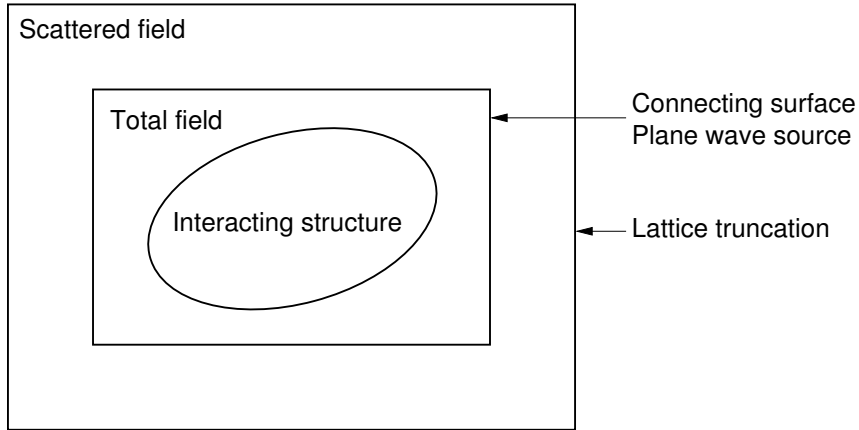
Figure 4.4: Total-field/scattered-field zoning [16]

Using the TF/SF technique the Yee simulation space can be zoned into the TF and SF regions. Figure 4.4 presents the TF and SF regions in the FDTD simulation domain. Elliptical interacting structure is placed inside of the TF zone. TF region in the centre of the domain contains the fields generated by the incident and the scattered waves. Connecting surface is a non-physical virtual surface connecting the TF and SF zones. Connecting surface bounds the TF region and serves as an incident wave source. SF region surrounds the TF. Both TF and SF region values are assumed to be stored in computer memory. In SF region the FDTD algorithm operates with the SF values only. No incident wave is computed in the SF zone. Finally, the lattice truncation surrounds the SF region. Usually an Absorbing Boundary Condition (ABC) acts as a lattice truncation. The purpose of ABC is to simulate a numerical wave propagation to infinity with zero or almost zero reflection.

In context of HSG connecting interface separating the simulation domain into the Total-Field/Scattered-Field zones is the Huygens Surface. In accordance with the equivalence theorem the electromagnetic current densities induced onto the Huygens Surface will represent electromagnetic fields radiated inside or outside of the surface. Location of the field source determines the location of the Scattered Field zone, i.e. the Scattered Field zone will always contain the source.

Consider the Outer and Inner Huygens Surfaces depicted in Figure 4.5. The leftmost sphere represents the Outer Huygens Surface. An excitation source will be located inside of this sphere. The SF region will be positioned inside and the TF outside of the sphere. Via the equivalence theorem all the field radiated from inside
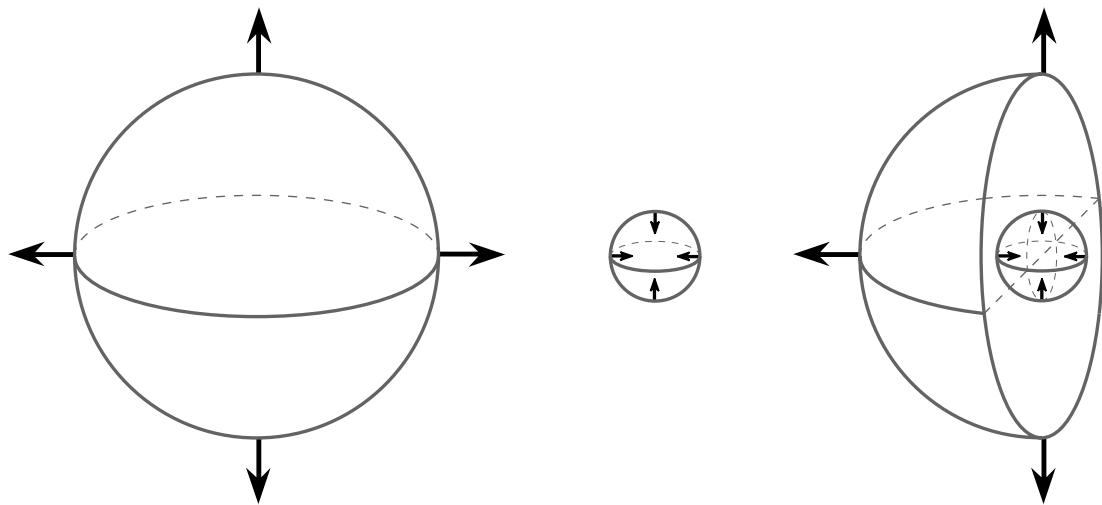
Figure 4.5: Inner and Outer Huygens Surfaces. Black arrows show the direction of electromagnetic field radiation in the HSG.

and landing onto the surface of the sphere can be propagated further by the sphere. Purpose of the Outer Huygens Surface is to transfer the influence from the subgrid to the main grid of the HSG.

Small sphere in the centre of Figure 4.5 illustrates the Inner Huygens Surface. In this case the source is located outside of the sphere. Therefore, the TF region is outside and the SF region is inside of the central sphere. Electromagnetic fields landing on the surface from outside will be propagated by the sphere inside of the domain. The Inner Huygens Surface passes the influence from the main into the subgrid of the HSG.

The rightmost hemisphere in Figure 4.5 shows the Outer and Inner Huygens Surfaces inside of each other. This surface positioning is adopted in the HSG method. Hence, a single TF/SF interface is represented by two Huygens Surfaces, where each surface deals with a one-directional field radiation (main-to-subgrid in case of the Inner Surface and sub-to-main grid in case of the Outer Surface).

It is important to notice that the TF/SF positions depend on the point of view. In case of the Outer Surface the TF will be outside and the SF—inside of the big sphere. In case of the Inner Surface the SF will be outside and the TF—inside of the small sphere.

4.3.2   Advantages of TF/SF Technique

Application of the TF/SF techniques has a number of advantages:

Connecting surface allows to create highly customised time waveform with user-defined duration, angle of incidence and angle of polarisation. Numerical incident wave is confined to the TF region only. Connecting surface, transparent to outgoing numerical waves, enables a well-defined SF zone.

Simple programming of interaction structures is possible with the TF/SF technique. Incident field needs to be calculated only along the connecting surface between the TF and SF regions.

Wide computational dynamic range[1] of the TF/SF technique allows direct calculation of the low field amplitude levels in the TF region. Typically the FDTD methods implement the SF only approach. In order to calculate the low field amplitude levels necessary in certain CEM problems, conventional SF only FDTD methods require an addition of the incident field to the scattered field. The field addition may result in high amount of numerical errors [16].

Improved ABC functionality can be achieved with the TF/SF scheme, while SF region serves as a buffering zone between the TF area and lattice termination.

Far-field response calculation can be simplified by placing the near-to-far field transformation surface inside the SF zone.

4.3.3   Mathematical Formulation in 1D

Consider Figure 4.6 that shows a 1D x-directed cut through the 2D surface presented in Figure 4.4.

The following free-space finite-difference expression for E_z in 1D will be valid for both all total or all scattered field components:

$$E_z^{n+1}(i) = E_z^n(i) + \frac{\Delta t}{\varepsilon_0 \Delta x}\left(H_y^{n+\frac{1}{2}}\left(i+\tfrac{1}{2}\right) - H_y^{n+\frac{1}{2}}\left(i-\tfrac{1}{2}\right)\right). \tag{4.5}$$

Calculation at left-side with $x = i_L$

However, at the left-side point i_L on the connecting surface the situation is different. According to Figure 4.6 component E_z at the i_L is located in the TF region. But the

---

[1]Computational dynamic range is the maximum to minimum ratio of an accurately computed TF level in the space lattice [16].
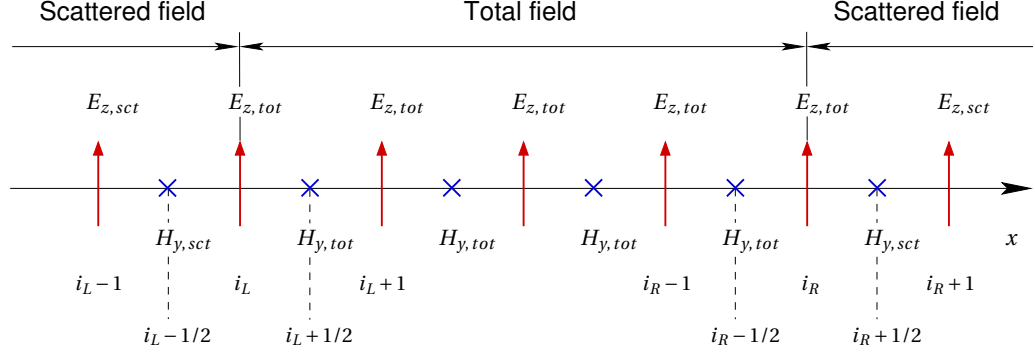
Figure 4.6: Total-field/scattered-field component locations, 1D [16]. Upwards-directed red arrows denote electric field components E_z and blue crosses stand for magnetic field components H_y. Indices tot and sct signify total and scattered region fields. Coordinates i_L and i_R illustrate the locations of the left-side and right-side connecting surfaces. Electric and magnetic field components are offset by a half space-step $1/2$. TF region is located in the middle of the figure and is surrounded by the SF region.

two magnetic field components required for the $E^{n+1}_{z,tot}(i_L)$ calculation are in the TF and SF regions:

$$E^{n+1}_{z,tot}(i_L) = E^n_{z,tot}(i_L) + \frac{\Delta t}{\varepsilon_0 \Delta x}\left(H^{n+\frac{1}{2}}_{y,tot}\left(i_L + \tfrac{1}{2}\right) - H^{n+\frac{1}{2}}_{y,sct}\left(i_L - \tfrac{1}{2}\right)\right). \qquad (4.6)$$

Equation (4.6) is inconsistent, since the calculation of TF region component relies on the difference of TF and SF region components. To obtain a TF region value only TF region values must be used. Therefore, to achieve the TF balance another term is added to (4.6):

$$E^{n+1}_{z,tot}(i_L) = E^n_{z,tot}(i_L) + \frac{\Delta t}{\varepsilon_0 \Delta x}\left(H^{n+\frac{1}{2}}_{y,tot}\left(i_L + \tfrac{1}{2}\right) - H^{n+\frac{1}{2}}_{y,sct}\left(i_L - \tfrac{1}{2}\right) - H^{n+\frac{1}{2}}_{y,inc}\left(i_L - \tfrac{1}{2}\right)\right), \quad (4.7)$$

since

$$-H^{n+\frac{1}{2}}_{y,sct}\left(i_L - \tfrac{1}{2}\right) - H^{n+\frac{1}{2}}_{y,inc}\left(i_L - \tfrac{1}{2}\right) = -H^{n+\frac{1}{2}}_{y,tot}\left(i_L - \tfrac{1}{2}\right). \qquad (4.8)$$

Similar situation occurs in the magnetic field calculation at the left-side point $i_L - \frac{1}{2}$:

$$H^{n+\frac{1}{2}}_{y,sct}\left(i_L - \tfrac{1}{2}\right) = H^{n-\frac{1}{2}}_{y,sct}\left(i_L - \tfrac{1}{2}\right) + \frac{\Delta t}{\mu_0 \Delta x}\left(E^n_{z,tot}(i_L) - E^n_{z,sct}(i_L - 1)\right), \qquad (4.9)$$

SF value $H_{y,sct}^{n+\frac{1}{2}}\left(i_L - \frac{1}{2}\right)$ calculation (4.9) is inconsistent, since it involves the difference of TF and SF region values. For consistency the SF value must be computed based on the difference of SF values only. Therefore, equation (4.9) is corrected by subtracting the incident field term $E_{z,inc}^n(i_L)$:

$$H_{y,sct}^{n+\frac{1}{2}}\left(i_L - \tfrac{1}{2}\right) = H_{y,sct}^{n-\frac{1}{2}}\left(i_L - \tfrac{1}{2}\right) + \frac{\Delta t}{\mu_0 \Delta x}\left(E_{z,tot}^n(i_L) - E_{z,inc}^n(i_L) - E_{z,sct}^n(i_L - 1)\right),$$

$$(4.10)$$

since

$$E_{z,tot}^n(i_L) - E_{z,inc}^n(i_L) = E_{z,sct}^n(i_L). \tag{4.11}$$

Calculation at right-side with $x = i_R$

Analogously at the right-side point i_R electric field component $E_{z,tot}^{n+1}(i_R)$ is obtained as:

$$E_{z,tot}^{n+1}(i_R) = E_{z,tot}^n(i_R) + \frac{\Delta t}{\varepsilon_0 \Delta x}\left(H_{y,sct}^{n+\frac{1}{2}}\left(i_R + \tfrac{1}{2}\right) + H_{y,inc}^{n+\frac{1}{2}}\left(i_R + \tfrac{1}{2}\right) - H_{y,tot}^{n+\frac{1}{2}}\left(i_R - \tfrac{1}{2}\right)\right),$$

$$(4.12)$$

since

$$H_{y,sct}^{n+\frac{1}{2}}\left(i_R + \tfrac{1}{2}\right) + H_{y,inc}^{n+\frac{1}{2}}\left(i_R + \tfrac{1}{2}\right) = H_{y,tot}^{n+\frac{1}{2}}\left(i_R + \tfrac{1}{2}\right). \tag{4.13}$$

Magnetic field component $H_{y,sct}^{n+\frac{1}{2}}\left(i_R + \frac{1}{2}\right)$ on the connecting surface at location $i_R + \frac{1}{2}$ is calculated in the following manner:

$$H_{y,sct}^{n+\frac{1}{2}}\left(i_R + \tfrac{1}{2}\right) = H_{y,sct}^{n-\frac{1}{2}}\left(i_R + \tfrac{1}{2}\right) + \frac{\Delta t}{\mu_0 \Delta x}\left(E_{z,sct}^n(i_R + 1) - E_{z,tot}^n(i_R) + E_{z,inc}^n(i_R)\right),$$

$$(4.14)$$

since

$$-E_{z,tot}^n(i_R) + E_{z,inc}^n(i_R) = -E_{z,sct}^n(i_R). \tag{4.15}$$

4.4   Equivalent Currents at Huygens Surfaces

4.4.1   Inner Surface

Refer to the equivalence theorem and Figure 4.2b presented in Section 4.2. Consider electric and magnetic fields at the IS location in the main grid $\boldsymbol{E}_a(IS), \boldsymbol{H}_a(IS)$. Electric and magnetic fields $\boldsymbol{E}_a(IS), \boldsymbol{H}_a(IS)$ are enforced by equivalent currents $\boldsymbol{K}_b(IS), \boldsymbol{L}_b(IS)$ at IS locations in the subgrid:

$$K_b(IS) = \quad n \times H_a(IS), \tag{4.16}$$

$$L_b(IS) = -n \times E_a(IS). \tag{4.17}$$

In this case the unit vector n is normal to IS and is oriented towards the working region of the subgrid (region 5 in Figure 4.2b). Therefore, fields entering the non-working region of the main grid (region 2 in Figure 4.2b) are radiated into the working region of the subgrid. Identical approach is applied at the OS [101].
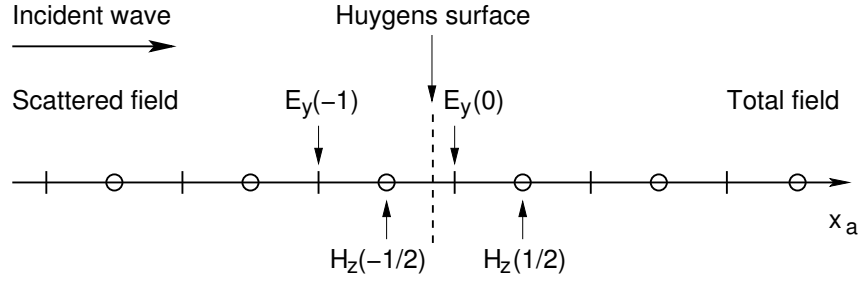
Figure 4.7: Huygens surface, 1D [102]

For a better understanding of the Huygens Subgridding functionality consider a hypothetical Huygens surface presented in 1D in Figure 4.7. An analytical incident wave propagates from left to right of Figure 4.7. Magnetic field component $H_z\left(-\frac{1}{2}\right)$ is located in the Scattered Field (SF) region and the electric field component $E_y(0)$ is positioned in the Total Field (TF) region. According to the TF/SF theory [16] the incident field contribution is either added to or subtracted from the normal FDTD update equation:

$$E_y^{n+1}(0) = E_y^n(0) - \frac{\Delta t}{\varepsilon_0 \Delta x}\left(H_z^{n+\frac{1}{2}}\left(\tfrac{1}{2}\right) - H_z^{n+\frac{1}{2}}\left(-\tfrac{1}{2}\right) - H_{z,inc}^{n+\frac{1}{2}}\left(-\tfrac{1}{2}\right)\right), \tag{4.18}$$

$$H_z^{n+\frac{3}{2}}\left(-\tfrac{1}{2}\right) = H_z^{n+\frac{1}{2}}\left(-\tfrac{1}{2}\right) - \frac{\Delta t}{\mu_0 \Delta x}\left(E_y^{n+1}(0) - E_{y,inc}^{n+1}(0) - E_y^{n+1}(-1)\right). \tag{4.19}$$

where $H_{z,inc}^{n+\frac{1}{2}}\left(-\frac{1}{2}\right)$ is the incident H_z field at time moment $n+\frac{1}{2}$ and spatial location $-\frac{1}{2}$ and $E_{y,inc}^{n+1}(0)$ is the incident field E_y at time moment $n+1$ and spatial location 0.

Refer to Figure 4.8 to analyse the real HSG Inner Surface functionality. The key difference between the cases presented in Figures 4.7 and 4.8 is that the analytical wave is replaced with a discretised wave radiating from the FDTD main grid into the FDTD subgrid. Subgrid field advancement at the two nodes closest to the IS
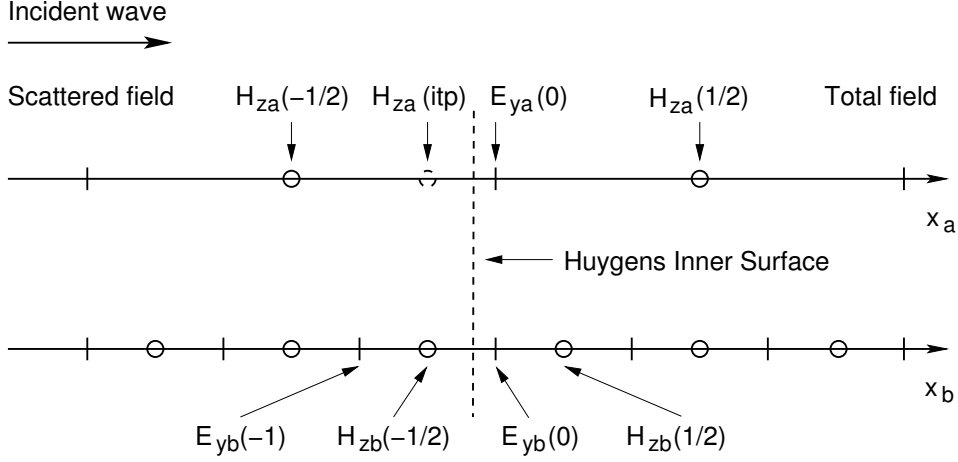
Figure 4.8: Inner Surface, 1D [102]. This figure corresponds to the IS on the left hand-side of Figure 4.2.

interface is governed by the following equations:

$$E_{yb}^{n+m}(0) = E_{yb}^{n+m-1}(0) - \frac{\Delta t_b}{\varepsilon_0 \Delta x_b} \left(H_{zb}^{n+m-\frac{1}{2}}\left(\tfrac{1}{2}\right) - H_{zb}^{n+m-\frac{1}{2}}\left(-\tfrac{1}{2}\right) - H_{za}^{n+m-\frac{1}{2}}\left(itp\right) \right),$$
(4.20)

$$H_{zb}^{n+m+\frac{1}{2}}\left(-\tfrac{1}{2}\right) = H_{zb}^{n+m-\frac{1}{2}}\left(-\tfrac{1}{2}\right) - \frac{\Delta t_b}{\mu_0 \Delta x_b} \left(E_{yb}^{n+m}(0) - E_{ya}^{n+m}(0) - E_{yb}^{n+m}(-1) \right), \quad (4.21)$$

where m is an integer iterator on the subgrid time loop, such that $m \in [1, r]$. Time in (4.20) and (4.21) is advanced in the subgrid time-steps. Since $E_{yb}(0)$ in Figure 4.8 is located in the TF region, the incident field value of $H_{za}^{n+m-\frac{1}{2}}(itp)$ in (4.20) is required to balance the scattered field value of $H_{zb}^{n+m-\frac{1}{2}}\left(-\tfrac{1}{2}\right)$. Incident field component $H_{za}^{n+m-\frac{1}{2}}(itp)$ in (4.20) is identical to $H_{z,inc}^{n+\frac{1}{2}}\left(-\tfrac{1}{2}\right)$ in (4.18) and provides an elegant mechanism to inject the main grid field influence into the subgrid.

Similar action occurs in (4.21). In Figure 4.8 magnetic field component $H_{zb}\left(-\tfrac{1}{2}\right)$ is located in the SF region and is calculated in (4.21) using the difference of TF electric field component $E_{yb}^{n+m}(0)$ and SF electric field component $E_{yb}^{n+m}(-1)$. Therefore, an incident electric field component $E_{ya}^{n+m}(0)$ is required to balance the TF/SF relation. Component $E_{ya}^{n+m}(0)$ is identical to $E_{y,inc}^{n+1}(0)$ in (4.19) and introduces the main grid field influence to the subgrid.

Figure 4.8 shows that the node $H_{za}^{n+m-\frac{1}{2}}(itp)$ is non-existent in the main grid

at the spatial location itp and the time moment $n + m - \frac{1}{2}$. Therefore, this node is obtained in two sequences of interpolations, one on space and one on time. Spatial interpolation is given by (4.22):

$$H_{za}^{n+\frac{r}{2}}\left(itp\right) = X_1\, H_{za}^{n+\frac{r}{2}}\left(-\tfrac{1}{2}\right) + X_2\, H_{za}^{n+\frac{r}{2}}\left(\tfrac{1}{2}\right),\qquad(4.22)$$

where

$$X_1 = \frac{r+1}{2r},\quad X_2 = \frac{r-1}{2r}.\qquad(4.23)$$

Symbol r denotes the subgridding ratio, while parameters X_1 and X_2 stand for spatial interpolation coefficients. H_{za} nodes in (4.22) are the closest nodes to the target node $H_{za}^{n+\frac{r}{2}}\left(itp\right)$ from the left and the right sides at locations $-\frac{1}{2}$ and $\frac{1}{2}$. According to Figure 4.8 the node $H_{za}\left(-\frac{1}{2}\right)$ is located closer to $H_{za}\left(itp\right)$, than the node $H_{za}\left(\frac{1}{2}\right)$. Interpolation coefficients X_1 and X_2 allow to increase the influence of the closer node $H_{za}\left(-\frac{1}{2}\right)$ and decrease the influence of the farther node $H_{za}\left(\frac{1}{2}\right)$ onto the target value of $H_{za}\left(itp\right)$, e.g. in case of $r = 5$ the spatial interpolation coefficients will be $X_1 = 0.6$ and $X_2 = 0.4$ and the target node $H_{za}\left(itp\right)$ will consist of 60% influence of the closer node $H_{za}\left(-\frac{1}{2}\right)$ and 40% influence of the farther node $H_{za}\left(\frac{1}{2}\right)$.

After the value of $H_{za}^{n+\frac{r}{2}}\left(itp\right)$ is determined by (4.22) this node is interpolated on time to yield its values at subgrid time steps.

For $m \in \left[1, \frac{r}{2} - \frac{1}{2}\right]$, $m_1 = m + \frac{r}{2} - \frac{1}{2}$, $\Upsilon_1 = \frac{r - m_1}{r}$ and $\Upsilon_2 = \frac{m_1}{r}$:

$$H_{za}^{n+m-\frac{1}{2}}\left(itp\right) = \Upsilon_1\, H_{za}^{n-\frac{r}{2}}\left(itp\right) + \Upsilon_2\, H_{za}^{n+\frac{r}{2}}\left(itp\right).\qquad(4.24)$$

For $m \in \left[\frac{r}{2} + \frac{1}{2}, r\right]$, $m_2 = m - \frac{r}{2} - \frac{1}{2}$, $\Upsilon_1 = \frac{r - m_2}{r}$ and $\Upsilon_2 = \frac{m_2}{r}$:

$$H_{za}^{n+m-\frac{1}{2}}\left(itp\right) = \Upsilon_1\, H_{za}^{n+\frac{r}{2}}\left(itp\right) + \Upsilon_2\, H_{za}^{n+\frac{3r}{2}}\left(itp\right).\qquad(4.25)$$

Figure 4.9 gives an example of the temporal interpolation of the main grid magnetic field component $H_{za}\left(itp\right)$ for the subgridding ratio $r = 7$. Two temporal interpolation cases specified by (4.24) and (4.25) are required because the subgrid values of $H_{za}\left(itp\right)$ are located in between of two pairs of the main grid values. When $r = 7$ the first three interpolations will be calculated according to (4.24) and the next four according to (4.25).

Figure 4.8 illustrates that the node $E_{ya}^{n+m}\left(0\right)$ exists at the spatial location 0. Spatial interpolation is not necessary, since the main grid electric field values coincide with the subgrid values. Therefore, only temporal interpolation has to be applied to

$H_{za}\,(itp)$ $H_{za}\,(itp)$ $H_{za}\,(itp)$

$-7/2$ 0 $7/2$ 7 $21/2$ t_b

$m \in [1, 3],\ m_1 \in [4, 6]$ $m \in [4, 7],\ m_2 \in [0, 3]$

$\Upsilon_1 \in [3/7, 2/7, 1/7]$ $\Upsilon_1 \in [1, 6/7, 5/7, 4/7]$

$\Upsilon_2 \in [4/7, 5/7, 6/7]$ $\Upsilon_2 \in [0, 1/7, 2/7, 3/7]$
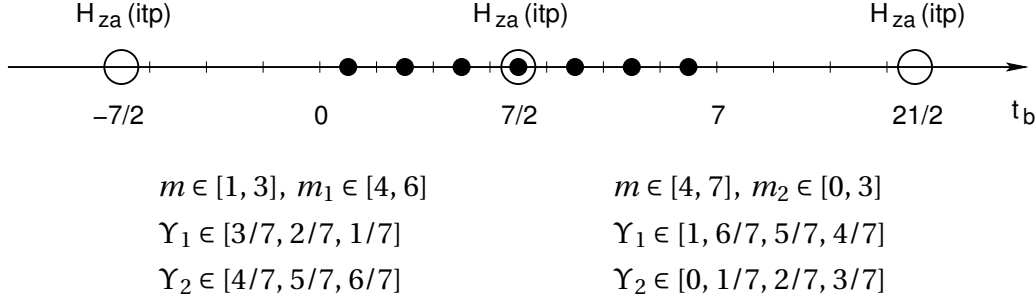
Figure 4.9: Temporal interpolation of $H_{za}\left(itp\right)$ for subgridding ratio $r = 7$. Large hollow circles show the main grid $H_{za}\left(itp\right)$ component values on the subgrid time axis t_b. Small filled circles denote the interpolated values of $H_{za}\left(itp\right)$ at subgrid time-steps. Vertical bars illustrate the integer subgrid time-steps. Values of 0 and 7 highlight the integer subgrid time-steps, while the main grid component locations are denoted by the fractions $-7/2$, $7/2$, $21/2$. For the sake of simplicity the main grid time step $n = 0$.

$E_{ya}^{n+m}(0)$ to obtain the electric field values at the subgrid time-steps.

For $m \in [1, r]$, $\Upsilon_1 = \frac{r-m}{r}$ and $\Upsilon_2 = \frac{m}{r}$:

$$E_{ya}^{n+m}(0) = \Upsilon_1 E_{ya}^{n}(0) + \Upsilon_2 E_{ya}^{n+r}(0). \tag{4.26}$$

Figure 4.10 shows the temporal interpolation of the main grid electric field component $E_{ya}(0)$. Subgrid values are positioned in between of only two main grid values. Temporal interpolation coefficients Υ_1, Υ_2 control the amount of each main grid component influence. Interpolation coefficients change their values depending on the subgrid time-step. The closer a requested $E_{ya}(0)$ value is to a real main grid value, the bigger is the corresponding interpolation coefficient. For example in case of $m = 2$, $\Upsilon_1 = 5/7$ and $\Upsilon_2 = 2/7$. Coefficient $\Upsilon_1 > \Upsilon_2$, since the requested value of $E_{ya}(0)$ is closer to time-step 0, than to time-step 7.

Temporal interpolations (4.24) to (4.26) use the future time values of the electric and magnetic fields $E_{ya}^{n+r}(0)$ and $H_{za}^{n+\frac{r}{2}}\left(itp\right)$, $H_{za}^{n+\frac{3r}{2}}\left(itp\right)$. These future time values are called "precursors" and are easily obtained by the local electric and magnetic field updates in the main grid. Regular FDTD equations are used to calculate precursors at the spatial points itp and 0 only. Calculated precursor values will be correct because of the OS–IS separation required by the HSG theory. The minimum OS–IS separation equals to $2\Delta s_a$ and $2\Delta t_a$. The OS–IS separation ensures that the subgrid influence will be delayed and will reach the main grid only after 2 main grid time steps. The physical separation between the OS and IS is a key feature of the

$$m \in [1, 7]$$
$$\Upsilon_1 \in [6/7, 5/7, 4/7, 3/7, 2/7, 1/7, 0]$$
$$\Upsilon_2 \in [1/7, 2/7, 3/7, 4/7, 5/7, 6/7, 1]$$
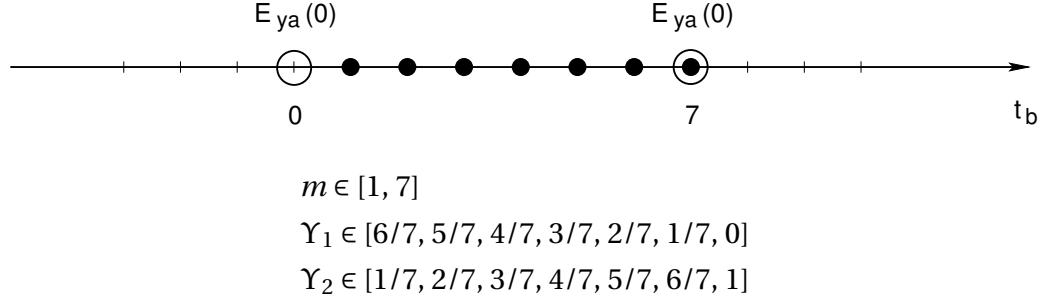
Figure 4.10: Temporal interpolation of $E_{ya}(0)$ for subgridding ratio $r = 7$. Large hollow circles show the main grid $E_{ya}(0)$ component values on the subgrid time axis t_b. Small filled circles denote the interpolated values of $E_{ya}(0)$ at subgrid time-steps. Vertical bars illustrate the integer subgrid time-steps. Values of 0 and 7 highlight the integer subgrid time-steps. For the sake of simplicity the main grid time step $n = 0$.

HSG method, which allows to avoid the field extrapolation on time [101, 102].

Since the starting point of the HSG algorithm can be chosen arbitrarily, it is possible to avoid the calculation of future precursor values. If the electric field values E_a, E_b are assumed to be known at time-step n and the magnetic field values H_a, H_b at time-steps $n + \frac{r}{2}$ and $n + \frac{1}{2}$, the HSG method does not require the future time-step values of the field precursors as mentioned in (4.24) to (4.26). Due to a different initial condition of the HSG algorithm the implementation is simplified. Precursor values become only the spatial and temporal interpolations, with no local FDTD field advance.

4.4.2 Outer Surface

Figure 4.11 presents the Outer Surface in 1D. Subgrid nodes exist at each space location and each time moment, and overlap with the main grid nodes. Therefore, the OS implementation is much simpler than the IS. Neither time nor space interpolations are required for the OS calculation:

$$E_{ya}^{n+r}(0) = E_{ya}^n(0) - \frac{\Delta t_a}{\varepsilon_0 \Delta x_a} \left(H_{za}^{n+\frac{r}{2}}\left(\tfrac{1}{2}\right) - H_{za}^{n+\frac{r}{2}}\left(-\tfrac{1}{2}\right) - H_{zb}^{n+\frac{r}{2}}\left(\tfrac{r}{2}\right) \right), \tag{4.27}$$

$$H_{za}^{n+\frac{3r}{2}}\left(\tfrac{1}{2}\right) = H_{za}^{n+\frac{r}{2}}\left(\tfrac{1}{2}\right) - \frac{\Delta t_a}{\mu_0 \Delta x_a} \left(E_{ya}^{n+1}(1) - E_{yb}^{n+1}(0) - E_{ya}^{n+1}(0) \right). \tag{4.28}$$

According to Figure 4.11 the electric field value $E_{ya}^{n+r}(0)$ and the magnetic field
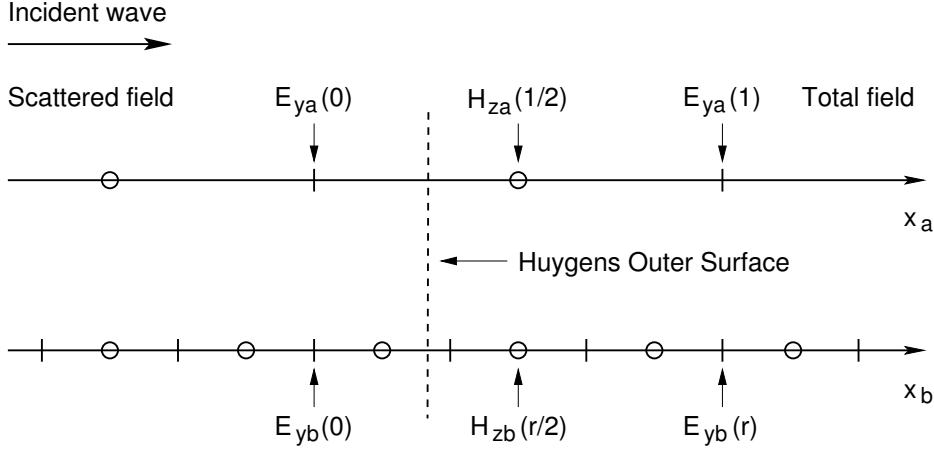
Figure 4.11: Outer Surface, 1D [102]. This figure corresponds to the OS on the right hand-side of Figure 4.2.

value $H_{za}^{n+\frac{r}{2}}\left(-\frac{1}{2}\right)$ are located in the SF region. Electric field $E_{ya}^{n+r}(0)$ in (4.27) is calculated using the TF and SF magnetic field values $H_{za}^{n+\frac{r}{2}}\left(\frac{1}{2}\right)$ and $H_{za}^{n+\frac{r}{2}}\left(-\frac{1}{2}\right)$. To balance the TF/SF relation in (4.27) the incident magnetic field $H_{zb}^{n+\frac{r}{2}}\left(\frac{r}{2}\right)$ is subtracted from the main grid magnetic field difference. The subgrid influence to the main grid is passed with the subtraction of $H_{zb}^{n+\frac{r}{2}}\left(\frac{r}{2}\right)$.

Magnetic field at the OS is updated in a similar manner. In Figure 4.11 components $H_{za}^{n+\frac{3r}{2}}\left(\frac{1}{2}\right)$, $E_{ya}^{n+1}(1)$ are located in the TF region and component $E_{ya}^{n+1}(0)$ is positioned in the SF region. To balance the TF/SF relation in (4.28) the incident electric field $E_{yb}^{n+1}(0)$ of the subgrid is subtracted from the main grid electric field difference. The electric equivalent current from the subgrid to the main grid is transferred with the $E_{yb}^{n+1}(0)$.

4.5   Huygens Subgridding Algorithm

Algorithm 3 describes the HSG method operation within one main grid iteration. Symbol "*" denotes all spatial locations in the simulation domain. Indices a and b stand for the main and subgrids respectively. Variable m is used to iterate over the subgrid time loop. Subgridding ratio is r. For the sake of clarity value re-arrangement, source excitation, value output and spatial domain termination with the ABC are not shown in Algorithm 3.

The HSG algorithm consists of two symmetric parts, where the subgrid time

1: **calc** $E_a(*)$

2: **iface** $E_a(IS)$

3: **for** $m \in [1, \frac{r-1}{2}]$ **do**

4:     **calc** $H_b(*)$

5:     **infl** $IS : E_a(IS) \to H_b(IS)$

6:     **calc** $E_b(*)$

7:     **infl** $IS : H_a(IS) \to E_b(IS)$

8: **end for**

9: **calc** $H_b(*)$

10: **infl** $IS : E_a(IS) \to H_b(IS)$

11: **infl** $OS : H_b(OS) \to E_a(OS)$

12: **calc** $H_a(*)$

13: **iface** $H_a(IS)$

14: **for** $m \in [1, \frac{r-1}{2}]$ **do**

15:     **calc** $E_b(*)$

16:     **infl** $IS : H_a(IS) \to E_b(IS)$

17:     **calc** $H_b(*)$

18:     **infl** $IS : E_a(IS) \to H_b(IS)$

19: **end for**

20: **calc** $E_b(*)$

21: **infl** $IS : H_a(IS) \to E_b(IS)$

22: **infl** $OS : E_b(OS) \to H_a(OS)$

Algorithm 3: HSG pseudocode. Abbreviations "calc", "iface" and "infl" stand for calculate, calculate interface and calculate influence. Calculate is a regular FDTD update, calculate interface is the spatial and temporal interpolation at the OS–IS interface, and calculate influence is the equivalent magnetic or electric current transfer via the OS or IS.

loops (lines: 3–8, 14–19) are inserted after the electric and magnetic field calculations in the main grid. These loops are used in order to synchronise the subgrid field updates with the main grid. An important point to notice is the IS influence injection into the subgrid. IS equivalent current is always injected straight after the electric or magnetic field calculation in the subgrid. Main grid field interpolations at the IS interface (lines: 2 and 13) are calculated after the ordinary $E_a(*)$ and $H_a(*)$ updates. Interpolated values of $E_a(IS)$ and $H_a(IS)$ will be used at each IS current injection into the subgrid (lines: 5, 10, 18 and 7, 16, 21).

Since the subgridding ratio is an odd number each time loop of the subgrid is complemented with an additional $H_b(*)$ or $E_b(*)$ calculation (lines: 9, 10 and 20, 21). These additional calculations occur because half of the subgrid components are calculated in the first symmetric part of the HSG algorithm (lines: 1 to 11) and half of the subgrid components are calculated in the second half of the HSG scheme (lines: 12 to 22). The OS influence is injected into the main grid at the end of each symmetric part (lines: 11 and 22). The OS injection happens at last because it is only valid after the subgrid has synchronised with the main grid calculation and the corresponding temporal value of the $H_b(OS)$ or $E_b(OS)$ node is available.

Figure 4.12 illustrates the HSG method's advancement on time. One main grid time iteration is shown in Figure 4.12. Figure 4.12 is also symmetric, where its left

part corresponds to the left part of Algorithm 3 and the right part to the right part of Algorithm 3. Upper part of Figure 4.12 highlights the main grid time domain and the lower part—the subgrid time domain. Subgridding ratio of 5 is used throughout the figure. Thin horizontal and diagonal lines with arrows show the HSG computation order.
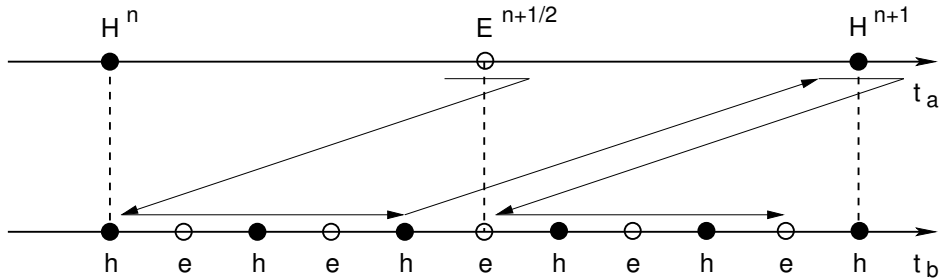
Figure 4.12: HSG advancement on time. Subgridding ratio $r = 5$. Hollow points mark the electric and filled points—the magnetic fields. Capital letters denote fields in the main and small letters—in the subgrid. Vertical dotted lines show the coinciding field values.

First the $E_a^{n+\frac{1}{2}}$ is calculated in the main grid, then HSG switches to the subgrid. Calculation in the subgrid is always delayed. Subgrid synchronises with the main grid at each main grid half time-step. After five subgrid iterations (at the end of the first HSG symmetric part) the algorithm switches back to the main grid. When the magnetic field H_a^{n+1} is calculated the HSG reverts to the subgrid to finish the remaining subgrid iterations. At the end of the process shown in Figure 4.12 the main grid has advanced one complete time-step and the subgrid—five complete time-steps.

4.6   Instability of Huygens Subgridding

4.6.1   Instability Analysis

Stability is a defined system property. Most common definitions of stability refer to energy, while in stable system the energy remains bounded. Stability is also a property of a numerical method. Energy computed with the discrete solution exhibits an exponential growth, where the speed of energy growth relates to the exponent of the *e*-function. In case of small exponents the energy growth is small and the instability is not visible until a certain time moment.

Stability of a subgridding algorithm is a critical issue affecting the accuracy of the final results. Unfortunately, the HSG method is naturally unstable. In the HSG scheme the instability is visible after approximately 1000 time-steps in 1D with $r = 99$ and the subgrid size 1880 subgrid cells long [99], 1000–2000 in 2D with $r = 11$ and the subgrid size of 550×1 subgrid cells [101], and 4000–5000 in 3D with $r = 5$ and the subgrid size of $80 \times 80 \times 160$ [102]. Bérenger suggests that the visibility of HSG instability depends on the subgridding ratio r, size of temporal increments Δt_a, Δt_b and presence of objects in the main and subgrids [99].

Instability in the HSG method is expressed in periodic artificial oscillations of the signal curve that grow over time. Eventually the instability oscillations will outgrow and eliminate the original signal. Period of instability oscillations is identical for both main and subgrids and depends on Δs_a and slightly on the ratio $\frac{c\Delta t_a}{\Delta s_a}$.

Numerical dispersion in the FDTD method in 1D is governed by the following equation:

$$\sin\left(\frac{\omega\Delta t}{2}\right) = \frac{c\Delta t}{\Delta x}\sin\left(\frac{k_x\Delta x}{2}\right), \tag{4.29}$$

where $c\Delta t < \Delta x$. At low frequencies k_x is a real number and the propagating waves are travelling waves. At high frequencies the term $\sin\left(\frac{k_x\Delta x}{2}\right) > 1$, therefore k_x is a complex number and propagating waves are evanescent waves. Transition frequency between the two regimes is:

$$f_{tr} = \frac{1}{\pi\Delta t}\arcsin\left(\frac{c\Delta t}{\Delta x}\right). \tag{4.30}$$

Above f_{tr} the wave magnitude decreases with distance, but the wavelength λ does not depend on the wave frequency f_w and equals $\lambda = 2\Delta x$ at any frequency beyond f_{tr}. It appears that the frequencies of instability are limited to a narrow band of frequencies centred at transition frequency f_{tr} of the main grid [99].

4.6.2 Filtering

Since the wavelength of unstable frequencies is constant ($\lambda = 2\Delta x$) a cosine filter[2] can be applied to the equivalent IS currents in order to reduce the instability:

---

[2]Low pass filtering dissipates the system energy. The energy dissipation with a sufficiently high rate can make any numerical method stable.

$$E_a(ia1) = \frac{E_a(ia1-1) + E_a(ia1)}{2}, \quad H_a(itp) = \frac{H_a(itp-1) + H_a(itp)}{2}. \quad (4.31)$$

Figure 4.8 shows the main grid field $E_a(ia1)$ and $H_a(itp)$ locations used in (4.31). $E_a(ia1)$ is the closest field location to the IS, i.e. in Figure 4.8 it is $E_{ya}(0)$. For wave number k_x the averaging (4.31) is equivalent to a multiplication of the wave magnitude with:

$$P(k_x) = \frac{\exp(jk_x\Delta x_a) + 1}{2} = \exp\left(\frac{jk_x\Delta x_a}{2}\right)\cos\left(\frac{k_x\Delta x_a}{2}\right). \quad (4.32)$$

Higher order filters can be obtained by cascading (4.31), e.g. a three point filter is:

$$E_a(ia1) = \frac{1}{4}E_a(ia1-1) + \frac{1}{2}E_a(ia1) + \frac{1}{4}E_a(ia1+1), \quad (4.33)$$

$$H_a(itp) = \frac{1}{4}H_a(itp-2) + \frac{1}{2}H_a(itp-1) + \frac{1}{4}H_a(itp). \quad (4.34)$$
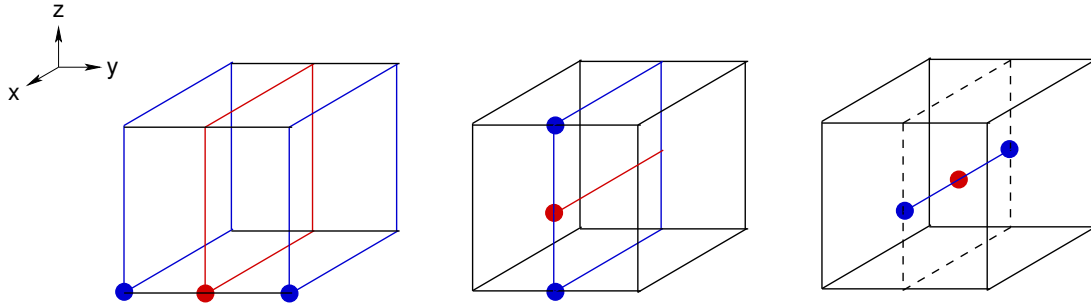
Figure 4.13: Filtering in HSG, summary. Participating elements are shown in blue and the target element—in red. Filled circles give examples of the participating nodes. Target point is calculated in three steps: (i) three planes of 9 points each are reduced into a centre plane on the left-most figure, (ii) three lines of 3 points each are averaged into a middle line on the central figure and (iii) three points on the central line and averaged into a single target point on the right-most figure.

Figure 4.13 gives a visual representation of the three point filter specified by (4.33) and (4.34). The general filtering process consists of three steps of averaging. First, 27 initial points surrounding the target point[3] are used to calculate the plane of 9 points, i.e. three planes of 9 points are averaged into a single plane of 9 points in

the centre of the cube. Then the central plane is averaged and reduced to a line, i.e. three lines with 3 points each are averaged into a middle line of 3 points. Finally, the middle line of three points is averaged to a central point to obtain the requested result.

Figures 4.14a to 4.14c describe the averaging process in detail: 27 initial points are reduced from a volume to a plane of 9 points (Figure 4.14a), then from a plane to a line of 3 points (Figure 4.14b) and finally from a line to a single point (Figure 4.14c).

Using the one point filter (4.31) in the 1D HSG approach delays the instability from 1000 to 40000 time-steps for the subgrid size of 1880 subgrid cells and $r = 99$ [99]. The three point filter (4.33) and (4.34) completely suppresses the instability (tested up to 10^6 main grid iterations) [99].

4.7 Mathematical Formulation

This section presents the mathematical formulation of the HSG method in 3D.

4.7.1 Magnetic Field Calculation

To simplify the FDTD method's equations for magnetic field calculation the following coefficients were defined:

$$Z_{1g}(i, j, k) = \frac{1 - \zeta_{1g}(i, j, k)}{1 + \zeta_{1g}(i, j, k)}, \quad Z_{2g}(i, j, k) = \frac{\zeta_{2g}(i, j, k)}{1 + \zeta_{1g}(i, j, k)}, \tag{4.35}$$

where

$$\zeta_{1g}(i, j, k) = \frac{\sigma_g^*(i, j, k) \Delta t_g}{2 \mu_g(i, j, k)}, \quad \zeta_{2g}(i, j, k) = \frac{\Delta t_g}{\mu_g(i, j, k)}. \tag{4.36}$$

Symbol g in (4.37) to (4.39) and (4.42) to (4.44) denotes the grid type, $g \in [a, b]$. Magnetic field components have to be calculated for both main and subgrids using the same equations:

$$H_{xg}^n(i, j, k) = Z_{1g}(i, j, k) H_{xg}^{n-1}(i, j, k)$$

---

[3]Target point is the requested point, that lies on the IS and will participate in the main to subgrid influence calculation. In case of a three point filter the target point is obtained by averaging 27 surrounding points.
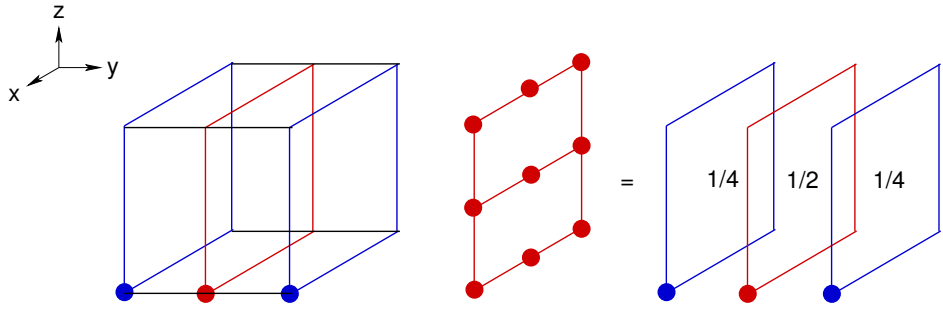
(a) Filtering in HSG, volume → plain reduction. Three planes of 9 points each are averaged into a central plane shown in red. Each node on the central plane is obtained by using the averaging coefficients of $1/4, 1/2, 1/4$.
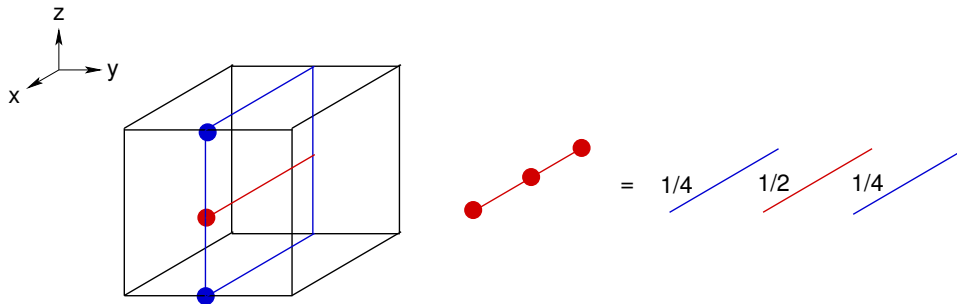
(b) Filtering in HSG, plane → line reduction. Three lines of 3 points each are averaged into a middle line depicted in red. Three points on the middle line are calculated using respective nodes of the participating lines multiplied by filtering coefficients $1/4, 1/2, 1/4$.
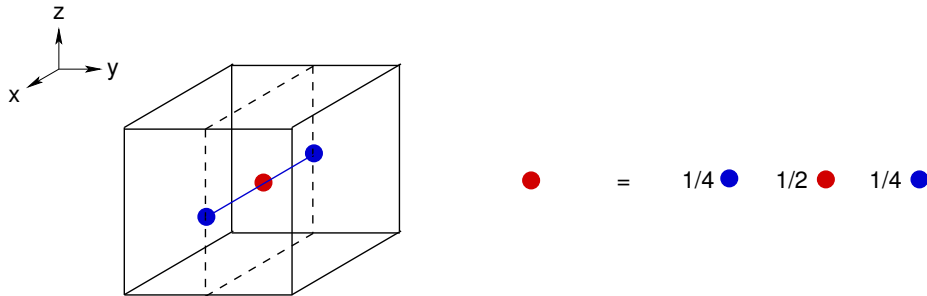
(c) Filtering in HSG, line → point reduction. Target point (highlighted in red) on the middle line of the central plane is obtained by averaging three points with the coefficients $1/4, 1/2, 1/4$.

Figure 4.14: Filtering in HSG. Participating planes, lines and points are shown in blue colour and target planes, lines and points—in red.

$$
+ Z_{2g}(i, j, k) \left(\begin{array}{c} \dfrac{E_{yg}^n(i, j, k+1) - E_{yg}^n(i, j, k)}{\Delta z_g} \\[2em] -\dfrac{E_{zg}^n(i, j+1, k) - E_{zg}^n(i, j, k)}{\Delta y_g} \\[2em] -M_{src,xg}^n(i, j, k) \end{array} \right), \quad (4.37)
$$

where $i \in [i_{g_{min}} + 1, i_{g_{max}} - 1]$; $j \in [j_{g_{min}}, j_{g_{max}} - 1]$; $k \in [k_{g_{min}}, k_{g_{max}} - 1]$;

$$H_{yg}^n (i, j, k) = Z_{1g} (i, j, k) H_{yg}^{n-1} (i, j, k)$$

$$+ Z_{2g} (i, j, k) \left(\begin{array}{c} \dfrac{E_{zg}^n (i+1, j, k) - E_{zg}^n (i, j, k)}{\Delta x_g} \\[3mm] -\dfrac{E_{xg}^n (i, j, k+1) - E_{xg}^n (i, j, k)}{\Delta z_g} \\[3mm] -M_{src, yg}^n (i, j, k) \end{array} \right), \quad (4.38)$$

where $i \in [i_{g_{min}}, i_{g_{max}} - 1]$; $j \in [j_{g_{min}} + 1, j_{g_{max}} - 1]$; $k \in [k_{g_{min}}, k_{g_{max}} - 1]$;

$$H_{zg}^n (i, j, k) = Z_{1g} (i, j, k) H_{zg}^{n-1} (i, j, k)$$

$$+ Z_{2g} (i, j, k) \left(\begin{array}{c} \dfrac{E_{xg}^n (i, j+1, k) - E_{xg}^n (i, j, k)}{\Delta y_g} \\[3mm] -\dfrac{E_{yg}^n (i+1, j, k) - E_{yg}^n (i, j, k)}{\Delta x_g} \\[3mm] -M_{src, zg}^n (i, j, k) \end{array} \right), \quad (4.39)$$

where $i \in [i_{g_{min}}, i_{g_{max}} - 1]$; $j \in [j_{g_{min}}, j_{g_{max}} - 1]$; $k \in [k_{g_{min}} + 1, k_{g_{max}} - 1]$.

4.7.2 Electric Field Calculation

To simplify the FDTD method's equations for electric field calculation analogous coefficients were defined:

$$\Gamma_{1g} (i, j, k) = \frac{1 - \gamma_{1g} (i, j, k)}{1 + \gamma_{1g} (i, j, k)}, \quad \Gamma_{2g} (i, j, k) = \frac{\gamma_{2g} (i, j, k)}{1 + \gamma_{1g} (i, j, k)}, \quad (4.40)$$

where

$$\gamma_{1g} (i, j, k) = \frac{\sigma_g (i, j, k) \Delta t_g}{2 \varepsilon_g (i, j, k)}, \quad \gamma_{2g} (i, j, k) = \frac{\Delta t_g}{\varepsilon_g (i, j, k)}. \quad (4.41)$$

Also electric field components are calculated for both main and subgrids using identical equations:

$$E_{xg}^n\left(i,j,k\right) = \Gamma_{1g}\left(i,j,k\right) E_{xg}^{n-1}\left(i,j,k\right)$$

$$+\Gamma_{2g}\left(i,j,k\right)\left(\begin{array}{c} \dfrac{H_{zg}^n\left(i,j,k\right)-H_{zg}^n\left(i,j-1,k\right)}{\Delta y_g} \\[2em] -\dfrac{H_{yg}^n\left(i,j,k\right)-H_{yg}^n\left(i,j,k-1\right)}{\Delta z_g} \\[2em] -J_{src,xg}^n\left(i,j,k\right) \end{array}\right),\quad (4.42)$$

where $\quad i \in [i_{g_{min}}, i_{g_{max}}-1];\quad j \in [j_{g_{min}}+1, j_{g_{max}}-1];\quad k \in [k_{g_{min}}+1, k_{g_{max}}-1];$

$$E_{yg}^n\left(i,j,k\right) = \Gamma_{1g}\left(i,j,k\right) E_{yg}^{n-1}\left(i,j,k\right)$$

$$+\Gamma_{2g}\left(i,j,k\right)\left(\begin{array}{c} \dfrac{H_{xg}^n\left(i,j,k\right)-H_{xg}^n\left(i,j,k-1\right)}{\Delta z_g} \\[2em] -\dfrac{H_{zg}^n\left(i,j,k\right)-H_{zg}^n\left(i-1,j,k\right)}{\Delta x_g} \\[2em] -J_{src,yg}^n\left(i,j,k\right) \end{array}\right),\quad (4.43)$$

where $\quad i \in [i_{g_{min}}+1, i_{g_{max}}-1];\quad j \in [j_{g_{min}}, j_{g_{max}}-1];\quad k \in [k_{g_{min}}+1, k_{g_{max}}-1];$

$$E_{zg}^n\left(i,j,k\right) = \Gamma_{1g}\left(i,j,k\right) E_{zg}^{n-1}\left(i,j,k\right)$$

$$+\Gamma_{2g}\left(i,j,k\right)\left(\begin{array}{c} \dfrac{H_{yg}^n\left(i,j,k\right)-H_{yg}^n\left(i-1,j,k\right)}{\Delta x_g} \\[2em] -\dfrac{H_{xg}^n\left(i,j,k\right)-H_{xg}^n\left(i,j-1,k\right)}{\Delta y_g} \\[2em] -J_{src,zg}^n\left(i,j,k\right) \end{array}\right),\quad (4.44)$$

where $\quad i \in [i_{g_{min}} + 1, i_{g_{max}} - 1]; \quad j \in [j_{g_{min}} + 1, j_{g_{max}} - 1]; \quad k \in [k_{g_{min}}, k_{g_{max}} - 1].$

Electric Field Update at the Excitation Source Location

In this section $i = i_{src}$, $j = j_{src}$, $k = k_{src}$ and $g \in [a, b]$. In case of the hard source excitation the electric field value at the source location i, j, k is overwritten with:

$$E_g^n(i, j, k) = -\Gamma_{2g}(i, j, k)\, J_{src,g}^n(i, j, k). \tag{4.45}$$

In case of the soft source excitation the electric field value is calculated according to (4.42) to (4.44).

4.7.3 Field Component Re-Arrangement

Field re-arrangement described in this section is necessary for the normal FDTD field updates, Absorbing Boundary Condition calculation and the main grid fields spatial and temporal interpolations at the IS. Symbol "*" stands for the entire spatial domain. Left-directed horizontal arrow "⟵" specifies the field value transfer and storage.

Magnetic Field Components in Main Grid

Magnetic field components at the IS in the main grid are re-arranged in order to preserve the previous time-step values $n - 1$ needed for spatial and temporal interpolations. For the sake of clarity only one spatial coordinate is specified. This coordinate defines the plane, where the given magnetic field components reside. For example in case of $H_{xa}^{n-1}(j_{bIL})$ the magnetic field components H_{xa}^{n-1} lie on the plane $j_b = j_{bIL}$. Subgrid coordinates in the main grid components are explained by a subgrid granularity required by the main grid components at the IS. Notions of IL and IR stand for Inner Left and Inner Right Inner Surfaces. IL and IR are the same as upper and lower or minimum and maximum IS planes. The other coordinates in $H_{xa}^{n-1}(j_{bIL})$ notation are assumed to span the entire IS range, e.g. in $H_{xa}^{n-1}(j_{bIL})$ the other coordinate ranges are $i_b \in [i_{bIL}, i_{bIR}]$, $k_b \in [k_{bIL}, k_{bIR}]$:

$$
\begin{aligned}
H_{xa}^{n-1}(*) &\longleftarrow H_{xa}^n(*), & H_{xa}^{n-1}(j_{bIL}) &\longleftarrow H_{xa}^n(j_{bIL}), \\
H_{ya}^{n-1}(*) &\longleftarrow H_{ya}^n(*), & H_{xa}^{n-1}(j_{bIR}) &\longleftarrow H_{xa}^n(j_{bIR}), \\
H_{za}^{n-1}(*) &\longleftarrow H_{za}^n(*), & H_{xa}^{n-1}(k_{bIL}) &\longleftarrow H_{xa}^n(k_{bIL}),
\end{aligned}
\tag{4.46}
$$

$$H_{xa}^{n-1}(k_{bIR}) \longleftarrow H_{xa}^{n}(k_{bIR}),$$

$$
\begin{aligned}
H_{ya}^{n-1}(i_{bIL}) &\longleftarrow H_{ya}^{n}(i_{bIL}), & H_{za}^{n-1}(i_{bIL}) &\longleftarrow H_{za}^{n}(i_{bIL}), \\
H_{ya}^{n-1}(i_{bIR}) &\longleftarrow H_{ya}^{n}(i_{bIR}), & H_{za}^{n-1}(i_{bIR}) &\longleftarrow H_{za}^{n}(i_{bIR}), \\
H_{ya}^{n-1}(k_{bIL}) &\longleftarrow H_{ya}^{n}(k_{bIL}), & H_{za}^{n-1}(j_{bIL}) &\longleftarrow H_{za}^{n}(j_{bIL}), \\
H_{ya}^{n-1}(k_{bIR}) &\longleftarrow H_{ya}^{n}(k_{bIR}), & H_{za}^{n-1}(j_{bIR}) &\longleftarrow H_{za}^{n}(j_{bIR}).
\end{aligned}
\tag{4.47}
$$

Magnetic field component re-arrangement in the entire simulation domain "*" can be avoided in the implementation, since at the moment of H_a^n update, the value H_a^{n-1} is still valid. In other words only one array is required to store H_{xa}^n and H_{xa}^{n-1} values. Likewise the storage of H_{ya} and H_{za} components requires only one array each. The re-arrangement procedures for the entire simulation domain are given for the completeness of mathematical formulation. Main grid component re-arrangement at the IS should occur prior to the new IS value calculation.

Magnetic Field Components in Subgrid

Magnetic field components in the subgrid are re-arranged before normal FDTD update equations:

$$
\begin{aligned}
H_{xb}^{n-1}(*) &\longleftarrow H_{xb}^{n}(*), \\
H_{yb}^{n-1}(*) &\longleftarrow H_{yb}^{n}(*), \\
H_{zb}^{n-1}(*) &\longleftarrow H_{zb}^{n}(*).
\end{aligned}
\tag{4.48}
$$

These re-arrangement procedures can be spared during the implementation. Re-arrangement process is shown only for mathematical completeness.

Electric Field Components in Main Grid

Electric field components in the entire simulation domain "*" and at the IS are preserved at time-step $n-1$, since they are required in normal FDTD updates, and spatial and temporal interpolations at the IS. Component re-arrangement notation is the same as in the magnetic field re-arrangement procedure described in Section 4.7.3:

$$E_{xa}^{n-1}(*) \longleftarrow E_{xa}^{n}(*), \qquad\qquad E_{xa}^{n-1}(j_{bIL}) \longleftarrow E_{xa}^{n}(j_{bIL}),$$

$$E_{ya}^{n-1}(*) \longleftarrow E_{ya}^{n}(*), \qquad\qquad E_{xa}^{n-1}\left(j_{bIR}\right) \longleftarrow E_{xa}^{n}\left(j_{bIR}\right), \qquad (4.49)$$
$$E_{za}^{n-1}(*) \longleftarrow E_{za}^{n}(*), \qquad\qquad E_{xa}^{n-1}(k_{bIL}) \longleftarrow E_{xa}^{n}(k_{bIL}),$$
$$E_{xa}^{n-1}(k_{bIR}) \longleftarrow E_{xa}^{n}(k_{bIR}),$$

$$E_{ya}^{n-1}(i_{bIL}) \longleftarrow E_{ya}^{n}(i_{bIL}), \qquad\qquad E_{za}^{n-1}(i_{bIL}) \longleftarrow E_{za}^{n}(i_{bIL}),$$
$$E_{ya}^{n-1}(i_{bIR}) \longleftarrow E_{ya}^{n}(i_{bIR}) \qquad\qquad E_{za}^{n-1}(i_{bIR}) \longleftarrow E_{za}^{n}(i_{bIR}), \qquad (4.50)$$
$$E_{ya}^{n-1}(k_{bIL}) \longleftarrow E_{ya}^{n}(k_{bIL}), \qquad\qquad E_{za}^{n-1}\left(j_{bIL}\right) \longleftarrow E_{za}^{n}\left(j_{bIL}\right),$$
$$E_{ya}^{n-1}(k_{bIR}) \longleftarrow E_{ya}^{n}(k_{bIR}), \qquad\qquad E_{za}^{n-1}\left(j_{bIR}\right) \longleftarrow E_{za}^{n}\left(j_{bIR}\right).$$

Similarly to the magnetic field, the electric field component re-arrangement in the entire simulation domain "*" can be avoided during the implementation. Main grid components at the IS should be re-arranged prior to the calculation of new main grid values at the IS.

Electric Field Components in Subgrid

Electric field components in the subgrid are re-arranged before normal FDTD update equations:

$$E_{xb}^{n-1}(*) \longleftarrow E_{xb}^{n}(*),$$
$$E_{yb}^{n-1}(*) \longleftarrow E_{yb}^{n}(*), \qquad (4.51)$$
$$E_{zb}^{n-1}(*) \longleftarrow E_{zb}^{n}(*).$$

Similarly to the main grid, these re-arrangement procedures can be bypassed during the implementation.

4.7.4 Filtering

Filtering is optional. It is done prior to the spatial interpolation of the main grid electric and magnetic field components at the Inner Huygens Surface (IS). There are two varieties of filtering in one and in three dimensions (1D, 3D).

One-Dimensional Filtering

In one dimension filtering equations use the field values lying perpendicular to the IS plane. Abbreviations used in this section include: IS ∈ [IL, IR], where IL and IR

stand for Left Inner Surface and Right Inner Surface,[4] u, v, w are the auxiliary co-ordinates, A is a 1D array of extracted field components, parameter d specifies the amount of points extracted from the field array to the left and to the right from the IS and ρ is the filtered value.

Electric Field Components

The cases construct below shows the electric field values extraction depending on the IS location. Symbol "$\perp$" denotes perpendicularity, e.g. IS $\perp$ y means that IS is perpendicular to y-axis. Consider the first line of the cases construct below. In case of E_{xa} and IS $\perp$ y, the coordinate of operation u equals to j. Parameter d specifies the number of points in y direction, that are extracted to the left and to the right from the IS, i.e. $j \in [j_{aIS} - d, j_{aIS} + d]$. The location of IS on y-axis j_{aIS} lies in between of the extracted values.

$$
A(u) = \begin{cases}
E_{xa}(i, j, k), & \text{IS} \perp y; & u = j, & j \in [j_{aIS} - d, j_{aIS} + d]; \\
E_{xa}(i, j, k), & \text{IS} \perp z; & u = k, & k \in [k_{aIS} - d, k_{aIS} + d]; \\
E_{ya}(i, j, k), & \text{IS} \perp z; & u = k, & k \in [k_{aIS} - d, k_{aIS} + d]; \\
E_{ya}(i, j, k), & \text{IS} \perp x; & u = i, & i \in [i_{aIS} - d, i_{aIS} + d]; \\
E_{za}(i, j, k), & \text{IS} \perp x; & u = i, & i \in [i_{aIS} - d, i_{aIS} + d]; \\
E_{za}(i, j, k), & \text{IS} \perp y; & u = j, & j \in [j_{aIS} - d, j_{aIS} + d].
\end{cases}
$$

Filtering is done with (4.52) to (4.54). Only one equation has to be chosen for value filtering. Major difference between the filtering equations consists in the total number of points and the filtering coefficient values used. Computation burden grows with the growth of parameter d.

3pt filtering, $d = 1$

$$
\rho = \frac{1}{4}A(u-1) + \frac{1}{2}A(u) + \frac{1}{4}A(u+1); \tag{4.52}
$$

5pt filtering (i), $d = 2$

$$
\rho = \frac{1}{4}(A(u-1) + A(u) + A(u+1)) + \frac{1}{8}(A(u-2) + A(u+2)); \tag{4.53}
$$

---

[4]In HSG it is necessary to distinguish between the left and right sides of the IS, since the calculation equations are different for each side.

5pt filtering (ii), $d = 2$

$$\rho = \frac{3}{8} A(u) + \frac{1}{4} (A(u-1) + A(u+1)) + \frac{1}{16} (A(u-2) + A(u+2)). \tag{4.54}$$

Magnetic Field Components

Magnetic field components are filtered in a similar manner to the electric field. Since magnetic field is shifted one half space step from the electric field, no magnetic field value exists exactly at the IS. Therefore, an exact magnetic field value at the IS is obtained with two sequences of filtering, where the interpolation coefficients are:

$$X_1 = \frac{r+1}{2r}, \quad X_2 = \frac{r-1}{2r}. \tag{4.55}$$

These coefficients are the same as the spatial interpolation coefficients used in (4.22). The main purpose of these coefficients is to control the amount of influence each node contributes to the final value ρ. Coefficients X_1, X_2 increase the influence of the closer node and decrease the influence of the farther node. Five point filtering for the magnetic field components is not implemented.

$$A(u) = \begin{cases} H_{xa}(i, j, k), & \text{IS} \perp y; & u = j, & j \in [j_{aIS} - d, j_{aIS} + d]; \\ H_{xa}(i, j, k), & \text{IS} \perp z; & u = k, & k \in [k_{aIS} - d, k_{aIS} + d]; \\ H_{ya}(i, j, k), & \text{IS} \perp z; & u = k, & k \in [k_{aIS} - d, k_{aIS} + d]; \\ H_{ya}(i, j, k), & \text{IS} \perp x; & u = i, & i \in [i_{aIS} - d, i_{aIS} + d]; \\ H_{za}(i, j, k), & \text{IS} \perp x; & u = i, & i \in [i_{aIS} - d, i_{aIS} + d]; \\ H_{za}(i, j, k), & \text{IS} \perp y; & u = j, & j \in [j_{aIS} - d, j_{aIS} + d]. \end{cases}$$

1pt filtering, $d = 1$**, IS** $=$ **IL** $- 1$

$$\rho = X_1 A(u) + X_2 A(u+1); \tag{4.56}$$

1pt filtering, $d = 1$**, IS** $=$ **IR**

$$\rho = X_1 A(u) + X_2 A(u-1); \tag{4.57}$$

3pt filtering, $d = 2$**, IS** $=$ **IL** $- 1$

$$\rho = X_1 \rho_1 + X_2 \rho_2, \tag{4.58}$$

where

$$\rho_1 = \frac{1}{4} A(u-1) + \frac{1}{2} A(u) + \frac{1}{4} A(u+1),$$

$$\rho_2 = \frac{1}{4} A(u) + \frac{1}{2} A(u+1) + \frac{1}{4} A(u+2);$$

3pt filtering, $d = 2$, IS = IR

$$\rho = X_1 \rho_1 + X_2 \rho_2, \qquad\qquad (4.59)$$

where

$$\rho_1 = \frac{1}{4} A(u-1) + \frac{1}{2} A(u) + \frac{1}{4} A(u+1),$$

$$\rho_2 = \frac{1}{4} A(u-2) + \frac{1}{2} A(u-1) + \frac{1}{4} A(u).$$

Three-Dimensional Filtering

Prior to reading this section, it might be beneficial to review Figure 4.14, that visualises the filtering process in 3D. Filtering in three dimensions uses the points lying in the rectangular cuboid surrounding the target point. Now the field value extraction and filtering occurs along three dimensions using the auxiliary coordinates u, v, w. Values of u_0, v_0, w_0 specify the location of the target point in x, y, z-axes. Target point will contain the interpolation result. Values of u_0, v_0, w_0 lie in the middle of the coordinate ranges specified by the cases construct below. Target point coordinates u_0, v_0, w_0 depend on the electric field component E_{xa}, E_{ya}, E_{za} and the orientation of the IS, e.g. in case of E_{xa} and IS $\perp y$ the value $v_0 = j_{aIS}$.

Three arrays of extracted values are used in explanation of the interpolation process: $A_v(u, v, w)$ is a 3D array storing the values in a volume, $A_p(u, v)$ is a 2D array storing the values on a central plane of the volume and $A_l(u)$ is a 1D array storing the values of the middle line of the plane. Indices v, p, l in arrays A stand for volume, plane and line respectively. In a programming language all three arrays A_v, A_p, A_l can be replaced with a single 3D array. Three arrays are used only for the clarity of explanation.

Electric Field Components

$$A_v(u, v, w) = \begin{cases} E_{xa}(i, j, k), & \text{IS} \perp y; & u = i \pm d, & v = j_{aIS} \pm d, & w = k \pm d; \\ E_{xa}(i, j, k), & \text{IS} \perp z; & u = i \pm d, & v = j \pm d, & w = k_{aIS} \pm d; \\ E_{ya}(i, j, k), & \text{IS} \perp x; & u = i_{aIS} \pm d, & v = j \pm d, & w = k \pm d; \\ E_{ya}(i, j, k), & \text{IS} \perp z; & u = i \pm d, & v = j \pm d, & w = k_{aIS} \pm d; \\ E_{za}(i, j, k), & \text{IS} \perp x; & u = i_{aIS} \pm d, & v = j \pm d, & w = k \pm d; \\ E_{za}(i, j, k), & \text{IS} \perp y; & u = i \pm d, & v = j_{aIS} \pm d, & w = k \pm d; \end{cases}$$

3pt filtering, $d = 1$

$$A_p(u, v) = \frac{1}{4} A_v(u, v, w_0 - 1) + \frac{1}{2} A_v(u, v, w_0) + \frac{1}{4} A_v(u, v, w_0 + 1), \quad u, v \in [-1, 1];$$

$$A_l(u) = \frac{1}{4} A_p(u, v_0 - 1) + \frac{1}{2} A_p(u, v_0) + \frac{1}{4} A_p(u, v_0 + 1), \quad u \in [-1, 1]; \qquad (4.60)$$

$$\rho = \frac{1}{4} A_l(u_0 - 1) + \frac{1}{2} A_l(u_0) + \frac{1}{4} A_l(u_0 + 1);$$

5pt filtering (i), $d = 2$

$$A_p(u, v) = \frac{1}{8} \left(A_v(u, v, w_0 - 2) + A_v(u, v, w_0 + 2) \right)$$
$$+ \frac{1}{4} \left(A_v(u, v, w_0 - 1) + A_v(u, v, w_0) + A_v(u, v, w_0 + 1) \right), \quad u, v \in [-2, 2];$$

$$A_l(u) = \frac{1}{8} \left(A_p(u, v_0 - 2) + A_p(u, v_0 + 2) \right)$$
$$+ \frac{1}{4} \left(A_p(u, v_0 - 1) + A_p(u, v_0) + A_p(u, v_0 + 1) \right), \quad u \in [-2, 2]; \quad (4.61)$$

$$\rho = \frac{1}{8} \left(A_l(u_0 - 2) + A_l(u_0 + 2) \right) + \frac{1}{4} \left(A_l(u_0 - 1) + A_l(u_0) + A_l(u_0 + 1) \right);$$

5pt filtering (ii), $d = 2$

$$A_p(u, v) = \frac{1}{16} \left(A_v(u, v, w_0 - 2) + A_v(u, v, w_0 + 2) \right) + \frac{3}{8} A_v(u, v, w_0)$$
$$+ \frac{1}{4} \left(A_v(u, v, w_0 - 1) + A_v(u, v, w_0 + 1) \right), \quad u, v \in [-2, 2];$$

$$A_l(u) = \frac{1}{16}\left(A_p(u, v_0 - 2) + A_p(u, v_0 + 2)\right) + \frac{3}{8}A_p(u, v_0)$$
$$+ \frac{1}{4}\left(A_p(u, v_0 - 1) + A_p(u, v_0 + 1)\right), \quad u \in [-2, 2]; \quad (4.62)$$

$$\rho = \frac{1}{16}\left(A_l(u_0 - 2) + A_l(u_0 + 2)\right) + \frac{3}{8}A_l(u_0) + \frac{1}{4}\left(A_l(u_0 - 1) + A_l(u_0 + 1)\right).$$

Magnetic Field Components

Magnetic field components are filtered in the same manner as the electric field components. The same interpolation (4.60) to (4.62) are used. The one half spatial step offset between the electric and magnetic fields in the HSG method is realised in the main grid value calculation at the IS (see Figure 4.15 for details).

4.7.5   Interpolation of Main Grid Values at Inner Surface

This section describes the process of main grid value interpolation at the IS. After each iteration of the subgrid the newly calculated values of electric or magnetic field receive a portion of equivalent current from the main grid. But main grid values are not available at all subgrid locations. Therefore, the missing locations of main grid values at the IS are obtained with spatial interpolation.

Table 4.1 lists the symbols used in this section. Parameter P stands for a generic filtering function (see Section 4.7.4 for details), field value with a tilde $\widetilde{E}_s$ denotes a filtered value and field value with a hat $\hat{E}_s$ describes a spatially interpolated value. Symbols L and R stand for the left and right IS coordinates where the values are interpolated, e.g. L and R in x-axis denote i_{aIL} and i_{aIR} planes. Parameters X_1, X_2 are the spatial interpolation coefficients, values i, j, k describe the spatial location of a field value, and indices aux and sub denote the triples of auxiliary coordinates necessary to iterate between the main grid points.

Electric Field Components

Prior to spatial interpolation the electric field values are filtered. The filtering procedure is optional. Field value selection process is described by the cases construct

Parameter	Description
r	subgridding ratio
P	filtering function; 1D or 3D; 1, 3, 5 point interpolation
$\widetilde{E}_s(i, j, k)$	filtered $E_s(i, j, k)$ values, where $s = x, y, z$
$\hat{E}_s(i, j, k)$	spatially interpolated $E_s(i, j, k)$ values
L, R	target planes for interpolation: left, right
X_1, X_2	interpolation coefficients
i, j, k	spatial coordinates
$i_{aux}, j_{aux}, k_{aux}$	coordinates to iterate in main grid spatial steps between main grid points at IS
$i_{sub}, j_{sub}, k_{sub}$	coordinates to iterate in subgrid spatial steps between two adjacent main grid points at IS

Table 4.1: Notation for main grid value interpolation at Inner Surface

below:

$$E_s(i, j, k) = \begin{cases} E_{xa}, & \text{IS} \perp y, & i \in [i_{aIL}-1, i_{aIR}], & k \in [k_{aIL}, k_{aIR}], & j = j_{aIL}, j_{aIR}; \\ E_{xa}, & \text{IS} \perp z, & i \in [i_{aIL}-1, i_{aIR}], & j \in [j_{aIL}, j_{aIR}], & k = k_{aIL}, k_{aIR}; \\ E_{ya}, & \text{IS} \perp z, & j \in [j_{aIL}-1, j_{aIR}], & i \in [i_{aIL}, i_{aIR}], & k = k_{aIL}, k_{aIR}; \\ E_{ya}, & \text{IS} \perp x, & j \in [j_{aIL}-1, j_{aIR}], & k \in [k_{aIL}, k_{aIR}], & i = i_{aIL}, i_{aIR}, \\ E_{za}, & \text{IS} \perp x, & k \in [k_{aIL}-1, k_{aIR}], & j \in [j_{aIL}, j_{aIR}], & i = i_{aIL}, i_{aIR}, \\ E_{za}, & \text{IS} \perp y, & k \in [k_{aIL}-1, k_{aIR}], & i \in [i_{aIL}, i_{aIR}], & j = j_{aIL}, j_{aIR}. \end{cases}$$

Selected electric field component values are filtered with the filtering function P:

$$\widetilde{E}_s(i, j, k) = P\left(E_s(i, j, k)\right). \tag{4.63}$$

For example in case of E_{xa} and IS $\perp y$ the filtering procedure will have the form:

$$\widetilde{E}_{xa}(i, j, k) = P\left(E_{xa}(i, j, k)\right), \tag{4.64}$$

where $i \in [i_{aIL}-1, i_{aIR}]$, $k \in [k_{aIL}, k_{aIR}]$. Additional spatial location $i_{aIL}-1$ in x-axis is necessary for correct operation of the filtering function. The -1 coordinate shift is dictated by the implementation of the filtering function in the programming language.

After filtering the IS values are calculated by interpolating electric field components. The case below is shown for $E_{xa}(i, j, k)$ and IS $\perp y$. Other cases are calculated in a similar manner by a circular permutation of the i, j, k coordinates.

Equations (4.65) and (4.66) filter and interpolate component E_{xa} along x and z-axes. Subgrid granularity in x-axis is achieved with the subgrid iterator i_{sub}. In z-axis the interpolation proceeds in main grid steps of k_{aux}.

For $i \in [i_{aIL}, i_{aIR} - 1]$, $j = j_{aIL}, j_{aIR}$, $k \in [k_{aIL}, k_{aIR}]$:

$$\hat{E}_{xa}(i_{aux}, j, k_{aux}) = \widetilde{E}_{xa}(i, j, k), \tag{4.65}$$

$$\hat{E}_{xa}(i_{aux} \pm i_{sub}, j, k_{aux}) = X_1 \widetilde{E}_{xa}(i \pm 1, j, k) + X_2 \widetilde{E}_{xa}(i, j, k), \tag{4.66}$$

where

$$i_{aux} \in \left[i_{bIL} + \frac{r-1}{2}, i_{bIR}, step = r \right], \quad k_{aux} \in \left[k_{bIL}, k_{bIR}, step = r \right]$$

$$i_{sub} \in \left[1, \frac{r-1}{2} \right], \quad X_1 = \frac{i_{sub}}{r}, \quad X_2 = 1 - X_1.$$

The "$\pm$" signs in (4.66) are responsible for the main and subgrid nodes selection to the left and to the right of the central subgrid node (see Figure 4.15a for more details). The "$\pm$" signs are identical on both sides of (4.66), i.e. in case the "$-$" sign is selected on the left-hand side of (4.66), the "$-$" sign is also used on the right-hand side of (4.66).

Iterator i_{aux} and k_{aux} ranges are specified with the triples of the form $[begin, end, step]$, where $begin$ and end denote the beginning and ending indices of the coordinate range and $step$ stands for the increment of the iterator. For example, the range $k_{aux} \in [k_{bIL}, k_{bIR}, step = r]$ means that k_{aux} will begin at k_{bIL} and end at k_{bIR}, while the iteration will proceed in main grid steps of $step = r$.

Equation (4.67) interpolates component E_{xa} along x and z-axes. This time the subgrid granularity is achieved in both x and z-axes with the subgrid iterators i and k_{sub}. In z-axis parameter k is responsible for the iteration between the main grid nodes and parameter k_{sub} for the iteration between the subgrid nodes.

For $i \in [i_{bIL}, i_{bIR} - 1]$, $j = j_{bIL}, j_{bIR}$, $k \in [k_{bIL} + r, k_{bIR}, step = r]$:

$$\hat{E}_{xa}(i, j, k - k_{sub}) = X_1 \hat{E}_{xa}(i, j, k - r) + X_2 \hat{E}_{xa}(i, j, k), \tag{4.67}$$

where

$$k_{sub} \in [1, r - 1], \quad X_1 = \frac{k_{sub}}{r}, \quad X_2 = 1 - X_1.$$

In summary the main grid values of E_{xa} are spatially interpolated with (4.65) to (4.67). At the end of the process the subgrid values of E_{xa} will be available in the xz-plane.

Figure 4.15 gives an example of the spatial interpolation for $i_{aIL} \sim i_{aIR} - 1 = 3$, $k_{aIL} \sim k_{aIR} = 3$ and $r = 5$. Step of i_{aux}, k_{aux} is equal to the distance between two main grid nodes and step of i_{sub}, k_{sub} equals to the distance between two subgrid nodes. Large hollow circles in Figure 4.15 denote locations of the main grid nodes and small vertical bars—of the subgrid nodes. Small filled circles show the initial subgrid nodes where the spatial interpolation starts. Red circles denote the current main grid nodes that participate in interpolation. Figure 4.15 illustrates the two parts of spatial interpolation. Part 1 governed by (4.65) and (4.66) is explained in Figure 4.15a and part 2 defined by (4.67) is depicted in Figure 4.15b.

Magnetic Field Components

Magnetic field components interpolation is identical to the electric field components shown above. Since magnetic field components are shifted one half space step relative to the electric field, it is important to distinguish between the left and right Inner Surfaces:

$$H_s\left(i, j, k\right) = \begin{cases} H_{xa}, & \text{IS} \perp y, & i \in [i_{aIL}, i_{aIR}], & k \in [k_{aIL} - 1, k_{aIR}], & L = j_{aIL}, & R = j_{aIR}; \\ H_{xa}, & \text{IS} \perp z, & i \in [i_{aIL}, i_{aIR}], & j \in [j_{aIL} - 1, j_{aIR}], & L = k_{aIL}, & R = k_{aIR}; \\ H_{ya}, & \text{IS} \perp z, & j \in [j_{aIL}, j_{aIR}], & i \in [i_{aIL} - 1, i_{aIR}], & L = k_{aIL}, & R = k_{aIR}; \\ H_{ya}, & \text{IS} \perp x, & j \in [j_{aIL}, j_{aIR}], & k \in [k_{aIL} - 1, k_{aIR}], & L = i_{aIL}, & R = i_{aIR}; \\ H_{za}, & \text{IS} \perp x, & k \in [k_{aIL}, k_{aIR}], & j \in [j_{aIL} - 1, j_{aIR}], & L = i_{aIL}, & R = i_{aIR}; \\ H_{za}, & \text{IS} \perp y, & k \in [k_{aIL}, k_{aIR}], & i \in [i_{aIL} - 1, i_{aIR}], & L = j_{aIL}, & R = j_{aIR}. \end{cases}$$

Optionally magnetic field values are filtered first. Filtering in 1D is defined by the relations below:[5]

$$\widetilde{H}_s\left(i, L, k\right) = P\left(H_s\left(i, L - 1, k\right)\right), \tag{4.68}$$

$$\widetilde{H}_s\left(i, R, k\right) = P\left(H_s\left(i, R, k\right)\right). \tag{4.69}$$

---

[5]Spatial interpolation is implemented inside the 1D filtering function.
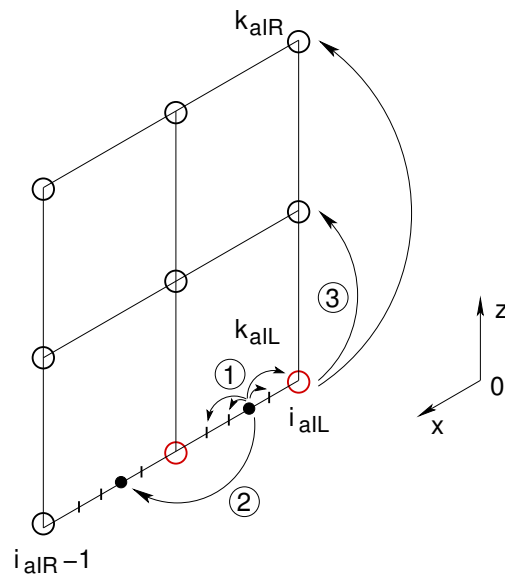
(a) Part 1. Encircled numbers show the main steps of interpolation: 1—a central subgrid node in between two main grid nodes (shown in red) is selected. Interpolation proceeds in subgrid steps governed by $\pm i_{sub}$ coordinate, 2—once all the subgrid values in between two main grid nodes are obtained a new central subgrid node is chosen in the middle of the next pair of main grid nodes, 3—once all subgrid nodes at a single line k_{aux} are calculated the new line is selected by incrementing k_{aux}.
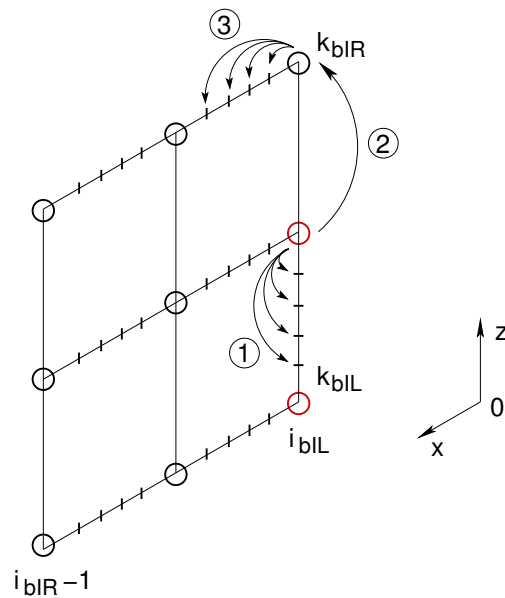
(b) Part 2. Encircled numbers show the main steps of interpolation: 1—interpolation in between two main grid nodes proceeds in small steps governed by k_{sub} coordinate, 2—once all the subgrid values in between two main grid nodes are obtained a new pair of main grid nodes is chosen by incrementing k_{bIL} by r, 3—once all subgrid nodes at a single line i are calculated the new line is selected by incrementing i.

Figure 4.15: Spatial interpolation of electric field component E_{xa} at IS $\perp y$

For example in case of H_{xa} and IS $\perp y$ the filtering function will have the form:

$$\widetilde{H}_{xa}\left(i, j_{aIL}, k\right) = P\left(H_{xa}\left(i, j_{aIL} - 1, k\right)\right), \tag{4.70}$$

where $i \in [i_{aIL}, i_{aIR}]$, $k \in [k_{aIL} - 1, k_{aIR}]$. Coordinate shift $k_{aIL} - 1$ in z-axis is necessary for correct operation of the filtering function. This shift depends on the implementation of the filter in a programming language.

Alternatively the magnetic field components can also be filtered in (3D):

$$\widetilde{H}_s\left(i, L, k\right) = X_1 \cdot P(H_s\left(i, L - 1, k\right)) + X_2 \cdot P(H_s\left(i, L, k\right)), \tag{4.71}$$

$$\widetilde{H}_s\left(i, R, k\right) = X_1 \cdot P(H_s\left(i, R, k\right)) + X_2 \cdot P(H_s\left(i, R - 1, k\right)), \tag{4.72}$$

where

$$X_1 = \frac{r + 1}{2r}, \quad X_2 = 1 - X_1.$$

The importance of clear distinction between IL and IR can be vividly seen in (4.71) and (4.72). Filtering at IS occurs between the IS node and the adjacent node outside of the IS. Coordinates L and R ensure that the adjacent node outside of IS is selected for the interpolation. Spatial interpolation coefficients X_1, X_2 control the amount that each main grid node contributes to the resulting value.

After filtering the IS values are calculated by interpolating magnetic field components. The case below is shown for $H_{xa}\left(i, j, k\right)$ and IS $\perp y$. Other cases are calculated in a similar manner by a circular permutation of the i, j, k coordinates.

Equations (4.73) and (4.74) filter and interpolate component H_{xa} along x and z-axes. In x-axis the interpolation proceeds in main grid steps of i_{aux}. Subgrid granularity in z-axis is achieved with the subgrid iterator k_{sub}. See commentary to (4.66) on the explanation of the "$\pm$" signs and the iterator ranges used in (4.74).

For $i \in [i_{aIL}, i_{aIR}]$, $j = j_{aIL}, j_{aIR}$, $k \in [k_{aIL}, k_{aIR} - 1]$:

$$\hat{H}_{xa}\left(i_{aux}, j, k_{aux}\right) = \widetilde{H}_{xa}\left(i, j, k\right), \tag{4.73}$$

$$\hat{H}_{xa}\left(i_{aux}, j, k_{aux} \pm k_{sub}\right) = X_1 \widetilde{H}_{xa}\left(i, j, k \pm 1\right) + X_2 \widetilde{H}_{xa}\left(i, j, k\right), \tag{4.74}$$

where

$$i_{aux} \in \left[i_{bIL}, i_{bIR}, step = r\right], \quad k_{aux} \in \left[k_{bIL} + \frac{r - 1}{2}, k_{bIR}, step = r\right]$$

$$k_{sub} \in \left[1, \frac{r-1}{2}\right], \quad X_1 = \frac{k_{sub}}{r}, \quad X_2 = 1 - X_1.$$

Equation (4.75) interpolates component H_{xa} along x and z-axes. This time the subgrid granularity is achieved in both x and z-axes with the subgrid iterators i_{sub} and k. In x-axis parameter i is responsible for the iteration between the main grid nodes and parameter i_{sub} for the iteration between the subgrid nodes.

For $i \in [i_{bIL} + r, i_{bIR}, step = r], \quad j = j_{bIL}, j_{bIR}, \quad k \in [k_{bIL}, k_{bIR} - 1]$:

$$\hat{H}_{xa}(i - i_{sub}, j, k) = X_1 \hat{H}_{xa}(i - r, j, k) + X_2 \hat{H}_{xa}(i, j, k), \qquad (4.75)$$

where

$$i_{sub} \in [1, r-1], \quad X_1 = \frac{i_{sub}}{r}, \quad X_2 = 1 - X_1.$$

Spatial interpolation of H_{xa} values with (4.71) to (4.75) will result in the subgrid values of $\hat{H}_{xa}$ in the xz-plane.

4.7.6   Equivalent Currents Calculation at Huygens Surfaces

This section presents the equations for the equivalent current calculation at the Inner and Outer Huygens Surfaces. Symbols $\ddot{E}$ and $\ddot{H}$ in Section 4.7.6 denote the electric and magnetic field components obtained with the normal FDTD updates.

Electric Field Components

Inner Surface

The Inner Surface value calculation consists in correcting previously calculated subgrid values by injecting the IS equivalent current from the main grid. Spatially and temporally interpolated main grid value is either added to or subtracted from a subgrid value. This subgrid value is calculated with a normal FDTD update. The plus or minus sign preceding the temporally interpolated main grid value depends on the component location in the SF or TF region. Since the spatial interpolation of the main grid values is accomplished by equations listed in Section 4.7.5, it is only the temporal interpolation that remains to be done at the IS. The values of temporal interpolation coefficients Υ_1, Υ_2 are defined by (4.24) and (4.25), and change depending on the time-step value of the subgrid (see Section 4.7.7 for details).

Correct E_{xb} :

$$E_{xb}^n\left(i, j_{bIL}, k\right) = \ddot{E}_{xb}^n\left(i, j_{bIL}, k\right)$$

$$- \frac{\Gamma_{2b}\left(i, j_{bIL}, k\right)}{\Delta y_b}\left(\Upsilon_1\, \hat{H}_{za}^{n-1}\left(i, j_{bIL}, k\right) + \Upsilon_2\, \hat{H}_{za}^n\left(i, j_{bIL}, k\right)\right), \quad (4.76)$$

$$E_{xb}^n\left(i, j_{bIR}, k\right) = \ddot{E}_{xb}^n\left(i, j_{bIR}, k\right)$$

$$+ \frac{\Gamma_{2b}\left(i, j_{bIR}, k\right)}{\Delta y_b}\left(\Upsilon_1\, \hat{H}_{za}^{n-1}\left(i, j_{bIR}, k\right) + \Upsilon_2\, \hat{H}_{za}^n\left(i, j_{bIR}, k\right)\right), \quad (4.77)$$

where $i \in [i_{bIL}, i_{bIR} - 1]; \quad k \in [k_{bIL}, k_{bIR}]$.

Consider equations (4.76) and (4.77) governing magnetic field equivalent current at the IS flowing from the main to the subgrid. Main grid component $\hat{H}_{za}$ influences the subgrid component E_{xb}. Normal FDTD update for the electric field component $E_{xb}^n\left(i, j_{bIL}, k\right)$ in the subgrid is:

$$E_{xb}^n\left(i, j_{bIL}, k\right) = \Gamma_{1b}\left(i, j_{bIL}, k\right) E_{xb}^{n-1}\left(i, j_{bIL}, k\right)$$

$$+ \Gamma_{2b}\left(i, j_{bIL}, k\right)\left(\begin{array}{c} \dfrac{\boxed{H_{zb}^n\left(i, j_{bIL}, k\right) - H_{zb}^n\left(i, j_{bIL} - 1, k\right)}}{\Delta y_b} \\[2ex] -\dfrac{H_{yb}^n\left(i, j_{bIL}, k\right) - H_{yb}^n\left(i, j_{bIL}, k-1\right)}{\Delta z_b} \\[2ex] -J_{src,xb}^n\left(i, j_{bIL}, k\right) \end{array}\right). \quad (4.78)$$

Figure 4.16 shows the subgrid nodes H_{zb} at IL and IR when IS $\perp y$. At IL the node $H_{zb}\left(i, j_{bIL}, k\right)$ is located in the total field region and the node $H_{zb}\left(i, j_{bIL} - 1, k\right)$ is positioned in the scattered field region. Magnetic field nodes crossing the IL $\perp y$ are outlined in (4.78), where

$$H_{zb,tot}^n\left(i, j_{bIL}, k\right) - H_{zb,sct}^n\left(i, j_{bIL} - 1, k\right). \quad (4.79)$$

(a) Inner Left (IL)   (b) Inner Right (IR)
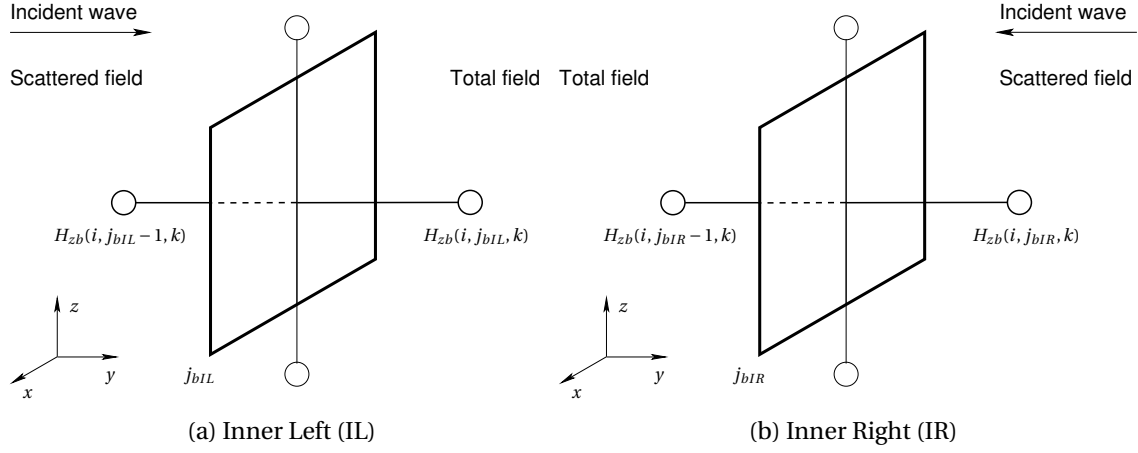
Figure 4.16: Magnetic field components H_{zb} at IS

To balance the TF/SF relation the incident field has to be subtracted from (4.79):

$$H_{zb,tot}^n\left(i, j_{bIL}, k\right) - H_{zb,sct}^n\left(i, j_{bIL} - 1, k\right) - \hat{H}_{za,inc}^*\left(i, j_{bIL}, k\right), \qquad (4.80)$$

where $\hat{H}_{za,inc}^*\left(i, j_{bIL}, k\right)$ denotes the temporally interpolated $\hat{H}_{za}\left(i, j_{bIL}, k\right)$ value:

$$\hat{H}_{za,inc}^*\left(i, j_{bIL}, k\right) = \Upsilon_1 \hat{H}_{za}^{n-1}\left(k, i, j_{bIR}\right) + \Upsilon_2 \hat{H}_{za}^n\left(k, i, j_{bIR}\right). \qquad (4.81)$$

Denoting normal FDTD update of $E_{xb}^n\left(i, j_{bIL}, k\right)$ (4.78) as $\ddot{E}_{xb}^n\left(i, j_{bIL}, k\right)$ and including the incident field value of $\hat{H}_{za,inc}^*\left(i, j_{bIL}, k\right)$ leads to the correction equation for $E_{xb}^n\left(i, j_{bIL}, k\right)$ at IL (4.76).

Figure 4.16b shows the IR when IS $\perp y$. In this case component $H_{zb}\left(i, j_{bIR}, k\right)$ is located in the scattered field region and component $H_{zb}\left(i, j_{bIR} - 1, k\right)$ is positioned in the total field region. To balance the TF/SF relation the incident field value $\hat{H}_{za,inc}^*\left(i, j_{bIR}, k\right)$ is added to the difference $H_{zb,sct}^n\left(i, j_{bIR}, k\right) - H_{zb,tot}^n\left(i, j_{bIR} - 1, k\right)$ in (4.77).

All other correction equations for components E_{xb}, E_{yb}, E_{zb} are derived similarly:

$$E_{xb}^n\left(i, j, k_{bIL}\right) = \ddot{E}_{xb}^n\left(i, j, k_{bIL}\right)$$

$$+ \frac{\Gamma_{2b}\left(i, j, k_{bIL}\right)}{\Delta z_b}\left(\Upsilon_1 \hat{H}_{ya}^{n-1}\left(i, j, k_{bIL}\right) + \Upsilon_2 \hat{H}_{ya}^n\left(i, j, k_{bIL}\right)\right), \quad (4.82)$$

$$E_{xb}^n(i, j, k_{bIR}) = \ddot{E}_{xb}^n(i, j, k_{bIR})$$

$$-\frac{\Gamma_{2b}(i, j, k_{bIR})}{\Delta z_b}\left(\Upsilon_1 \hat{H}_{ya}^{n-1}(i, j, k_{bIR}) + \Upsilon_2 \hat{H}_{ya}^n(i, j, k_{bIR})\right), \quad (4.83)$$

where $i \in [i_{bIL}, i_{bIR} - 1]; \quad j \in [j_{bIL}, j_{bIR}]$.

Correct E_{yb}:

$$E_{yb}^n(i, j, k_{bIL}) = \ddot{E}_{yb}^n(i, j, k_{bIL})$$

$$-\frac{\Gamma_{2b}(i, j, k_{bIL})}{\Delta z_b}\left(\Upsilon_1 \hat{H}_{xa}^{n-1}(i, j, k_{bIL}) + \Upsilon_2 \hat{H}_{xa}^n(i, j, k_{bIL})\right), \quad (4.84)$$

$$E_{yb}^n(i, j, k_{bIR}) = \ddot{E}_{yb}^n(i, j, k_{bIR})$$

$$+\frac{\Gamma_{2b}(i, j, k_{bIR})}{\Delta z_b}\left(\Upsilon_1 \hat{H}_{xa}^{n-1}(i, j, k_{bIR}) + \Upsilon_2 \hat{H}_{xa}^n(i, j, k_{bIR})\right), \quad (4.85)$$

where $j \in [j_{bIL}, j_{bIR} - 1]; \quad i \in [i_{bIL}, i_{bIR}]$.

$$E_{yb}^n(i_{bIL}, j, k) = \ddot{E}_{yb}^n(i_{bIL}, j, k)$$

$$+\frac{\Gamma_{2b}(i_{bIL}, j, k)}{\Delta x_b}\left(\Upsilon_1 \hat{H}_{za}^{n-1}(i_{bIL}, j, k) + \Upsilon_2 \hat{H}_{za}^n(i_{bIL}, j, k),\right), \quad (4.86)$$

$$E_{yb}^n(i_{bIR}, j, k) = \ddot{E}_{yb}^n(i_{bIR}, j, k)$$

$$-\frac{\Gamma_{2b}(i_{bIR}, j, k)}{\Delta x_b}\left(\Upsilon_1 \hat{H}_{za}^{n-1}(i_{bIR}, j, k) + \Upsilon_2 \hat{H}_{za}^n(i_{bIR}, j, k)\right), \quad (4.87)$$

where $j \in [j_{bIL}, j_{bIR} - 1]; \quad k \in [k_{bIL}, k_{bIR}]$.

Correct E_{zb}:

$$E_{zb}^n(i_{bIL}, j, k) = \ddot{E}_{zb}^n(i_{bIL}, j, k)$$

$$-\frac{\Gamma_{2b}\left(i_{bIL}, j, k\right)}{\Delta x_b}\left(\Upsilon_1\,\hat{H}_{ya}^{n-1}\left(i_{bIL}, j, k\right)+\Upsilon_2\,\hat{H}_{ya}^{n}\left(i_{bIL}, j, k\right)\right), \quad (4.88)$$

$$E_{zb}^{n}\left(i_{bIR}, j, k\right)=\ddot{E}_{zb}^{n}\left(i_{bIR}, j, k\right)i$$

$$+\frac{\Gamma_{2b}\left(i_{bIR}, j, k\right)}{\Delta x_b}\left(\Upsilon_1\,\hat{H}_{ya}^{n-1}\left(i_{bIR}, j, k\right)+\Upsilon_2\,\hat{H}_{ya}^{n}\left(i_{bIR}, j, k\right)\right), \quad (4.89)$$

where $k\in[k_{bIL}, k_{bIR}-1];\quad j\in[j_{bIL}, j_{bIR}]$.

$$E_{zb}^{n}\left(i, j_{bIL}, k\right)=\ddot{E}_{zb}^{n}\left(i, j_{bIL}, k\right)$$

$$+\frac{\Gamma_{2b}\left(i, j_{bIL}, k\right)}{\Delta y_b}\left(\Upsilon_1\,\hat{H}_{xa}^{n-1}\left(i, j_{bIL}, k\right)+\Upsilon_2\,\hat{H}_{xa}^{n}\left(i, j_{bIL}, k\right)\right), \quad (4.90)$$

$$E_{zb}^{n}\left(i, j_{bIR}, k\right)=\ddot{E}_{zb}^{n}\left(i, j_{bIR}, k\right)$$

$$-\frac{\Gamma_{2b}\left(i, j_{bIR}, k\right)}{\Delta y_b}\left(\Upsilon_1\,\hat{H}_{xa}^{n-1}\left(i, j_{bIR}, k\right)+\Upsilon_2\,\hat{H}_{xa}^{n}\left(i, j_{bIR}, k\right)\right), \quad (4.91)$$

where $k\in[k_{bIL}, k_{bIR}-1];\quad i\in[i_{bIL}, i_{bIR}]$.

Outer Surface

Since all subgrid values are available at the main grid locations at the OS no spatial and temporal interpolations are necessary. Similar to the IS the main grid values calculated normally are corrected with the equivalent current from the subgrid.

Correct E_{xa} :

$$E_{xa}^{n}\left(i, j, k_{aOL}\right)=\ddot{E}_{xa}^{n}\left(i, j, k_{aOL}\right)-\frac{\Gamma_{2a}\left(i, j, k_{aOL}\right)}{\Delta z_a}\,H_{yb}^{n}\left(i_b, j_b, k_{bOL}-\tfrac{r+1}{2}\right),$$

$$(4.92)$$

$$E_{xa}^{n}\left(i, j, k_{aOR}\right)=\ddot{E}_{xa}^{n}\left(i, j, k_{aOR}\right)+\frac{\Gamma_{2a}\left(i, j, k_{aOR}\right)}{\Delta z_a}\,H_{yb}^{n}\left(i_b, j_b, k_{bOR}+\tfrac{r-1}{2}\right),$$

where

$$i\in[i_{aOL}, i_{aOR}-1], \qquad\qquad j\in[j_{aOL}, j_{aOR}],$$

$$i_b = i_{bOL} + r(i - i_{aOL}) + \tfrac{r-1}{2}, \qquad\qquad j_b = j_{bOL} + r(j - j_{aOL}).$$

$$E_{xa}^n(i, j_{aOL}, k) = \ddot{E}_{xa}^n(i, j_{aOL}, k) + \frac{\Gamma_{2a}(i, j_{aOL}, k)}{\Delta y_a} H_{zb}^n\big(i_b, j_{bOL} - \tfrac{r+1}{2}, k_b\big),$$

$$(4.93)$$

$$E_{xa}^n(i, j_{aOR}, k) = \ddot{E}_{xa}^n(i, j_{aOR}, k) - \frac{\Gamma_{2a}(i, j_{aOR}, k)}{\Delta y_a} H_{zb}^n\big(i_b, j_{bOR} + \tfrac{r-1}{2}, k_b\big),$$

where

$$i \in [i_{aOL}, i_{aOR} - 1], \qquad\qquad k \in [k_{aOL}, k_{aOR}],$$
$$i_b = i_{bOL} + r(i - i_{aOL}) + \tfrac{r-1}{2}, \qquad k_b = k_{bOL} + r(k - k_{aOL}).$$

Correct E_{ya}:

$$E_{ya}^n(i_{aOL}, j, k) = \ddot{E}_{ya}^n(i_{aOL}, j, k) - \frac{\Gamma_{2a}(i_{aOL}, j, k)}{\Delta x_a} H_{zb}^n\big(i_{bOL} - \tfrac{r+1}{2}, j_b, k_b\big),$$

$$(4.94)$$

$$E_{ya}^n(i_{aOR}, j, k) = \ddot{E}_{ya}^n(i_{aOR}, j, k) + \frac{\Gamma_{2a}(i_{aOR}, j, k)}{\Delta x_a} H_{zb}^n\big(i_{bOR} + \tfrac{r-1}{2}, j_b, k_b\big),$$

where

$$j \in [j_{aOL}, j_{aOR} - 1], \qquad\qquad k \in [k_{aOL}, k_{aOR}],$$
$$j_b = j_{bOL} + r(j - j_{aOL}) + \tfrac{r-1}{2}, \qquad k_b = k_{bOL} + r(k - k_{aOL}).$$

$$E_{ya}^n(i, j, k_{aOL}) = \ddot{E}_{ya}^n(i, j, k_{aOL}) + \frac{\Gamma_{2a}(i, j, k_{aOL})}{\Delta z_a} H_{xb}^n\big(i_b, j_b, k_{bOL} - \tfrac{r+1}{2}\big),$$

$$(4.95)$$

$$E_{ya}^n(i, j, k_{aOR}) = \ddot{E}_{ya}^n(i, j, k_{aOR}) - \frac{\Gamma_{2a}(i, j, k_{aOR})}{\Delta z_a} H_{xb}^n\big(i_b, j_b, k_{bOR} + \tfrac{r-1}{2}\big),$$

where

$$j \in [j_{aOL}, j_{aOR} - 1], \qquad\qquad i \in [i_{aOL}, i_{aOR}],$$
$$j_b = j_{bOL} + r(j - j_{aOL}) + \tfrac{r-1}{2}, \qquad i_b = i_{bOL} + r(i - i_{aOL}).$$

Correct E_{za} :

$$E_{za}^n(i, j_{aOL}, k) = \ddot{E}_{za}^n(i, j_{aOL}, k) - \frac{\Gamma_{2a}(i, j_{aOL}, k)}{\Delta y_a} H_{xb}^n\left(i_b, j_{bOL} - \tfrac{r+1}{2}, k_b\right),$$

(4.96)

$$E_{za}^n(i, j_{aOR}, k) = \ddot{E}_{za}^n(i, j_{aOR}, k) + \frac{\Gamma_{2a}(i, j_{aOR}, k)}{\Delta y_a} H_{xb}^n\left(i_b, j_{bOR} + \tfrac{r-1}{2}, k_b\right),$$

where

$$i \in [i_{aOL}, i_{aOR}], \qquad\qquad k \in [k_{aOL}, k_{aOR} - 1],$$
$$i_b = i_{bOL} + r(i - i_{aOL}), \qquad\qquad k_b = k_{bOL} + r(k - k_{aOL}) + \tfrac{r-1}{2}.$$

$$E_{za}^n(i_{aOL}, j, k) = \ddot{E}_{za}^n(i_{aOL}, j, k) + \frac{\Gamma_{2a}(i_{aOL}, j, k)}{\Delta x_a} H_{yb}^n\left(i_{bOL} - \tfrac{r+1}{2}, j_b, k_b\right),$$

(4.97)

$$E_{za}^n(i_{aOR}, j, k) = \ddot{E}_{za}^n(i_{aOR}, j, k) - \frac{\Gamma_{2a}(i_{aOR}, j, k)}{\Delta x_a} H_{yb}^n\left(i_{bOR} + \tfrac{r-1}{2}, j_b, k_b\right),$$

where

$$j \in [j_{aOL}, j_{aOR}], \qquad\qquad k \in [k_{aOL}, k_{aOR} - 1],$$
$$j_b = j_{bOL} + r(j - j_{aOL}), \qquad\qquad k_b = k_{bOL} + r(k - k_{aOL}) + \tfrac{r-1}{2}.$$

Magnetic Field Components

Magnetic field components at the Inner and Outer Huygens Surfaces are calculated similarly to the electric field components. All comments in Section 4.7.6 are valid for the magnetic field calculation shown below.

Inner Surface

Correct H_{xb} :

$$H_{xb}^n(i, j_{bIL} - 1, k) = \ddot{H}_{xb}^n(i, j_{bIL} - 1, k)$$

$$+ \frac{Z_{2b}(i, j_{bIL} - 1, k)}{\Delta y_b}\left(\Upsilon_1 \hat{E}_{za}^{n-1}(i, j_{bIL} - 1, k) + \Upsilon_2 \hat{E}_{za}^n(i, j_{bIL} - 1, k)\right), \quad (4.98)$$

$$H_{xb}^n\left(i, j_{bIR}, k\right) = \ddot{H}_{xb}^n\left(i, j_{bIR}, k\right)$$

$$- \frac{Z_{2b}\left(i, j_{bIR}, k\right)}{\Delta y_b}\left(\Upsilon_1 \hat{E}_{za}^{n-1}\left(i, j_{bIR}, k\right) + \Upsilon_2 \hat{E}_{za}^n\left(i, j_{bIR}, k\right)\right), \quad (4.99)$$

where $i \in [i_{bIL}, i_{bIR}]; \quad k \in [k_{bIL}, k_{bIR} - 1]$.

$$H_{xb}^n\left(i, j, k_{bIL} - 1\right) = \ddot{H}_{xb}^n\left(i, j, k_{bIL} - 1\right)$$

$$- \frac{Z_{2b}\left(i, j, k_{bIL} - 1\right)}{\Delta z_b}\left(\Upsilon_1 \hat{E}_{ya}^{n-1}\left(i, j, k_{bIL} - 1\right)\Delta z_b + \Upsilon_2 \hat{E}_{ya}^n\left(i, j, k_{bIL} - 1\right)\right), \quad (4.100)$$

$$H_{xb}^n\left(i, j, k_{bIR}\right) = \ddot{H}_{xb}^n\left(i, j, k_{bIR}\right)$$

$$+ \frac{Z_{2b}\left(i, j, k_{bIR}\right)}{\Delta z_b}\left(\Upsilon_1 \hat{E}_{ya}^{n-1}\left(i, j, k_{bIR}\right) + \Upsilon_2 \hat{E}_{ya}^n\left(i, j, k_{bIR}\right)\right), \quad (4.101)$$

where $i \in [i_{bIL}, i_{bIR}]; \quad j \in [j_{bIL}, j_{bIR} - 1]$.

Correct H_{yb}:

$$H_{yb}^n\left(i, j, k_{bIL} - 1\right) = \ddot{H}_{yb}^n\left(i, j, k_{bIL} - 1\right)$$

$$+ \frac{Z_{2b}\left(i, j, k_{bIL} - 1\right)}{\Delta z_b}\left(\Upsilon_1 \hat{E}_{xa}^{n-1}\left(i, j, k_{bIL} - 1\right) + \Upsilon_2 \hat{E}_{xa}^n\left(i, j, k_{bIL} - 1\right)\right), \quad (4.102)$$

$$H_{yb}^n\left(i, j, k_{bIR}\right) = \ddot{H}_{yb}^n\left(i, j, k_{bIR}\right)$$

$$- \frac{Z_{2b}\left(i, j, k_{bIR}\right)}{\Delta z_b}\left(\Upsilon_1 \hat{E}_{xa}^{n-1}\left(i, j, k_{bIR}\right) + \Upsilon_2 \hat{E}_{xa}^n\left(i, j, k_{bIR}\right)\right), \quad (4.103)$$

where $j \in [j_{bIL}, j_{bIR}]; \quad i \in [i_{bIL}, i_{bIR} - 1]$.

$$H_{yb}^n\left(i_{bIL} - 1, j, k\right) = \ddot{H}_{yb}^n\left(i_{bIL} - 1, j, k\right)$$

$$- \frac{Z_{2b}\left(i_{bIL} - 1, j, k\right)}{\Delta x_b}\left(\Upsilon_1 \hat{E}_{za}^{n-1}\left(i_{bIL} - 1, j, k\right) + \Upsilon_2 \hat{E}_{za}^n\left(i_{bIL} - 1, j, k\right)\right), \quad (4.104)$$

$$H_{yb}^n\left(i_{bIR}, j, k\right) = \ddot{H}_{yb}^n\left(i_{bIR}, j, k\right)$$

$$+ \frac{Z_{2b}\left(i_{bIR}, j, k\right)}{\Delta x_b}\left(\Upsilon_1 \hat{E}_{za}^{n-1}\left(i_{bIR}, j, k\right) + \Upsilon_2 \hat{E}_{za}^n\left(i_{bIR}, j, k\right)\right), \quad (4.105)$$

where $j \in [j_{bIL}, j_{bIR}]; \quad k \in [k_{bIL}, k_{bIR} - 1]$.

Correct H_{zb}:

$$H_{zb}^n\left(i_{bIL} - 1, j, k\right) = \ddot{H}_{zb}^n\left(i_{bIL} - 1, j, k\right)$$

$$+ \frac{Z_{2b}\left(i_{bIL} - 1, j, k\right)}{\Delta x_b}\left(\Upsilon_1 \hat{E}_{ya}^{n-1}\left(i_{bIL} - 1, j, k\right) + \Upsilon_2 \hat{E}_{ya}^n\left(i_{bIL} - 1, j, k\right)\right), \quad (4.106)$$

$$H_{zb}^n\left(i_{bIR}, j, k\right) = \ddot{H}_{zb}^n\left(i_{bIR}, j, k\right)$$

$$- \frac{Z_{2b}\left(i_{bIR}, j, k\right)}{\Delta x_b}\left(\Upsilon_1 \hat{E}_{ya}^{n-1}\left(i_{bIR}, j, k\right) + \Upsilon_2 \hat{E}_{ya}^n\left(i_{bIR}, j, k\right)\right), \quad (4.107)$$

where $k \in [k_{bIL}, k_{bIR}]; \quad j \in [j_{bIL}, j_{bIR} - 1]$.

$$H_{zb}^n\left(i, j_{bIL} - 1, k\right) = \ddot{H}_{zb}^n\left(i, j_{bIL} - 1, k\right)$$

$$- \frac{Z_{2b}\left(i, j_{bIL} - 1, k\right)}{\Delta y_b}\left(\Upsilon_1 \hat{E}_{xa}^{n-1}\left(i, j_{bIL} - 1, k\right) + \Upsilon_2 \hat{E}_{xa}^n\left(i, j_{bIL} - 1, k\right)\right), \quad (4.108)$$

$$H_{zb}^n\left(i, j_{bIR}, k\right) = \ddot{H}_{zb}^n\left(i, j_{bIR}, k\right)$$

$$+ \frac{Z_{2b}\left(i, j_{bIR}, k\right)}{\Delta y_b}\left(\Upsilon_1 \hat{E}_{xa}^{n-1}\left(i, j_{bIR}, k\right) + \Upsilon_2 \hat{E}_{xa}^n\left(i, j_{bIR}, k\right)\right), \quad (4.109)$$

where $k \in [k_{bIL}, k_{bIR}]; \quad i \in [i_{bIL}, i_{bIR} - 1]$.

Outer Surface

Correct H_{xa} :

$$H_{xa}^n\left(i, j_{aOL} - 1, k\right) = \ddot{H}_{xa}^n\left(i, j_{aOL} - 1, k\right) - \frac{Z_{2a}\left(i, j_{aOL} - 1, k\right)}{\Delta y_a} E_{zb}^n\left(i_b, j_{bOL}, k_b\right),$$

$$H_{xa}^n\left(i, j_{aOR}, k\right) = \ddot{H}_{xa}^n\left(i, j_{aOR}, k\right) + \frac{Z_{2a}\left(i, j_{aOR}, k\right)}{\Delta y_a} E_{zb}^n\left(i_b, j_{bOR}, k_b\right),$$

$$\text{(4.110)}$$

where

$$i \in [i_{aOL}, i_{aOR}], \qquad\qquad k \in [k_{aOL}, k_{aOR} - 1],$$
$$i_b = i_{bOL} + r(i - i_{aOL}), \qquad\qquad k_b = k_{bOL} + r(k - k_{aOL}) + \tfrac{r-1}{2}.$$

$$H_{xa}^n\left(i, j, k_{aOL} - 1\right) = \ddot{H}_{xa}^n\left(i, j, k_{aOL} - 1\right) + \frac{Z_{2a}\left(i, j, k_{aOL} - 1\right)}{\Delta z_a} E_{yb}^n\left(i_b, j_b, k_{bOL}\right),$$

$$H_{xa}^n\left(i, j, k_{aOR}\right) = \ddot{H}_{xa}^n\left(i, j, k_{aOR}\right) - \frac{Z_{2a}\left(i, j, k_{aOR}\right)}{\Delta z_a} E_{yb}^n\left(i_b, j_b, k_{bOR}\right),$$

$$\text{(4.111)}$$

where

$$i \in [i_{aOL}, i_{aOR}], \qquad\qquad j \in [j_{aOL}, j_{aOR} - 1],$$
$$i_b = i_{bOL} + r(i - i_{aOL}), \qquad\qquad j_b = j_{bOL} + r(j - j_{aOL}) + \tfrac{r-1}{2}.$$

Correct H_{ya} :

$$H_{ya}^n\left(i, j, k_{aOL} - 1\right) = \ddot{H}_{ya}^n\left(i, j, k_{aOL} - 1\right) - \frac{Z_{2a}\left(i, j, k_{aOL} - 1\right)}{\Delta z_a} E_{xb}^n\left(i_b, j_b, k_{bOL}\right),$$

$$H_{ya}^n\left(i, j, k_{aOR}\right) = \ddot{H}_{ya}^n\left(i, j, k_{aOR}\right) + \frac{Z_{2a}\left(i, j, k_{aOR}\right)}{\Delta z_a} E_{xb}^n\left(i_b, j_b, k_{bOR}\right),$$

$$\text{(4.112)}$$

where

$$i \in [i_{aOL}, i_{aOR} - 1], \qquad\qquad\qquad j \in [j_{aOL}, j_{aOR}],$$

$$i_b = i_{bOL} + r(i - i_{aOL}) + \tfrac{r-1}{2}, \qquad\qquad j_b = j_{bOL} + r(j - j_{aOL}).$$

$$H_{ya}^n\left(i_{aOL} - 1, j, k\right) = \ddot{H}_{ya}^n\left(i_{aOL} - 1, j, k\right) + \frac{Z_{2a}\left(i_{aOL} - 1, j, k\right)}{\Delta x_a} E_{zb}^n\left(i_{bOL}, j_b, k_b\right),$$

$$H_{ya}^n\left(i_{aOR}, j, k\right) = \ddot{H}_{ya}^n\left(i_{aOR}, j, k\right) - \frac{Z_{2a}\left(i_{aOR}, j, k\right)}{\Delta x_a} E_{zb}^n\left(i_{bOR}, j_b, k_b\right),$$

$$\tag{4.113}$$

where

$$\begin{aligned} j &\in [j_{aOL}, j_{aOR}], &\qquad k &\in [k_{aOL}, k_{aOR} - 1], \\ j_b &= j_{bOL} + r(j - j_{aOL}), &\qquad k_b &= k_{bOL} + r(k - k_{aOL}) + \tfrac{r-1}{2}. \end{aligned}$$

Correct H_{za}:

$$H_{za}^n\left(i_{aOL} - 1, j, k\right) = \ddot{H}_{za}^n\left(i_{aOL} - 1, j, k\right) - \frac{Z_{2a}\left(i_{aOL} - 1, j, k\right)}{\Delta x_a} E_{yb}^n\left(i_{bOL}, j_b, k_b\right),$$

$$H_{za}^n\left(i_{aOR}, j, k\right) = \ddot{H}_{za}^n\left(i_{aOR}, j, k\right) + \frac{Z_{2a}\left(i_{aOR}, j, k\right)}{\Delta x_a} E_{yb}^n\left(i_{bOR}, j_b, k_b\right),$$

$$\tag{4.114}$$

where

$$\begin{aligned} j &\in [j_{aOL}, j_{aOR} - 1], &\qquad k &\in [k_{aOL}, k_{aOR}], \\ j_b &= j_{bOL} + r(j - j_{aOL}) + \tfrac{r-1}{2}, &\qquad k_b &= k_{bOL} + r(k - k_{aOL}). \end{aligned}$$

$$H_{za}^n\left(i, j_{aOL} - 1, k\right) = \ddot{H}_{za}^n\left(i, j_{aOL} - 1, k\right) + \frac{Z_{2a}\left(i, j_{aOL} - 1, k\right)}{\Delta y_a} E_{xb}^n\left(i_b, j_{bOL}, k_b\right),$$

$$H_{za}^n\left(i, j_{aOR}, k\right) = \ddot{H}_{za}^n\left(i, j_{aOR}, k\right) - \frac{Z_{2a}\left(i, j_{aOR}, k\right)}{\Delta y_a} E_{xb}^n\left(i_b, j_{bOR}, k_b\right),$$

$$\tag{4.115}$$

where

$$i \in [i_{aOL}, i_{aOR} - 1], \qquad\qquad k \in [k_{aOL}, k_{aOR}],$$

$$i_b = i_{bOL} + r(i - i_{aOL}) + \tfrac{r-1}{2}, \qquad\qquad k_b = k_{bOL} + r(k - k_{aOL}).$$

4.7.7   Calculation Order

The HSG method's calculation order is listed below. Symbol "*" denotes the entire spatial domain. Right-directed horizontal arrow "⟶" signifies the equivalent current injection at the IS or OS. A reference to a section containing relevant equations is given on each line. Thick horizontal line separates the two symmetric parts of the HSG method.

  Temporal interpolation coefficients Υ_1, Υ_2 are used in the subgrid time loops in both symmetric parts of the HSG algorithm. Prior to subgrid time loops the temporal interpolation coefficients are $\Upsilon_1 = 1, \Upsilon_2 = 0$. In this case the subgrid node coincides with the main grid node and only one component's value will be selected, since the other will be multiplied by 0. Inside of the subgrid time loops the interpolation coefficients change their values depending on the loop iterator m. The closer in time the subgrid node is to the most recent main grid node, the higher is this main grid node's influence on the interpolated subgrid value. Additional parameters m_1, m_2 are necessary to obtain a one half time-step shift between the electric and magnetic field values in the subgrid.

1. Calculate coefficients $\Gamma_{1g}(*), \Gamma_{2g}(*), Z_{1g}(*), Z_{2g}(*)$, where $g \in [a, b]$ (Sections 4.7.1 and 4.7.2)

2. Generate excitation source signal

3. Enter main grid time loop $n \in [1, n_{max}]$:

    (a) Re-arrange $H_a(*)$ (Section 4.7.3)

    (b) Calculate $H_a(*)$ (Section 4.7.1)

    (c) Calculate $H_a(ABC)$

    (d) Re-arrange $\hat{H}_a(IS)$ (Section 4.7.3)

    (e) Calculate $\hat{H}_a(IS)$ (Figure 4.15)

    (f) Re-arrange $E_b(*)$ ((4.50))

(g) Calculate $E_b(*)$ (Section 4.7.2)

(h) Calculate $E_b(ABC)$

(i) Calculate $\hat{H}_a(IS) \longrightarrow E_b(IS)$, $\Upsilon_1 = 1$, $\Upsilon_2 = 0$ (Section 4.7.6)

(j) Enter subgrid time loop 1: $m \in \left[1, \frac{r-1}{2}\right]$ and $m_1 = m + \frac{r-1}{2}$

    i. Calculate $H_b(*)$ (Section 4.7.1)

    ii. Calculate $H_b(ABC)$

    iii. Calculate $\hat{E}_a(IS) \longrightarrow H_b(IS)$, $\Upsilon_1 = \frac{r-m}{r}$, $\Upsilon_2 = \frac{m}{r}$ ((4.97))

    iv. Re-arrange $E_b(*)$ ((4.50))

    v. Calculate $E_b(*)$ (Section 4.7.2)

    vi. Calculate $E_b(ABC)$

    vii. Calculate $\hat{H}_a(IS) \longrightarrow E_b(IS)$, $\Upsilon_1 = \frac{r-m_1}{r}$, $\Upsilon_2 = \frac{m_1}{r}$ (Section 4.7.6)

(k) Calculate $E_b(OS) \longrightarrow H_a(OS)$ ((4.109))

(l) Re-arrange $E_a(*)$ ((4.48))

(m) Calculate $E_a(*)$ (Section 4.7.2)

(n) Calculate $E_a(ABC)$

(o) Calculate $E_a(src)$ ((4.44))

(p) Re-arrange $\hat{E}_a(IS)$ ((4.48))

(q) Calculate $\hat{E}_a(IS)$ (Table 4.1)

(r) Calculate $H_b(*)$ (Section 4.7.1)

(s) Calculate $H_b(ABC)$

(t) Calculate $\hat{E}_a(IS) \longrightarrow H_b(IS)$, $\Upsilon_1 = 1$, $\Upsilon_2 = 0$ ((4.97))

(u) Enter fine grid time loop 2: $m \in \left[\frac{r+1}{2}, r\right]$ and $m_2 = m - \frac{r-1}{2}$

    i. Re-arrange $E_b(*)$ ((4.50))

    ii. Calculate $E_b(*)$ (Section 4.7.2)

    iii. Calculate $E_b(ABC)$

    iv. Calculate $\hat{H}_a(IS) \longrightarrow E_b(IS)$, $\Upsilon_1 = \frac{r-m_2}{r}$, $\Upsilon_2 = \frac{m_2}{r}$ (Section 4.7.6)

    v. Calculate $H_b(*)$ (Section 4.7.1)

    vi. Calculate $H_b(ABC)$

vii. Calculate $\hat{E}_a(IS) \longrightarrow H_b(IS)$, $\quad \Upsilon_1 = \frac{r-m}{r}$, $\quad \Upsilon_2 = \frac{m}{r}$ $\quad$ ((4.97))

(v) Calculate $H_b(OS) \longrightarrow E_a(OS)$ $\quad$ ((4.91))

(w) Output $E_a(*)$, $H_a(*)$

(x) Output $E_b(*)$, $H_b(*)$

4. Finalise simulation

In the HSG method implementation it is possible to use only one subgrid iterator m instead of three m, m_1, m_2. This is achieved by enforcing $m \in \left[1, \frac{r-1}{2}\right]$ at both steps (j) and (u). Then the temporal interpolation coefficients at substeps (j).iii and (u).iv are calculated as:

$$\Upsilon_1 = \frac{r+1-2m}{2r}, \quad \Upsilon_2 = 1 - \Upsilon_1. \tag{4.116}$$

At substeps (j).vii and (u).vii the temporal interpolation coefficients are equal to:

$$\Upsilon_1 = 1 - \frac{m}{r}, \quad \Upsilon_2 = 1 - \Upsilon_1. \tag{4.117}$$

Chapter 5

Frequency Dispersive Huygens Subgridding

This chapter explains the frequency dispersive HSG method. Section 5.1 gives the motivation for the frequency dispersive HSG approach. The main principles and the pseudocode of the dispersive HSG method are presented in Sections 5.2 and 5.3. The mathematical formulation (Section 5.4) highlights the new equations introduced in the dispersive HSG relative to the classic HSG scheme.

5.1 Introduction

With a ubiquitous use of the miniaturised computer devices it becomes extremely important to track any health effects caused by the constant presence of personal electronic devices. Practical experiments exposing the volunteers to high power electromagnetic radiation are considered unethical and can be potentially harmful. An alternative solution is offered by numerical simulation methods, that can predict the electromagnetic radiation patterns. When tracking the wave propagation inside and around the human body, it is especially important to consider the frequency dispersion of the biological tissues. The Frequency Dependent–Finite-Difference Time-Domain (FD–FDTD) method presents a numerical algorithm very well suited to the simulation of electromagnetic waves inside the human body. However, the geometric complexity of the human organs and high relative permittivities of human body tissues require a simulation grid with 10 to 15 times higher resolution than a grid to sample wave propagation in free-space [109]. Solution of Maxwell's

equations on such a finely resolved model will place a heavy burden on computational resources: CPU time and memory.

Subgridding techniques were proposed in order to reduce the computational burden. Application of a subgridding approach allows to save the resource usage by placing the finely discretised mesh in a volume of interest and discretise the rest of the space with a normal spatio-temporal resolution. This work focuses on a particular subgridding technique called the Huygens Subgridding. Costen and Bérenger [109] have already reported the HSG method's extension to the frequency dispersive media in 1D. Their work tested the dispersive HSG method applied to a human body model. One-pole Debye relaxation model was used to accommodate the frequency-dependent media. Three separate subgrids, each with a ratio of 15, were used to successfully simulate the electromagnetic wave propagation.

This chapter describes the extension of the dispersive HSG method to 3D. The research conducted within the current project is a continuation of Costen's and Bérenger's work [109]. Three-dimensional frequency dispersive HSG method is also the major contribution of the current PhD work and the major focus of the current dissertation.

5.2   Basics of Dispersive Huygens Subgridding

The main quantities operated upon in the dispersive HSG approach are electric flux density $\boldsymbol{D}$ and magnetic field $\boldsymbol{H}$, in contrast to electric and magnetic fields $\boldsymbol{E}$ and $\boldsymbol{H}$ in the normal HSG method. An Auxiliary Differential Equation (ADE) method is used at every D node to calculate the electric field value E. In this project the classical FDTD method is extended to FD–FDTD algorithm using the one-pole Debye relaxation model. Hence, the dispersive HSG method is a combination of classical HSG and the FD–FDTD schemes.

In 1D the energy source free Maxwell's curl equations reduce to:

Faraday's law:

$$\frac{\partial H_z}{\partial t} = -\frac{1}{\mu} \cdot \frac{\partial E_y}{\partial x}.$$ (5.1)

Ampère's law:

$$\frac{\partial D_y}{\partial t} = \frac{\partial H_z}{\partial x}.$$ (5.2)

Incident wave   Huygens surface

Scattered field $D_y(-1)$ $D_y(0)$ Total field
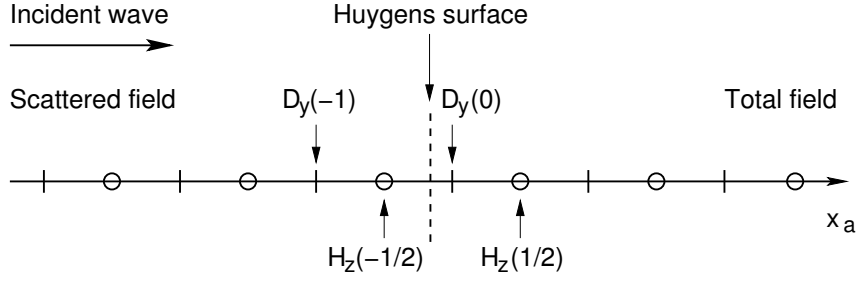
$H_z(-1/2)$ $H_z(1/2)$

Figure 5.1: Huygens surface with electric flux density and magnetic field, 1D

Figure 5.1 depicts a hypothetical Huygens surface in 1D. The main quantities of operation are D_y and H_z. Discretising (5.2) with finite-differences and expressing the node $D_y(0)$ yields:

$$D_y^{n+1}(0) = D_y^n(0) - \frac{\Delta t}{\Delta x}\left(H_z^{n+\frac{1}{2}}\left(\tfrac{1}{2}\right) - H_z^{n+\frac{1}{2}}\left(-\tfrac{1}{2}\right)\right). \tag{5.3}$$

The node $D_y(0)$ lies in the total field region and the H_z nodes used in the finite-difference expression are $H_z^{n+\frac{1}{2}}\left(\tfrac{1}{2}\right)$, situated in the total field region, and $H_z^{n+\frac{1}{2}}\left(-\tfrac{1}{2}\right)$, positioned in the scattered field region. According to the TF/SF theory the total field value can be represented as a sum of scattered and incident field values. Hence the magnetic field value on the left-hand side from the HS in Figure 5.1 can be viewed as:

$$H_{z,tot}^{n+\frac{1}{2}}\left(-\tfrac{1}{2}\right) = H_{z,sct}^{n+\frac{1}{2}}\left(-\tfrac{1}{2}\right) + H_{z,inc}^{n+\frac{1}{2}}\left(-\tfrac{1}{2}\right). \tag{5.4}$$

Applying the TF/SF regions as shown in Figure 5.1 onto (5.3) leads to the following expression:

$$D_y^{n+1}(0) = D_y^n(0) - \frac{\Delta t}{\Delta x}\left(H_{z,tot}^{n+\frac{1}{2}}\left(\tfrac{1}{2}\right) - H_{z,sct}^{n+\frac{1}{2}}\left(-\tfrac{1}{2}\right)\right). \tag{5.5}$$

To balance the magnetic field in the total field region $H_{z,tot}^{n+\frac{1}{2}}\left(\tfrac{1}{2}\right)$, the node in the scattered field region, left from the Huygens surface, $H_{z,sct}^{n+\frac{1}{2}}\left(-\tfrac{1}{2}\right)$ lacks the incident magnetic field $H_{z,inc}^{n+\frac{1}{2}}\left(-\tfrac{1}{2}\right)$. This process can also be seen as a substitution of (5.4) into (5.3). Therefore, the discretised (5.3) at Huygens surface becomes:

$$D_y^{n+1}(0) = D_y^n(0) - \frac{\Delta t}{\Delta x}\left(H_{z,tot}^{n+\frac{1}{2}}\left(\tfrac{1}{2}\right) - H_{z,sct}^{n+\frac{1}{2}}\left(-\tfrac{1}{2}\right) - H_{z,inc}^{n+\frac{1}{2}}\left(-\tfrac{1}{2}\right)\right). \tag{5.6}$$

The discretised magnetic field expression remains unchanged relative to the classical HSG method:

$$H_z^{n+\frac{3}{2}}\left(-\tfrac{1}{2}\right) = H_z^{n+\frac{1}{2}}\left(-\tfrac{1}{2}\right) - \frac{\Delta t}{\mu_0 \Delta x}\left(E_y^{n+1}(0) - E_y^{n+1}(-1)\right), \qquad (5.7)$$

where $\mu = \mu_r \mu_0$ and $\mu_r = 1$. In this case the finite-difference expression has to be evaluated between two SF values $E_y^{n+1}(0)$ and $E_y^{n+1}(-1)$. The SF value of $E_{y,sct}^{n+1}(0)$ is obtained from the TF/SF balancing equation:

$$E_{y,sct}^{n+1}(0) = E_{y,tot}^{n+1}(0) - E_{y,inc}^{n+1}(0). \qquad (5.8)$$

Substituting (5.8) into (5.7) leads to a discretised magnetic field equation at Huygens surface:

$$H_z^{n+\frac{3}{2}}\left(-\tfrac{1}{2}\right) = H_z^{n+\frac{1}{2}}\left(-\tfrac{1}{2}\right) - \frac{\Delta t}{\mu_0 \Delta x}\left(E_{y,tot}^{n+1}(0) - E_{y,inc}^{n+1}(0) - E_{y,sct}^{n+1}(-1)\right). \qquad (5.9)$$

5.3 Dispersive Huygens Subgridding Algorithm

Algorithm 4 shows the pseudocode of the dispersive HSG method. One iteration of the main grid time loop is illustrated by Algorithm 4. Symbol "*" denotes all spatial locations in the simulation domain. Indices a and b signify the main and the subgrid respectively. Parameter m stands for the subgrid time loops iterator. Subgridding ratio is r. For the sake of clarity value re-arrangement, source excitation, value output and the simulation domain termination with the ABC are hidden in Algorithm 4.

Frequency dispersion is realised with the ADE approach, which enforces a circular calculation order between the mathematical quantities: $D \to E \to H$. Therefore, a number of changes were introduced into Algorithm 4 in comparison with the classical HSG method described by Algorithm 3:

- every electric field E calculation is preceded with the electric flux density D calculation for both main and subgrids (lines: 1, 6, 17 and 23),

- IS current from magnetic field in the main grid $H_a(IS)$ is injected into the current flux density $D_b(IS)$ of the subgrid (lines: 7, 18 and 24),

- electric field at the IS in the subgrid $E_b(IS)$ is re-calculated, triggered by the change of the electric flux density $D_b(IS)$ (lines: 8, 19 and 25),

- identical operations occur at the OS: magnetic field in the subgrid $H_b(OS)$ injects the OS current into electric flux density of the main grid $D_a(OS)$ (line: 12),

- electric field at the OS in the main grid $E_a(OS)$ is re-calculated, stimulated by the electric flux density change (line: 13).

1: **calc** $D_a(*), E_a(*)$
2: **iface** $E_a(IS)$

3: **for** $m \in [1, \frac{r-1}{2}]$ **do**
4:     **calc** $H_b(*)$
5:     **infl** $IS : E_a(IS) \to H_b(IS)$
6:     **calc** $D_b(*), E_b(*)$
7:     **infl** $IS : H_a(IS) \to D_b(IS)$
8:     **recalc** $E_b(IS)$
9: **end for**

10: **calc** $H_b(*)$
11: **infl** $IS : E_a(IS) \to H_b(IS)$
12: **infl** $OS : H_b(OS) \to D_a(OS)$
13: **recalc** $E_a(OS)$

14: **calc** $H_a(*)$
15: **iface** $H_a(IS)$

16: **for** $m \in [1, \frac{r-1}{2}]$ **do**
17:     **calc** $D_b(*), E_b(*)$
18:     **infl** $IS : H_a(IS) \to D_b(IS)$
19:     **recalc** $E_b(IS)$
20:     **calc** $H_b(*)$
21:     **infl** $IS : E_a(IS) \to H_b(IS)$
22: **end for**

23: **calc** $D_b(*), E_b(*)$
24: **infl** $IS : H_a(IS) \to D_b(IS)$
25: **recalc** $E_b(IS)$
26: **infl** $OS : E_b(OS) \to H_a(OS)$

Algorithm 4: Dispersive HSG pseudocode. Abbreviations "calc", "recalc", "iface" and "infl" stand for calculate, re-calculate, calculate interface and calculate influence. Calculate and re-calculate are the regular FDTD updates, calculate interface is the spatial and temporal interpolation at the OS–IS interface, and calculate influence is the equivalent magnetic or electric current transfer via the OS or IS.

Apart from the modifications introduced due to the circular components dependency, the dispersive HSG algorithm is exactly the same as the classical HSG approach. The symmetry of the classical HSG scheme is also preserved in the dispersive HSG method.

5.4   Mathematical Formulation

This section describes the mathematical formulation of the frequency dispersive HSG method. Only the equations different from the classical HSG approach are presented here.

5.4.1 Electric Flux Density Calculation

Equations for calculation of the electric flux density values remain unchanged relative to the standard FD–FDTD method. Symbol g denotes a generic calculation grid with $g \in [a, b]$, where a and b denote the main and subgrids respectively. Equations shown below already accommodate the origin shifts for easier implementation in a computer programming language:

$$D_{xg}^n (i, j, k) = D_{xg}^{n-1} (i, j, k) + \Delta t_g \cdot \left(\begin{array}{c} \dfrac{H_{zg}^n (i, j, k) - H_{zg}^n (i, j-1, k)}{\Delta y_g} \\[2ex] -\dfrac{H_{yg}^n (i, j, k) - H_{yg}^n (i, j, k-1)}{\Delta z_g} \\[2ex] -J_{src,xg}^n (i, j, k) \end{array} \right), \qquad (5.10)$$

where $i \in [i_{g_{min}}, i_{g_{max}} - 1]$; $\quad j \in [j_{g_{min}} + 1, j_{g_{max}} - 1]$; $\quad k \in [k_{g_{min}} + 1, k_{g_{max}} - 1]$;

$$D_{yg}^n (i, j, k) = D_{yg}^{n-1} (i, j, k) + \Delta t_g \cdot \left(\begin{array}{c} \dfrac{H_{xg}^n (i, j, k) - H_{xg}^n (i, j, k-1)}{\Delta z_g} \\[2ex] -\dfrac{H_{zg}^n (i, j, k) - H_{zg}^n (i-1, j, k)}{\Delta x_g} \\[2ex] -J_{src,yg}^n (i, j, k) \end{array} \right), \qquad (5.11)$$

where $i \in [i_{g_{min}} + 1, i_{g_{max}} - 1]$; $\quad j \in [j_{g_{min}}, j_{g_{max}} - 1]$; $\quad k \in [k_{g_{min}} + 1, k_{g_{max}} - 1]$;

$$D_{zg}^n (i, j, k) = D_{zg}^{n-1} (i, j, k) + \Delta t_g \cdot \left(\begin{array}{c} \dfrac{H_{yg}^n (i, j, k) - H_{yg}^n (i-1, j, k)}{\Delta x_g} \\[2ex] -\dfrac{H_{xg}^n (i, j, k) - H_{xg}^n (i, j-1, k)}{\Delta y_g} \\[2ex] -J_{src,zg}^n (i, j, k) \end{array} \right), \qquad (5.12)$$

where $i \in [i_{g_{min}} + 1, i_{g_{max}} - 1]$; $\quad j \in [j_{g_{min}} + 1, j_{g_{max}} - 1]$; $\quad k \in [k_{g_{min}}, k_{g_{max}} - 1]$.

5.4.2   Electric Field Calculation

Electric field calculation is expressed with the ADE from the FD–FDTD approach. Symbol g stands for a generic computation grid, where $g \in [a, b]$.

$$
\begin{aligned}
E_g^n (i, j, k) = {} & \Phi_{1g} (i, j, k) \, D_g^n (i, j, k) \\
& - \Phi_{2g} (i, j, k) \, D_g^{n-1} (i, j, k) \\
& + \Phi_{3g} (i, j, k) \, D_g^{n-2} (i, j, k) \\
& + \Phi_{4g} (i, j, k) \, E_g^{n-1} (i, j, k) \\
& - \Phi_{5g} (i, j, k) \, E_g^{n-2} (i, j, k),
\end{aligned}
\tag{5.13}
$$

where

$$
\Phi_{1g} (i, j, k) = \frac{\tau (i, j, k) + \Delta t}{\varphi_{3g} (i, j, k)},
\qquad\qquad
\Phi_{4g} (i, j, k) = \frac{\varphi_{4g} (i, j, k)}{\varphi_{3g} (i, j, k)},
$$

$$
\Phi_{2g} (i, j, k) = \frac{2\tau (i, j, k) + \Delta t}{\varphi_{3g} (i, j, k)},
\qquad\qquad
\Phi_{5g} (i, j, k) = \frac{\varphi_{1g} (i, j, k)}{\varphi_{3g} (i, j, k)},
$$

$$
\Phi_{3g} (i, j, k) = \frac{\tau (i, j, k)}{\varphi_{3g} (i, j, k)}
$$

with

$$
\varphi_{1g} (i, j, k) = \varepsilon_0 \, \varepsilon_\infty (i, j, k) \, \tau (i, j, k),
$$

$$
\varphi_{2g} (i, j, k) = \varepsilon_0 \, \varepsilon_s (i, j, k) + \sigma (i, j, k) \, \tau (i, j, k),
$$

$$
\varphi_{3g} (i, j, k) = \varphi_{1g} (i, j, k) + \Delta t \, \varphi_{2g} (i, j, k) + \frac{\Delta t^2 \, \sigma (i, j, k)}{2},
$$

$$
\varphi_{4g} (i, j, k) = 2 \varphi_{1g} (i, j, k) + \Delta t \, \varphi_{2g} (i, j, k) - \frac{\Delta t^2 \, \sigma (i, j, k)}{2}.
$$

Electric field calculation ranges change depending on the field component direction x, y, z:

$$E_g = \begin{cases} E_{xg}: & [i_{g_{min}}, & i_{g_{max}} - 1]; & [j_{g_{min}} + 1, & j_{g_{max}} - 1]; & [k_{g_{min}} + 1, & k_{g_{max}} - 1]; \\ E_{yg}: & [i_{g_{min}} + 1, & i_{g_{max}} - 1]; & [j_{g_{min}}, & j_{g_{max}} - 1]; & [k_{g_{min}} + 1, & k_{g_{max}} - 1]; \\ E_{zg}: & [i_{g_{min}} + 1, & i_{g_{max}} - 1]; & [j_{g_{min}} + 1, & j_{g_{max}} - 1]; & [k_{g_{min}}, & k_{g_{max}} - 1]. \end{cases}$$
(5.14)

5.4.3 Electric Flux Density Component Re-Arrangement

In order to calculate the electric flux density and the electric field values, the previous time-step values $n - 1$ and $n - 2$ of the electric flux density at all locations in both grids have to be preserved.

Since the electric field calculation involves the field values of one and two time-steps back in the past, also the electric field values at $n-1$ and $n-2$ have to be saved. Re-arrangement procedure for the electric field is identical to the one presented below.

Main grid

$$\begin{aligned} D_{xa}^{n-2}(*) &\longleftarrow D_{xa}^{n-1}(*), & D_{xa}^{n-1}(*) &\longleftarrow D_{xa}^{n}(*), \\ D_{ya}^{n-2}(*) &\longleftarrow D_{ya}^{n-1}(*), & D_{ya}^{n-1}(*) &\longleftarrow D_{ya}^{n}(*), \\ D_{za}^{n-2}(*) &\longleftarrow D_{za}^{n-1}(*), & D_{za}^{n-1}(*) &\longleftarrow D_{za}^{n}(*). \end{aligned}$$
(5.15)

Subgrid

$$\begin{aligned} D_{xb}^{n-2}(*) &\longleftarrow D_{xb}^{n-1}(*), & D_{xb}^{n-1}(*) &\longleftarrow D_{xb}^{n}(*), \\ D_{yb}^{n-2}(*) &\longleftarrow D_{yb}^{n-1}(*), & D_{yb}^{n-1}(*) &\longleftarrow D_{yb}^{n}(*), \\ D_{zb}^{n-2}(*) &\longleftarrow D_{zb}^{n-1}(*), & D_{zb}^{n-1}(*) &\longleftarrow D_{zb}^{n}(*). \end{aligned}$$
(5.16)

5.4.4 Equivalent Currents Calculation at Huygens Surfaces

This section highlights the changes necessary in the classical HSG method to incorporate the frequency dispersion.

Electric Flux Density

The major alteration to the classical HSG method consists in the replacement of electric field with the electric flux density at the receiving side of the Inner and Outer Surface currents.

Inner Surface

After the replacement of electric field with the electric flux density in the IS influence equation, the auxiliary coefficient $\Gamma_{2b}(i, j, k)$ defined in (4.40) is substituted with a subgrid temporal increment Δt_b. Essentially, the coefficient $\Gamma_{2b}(i, j, k)$ incorporated two important parameters: electric permittivity ε and electric conductivity σ.

   Parameter ε vanishes because the constitutive relationship $\boldsymbol{D} = \varepsilon \boldsymbol{E}$ is no longer used. The Ampère's law is solved directly for $\boldsymbol{D}$. Parameter σ, responsible for the heat energy loss, is transferred to the ADE. Apart from the $\Gamma_{2b}(i, j, k)$ coefficient substitution the IS influence equations are identical to the classical HSG approach. Equations are listed below for the reader's convenience. Temporal interpolation coefficients values Υ_1, Υ_2 depend on the subgrid time-step value m (see Section 5.4.6 for details). Parameter $\ddot{D}$ denotes the electric flux density value obtained with a normal FDTD update equation.

Correct D_{xb}:

$$D_{xb}^n(i, j_{bIL}, k) = \ddot{D}_{xb}^n(i, j_{bIL}, k) - \frac{\Delta t_b}{\Delta y_b}\left(\Upsilon_1\,\hat{H}_{za}^{n-1}(i, j_{bIL}, k) + \Upsilon_2\,\hat{H}_{za}^n(i, j_{bIL}, k)\right),$$

$$D_{xb}^n(i, j_{bIR}, k) = \ddot{D}_{xb}^n(i, j_{bIR}, k) + \frac{\Delta t_b}{\Delta y_b}\left(\Upsilon_1\,\hat{H}_{za}^{n-1}(i, j_{bIR}, k) + \Upsilon_2\,\hat{H}_{za}^n(i, j_{bIR}, k)\right),$$

$$(5.17)$$

where $i \in [i_{bIL}, i_{bIR} - 1]; \quad k \in [k_{bIL}, k_{bIR}]$.

$$D_{xb}^n(i, j, k_{bIL}) = \ddot{D}_{xb}^n(i, j, k_{bIL}) + \frac{\Delta t_b}{\Delta z_b}\left(\Upsilon_1\,\hat{H}_{ya}^{n-1}(i, j, k_{bIL}) + \Upsilon_2\,\hat{H}_{ya}^n(i, j, k_{bIL})\right),$$

$$D_{xb}^n(i, j, k_{bIR}) = \ddot{D}_{xb}^n(i, j, k_{bIR}) - \frac{\Delta t_b}{\Delta z_b}\left(\Upsilon_1\,\hat{H}_{ya}^{n-1}(i, j, k_{bIR}) + \Upsilon_2\,\hat{H}_{ya}^n(i, j, k_{bIR})\right),$$

$$(5.18)$$

where $i \in [i_{bIL}, i_{bIR} - 1]; \quad j \in [j_{bIL}, j_{bIR}]$.

Correct D_{yb}:

$$D_{yb}^n(i, j, k_{bIL}) = \ddot{D}_{yb}^n(i, j, k_{bIL}) - \frac{\Delta t_b}{\Delta z_b} \left(\Upsilon_1 \hat{H}_{xa}^{n-1}(i, j, k_{bIL}) + \Upsilon_2 \hat{H}_{xa}^n(i, j, k_{bIL}) \right),$$

$$D_{yb}^n(i, j, k_{bIR}) = \ddot{D}_{yb}^n(i, j, k_{bIR}) + \frac{\Delta t_b}{\Delta z_b} \left(\Upsilon_1 \hat{H}_{xa}^{n-1}(i, j, k_{bIR}) + \Upsilon_2 \hat{H}_{xa}^n(i, j, k_{bIR}) \right),$$

$$(5.19)$$

where $j \in [j_{bIL}, j_{bIR} - 1]; \quad i \in [i_{bIL}, i_{bIR}]$.

$$D_{yb}^n(i_{bIL}, j, k) = \ddot{D}_{yb}^n(i_{bIL}, j, k) + \frac{\Delta t_b}{\Delta x_b} \left(\Upsilon_1 \hat{H}_{za}^{n-1}(i_{bIL}, j, k) + \Upsilon_2 \hat{H}_{za}^n(i_{bIL}, j, k), \right),$$

$$D_{yb}^n(i_{bIR}, j, k) = \ddot{D}_{yb}^n(i_{bIR}, j, k) - \frac{\Delta t_b}{\Delta x_b} \left(\Upsilon_1 \hat{H}_{za}^{n-1}(i_{bIR}, j, k) + \Upsilon_2 \hat{H}_{za}^n(i_{bIR}, j, k) \right),$$

$$(5.20)$$

where $j \in [j_{bIL}, j_{bIR} - 1]; \quad k \in [k_{bIL}, k_{bIR}]$.

Correct D_{zb}:

$$D_{zb}^n(i_{bIL}, j, k) = \ddot{D}_{zb}^n(i_{bIL}, j, k) - \frac{\Delta t_b}{\Delta x_b} \left(\Upsilon_1 \hat{H}_{ya}^{n-1}(i_{bIL}, j, k) + \Upsilon_2 \hat{H}_{ya}^n(i_{bIL}, j, k) \right),$$

$$D_{zb}^n(i_{bIR}, j, k) = \ddot{D}_{zb}^n(i_{bIR}, j, k) + \frac{\Delta t_b}{\Delta x_b} \left(\Upsilon_1 \hat{H}_{ya}^{n-1}(i_{bIR}, j, k) + \Upsilon_2 \hat{H}_{ya}^n(i_{bIR}, j, k) \right),$$

$$(5.21)$$

where $k \in [k_{bIL}, k_{bIR} - 1]; \quad j \in [j_{bIL}, j_{bIR}]$.

$$D_{zb}^n(i, j_{bIL}, k) = \ddot{D}_{zb}^n(i, j_{bIL}, k) + \frac{\Delta t_b}{\Delta y_b} \left(\Upsilon_1 \hat{H}_{xa}^{n-1}(i, j_{bIL}, k) + \Upsilon_2 \hat{H}_{xa}^n(i, j_{bIL}, k) \right),$$

$$D_{zb}^n(i, j_{bIR}, k) = \ddot{D}_{zb}^n(i, j_{bIR}, k) - \frac{\Delta t_b}{\Delta y_b} \left(\Upsilon_1 \hat{H}_{xa}^{n-1}(i, j_{bIR}, k) + \Upsilon_2 \hat{H}_{xa}^n(i, j_{bIR}, k) \right),$$

$$(5.22)$$

where $k \in [k_{bIL}, k_{bIR} - 1]; \quad i \in [i_{bIL}, i_{bIR}]$.

Outer Surface

Also at the OS the auxiliary coefficient $\Gamma_{2a}(i, j, k)$ defined in (4.40) is substituted with the main grid temporal increment value Δt_a. OS influence equations are given below.

Correct D_{xa}:

$$D_{xa}^n(i, j, k_{aOL}) = \ddot{D}_{xa}^n(i, j, k_{aOL}) - \frac{\Delta t_a}{\Delta z_a} H_{yb}^n\left(i_b, j_b, k_{bOL} - \tfrac{r+1}{2}\right),$$

$$D_{xa}^n(i, j, k_{aOR}) = \ddot{D}_{xa}^n(i, j, k_{aOR}) + \frac{\Delta t_a}{\Delta z_a} H_{yb}^n\left(i_b, j_b, k_{bOR} + \tfrac{r-1}{2}\right),$$

(5.23)

where

$$i \in [i_{aOL}, i_{aOR} - 1], \qquad\qquad j \in [j_{aOL}, j_{aOR}],$$
$$i_b = i_{bOL} + r(i - i_{aOL}) + \tfrac{r-1}{2}, \qquad\qquad j_b = j_{bOL} + r(j - j_{aOL}).$$

$$D_{xa}^n(i, j_{aOL}, k) = \ddot{D}_{xa}^n(i, j_{aOL}, k) + \frac{\Delta t_a}{\Delta y_a} H_{zb}^n\left(i_b, j_{bOL} - \tfrac{r+1}{2}, k_b\right),$$

$$D_{xa}^n(i, j_{aOR}, k) = \ddot{D}_{xa}^n(i, j_{aOR}, k) - \frac{\Delta t_a}{\Delta y_a} H_{zb}^n\left(i_b, j_{bOR} + \tfrac{r-1}{2}, k_b\right),$$

(5.24)

where

$$i \in [i_{aOL}, i_{aOR} - 1], \qquad\qquad k \in [k_{aOL}, k_{aOR}],$$
$$i_b = i_{bOL} + r(i - i_{aOL}) + \tfrac{r-1}{2}, \qquad\qquad k_b = k_{bOL} + r(k - k_{aOL}).$$

Correct D_{ya}:

$$D_{ya}^n(i_{aOL}, j, k) = \ddot{D}_{ya}^n(i_{aOL}, j, k) - \frac{\Delta t_a}{\Delta x_a} H_{zb}^n\left(i_{bOL} - \tfrac{r+1}{2}, j_b, k_b\right),$$

$$D_{ya}^n(i_{aOR}, j, k) = \ddot{D}_{ya}^n(i_{aOR}, j, k) + \frac{\Delta t_a}{\Delta x_a} H_{zb}^n\left(i_{bOR} + \tfrac{r-1}{2}, j_b, k_b\right),$$

(5.25)

where

$$j \in [j_{aOL}, j_{aOR} - 1], \qquad\qquad k \in [k_{aOL}, k_{aOR}],$$

$$j_b = j_{bOL} + r(j - j_{aOL}) + \tfrac{r-1}{2}, \qquad k_b = k_{bOL} + r(k - k_{aOL}).$$

$$D_{ya}^n(i, j, k_{aOL}) = \ddot{D}_{ya}^n(i, j, k_{aOL}) + \frac{\Delta t_a}{\Delta z_a} H_{xb}^n\left(i_b, j_b, k_{bOL} - \tfrac{r+1}{2}\right),$$

$$(5.26)$$

$$D_{ya}^n(i, j, k_{aOR}) = \ddot{D}_{ya}^n(i, j, k_{aOR}) - \frac{\Delta t_a}{\Delta z_a} H_{xb}^n\left(i_b, j_b, k_{bOR} + \tfrac{r-1}{2}\right),$$

where

$$i \in [i_{aOL}, i_{aOR}], \qquad\qquad j \in [j_{aOL}, j_{aOR} - 1],$$
$$i_b = i_{bOL} + r(i - i_{aOL}), \qquad\qquad j_b = j_{bOL} + r(j - j_{aOL}) + \tfrac{r-1}{2}.$$

Correct D_{za}:

$$D_{za}^n(i, j_{aOL}, k) = \ddot{D}_{za}^n(i, j_{aOL}, k) - \frac{\Delta t_a}{\Delta y_a} H_{xb}^n\left(i_b, j_{bOL} - \tfrac{r+1}{2}, k_b\right),$$

$$(5.27)$$

$$D_{za}^n(i, j_{aOR}, k) = \ddot{D}_{za}^n(i, j_{aOR}, k) + \frac{\Delta t_a}{\Delta y_a} H_{xb}^n\left(i_b, j_{bOR} + \tfrac{r-1}{2}, k_b\right),$$

where

$$i \in [i_{aOL}, i_{aOR}], \qquad\qquad k \in [k_{aOL}, k_{aOR} - 1],$$
$$i_b = i_{bOL} + r(i - i_{aOL}), \qquad\qquad k_b = k_{bOL} + r(k - k_{aOL}) + \tfrac{r-1}{2}.$$

$$D_{za}^n(i_{aOL}, j, k) = \ddot{D}_{za}^n(i_{aOL}, j, k) + \frac{\Delta t_a}{\Delta x_a} H_{yb}^n\left(i_{bOL} - \tfrac{r+1}{2}, j_b, k_b\right),$$

$$(5.28)$$

$$D_{za}^n(i_{aOR}, j, k) = \ddot{D}_{za}^n(i_{aOR}, j, k) - \frac{\Delta t_a}{\Delta x_a} H_{yb}^n\left(i_{bOR} + \tfrac{r-1}{2}, j_b, k_b\right),$$

where

$$j \in [j_{aOL}, j_{aOR}], \qquad\qquad k \in [k_{aOL}, k_{aOR} - 1],$$
$$j_b = j_{bOL} + r(j - j_{aOL}), \qquad\qquad k_b = k_{bOL} + r(k - k_{aOL}) + \tfrac{r-1}{2}.$$

5.4.5   Absorbing Boundary Condition Calculation

According to practical experiments conducted by Bérenger [98–102] PML boundary condition slightly contributes to the HSG method's stability. Therefore, the dispersive HSG method applies the classical split PML [27, 141] to D and H components in both main and subgrids. As usual in the dispersive approach with ADE, the electric field components in the PML region have to be re-calculated straight after the calculation of D in the PML.

For the sake of brevity the mathematical formulation of split PML is not given in this work. Books by Bérenger [142] and Taflove [16] present the theory and practice of the PML application in extensive detail.

5.4.6   Calculation Order

This section illustrates the calculation order of the dispersive HSG method. Symbol "*" stands for the entire spatial domain. Right-directed horizontal arrow "$\longrightarrow$" marks the equivalent current injection at the IS or OS. Section number containing the relevant equations is given on each line of the algorithm. Horizontal line in the middle of the calculation order separates two symmetric parts of the dispersive HSG method. Parameters Υ_1, Υ_2 denote the temporal interpolation coefficients. These coefficients control the contribution of the adjacent main grid nodes to the temporally interpolated main grid value. Values of Υ_1, Υ_2 change depending on the subgrid time-step m. Parameters m_1, m_2 provide the half time-step shift between the electric and magnetic field components in the subgrid. Comments on the HSG method implementation with a single subgrid iterator m are also applicable to the dispersive HSG method implementation (see Section 4.7.7).

1. Calculate coefficients $\Phi_{1g}(*), \Phi_{2g}(*), \Phi_{3g}(*), \Phi_{4g}(*), \Phi_{5g}(*), Z_{1g}(*), Z_{2g}(*)$, where $g \in [a, b]$ (Sections 4.7.1 and 5.4.2)

2. Generate excitation source signal

3. Enter main grid time loop $n \in [1, n_{max}]$:

    (a) Re-arrange $D_a(*), E_a(*), \hat{H}_a(IS)$ (Sections 4.7.3 and 5.4.3 and (4.48))

    (b) Calculate $H_a(*)$ (Section 4.7.1)

    (c) Calculate $H_a(PML)$

(d) Calculate $\hat{H}_a\,(IS)$ (Figure 4.15)

(e) Re-arrange $D_b\,(*)$, $E_b\,(*)$ ((4.50) and (5.15))

(f) Calculate $D_b\,(*)$, $E_b\,(*)$ (Sections 4.7.2 and 5.4.1)

(g) Calculate $D_b\,(PML)$, $E_b\,(PML)$

(h) Calculate $\hat{H}_a\,(IS) \longrightarrow D_b\,(IS)$, $\Upsilon_1 = 1$, $\Upsilon_2 = 0$ (Section 5.4.4)

(i) Re-calculate $E_b\,(IS)$ (Section 4.7.2)

(j) Enter subgrid time loop 1: $m \in [1, \frac{r-1}{2}]$ and $m_1 = m + \frac{r-1}{2}$

    i. Calculate $H_b\,(*)$ (Section 4.7.1)

    ii. Calculate $H_b\,(PML)$

    iii. Calculate $\hat{E}_a\,(IS) \longrightarrow H_b\,(IS)$, $\Upsilon_1 = \frac{r-m}{r}$, $\Upsilon_2 = \frac{m}{r}$ ((4.97))

    iv. Re-arrange $D_b\,(*)$, $E_b\,(*)$ ((4.50) and (5.15))

    v. Calculate $D_b\,(*)$, $E_b\,(*)$ (Sections 4.7.2 and 5.4.1)

    vi. Calculate $D_b\,(PML)$, $E_b\,(PML)$

    vii. Calculate $\hat{H}_a\,(IS) \longrightarrow D_b\,(IS)$, $\Upsilon_1 = \frac{r-m_1}{r}$, $\Upsilon_2 = \frac{m_1}{r}$ (Section 5.4.4)

    viii. Re-calculate $E_b\,(IS)$ (Section 4.7.2)

(k) Calculate $E_b\,(OS) \longrightarrow H_a\,(OS)$ ((4.109))

(l) Calculate $D_a\,(*)$, $E_a\,(*)$ (Sections 4.7.2 and 5.4.1)

(m) Calculate $D_a\,(PML)$, $E_a\,(PML)$

(n) Calculate $E_a\,(src)$ ((4.44))

(o) Re-arrange $\hat{E}_a\,(IS)$ ((4.48))

(p) Calculate $\hat{E}_a\,(IS)$ (Table 4.1)

(q) Calculate $H_b\,(*)$ (Section 4.7.1)

(r) Calculate $H_b\,(PML)$

(s) Calculate $\hat{E}_a\,(IS) \longrightarrow H_b\,(IS)$, $\Upsilon_1 = 1$, $\Upsilon_2 = 0$ ((4.97))

(t) Enter fine grid time loop 2: $m \in [\frac{r+1}{2}, r]$ and $m_2 = m - \frac{r-1}{2}$

    i. Re-arrange $D_b\,(*)$, $E_b\,(*)$ ((4.50) and (5.15))

    ii. Calculate $D_b\,(*)$, $E_b\,(*)$ (Sections 4.7.2 and 5.4.1)

    iii. Calculate $D_b\,(PML)$, $E_b\,(PML)$

    iv. Calculate $\hat{H}_a(IS) \longrightarrow D_b(IS)$, $\Upsilon_1 = \frac{r-m_2}{r}$, $\Upsilon_2 = \frac{m_2}{r}$ (Section 5.4.4)

    v. Re-calculate $E_b(IS)$ (Section 4.7.2)

    vi. Calculate $H_b(*)$ (Section 4.7.1)

    vii. Calculate $H_b(PML)$

    viii. Calculate $\hat{E}_a(IS) \longrightarrow H_b(IS)$, $\Upsilon_1 = \frac{r-m}{r}$, $\Upsilon_2 = \frac{m}{r}$ ((4.97))

  (u) Calculate $H_b(OS) \longrightarrow D_a(OS)$ ((5.22))

  (v) Re-calculate $E_a(OS)$ (Section 4.7.2)

  (w) Output $E_a(*)$, $H_a(*)$

  (x) Output $E_b(*)$, $H_b(*)$

4. Finalise simulation

Chapter 6

Numerical Results

This chapter presents numerical simulation results of the dispersive HSG method. Five major testing scenarios with artificial material placement verify correct method's behaviour in the Debye media. One realistic test case shows the wave propagation inside of human torso. Finally, Section 6.14 gives the details of the HSG memory and CPU time consumption.

6.1   Simulation Settings

In context of this work the words "coarse" and "fine" grids refer to the all coarse and all fine FDTD grids, while words "main" and "subgrid" refer to the main and subgrid regions of the HSG. Abbreviations FDTD and HSG refer to the Finite-Difference Time-Domain and the Huygens Subgridding methods. Split Perfectly Matched Layer (PML) bounds the simulation domain [27, 141]. PML thickness of 10 and 6 points is used for the main and subgrids, unless stated otherwise. Table 6.1 lists the simulation settings. Columns "HSG" and "Fine" show settings specific to the HSG and the all fine grid reference.

The following notation is used in Table 6.1: symbols ni, nj and nk denote the computation domain ranges in x, y and z directions, t_{max} shows the maximum amount of time steps and r stands for the subgridding ratio. Parameters OL and OR specify the location of the Outer Huygens Surface (OS), where OL sets the minimum (leftmost) point and OR sets the maximum (rightmost) point in x, y and z directions. The Inner Huygens Surface (IS) is defined in an identical manner by parameters IL and IR, where IL and IR denote the minimum and maximum points in x, y and z axes respectively. Parameter $zone_b$, given in subgrid points, specifies the buffer

147

Parameter	HSG	Fine
ni, nj, nk	$1 \sim 80$	$1 \sim 400$
t_{max}	2000	10000
r	5	
OL	29, 29, 29	
IL	32, 32, 32	
IR	48, 48, 48	
OR	51, 51, 51	
$zone_b$	5	
n_{pml_a}	10	
n_{pml_b}	6	
source type	soft	soft
source location	15, 40, 40	75, 200, 200
Δs_a	10 mm	–
Δs_b	2 mm	2 mm
Δt_a	0.179 ps	–
Δt_b	3.582 ps	3.582 ps
N_{CFL}	0.93	0.93
χ_a	5	–
χ_b	25	25

Table 6.1: Simulation settings

zone thickness in between the OS and the beginning of PML in the subgrid. PML thickness in the main and subgrids is denoted by n_{pml_a} and n_{pml_b} and is measured in main and subgrid points respectively. Rows "source type" and "location" list the excitation source type [143] and location in the x, y and z coordinates. Spatial and temporal increments in the main and subgrids are given by $\Delta s_a, \Delta s_b$ and $\Delta t_a, \Delta t_b$. Parameter N_{CFL} specifies the value of the Courant-Friedrichs-Lewy number. Values χ_a and χ_b denote the spatial resolution of the main and subgrids (see Section 6.3 for more details on spatial resolution).

In this work a Gaussian pulse, formed according to (6.1), serves as the excitation wave form:

$$J_z^t = \exp\left[-\left(\frac{t - 3T}{T} \right)^2 \right],$$ (6.1)

where

$$T = \frac{1}{2 f_{max}}, \quad f_{max} = 6 \cdot 10^9 \text{ Hz}.$$

J_z^t is the z component of the current density at time moment t, T is the period of pulse fluctuation and f_{max} is the maximum wave frequency. Figures 6.1a and 6.1b depict the excitation wave form in time and frequency domains. Signal is the collection of electric field amplitude values measured during the simulation time at the given observation location. Title of each plot in this work contains the information on the excitation waveform, boundary condition and its thickness, propagation environment and object material, e.g. title of Figure 6.1a signifies that Gaussian pulse was used as the excitation waveform, PML of thickness 10 in main and 6 in subgrid terminated the simulation domain. Propagation environment was set to Air with the Fat object. When referred to propagation environment material or a tissue description first letter of the word is capitalised, as in Air, Skin, Fat, Bone, Muscle and Heart. Notions of weak and strong Debye media used in this work relate to the Debye materials with low and high electric conductivity, e.g. Fat and Bone are weak, whereas Skin, Muscle and Heart are strong Debye media.

Human body tissue parameters for the Debye relaxation model fitted for the high frequency region of 100 MHz to 6 GHz are listed in Table 6.2. Symbols σ, ε_s and ε_∞ denote the electric conductivity, and relative static and optical permittivities, respectively. Parameter τ specifies the dipole relaxation time in molecules.

(a) Time domain. $T_{xa} = 15$
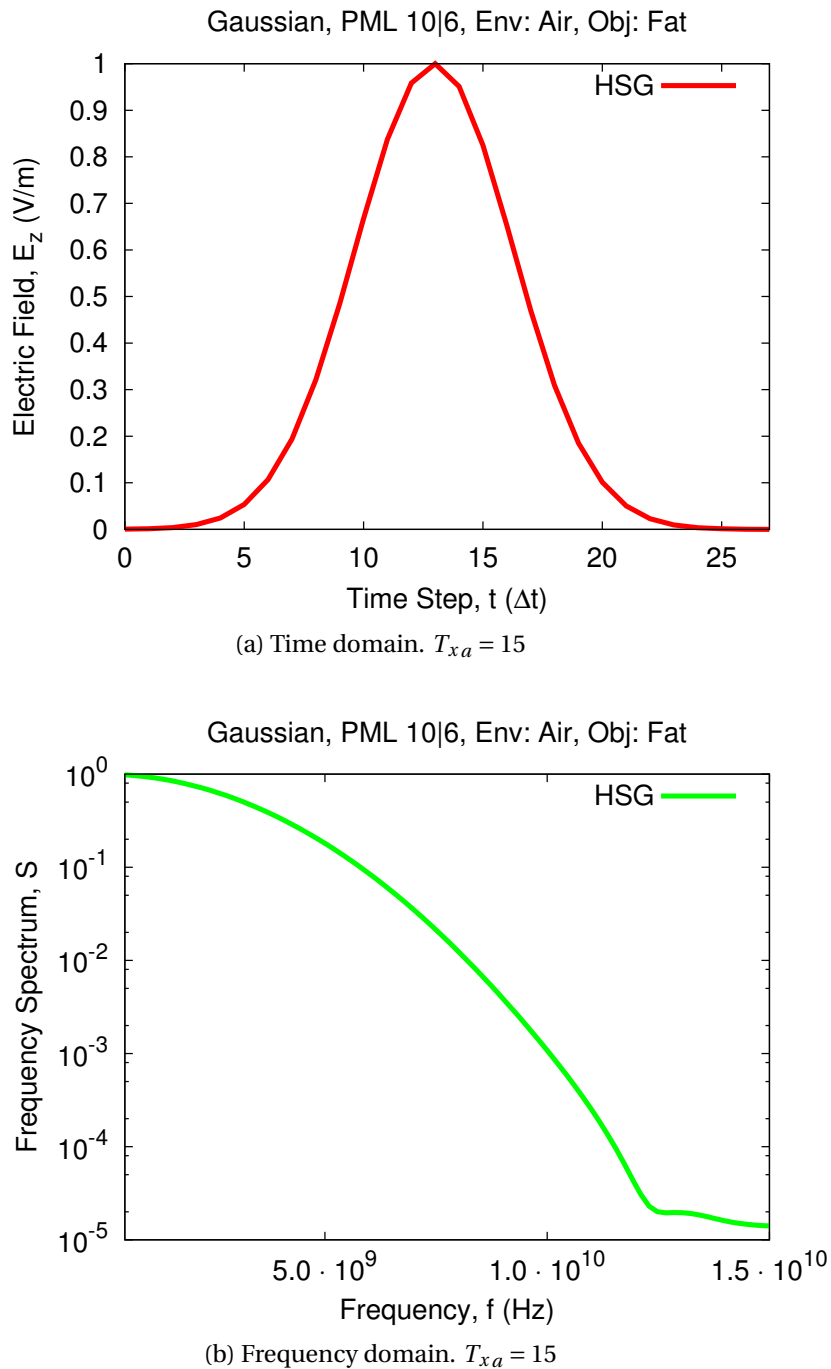

(b) Frequency domain. $T_{xa} = 15$

Figure 6.1: Initial Gaussian pulse signal at excitation location in Air. Ordinate shows normalised values in both time and frequency domain plots.

Japanese researchers from the RIKEN centre[1] segmented each human body tissue within a high resolution MRI data and assigned a material code to each tissue. The digital human phantom and the mapping of material codes to human body tissues was kindly provided by RIKEN. Material codes are listed in the first column of Table 6.2. José Manuel Padilla González[2] and Aleksandr Kudasev[3] obtained the media parameters for the one pole Debye relaxation model from the four pole Cole–Cole parameters [33] using the Newton–Raphson data fitting technique [144].

Code	Parameter	σ [S/m]	ε_s	ε_∞	τ [ps]
0	Air	0.000	1.000	1.000	0.000
1	Cerebral Cortex	0.595	56.444	33.057	0.352
2	White Matter	0.348	41.281	24.371	0.336
3	Cerebellum	0.826	58.155	35.195	0.683
4	Midbrain	0.348	41.281	24.371	0.336
5	Eyeball	1.445	67.711	10.308	8.271
6	Optic Nerve	0.360	34.749	20.980	0.365
7	Cornea	1.069	57.842	32.372	0.288
8	Crystalline Lens	0.346	37.825	18.283	0.211
9	Pituitary Gland	0.809	60.543	27.708	0.177
10	Thalamus	0.595	56.444	33.057	0.352
11	Hypothalamus	0.595	56.444	33.057	0.352
12	Pineal Gland	0.809	60.543	27.708	0.177
13	Tongue	0.693	56.523	28.257	0.205
14	Cerebrospinal Fluid	2.144	70.400	33.148	0.182
15	Adrenal Gland, Right	0.809	60.543	27.708	0.177
16	Urinary Bladder	0.300	19.331	9.675	0.208
18	Large Intestine	0.716	61.121	34.665	0.312
20	Duodenum	0.919	66.279	31.503	0.190
21	Esophagus	0.919	66.279	31.503	0.190
23	Gall Bladder	1.042	60.735	28.181	0.159

[1]Advanced Center for Computing and Communication, Integrated Simulation of Living Matter Group, RIKEN, Japan, himeno@riken.jp

[2]School of Engineering, The University of Seville, Spain, jospadgon@alum.us.es

[3]School of Computer Science, The University of Manchester, United Kingdom, aleksandr.kudasev@student.manchester.ac.uk

Code	Parameter	σ [S/m]	ε_s	ε_∞	τ [ps]
24	Heart	1.019	63.549	34.910	0.289
25	Kidney, Right	0.857	67.508	39.860	0.606
26	Liver	0.520	50.153	27.986	0.357
27	Lung, Right	0.452	38.254	21.436	0.274
29	Pancreas	0.809	60.543	27.708	0.177
30	Prostate Gland	0.809	60.543	27.708	0.177
31	Small Intestine	1.701	65.790	39.191	0.459
32	Spleen	0.844	62.585	37.115	0.427
33	Stomach	0.919	66.279	31.503	0.190
37	Nasal Cavity	0.000	1.000	1.000	0.000
38	Thyroid Gland	0.809	60.551	27.734	0.177
39	Trachea	0.565	43.185	22.140	0.225
45	Bone	0.104	14.169	7.363	0.341
48	Fat	0.037	5.531	3.998	0.236
49	Muscle	0.747	56.932	28.001	0.187
51	Skin	0.541	47.930	29.851	0.436
55	Diaphragm	0.747	56.931	28.001	0.187
56	Seminal Vesicle	0.809	60.543	27.708	0.177
57	Erectile Tissue	1.256	62.900	30.598	0.210
80	Spinal Cord	0.360	34.749	20.980	0.365
82	Paranasal Sinus	0.000	1.000	1.000	0.000
83	Testicle	0.934	62.064	31.306	0.211
84	Kidney, Left	0.857	67.508	39.860	0.606
85	Lung, Left	0.452	38.254	21.436	0.274
86	Epiglottis	0.493	44.559	19.392	0.300
87	Oral Cavity	0.000	1.000	1.000	0.000
88	External Ear	0.000	1.000	1.000	0.000
89	Salivary Gland	0.809	60.543	27.708	0.177
90	Middle Ear	0.055	7.318	3.962	0.377
91	Inner Ear	2.144	70.400	33.148	0.182
92	Pharynx	0.565	43.185	22.140	0.225
94	Adrenal Gland, Left	0.809	60.543	27.708	0.177

Table 6.2: Media parameters for Debye relaxation model, all materials

6.2   Testing Scenarios Overview

For the majority of test cases the signal is shown in both time and frequency domains for a number of observation points placed along the central line $y_a = z_a = 40$. The main reason in illustrating multiple observation points is educational. Tracking the HSG signal at various locations will provide a better understanding and overview of the HSG accuracy relative to the all fine and all coarse grid FD–FDTD results.

Scenarios 1 to 4 present the basic HSG accuracy tests. Scenario 1 illustrates correct HSG behaviour with the OS–IS interface in the Air and strong and weak Debye media in the subgrid. Scenario 1 is equivalent to non-dispersive HSG tests reported in [102]. A homogeneous Debye medium covers the OS–IS interface in Scenario 2, while the excitation source is placed in the main grid. Scenario 3 presents a more sophisticated case with two different Debye media: one filling the OS–IS region and the other occupying the subgrid. Results with the excitation locations in the main and in the subgrid are reported. Scenario 4 offers the data from the HSG simulation with four distinct Debye media surrounding the subgrid region.

Scenario 5 tests the effect of electric conductivity σ on the visibility of the HSG instability. Two realistic scenarios with a human torso in the main and human heart in the subgrid conclude the HSG accuracy verification. Finally, the HSG computational efficiency in terms of memory and execution time is measured and reported in Section 6.14.

6.3   Setting of Spatial Resolution

This section illustrates the process of the spatial resolution calculation. Formulae for the frequency threshold and the spatial resolution are given in Section 6.3.1. Spatial resolution values for Scenarios 1 to 4 are calculated in Section 6.3.1 and for Scenario of human torso—in Section 6.3.2.

6.3.1   Scenarios 1 to 4

The frequency spectrum threshold value $S_{dB} = -20$ dB is chosen for Scenarios 1 to 4. The spectrum threshold value S_{dB} is calculated as:

$$S_{dB} = 20\log_{10}(S),\tag{6.2}$$

where S denotes the frequency spectrum.[4] From (6.2) the frequency spectrum value S at the spectrum threshold S_{dB} can be obtained as:

$$S = 10^{S_{dB}/20}$$ (6.3)

Substituting selected spectrum threshold of -20 dB into (6.3) yields the spectrum value $S = 0.1$.

   According to the excitation signal plot in Figure 6.1b the wave frequency equals to 6 GHz at the normalised frequency spectrum value of 0.1. This frequency will be chosen as the highest frequency of interest for Scenarios 1 to 4.

   The spatial resolution (number of elements per wavelength) of all coarse and all fine grid cases in the Air is calculated according to the following formula:

$$\chi = \frac{\lambda}{\Delta s} = \frac{c}{f_w \Delta s},$$ (6.4)

where

$$\lambda = \frac{c}{f_w}.$$ (6.5)

Symbols χ, λ, Δs, c, f_w in (6.4) and (6.5) denote the spatial resolution, wavelength, spatial discretisation step, speed of light in Air and the highest wave frequency respectively.

   The all coarse and all fine grid resolutions at the spectrum threshold of -20 dB are calculated by substituting $\Delta s_a = 10$ mm, $\Delta s_b = 2$ mm and $f_w = 6$ GHz into (6.4). The resolution values for Scenarios 1 to 4 shown in the two last rows of Table 6.1 are $\chi_a = 5$ and $\chi_b = 25$ elements per wavelength.

6.3.2   Scenario of Human Torso

Using the same frequency spectrum threshold as in Scenarios 1 to 4 $S_{dB} = -20$dB leads to the same frequency spectrum value of 0.1 and the same highest wave frequency of 6 GHz. The frequency spectrum $S = 0.1$ is obtained by substituting $S_{dB} = -20$ dB into (6.3).

   Figure 6.2 shows the initial excitation source signal in Scenario of human torso. According to Figure 6.2b the wave frequency equals to 6 GHz at the frequency spectrum of 0.1.

---

[4]In case power spectrum P is used in place of frequency spectrum S, the power spectrum threshold is calculated as $P_{dB} = 10\log_{10}(P)$.

(a) Time domain. $T_{xa} = 15$

(b) Frequency domain. $T_{xa} = 15$
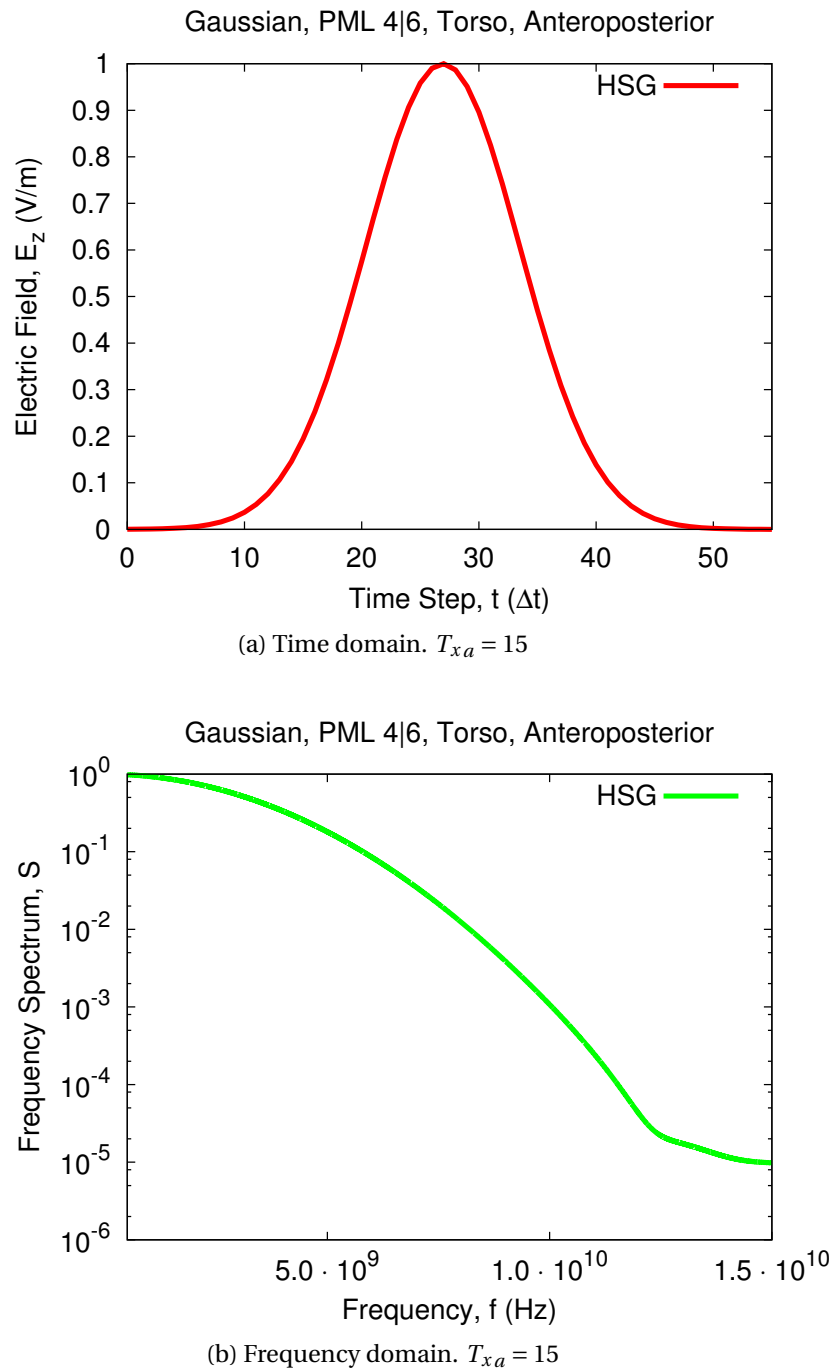
Figure 6.2: Initial Gaussian pulse signal at excitation location in Air, human torso. Ordinate shows normalised values in both time and frequency domain plots.

The all coarse and all fine grid resolutions at the spectrum threshold of -20 dB are calculated with (6.4) using the spatial discretisation steps $\Delta s_a = 5$ mm, $\Delta s_b = 1$ mm and the wave frequency $f_w = 6$ GHz. The all coarse and all fine grid resolution values $\chi_a =$ and $\chi_b =$ are listed in the last two rows of Table 6.5.

6.4   Scenario 1. HSG in Air

6.4.1   Scenario Setting

Testing Scenarios 1a and 1b show the signal propagation in the non-dispersive HSG method. The aims of these scenarios are (i) to remind the reader of the HSG behaviour in frequency-independent environments and (ii) illustrate the effect of excitation source placement on the visibility of the HSG instability. Figure 6.3 shows a 2D cross-section of Scenario 1a setting. Scenario 1b is identical with the only difference in placement of the excitation and observation points. In Scenario 1b the excitation source T_{xa} is located in the middle of the subgrid at $x_a = 40$ and the observation point R_{xa} at $x_a = 15$.

In Scenario 1a the excitation T_{xa} is placed in the main grid in the Air environment at $x_a = 15$, while in Scenario 1b the excitation is located in the middle of the subgrid in the Fat environment at $x_a = 40$. Excitation in the Air allows the high frequency components to reach the HSG interface and cause spurious frequency. The cut-off frequency of Air in the main grid is 10.073 GHz and in the subgrid is 50.367 GHz. Excitation signal in the main grid contains frequencies up to 6 GHz, therefore all major signal components reach the subgridding interface.

In case of excitation source in the Fat the high frequency components are partially absorbed by the Fat medium. By the time the propagating signal reaches the HSG interface some of the high frequency has vanished and less spurious signals are produced at the interface. The cut-off frequency of Fat in the subgrid is 21.888 GHz and in the main grid is 4.378 GHz.

Therefore, it is expected to observe an HSG instability later in Scenario 1b with the excitation located in the Fat in the subgrid, compared to Scenario 1a with the excitation placed in the Air in the main grid.
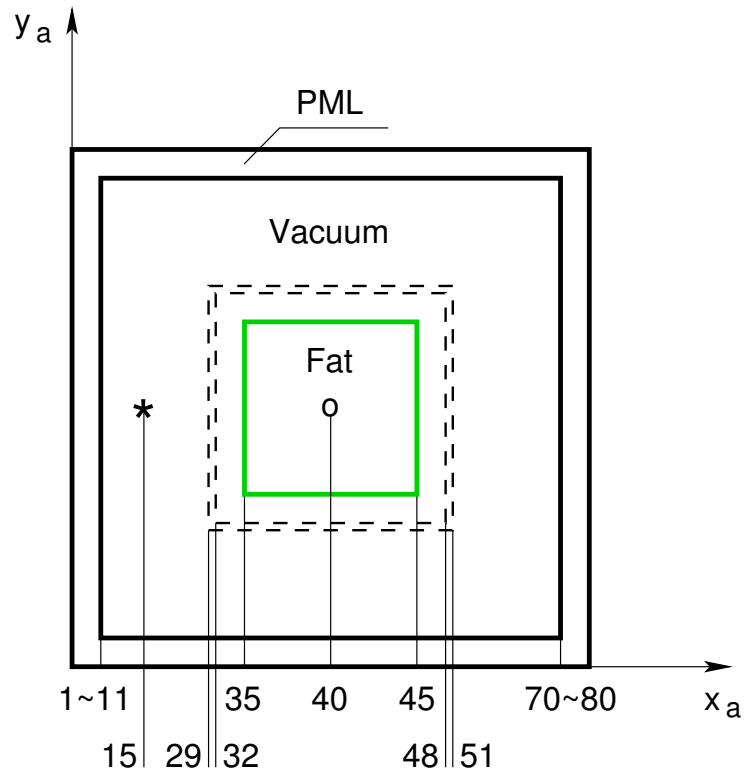
Figure 6.3: Cross-section of Scenario 1a setting, plane $z_a = 40$. Dotted lines denote the Outer and Inner Huygens Surfaces (OS, IS). Symbols "*" and "o" mark the excitation and observation locations respectively. Symbol "~" specifies an inclusive range with integer stepping as in $x_a \in [1, 11]$. Fat object in Air environment. Fat occupies the entire Inner Box. Inner Box is a subgrid region bound by the IS excluding a minimum separation of $3\Delta s_a$ between the IS and the Inner Box in all coordinate directions x, y, z. The Inner Box cross-section is shown in green colour. OS, IS are placed in the Air. Scenario 1a is symmetric relative to the centre line. Cross-section at plane $y_a = 40$ is the same as presented here.

6.4.2   Time Domain Signal

Figures 6.4a and 6.4b show the signal in time domain after it has travelled an equal distance of $25\Delta s_a$ in Scenarios 1a and 1b. When the source is placed in the main grid in non-dispersive medium (Scenario 1a) the instability in HSG is visible 400 time-steps earlier, than when the source is located in the subgrid in dispersive medium (Scenario 1b). Compare Figure 6.4a with $t_{inst} = 1100$ and Figure 6.4b with $t_{inst} = 1500$, where t_{inst} denotes the time when the instability becomes visible. The value of t_{inst} is taken from the signal plots. It signifies the time moment at which the minor amplitude fluctuations become visible in the plot.

Figure 6.4c shows the time domain signal of Scenario 1b measured in a simulation with 10^5 main grid iterations. Figure 6.4c indicates that instability in HSG with the source placed inside of a dispersive medium becomes visible at a much later time. At time $t_a = 4000$ the instability will overtake the maximum amplitude of the original signal.

6.5   Scenario 2a.
HSG in Homogeneous Strong Debye Medium

Scenarios described in this section illustrate the HSG accuracy, when the OS–IS interface is covered by a homogeneous Debye medium and the excitation source is positioned in the main grid.

6.5.1   Scenario Setting

Purpose of Scenario 2a is to show the signal propagation modelled with HSG when the OS–IS interface is covered by a strong Debye medium. It is expected that native HSG instabilities occurring at the interface will be suppressed by a strong dispersive medium. Figure 6.5 depicts a 2D cross-section of Scenario 2a setting. Excitation source is placed at $T_{xa} = 15$ and two observation points $R_{xa} = 27, 40$ are located at the centre line $y_a = z_a = 40$.

6.5.2   Time Domain Signal

Figure 6.6 depicts the signal in time domain at two observation locations $R_{xa} = 27, 40$. In the simulation domain where $x_a \in [25, 55]$ the wave propagates inside the
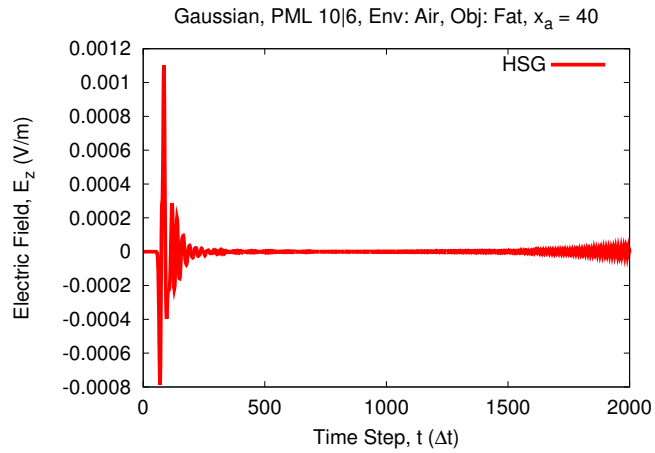
(a) Scenario 1a. $T_{xa} = 15$, $R_{xa} = 40$
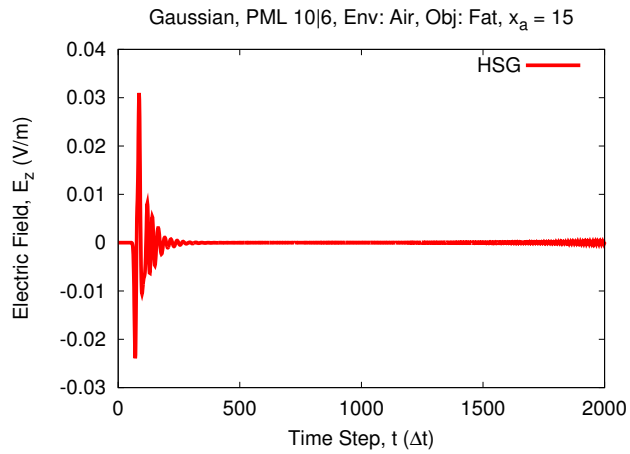
(b) Scenario 1b. $T_{xa} = 40$, $R_{xa} = 15$, $t_{max} = 2000$
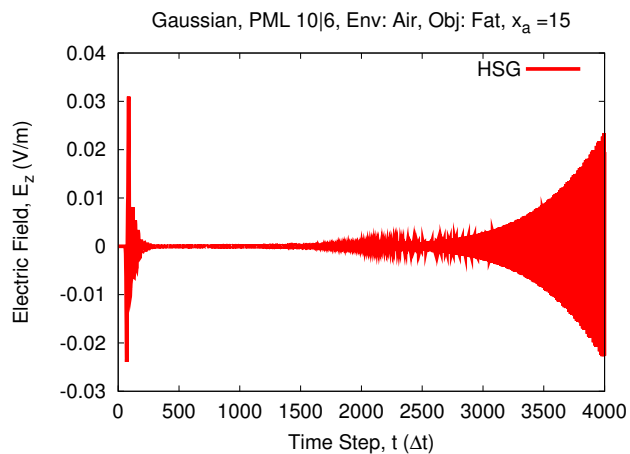
(c) Scenario 1b. $T_{xa} = 40$, $R_{xa} = 15$, $t_{max} = 10000$

Figure 6.4: Time domain signal of Scenarios 1a and 1b. HSG instability is visible at a later time with the excitation source in Fat medium in the subgrid region.
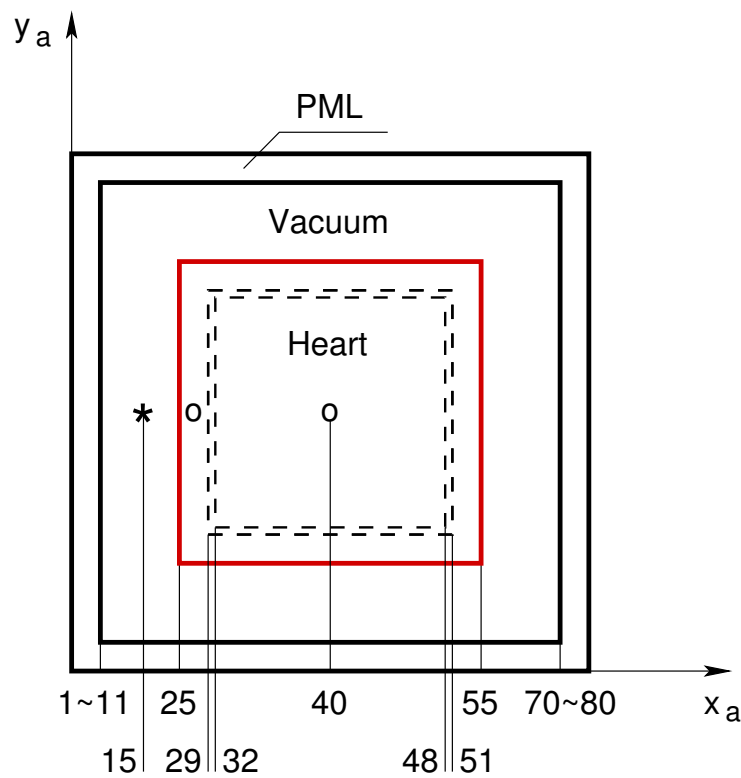
Figure 6.5: Cross-section of Scenario 2a setting, plane $z_a = 40$. Heart object in Air environment. Heart occupies part of the main grid and the entire Inner Box. OS, IS are placed in the Heart. Scenario 2a is symmetric relative to the centre line. Cross-section at plane $y_a = 40$ is the same as presented here.

Heart. Electric field amplitude decays rapidly in this region due to high electric conductivity of the Heart. In Figure 6.6a the HSG signal curve tends to follow the coarse grid signal more than the fine grid. This is explained by the observation point location already inside the Heart, but still in the main grid. Insufficient main grid resolution combined with the high conductivity of Heart results in the HSG signal following the coarse grid curve. At central point in the subgrid Figure 6.6b shows the amplitude values in the order of $10.^{-6}$ Electric field amplitude was reduced 100 times in comparison to the observation point $R_{xa} = 27$. Higher spatio-temporal resolution of the subgrid allows to reduce the discrepancy between the HSG and the fine grid curves. No sign of instability is visible in HSG throughout the total simulation time of $t_{max} = 2000$ time steps.

6.5.3 Frequency Domain Signal

Figures 6.7a and 6.7b show the signal propagation of Scenario 2a in frequency domain. Frequency domain plots were obtained with the Discrete Fourier Transform (DFT) program,[5] developed by Dr Arnaud Thiry. Entire range of the time domain data with $t_a \in [1, 2000]$ was used for the frequency domain data production.

Transferable frequency range used in the frequency domain plots analysis is the range of frequencies, from minimum to maximum, easily transferred by the simulation. The minimum transferable frequency bound is assumed to be 500 MHz. The maximum value limiting the transferable frequency range is taken from the signal plots at the cavity where the curve abruptly changes its inclination, e.g. 5 GHz in Figure 6.7a and 1.3 GHz in Figure 6.7b in case of HSG curve.

A large difference in the transferable frequency range exists between the HSG and fine grid signals at points $x_a = 27, 40$ (Figures 6.7a and 6.7b). The main grid is unable to transfer as much high frequency component as the fine grid reference. By the time the HSG signal reaches the higher resolution subgrid there is little high frequency component left to be transferred. Therefore, a notable difference between the HSG and the fine grid curves is present.

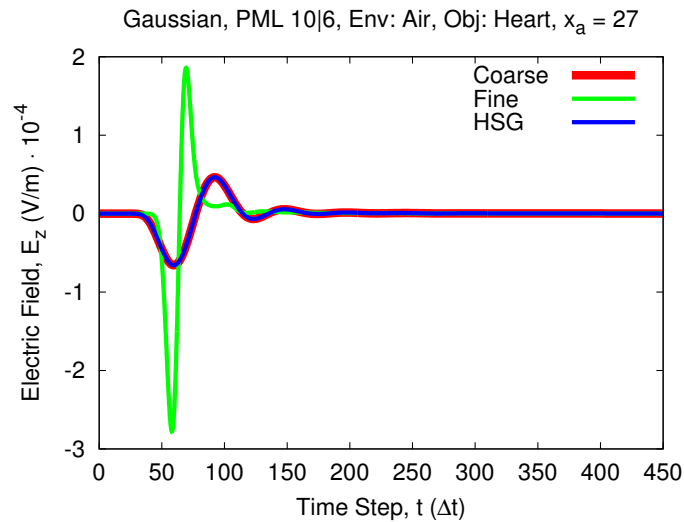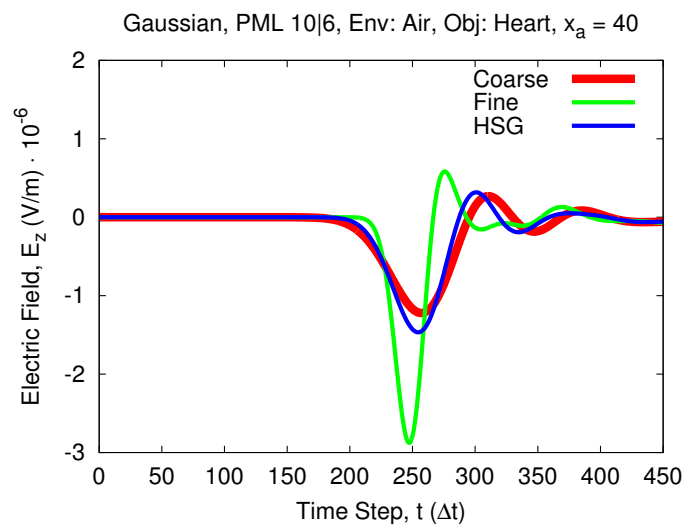[5]This program relies on the FFTW library [145].

(a) Scenario 2a. $T_{xa} = 15$, $R_{xa} = 27$

(b) Scenario 2a. $T_{xa} = 15$, $R_{xa} = 40$

Figure 6.6: Time domain signal of Scenario 2a. Due to high conductivity of the Heart the signal amplitudes are strongly reduced. HSG signal follows the coarse grid because the majority of high frequency components were lost during the propagation in the Heart in the main grid.
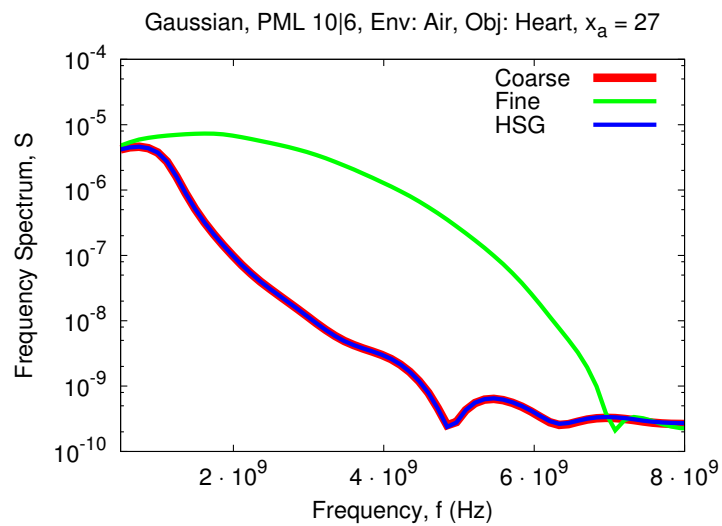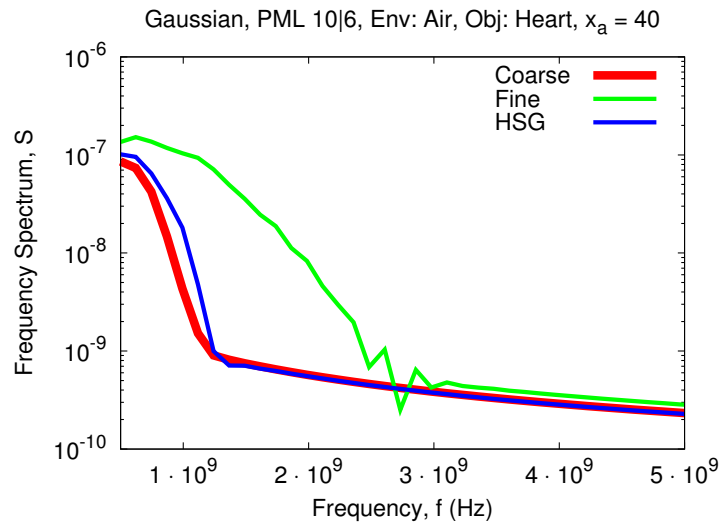
(a) Scenario 2a. $T_{xa} = 15$, $R_{xa} = 27$

(b) Scenario 2a. $T_{xa} = 15$, $R_{xa} = 40$

Figure 6.7: Frequency domain signal of Scenario 2a. Strong Debye medium crossing OS–IS interface absorbs high frequency components of the HSG signal.

6.6   Scenario 2b.

HSG in Homogeneous Weak Debye Medium

6.6.1   Scenario Setting

Purpose of Scenario 2b is to show the signal propagation modelled with HSG when the OS–IS interface is covered by a weak Debye medium. Comparison of Scenario 2a with Scenario 2b illustrates the effect of Debye medium strength onto the visibility of HSG instability. Figure 6.8 depicts a 2D cross-section of Scenario 2b setting. Excitation source is placed at $T_{xa} = 15$ and two observation points $R_{xa} = 27, 40$ are located at the centre line $y_a = z_a = 40$. In comparison with Scenario 2a, it is anticipated that the HSG curve will match the fine grid reference more closely, because the Fat medium absorbs less high frequency components than the Heart.
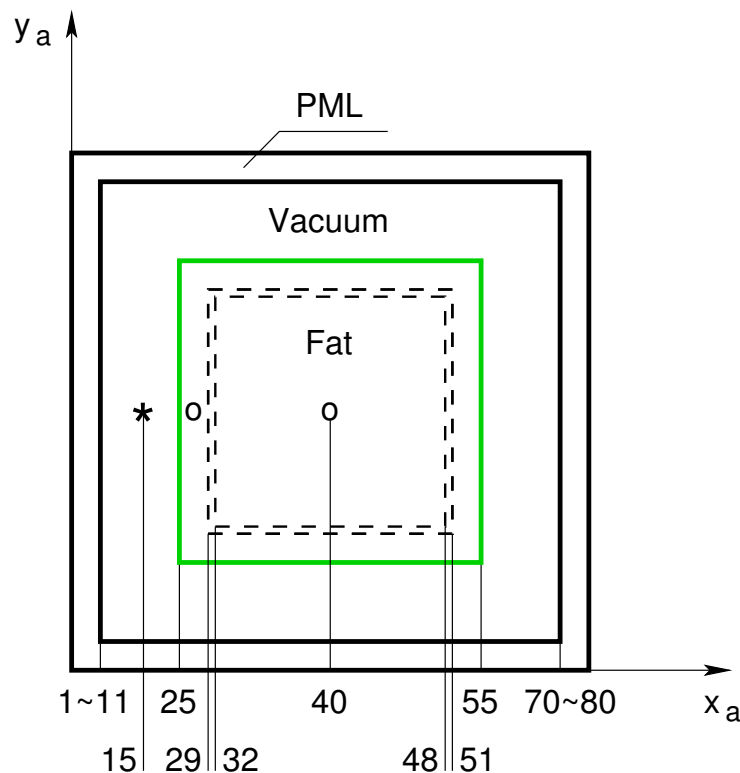
Figure 6.8: Cross-section of Scenario 2b setting, plane $z_a = 40$. Fat object in Air environment. Fat occupies part of the main grid and the entire Inner Box. OS, IS are placed in the Fat. Scenario 2b is symmetric relative to the centre line. Cross-section at plane $y_a = 40$ is the same as presented here.

6.6.2   Time Domain Signal

Figures 6.9a and 6.9b illustrate the signal propagation inside the Fat medium. Compared to the same positions in the Heart medium (Figures 6.6a and 6.6b) the discrepancy between the HSG and the fine grid reference curve is much smaller in Scenario 2b. This is due to the lower electric conductivity of Fat, which can be confirmed by observing the middle point $x_a = 40$ inside of the subgrid. Strong Debye medium in the main grid of Scenario 2a absorbs the majority of high frequency components. By the time the signal enters a high resolution subgrid there is little frequency components to benefit from the high subgrid resolution. On the contrary weak Debye medium in the main grid of Scenario 2b absorbs only a minor part of high frequency components. Therefore, a large amount of high frequency reaches the subgrid region and benefits from high spatio-temporal resolution. In a strong Debye medium (Scenario 2a) the electric field amplitudes are 100 times smaller than in a weak medium (Scenario 2b): 10^{-6} versus 10^{-4}. Since the OS–IS interface is positioned in the frequency dependent Fat medium no sign of HSG instability is visible throughout the entire simulation time of $t_{max} = 2000$.

6.6.3   Frequency Domain Signal

Similar observation holds in the frequency domain—inside of the Fat medium (Figures 6.10a and 6.10b) the HSG curve parts with the fine grid reference approximately at the frequency of 3 GHz. On the contrary in the strong Debye medium of Scenario 2a (Figures 6.7a and 6.7b) the curves part each other at approximately 1 GHz or lower.

6.7   Scenario 3a. HSG in Inhomogeneous Debye Media

6.7.1   Scenario Setting

Purpose of Scenario 3a is to present a more sophisticated scenario setting, that consists of two dispersive media: weak—Fat and strong—Heart. Figure 6.11 depicts a 2D cross-section of Scenario 3a setting. Excitation source is placed at $T_{xa} = 15$ and two observation points $R_{xa} = 27, 40$ are located at the centre line $y_a = z_a = 40$.
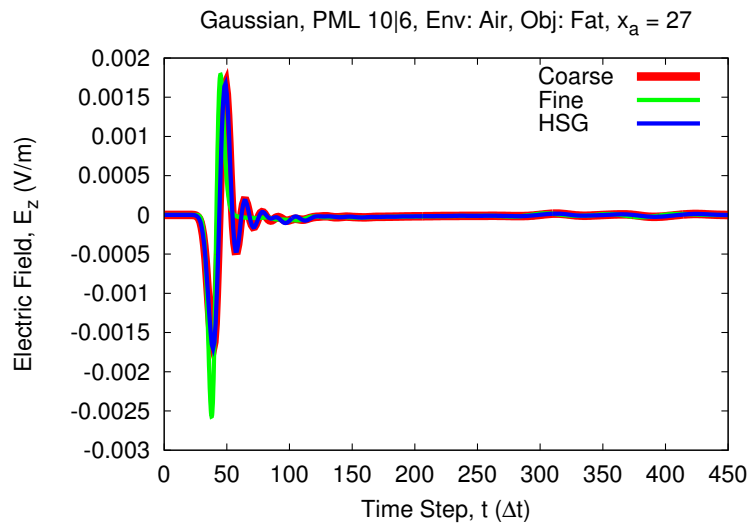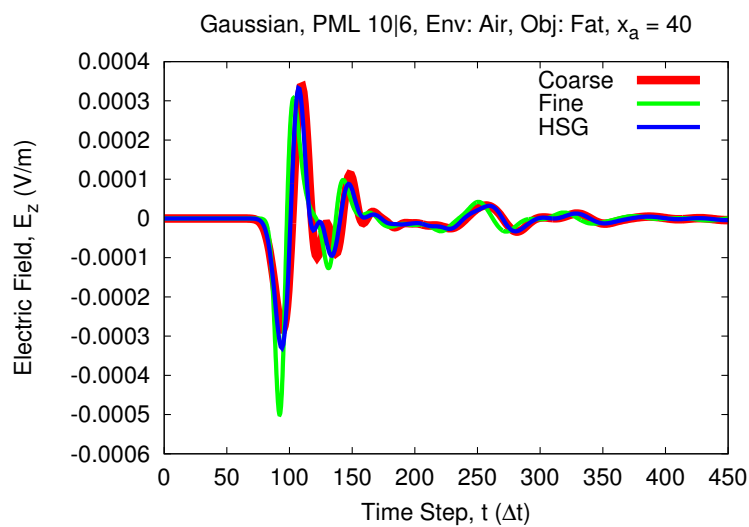
(a) Scenario 2b. $T_{xa} = 15$, $R_{xa} = 27$

(b) Scenario 2b. $T_{xa} = 15$, $R_{xa} = 40$

Figure 6.9: Time domain signal of Scenario 2b. Weak Debye medium crossing OS–IS interface absorbs low amount of high frequency components. HSG signal in the subgrid is an average of the coarse and fine grid signals.
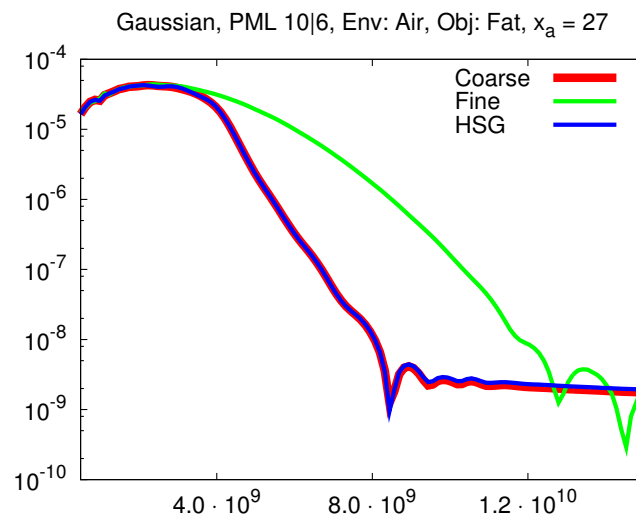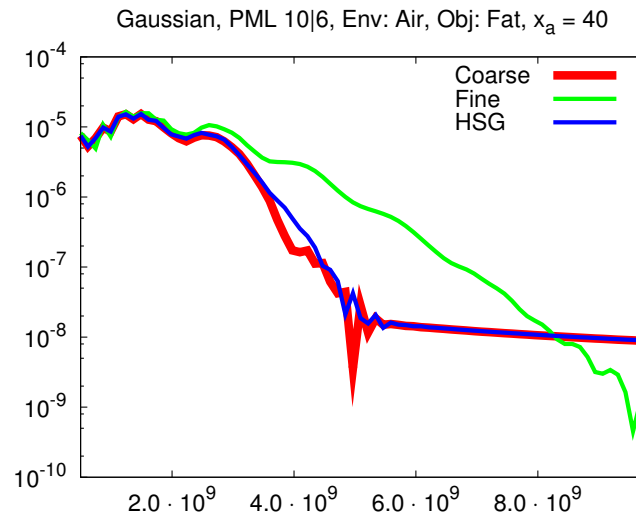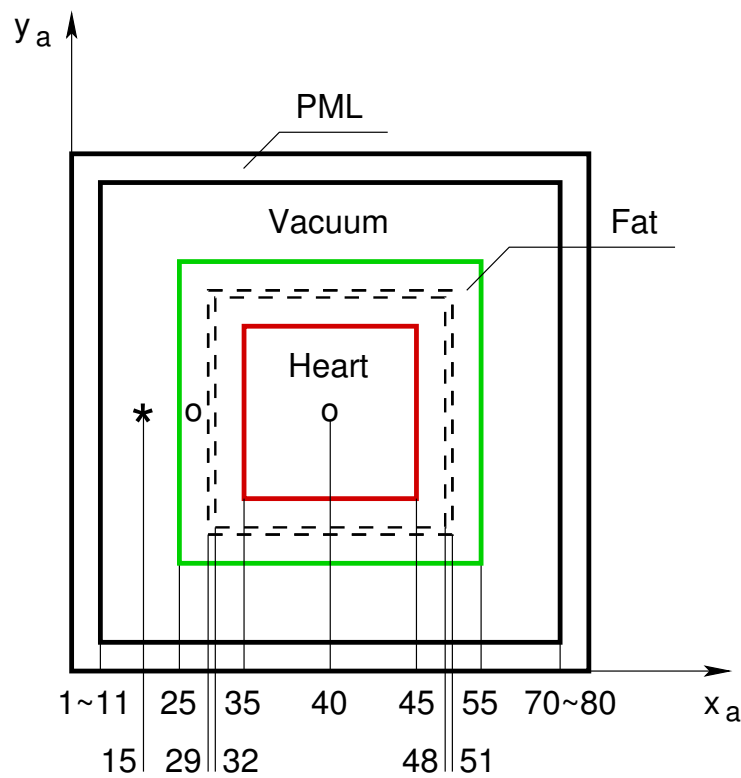
(a) Scenario 2b. $T_{xa} = 15$, $R_{xa} = 27$

(b) Scenario 2b. $T_{xa} = 15$, $R_{xa} = 40$

Figure 6.10: Frequency domain signal of Scenario 2b. Weak Debye medium crossing OS–IS interface enables larger transferable frequency range of the HSG signal.

Figure 6.11: Cross-section of Scenario 3a setting, plane $z_a = 40$. Fat and Heart objects in Air environment. Fat occupies part of the main grid and covers the OS–IS interface. Heart takes up the entire Inner Box. Scenario 3a is symmetric relative to the centre line. Cross-section at plane $y_a = 40$ is the same as presented here.

6.7.2 Time Domain Signal

Interesting dependency illustrating the HSG accuracy performance can be seen in Scenario 3a plots. In the main grid the HSG curve tends to follow the coarse grid signal (Figure 6.12a) while in the subgrid (Figure 6.12b) the HSG matches the fine grid curve. The tendency to follow coarse grid is explained by the lack of spatio-temporal resolution in the HSG main grid. On the other hand the ability to match the fine grid signal in the subgrid shows the expected HSG accuracy. Purpose of any subgridding algorithm is to provide an accuracy level similar to the fine grid signal. Scenario 3a is one of the most important testing scenarios presented in this work, because it vividly presents the expected HSG accuracy. Since Fat crosses the OS–IS interface no HSG instability is visible during the simulation time of $t_{max} = 2000$.

6.7.3 Frequency Domain Signal

Figures 6.13a and 6.13b show the HSG results in the frequency domain. Figure 6.13b illustrates a very good HSG accuracy performance in the centre of the subgrid at $x_a = 40$, where the HSG signal lies in a much closer proximity to the fine grid curve, than to the coarse. Figure 6.13b highlights a major difference between the fine and coarse grid results. This discrepancy is expected and is explained by the insufficient signal sampling in the Heart in the coarse grid. On the contrary, fine discretisation of the Heart tissue by the subgrid results in a good matching between the HSG and the fine grid signals. Minor difference between the HSG and the fine grid curves at the highest frequencies is attributed to the HSG signal propagation in the Fat tissue inside the main grid. Figure 6.13b clearly illustrates the key strength of the HSG—using a finely discretised grid in the HSG subgrid only yields a similar result to the one achievable by the all fine grid approach.

6.8 Scenario 3b. HSG in Inhomogeneous Strong and Weak Debye Media with Excitation in Subgrid

6.8.1 Scenario Setting

Setting of Scenario 3b is similar to Scenario 3a. There are two minor differences in the layout: (i) excitation source is located in the middle of the subgrid at $T_{xa} = 40$ and (ii) weak and strong media changed places. A strong Heart medium surrounds
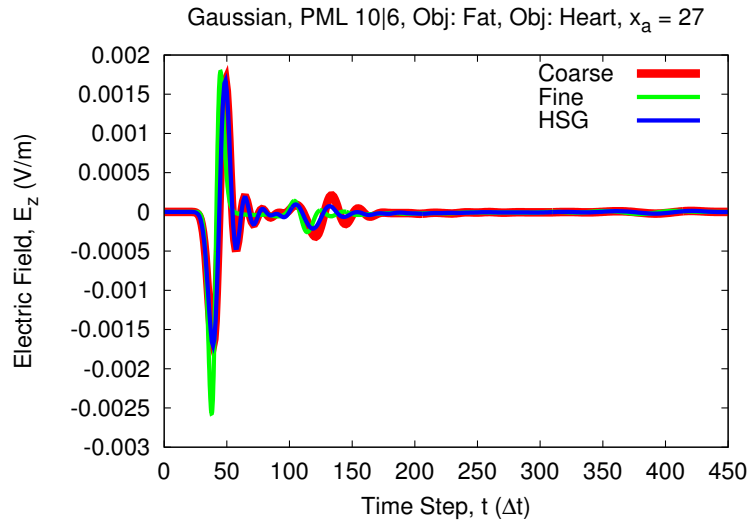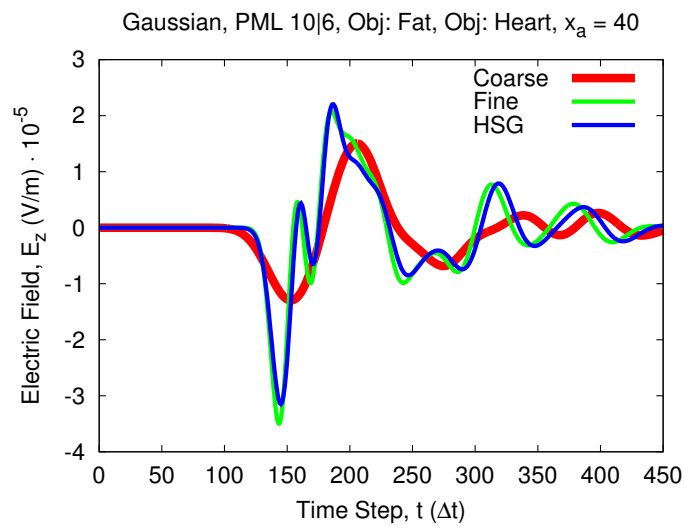
(a) Scenario 3a. $T_{xa} = 15$, $R_{xa} = 27$

(b) Scenario 3a. $T_{xa} = 15$, $R_{xa} = 40$

Figure 6.12: Time domain signal of Scenario 3a. Strong Debye medium in the Inner Box reduces the signal amplitudes. Coarse grid curve in the Inner Box is very smooth due to insufficient resolution of the main grid.
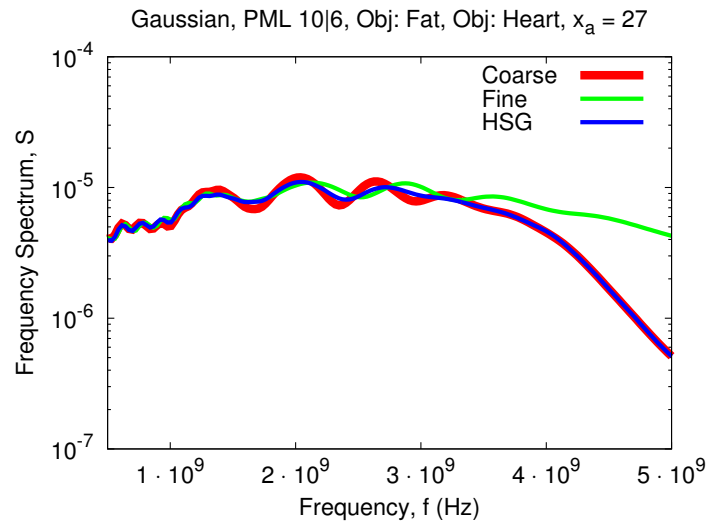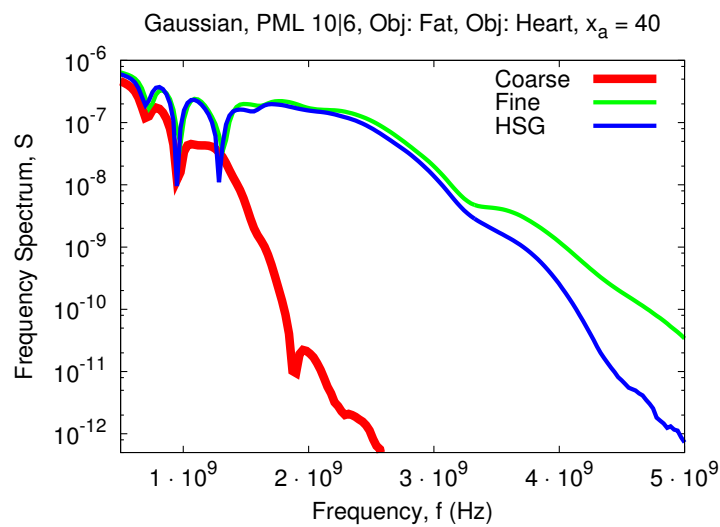
(a) Scenario 3a. $T_{xa} = 15$, $R_{xa} = 27$

(b) Scenario 3a. $T_{xa} = 15$, $R_{xa} = 40$

Figure 6.13: Frequency domain signal of Scenario 3a. Weak Debye medium at HSG interface contributes to small discrepancy between the HSG and fine grid curves. Strong Debye medium in Inner Box has little effect on the HSG signal because of the high spatio-temporal resolution of the subgrid.

a weak Fat medium. Figure 6.14 depicts a 2D cross-section of Scenario 3b setting. Three observation points $R_{xa} = 33, 27, 15$ are located at the centre line $y_a = z_a = 40$.
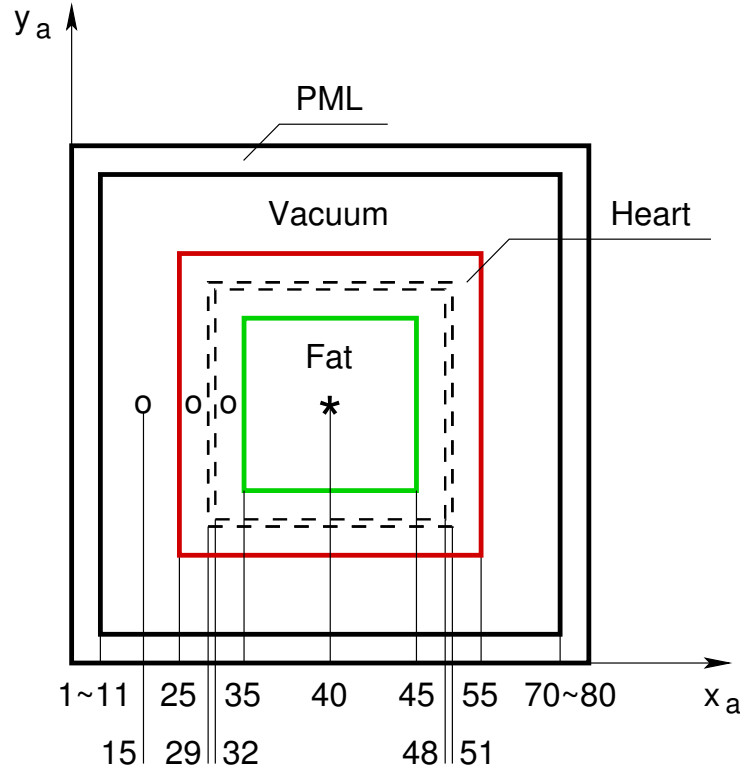

Figure 6.14: Cross-section of Scenario 3b setting, plane $z_a = 40$. Heart and Fat objects in Air environment. Heart occupies part of the main grid and covers the OS–IS interface. Fat takes up the entire Inner Box. Excitation source is placed in the middle of the subgrid at $x_a = 40$. Scenario 3b is symmetric relative to the centre line. Cross-section at plane $y_a = 40$ is the same as presented here.

6.8.2   Time Domain Signal

Figure 6.15a shows a perfect matching between the HSG and the fine grid curves. This is due to the excitation source being placed into the high resolution subgrid area. The difference between the HSG and the fine grid curves at locations $x_a = 27$ and $x_a = 15$ is directly proportional to the maximum signal amplitudes. At $x_a = 27$ Figure 6.15b illustrates an amplitude difference of $2.5 \cdot 10^{-4}$ V/m at the maximum HSG signal of 10^{-3} V/m. While at $x_a = 15$ Figure 6.15c highlights an amplitude difference of $1.8 \cdot 10^{-4}$ V/m at the maximum HSG signal of 10^{-4} V/m. The discrepancy between the HSG and the fine grid signals is caused by coarser spatio-temporal

sampling of the main grid and higher electric conductivity of the Heart compared to Fat.

6.8.3   Frequency Domain Signal

Figures 6.16a to 6.16c show the signal propagation of Scenario 3b in frequency domain. Figure 6.16a illustrates the HSG signal overlap with the fine grid curve inside of the subgrid. Figure 6.16b depicts the signal as it enters the main grid. At observation location $x_a = 27$ the HSG curve is approximately an average of the fine and the coarse grid curves. Figure 6.16c presents the signals at the observation point in the Air in the main grid at $x_a = 15$. Near the simulation domain boundary the HSG curve is located much closer to the coarse grid signal. This is explained with an especially strong high frequency component absorption in the main grid by the Heart at $x_a \in [25, 32]$.

6.9   Scenario 3c. HSG in Inhomogeneous Weak and Strong Debye Media with Excitation in Subgrid

6.9.1   Scenario Setting

Scenario 3c is analogous to Scenario 3b with the only difference in placement of the Debye media. In Scenario 3c Fat (weak medium) surrounds the Heart (strong medium). The excitation source is placed in the middle of the subgrid at $T_{xa} = 40$. It is interesting to compare the HSG signal propagation between Scenario 3b and Scenario 3c. Since the source is located in the middle of the high resolution region it is expected that the HSG curve will match the fine grid very well near the excitation source. After the subgrid the signal enters the main grid filled with Fat. Because Fat medium has lower conductivity than Heart, it is anticipated to see a relatively small difference between the HSG and the fine grid signals. Figure 6.17 depicts a 2D cross-section of Scenario 3c setting. Three observation points $R_{xa} = 33, 27, 15$ are located at the centre line $y_a = z_a = 40$.

6.9.2   Time Domain Signal

Figure 6.18a illustrates an expected overlap of the HSG and the fine grid curves inside of the subgrid. The same as in Scenario 3b, presented in Figure 6.15a, matching
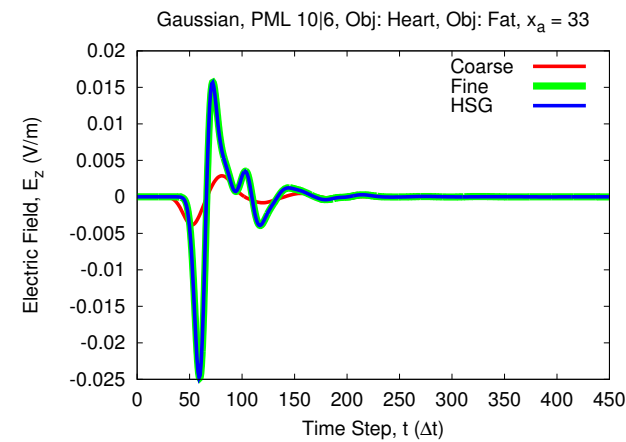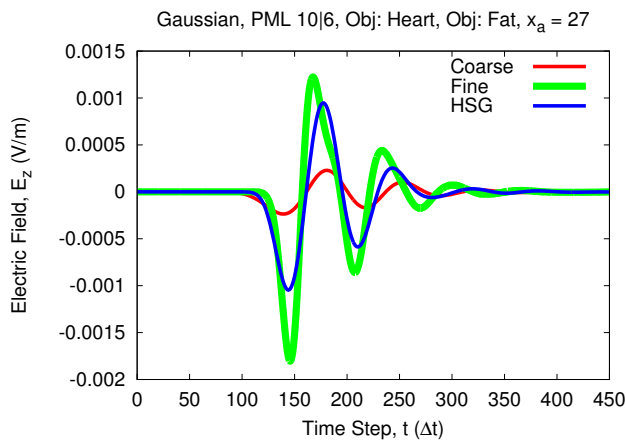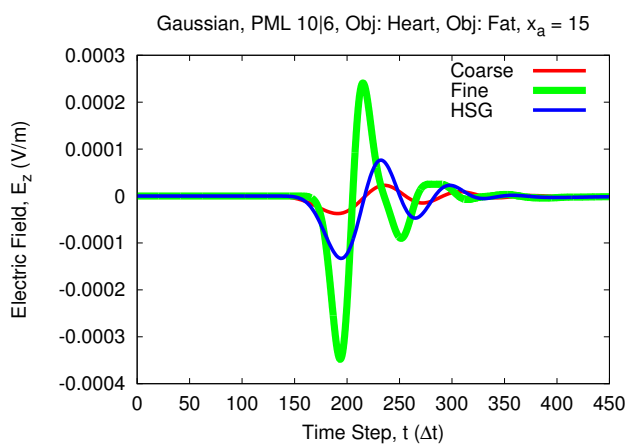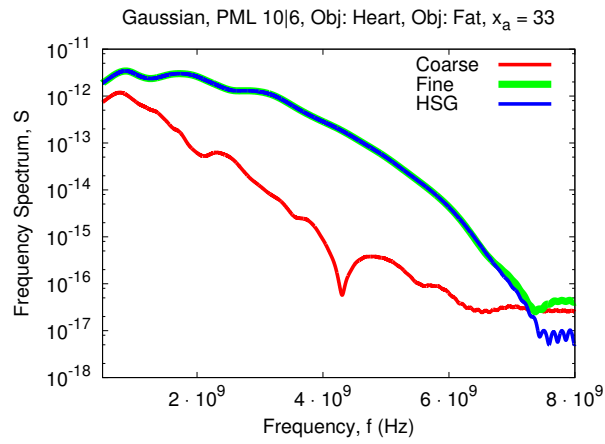
(a) Scenario 3b. $T_{xa} = 40$, $R_{xa} = 33$

(b) Scenario 3b. $T_{xa} = 40$, $R_{xa} = 27$

(c) Scenario 3b. $T_{xa} = 40$, $R_{xa} = 15$

Figure 6.15: Time domain signal of Scenario 3b. HSG signal quality deteriorates gradually with distance from the source due to a strong Debye medium in the main grid.
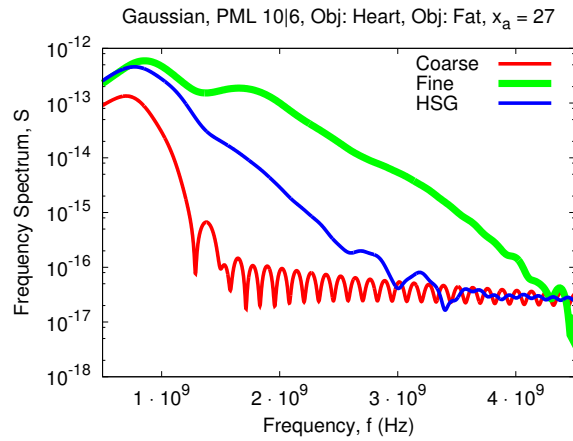
(a) Scenario 3b. $T_{xa} = 40$, $R_{xa} = 33$

(b) Scenario 3b. $T_{xa} = 40$, $R_{xa} = 27$
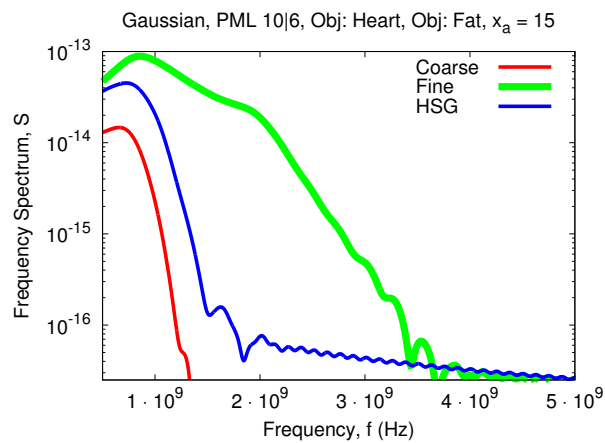

(c) Scenario 3b. $T_{xa} = 40$, $R_{xa} = 15$

Figure 6.16: Frequency domain signal of Scenario 3b. Strong Debye media at HSG interface reduces transferable frequency range of the HSG signal.

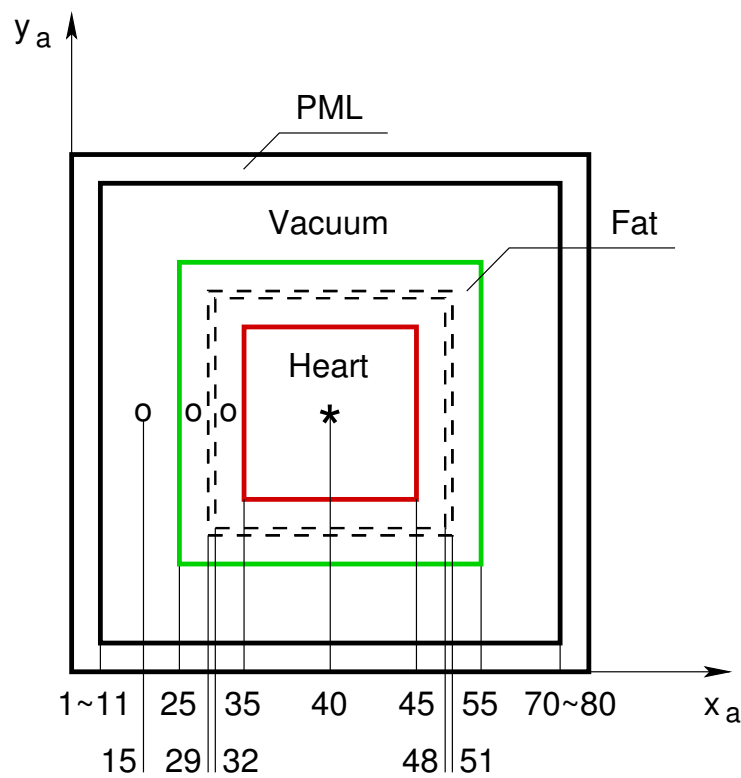Figure 6.17: Cross-section of Scenario 3c setting, plane $z_a = 40$. Fat and Heart objects in Air environment. Fat occupies part of the main grid and covers the OS–IS interface. Heart takes up the entire Inner Box. Excitation source is placed in the middle of the subgrid at $x_a = 40$. Scenario 3c is symmetric relative to the centre line. Cross-section at plane $y_a = 40$ is the same as presented here.

between the HSG and the fine grid curves is very good. The only difference lies in the maximum values of the electric field. Due to higher conductivity of Heart in Scenario 3b the amplitude values are approximately 10 times smaller in Scenario 3b than in Scenario 3c. Conversely in the main grid in Scenario 3c the HSG preserves matching with the fine grid relatively well, compared to Scenario 3b. Figure 6.15b shows the peak amplitude difference of $2.5 \cdot 10^{-4}$ V/m between the HSG and the fine grid signals at $R_{xa} = 27$ in Scenario 3b. On the contrary no peak amplitude difference is observed in Figure 6.18b showing the signal at the same location in Scenario 3c. Similarly, Figure 6.15c highlights the peak amplitude difference of $1.8 \cdot 10^{-4}$ V/m at $R_{xa} = 15$ in Scenario 3b, compared to no difference at the same location in Scenario 3c presented in Figure 6.18c.

6.9.3 Frequency Domain Signal

A very good matching between the HSG and the fine grid signals presented in Figures 6.19a to 6.19c holds throughout all observation locations $R_{xa} = 33, 27, 15$ in Scenario 3c. Conversely, as shown in Figures 6.16a to 6.16c, due to a strong Debye medium in the main grid in Scenario 3b, the HSG signal moves further away from the fine grid curve with increase of the distance from the excitation $T_{xa} = 40$.

6.10 Scenario 4. HSG in Multiple Inhomogeneous Weak and Strong Debye Media

6.10.1 Scenario Setting

Scenario 4 presents a realistic setting with different Debye media: Fat, Bone and Muscle. Scenario 4 verifies correct HSG behaviour when multiple weak and strong Debye media cross the OS–IS interface. The Heart, a strong Debye medium, occupies the entire Inner Box. Detailed scenario setting is given in Figure 6.20. Excitation source is placed in the main grid at $T_{xa} = 15$ and two observation points $R_{xa} = 27, 40$ are located on the centre line $y_a = z_a = 40$. Signal in the HSG is tracked in various media: Fat and Heart.
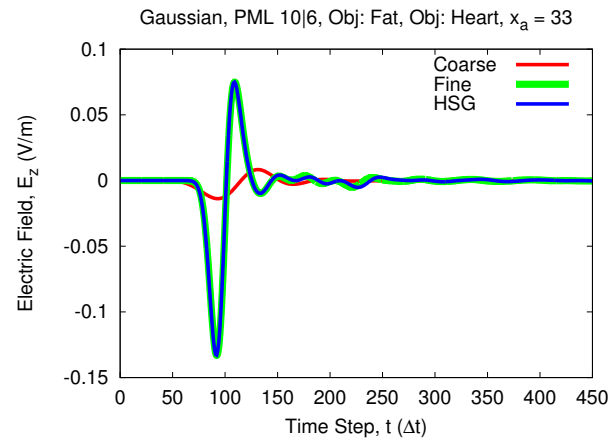
(a) Scenario 3c. $T_{xa} = 40$, $R_{xa} = 33$
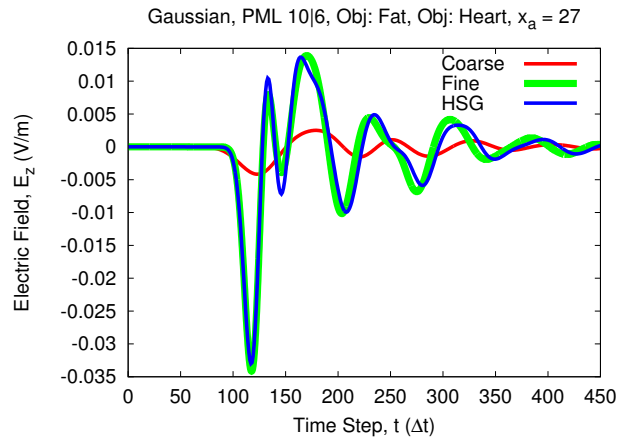
(b) Scenario 3c. $T_{xa} = 40$, $R_{xa} = 27$
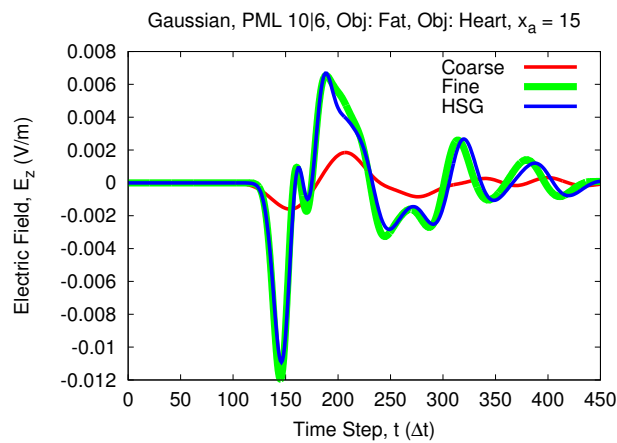
(c) Scenario 3c. $T_{xa} = 40$, $R_{xa} = 15$

Figure 6.18: Time domain signal of Scenario 3c. Strong Debye medium in Inner Box and subgrid excitation enables good matching between HSG and fine grid signals.
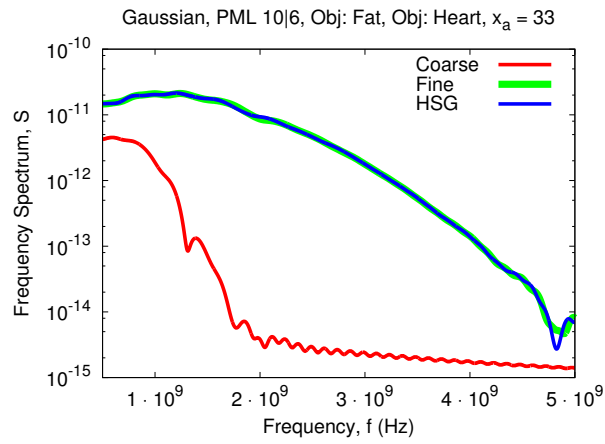
(a) Scenario 3c. $T_{xa} = 40$, $R_{xa} = 33$
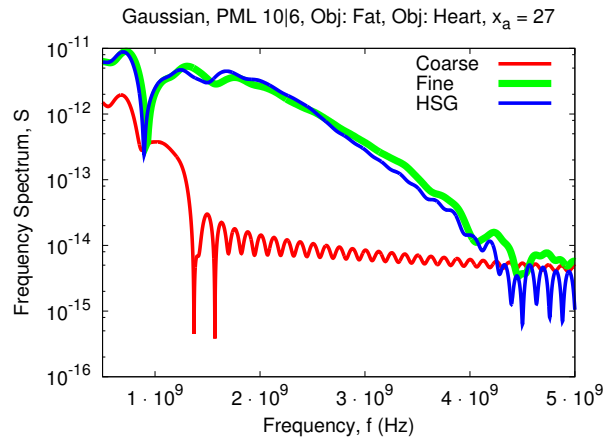
(b) Scenario 3c. $T_{xa} = 40$, $R_{xa} = 27$
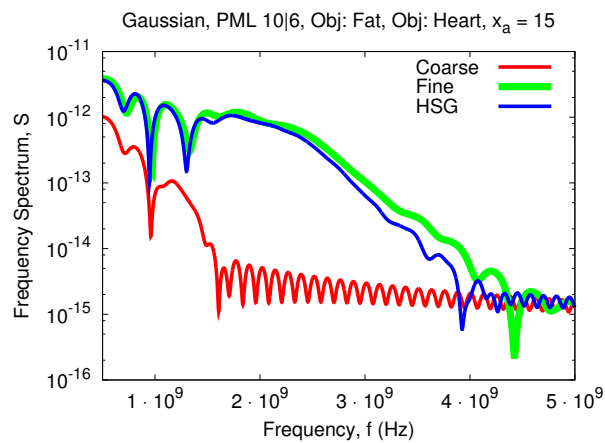
(c) Scenario 3c. $T_{xa} = 40$, $R_{xa} = 15$

Figure 6.19: Frequency domain signal of Scenario 3c. Subgrid excitation source contributes to a good matching between the HSG and fine grid signals.
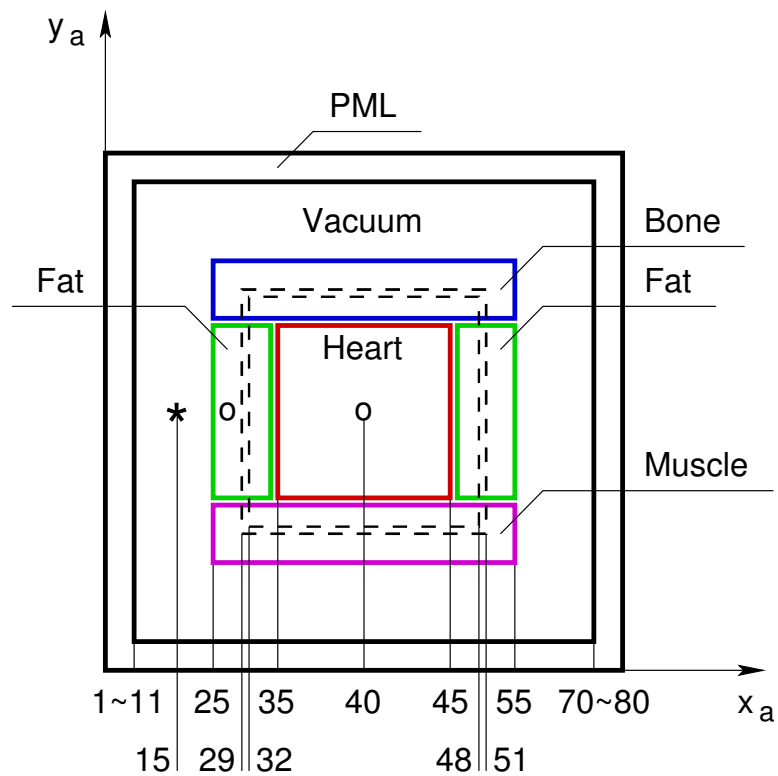
Figure 6.20: Cross-section of Scenario 4 setting, plane $z_a = 40$. Fat, Bone, Muscle and Heart objects in Air environment. Fat, Bone and Muscle tissues occupy part of the main grid and cover the OS–IS interface. Heart takes up the Inner Box.

6.10.2 Time Domain Signal

Figure 6.21a illustrates the tendency of the HSG signal in the main grid to follow the coarse grid curve in the Fat environment. This is explained by the insufficient resolution of the wavelength in Fat in the main grid and higher conductivity of Fat tissue relative to Air. Inside of the subgrid Figure 6.21b shows a very good matching of the HSG with the fine grid curve. Strong conductivity of Heart reduces the electric field amplitude. Heart absorbs the high frequency components of the signal in the coarse grid. Hence, the coarse grid curve is smooth and small in amplitude. Multiple minor peaks in Figure 6.21b possibly account for signal reflections from the strong Debye media—the Bone and Muscle tissues.

6.10.3 Frequency Domain Signal

Figures 6.22a and 6.22b show the signal propagation in frequency domain. Multiple peaks in Figure 6.22a occur due to the presence of different media influencing the signal. Notable is Figure 6.22b depicting the signal in the middle of the subgrid, where the HSG matches with the fine grid relatively well. Transferable frequency range in the coarse grid is dramatically smaller.

6.11 Cut-Off Frequency Estimation

Estimation of the wave propagation cut-off frequency f_c is beneficial to verify the HSG accuracy. In Air the cut-off frequency is expressed as [102]:

$$f_c = \frac{1}{\pi \Delta t} \arcsin\left(\frac{v \Delta t}{\Delta s}\right). \tag{6.6}$$

Parameter v in (6.6) denotes the speed of wave propagation in a given medium and is expressed as:

$$v = \frac{1}{\sqrt{\varepsilon \mu}} = \frac{1}{\sqrt{\varepsilon_0 \varepsilon_r \mu_0 \mu_r}} = \frac{c}{\sqrt{\varepsilon_r \mu_r}}. \tag{6.7}$$

The final form of the cut-off frequency equation is obtained by substituting (6.7) into (6.6):

$$f_c = \frac{1}{\pi \Delta t} \arcsin\left(\frac{c \Delta t}{\Delta s \sqrt{\varepsilon_r \mu_r}}\right). \tag{6.8}$$

(a) Scenario 4. $T_{xa} = 15$, $R_{xa} = 27$

(b) Scenario 4. $T_{xa} = 15$, $R_{xa} = 40$

Figure 6.21: Time domain signal of Scenario 4. Strong Debye medium in the Inner Box reduces the signal amplitudes. High resolution of the subgrid enables good matching between the HSG and the fine grid curves.
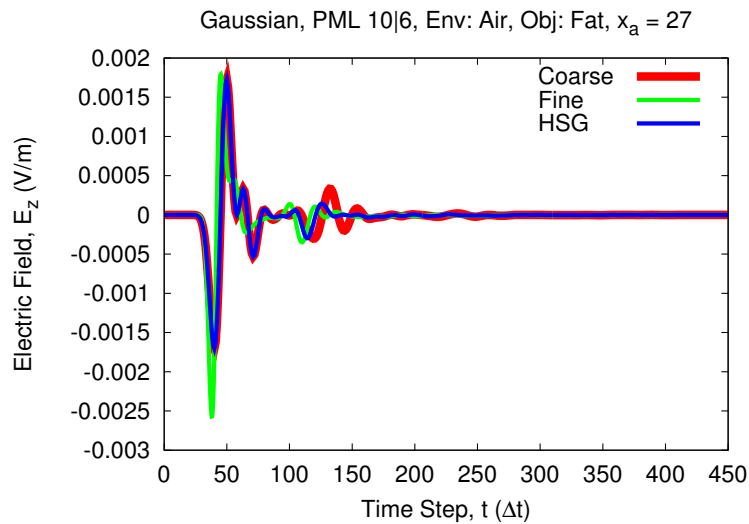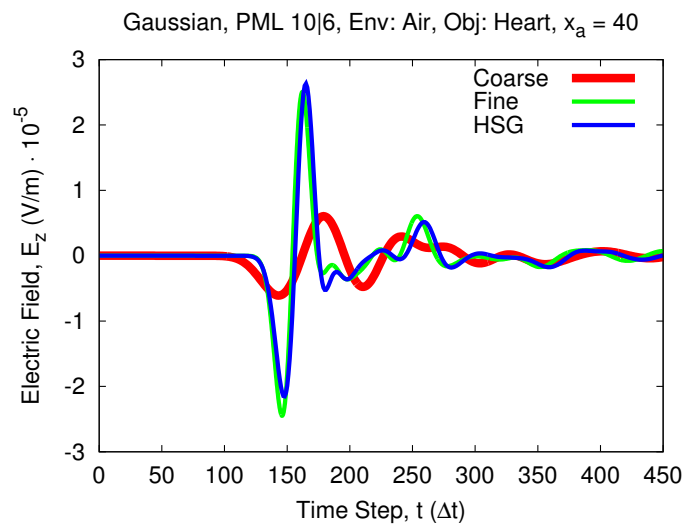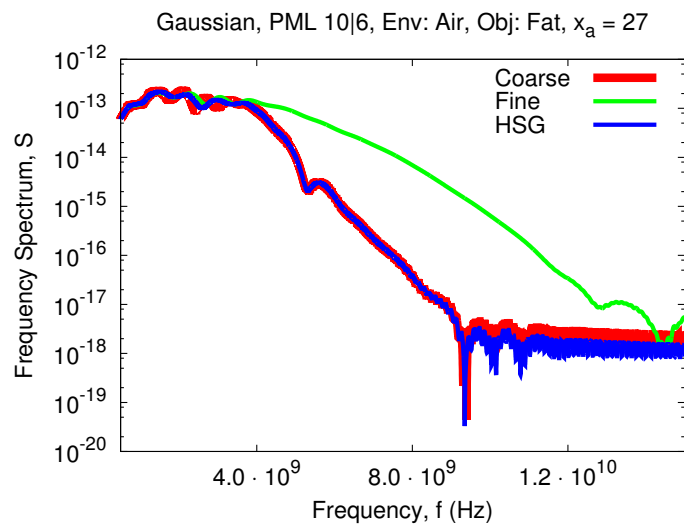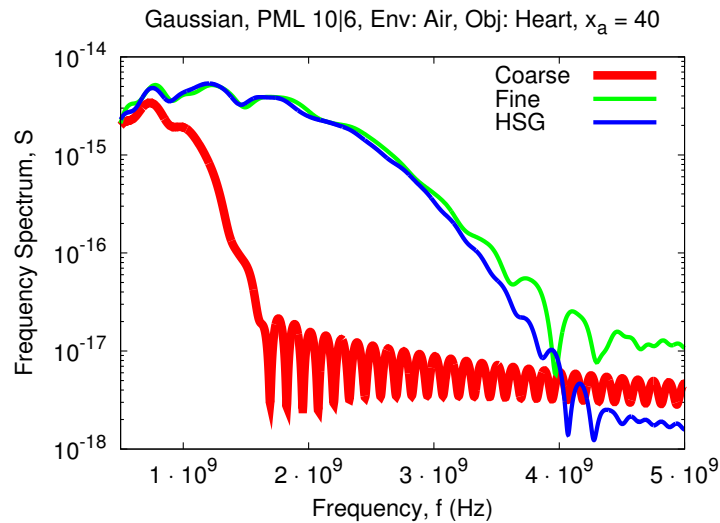
(a) Scenario 4. $T_{xa} = 15$, $R_{xa} = 27$

(b) Scenario 4. $T_{xa} = 15$, $R_{xa} = 40$

Figure 6.22: Frequency domain signal of Scenario 4. High resolution subgrid of the HSG allows it to reach an almost identical performance as the fine grid signal.

Since magnetic properties of a medium are not important in the context of this work, the relative magnetic permeability μ_r in (6.8) is assumed to be 1. Furthermore, to incorporate the Debye medium parameters into (6.8) the relative electric permittivity ε_r is derived as:

$$\varepsilon_r = \varepsilon_\infty + \frac{\varepsilon_s - \varepsilon_\infty}{1 + J\omega\tau} + \frac{\sigma}{J\omega\varepsilon_0}, \tag{6.9}$$

where $\omega = 2\pi f_w$. Table 6.3 shows the cut-off frequency ranges in GHz for the all coarse and all fine grid signals. The cut-off frequency ranges are calculated for Debye media parameters of the four tissues used in Scenarios 1a to 4: Heart, Muscle, Bone and Fat. Only the real part of complex relative permittivity in (6.9) was taken into account while calculating the cut-off frequency ranges. Spatial and temporal increments of Scenarios 1a to 4 $\Delta s_a = 10$ mm, $\Delta t_a = 0.179$ ps and $\Delta s_b = 2$ mm, $\Delta t_b = 3.582$ ps were used in the cut-off frequency estimation. The cut-off frequency ranges listed in Table 6.3 are estimated for the range of wave frequency, where Debye parameters are valid: $f_w \in [0.1, 6]$ GHz. Since there is only a minor change to the cut-off frequency depending on the relative permittivity, the data Table 6.3 is shown in ranges. Also the presentation of value ranges in Table 6.3 offers a better overview of the cut-off frequency dependence on the relative permittivity. Only the real part of relative permittivity is listed in Table 6.3.

Tissue	ε_r	f_c [GHz], Coarse	f_c [GHz], Fine
Heart	63.540 ~ 47.964	1.198 ~ 1.379	5.990 ~ 6.896
Muscle	56.927 ~ 47.291	1.266 ~ 1.389	6.329 ~ 6.945
Bone	14.166 ~ 9.915	2.544 ~ 3.046	12.720 ~ 15.228
Fat	5.530 ~ 4.849	4.094 ~ 4.378	20.470 ~ 21.888
Air	1.000	10.073	50.367

Table 6.3: Cut-off frequency ranges for human body tissues and air calculated for wave frequency $f_w \in [0.1, 6]$ GHz

Table 6.3 shows that the relative permittivity ε_r of all tissues is inversely proportional to the wave frequency f_w. The dependency between the relative permittivity and the cut-off frequency is also inversely proportional (higher relative permittivity results in a lower cut-off frequency value). Strong Debye media such as Heart and Muscle have lower cut-off frequency thresholds, than weak Debye media such as Bone and Fat. Another interesting observation, that holds for all media, is that a

relatively wide wave frequency range (6.0 GHz − 0.1 GHz = 5.9 GHz) results in a relatively narrow cut-off frequency range, e.g. in case of Bone (3.046 GHz − 2.544 GHz = 0.502 GHz) for coarse grid and (15.228 GHz − 12.720 GHz = 2.508 GHz) for fine grid.

It is possible to explain the HSG signal behaviour in the testing scenarios with a change in cut-off frequency. Refer to Scenario 3b and consider the frequency domain signal at the observation point R_{xa} = 33 presented in Figure 6.16a. Point R_{xa} = 33 is located inside the subgrid in the Heart medium. According to Table 6.3 the maximum cut-off frequency of the Heart in the subgrid is f_c = 6.896 GHz. Since the observation point is in the subgrid, the HSG signal matches the fine grid very well. Consider the next observation point R_{xa} = 27 in Figure 6.16b, that is located in the main grid, still inside the Heart. The maximum cut-off frequency there is f_c = 1.379 GHz. A sudden drop of cut-off frequency at the OS–IS interface by five times results in a rapid move of the HSG curve towards the coarse grid curve.

A contrasting example is presented by Figures 6.19a and 6.19b illustrating the frequency domain signal plots of Scenario 3c. Although the maximum cut-off frequency between Fat in the subgrid and Fat in the main grid differs by the subgridding ratio of 5, the main grid cut-off frequency of 4.378 GHz still provides a sufficient frequency span for the HSG signal to propagate accurately.[6] A minor change in the HSG signal is noticeable between the Figures 6.19a and 6.19b because the Heart in the subgrid cut off the frequencies beyond 6.896 GHz. Only the frequencies in between 6.896 GHz and 4.378 GHz were lost.

6.12 Scenario 5. HSG Stability in Homogeneous Weak Debye Medium

This section presents and analyses the effect of electric conductivity σ on the overall HSG instability.

Usually instability of the frequency-independent HSG method in 3D becomes visible after approximately 4000–5000 main grid iterations with r = 5 and the subgrid size of 80 × 80 × 160 [102] (see Section 4.6.1 for more details). Observing the results from Scenarios 1a to 4 leads to a hypothesis that dispersive medium delays

---

[6]In this case the notions of "sufficient frequency span" and "accurate propagation" are taken in relation to the signal plots. Since there is little change in HSG signal quality in Figures 6.19a and 6.19b compared with the fine grid signal, it is assumed the frequency span is sufficient and the propagation is accurate.

the visibility of the HSG instability. The aim of Scenario 5 is to verify the drawn hypothesis and test the effect of electric conductivity σ on the visibility of the HSG instability.

6.12.1   Scenario Setting

Figure 6.23 presents a detailed setting for Scenario 5. Excitation source was located at $T_{xa} = 5$ and the observation point was placed at $R_{xa} = 13$. Domain sizes of 46^3 for the main and 63^3 for the subgrid were used in Scenario 5. Given domain sizes include the 10 and 6 points thick PML in the main and in the subgrid. The HSG method was executed for 10^6 main grid iterations. Electric field component E_z was output at every 10th main grid iteration.
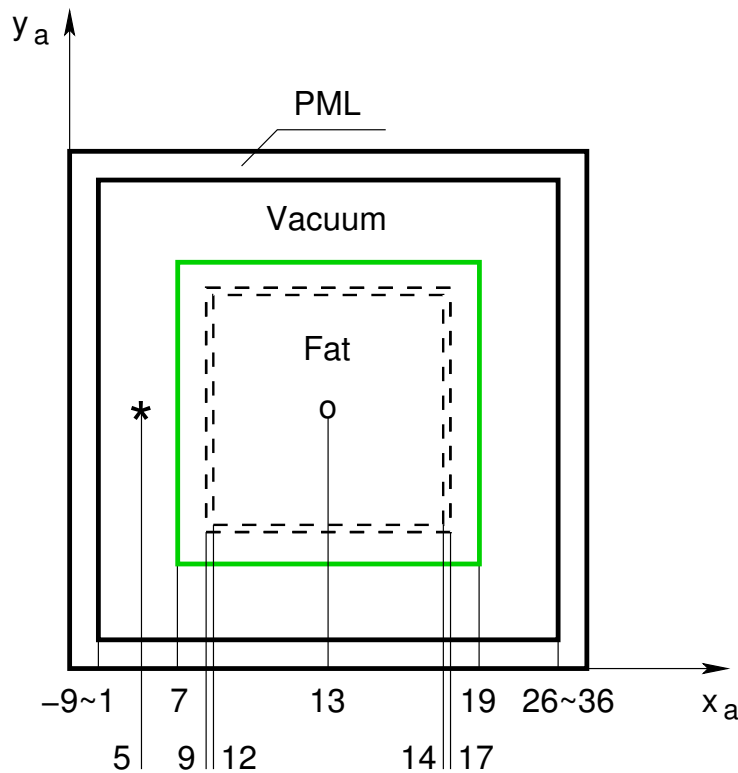
Figure 6.23: Cross-section of Scenario 5 setting, plane $z_a = 13$. Air environment with Fat object covering the OS–IS interface. Scenario 5 is symmetric relative to the centre line. Cross-section at plane $y_a = 13$ is the same as presented here.

Subgridding ratio and the CFL number were $r = 5$, $N_{CFL} = 0.93$. The spatial and temporal steps were set to $\Delta s_a = 0.9$ mm, $\Delta s_b = 0.18$ mm and $\Delta t_a = 1.612$ ps, $\Delta t_b = 0.322$ ps. Fat with Debye parameters of $\sigma = 3.71 \cdot 10^{-2}$ S/m, $\varepsilon_s = 5.531$, $\varepsilon_\infty = 3.998$

and $\tau = 0.236$ ps was taken for a basis tissue. Multiple tests were run with the setting of Scenario 5 and electric conductivity modified according to (6.10):

$$\sigma = 0 \quad \text{and} \quad \sigma = 3.71 \cdot 10^n, \tag{6.10}$$

where $n \in [-2, 0, 2]$. Given settings constitute four test cases with constant values of $\varepsilon_s, \varepsilon_\infty, \tau$ and variable σ. Only the case with $\sigma = 3.71 \cdot 10^{-2}$ S/m corresponds to a test with the realistic Fat medium. Other cases translate into three tests with artificial media.

6.12.2 Time Domain Signal

Figure 6.24 depicts a summary of all Scenario 5 tests with various values of electric conductivity. Table 6.4 lists the absolute maximum values of electric field E_z used in the amplitude normalisation of Figure 6.24.
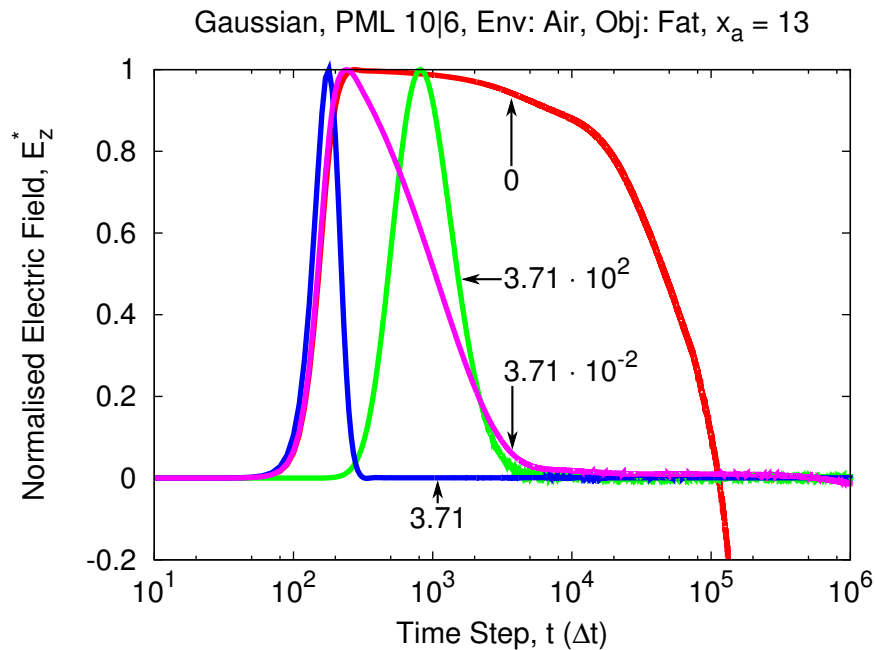
Figure 6.24: Time domain signal of Scenario 5 at the observation location $x_a = 13$ in the middle of the subgrid. Conductivity values of $\sigma = 0$, $3.71 \cdot 10^{-2}$ 3.71, $3.71 \cdot 10^2$ are shown on the plot. In case of $\sigma = 0$ the signal diverges after approximately 170 000 main grid iterations.

Results presented in Figure 6.24 support the drawn hypothesis. No instability growth is observed in any case with the non-zero conductivity. Most likely minor amplitude fluctuations in these cases are attributed to the numerical noise. In the

σ [S/m]	$\left|E_{z,max}\right|$ [V/m]
0	$5.32565685 \cdot 10^{-3}$
$3.71 \cdot 10^{-2}$	$4.85745305 \cdot 10^{-3}$
3.71	$6.46746310 \cdot 10^{-4}$
$3.71 \cdot 10^{2}$	$4.93262291 \cdot 10^{-7}$

Table 6.4: Absolute maximum values of E_z used for normalisation, Scenario 5

frequency-independent case with $\sigma = 0$ the HSG signal diverges after approximately 170 000 main grid iterations.

6.13   Scenario of Human Torso

6.13.1   Simulation Settings

A realistic test case with signal propagation inside a human torso follows the basic scenarios with artificial media placement. Wave propagation is simulated with the dispersive HSG method and a subgridding ratio $r = 5$. Entire human heart is placed into the subgrid region. Scenario of human torso was run using two kinds of excitations: (i) point source excitation and (ii) defibrillator pads excitations. Gaussian pulse formed according to (6.1) was applied at each point of the excitation. Major simulation parameters are listed in Table 6.5. Parameter notation is the same as in Section 6.1. Negative coordinate indices in the domain ranges ni, nj were used to allow $10\Delta s_a$ buffering zones of Air before and after the human torso in x-axis and 4 cells thick PML in x, y-axes. Negative coordinates were required because the human torso PGM data ranges started from 1.

Figure 6.25 presents the human torso simulation environment in 2D and 3D. Detailed simulation scenario setting used to verify the wave propagation through the human body is given in 1D in Figure 6.26.

Figure 6.26 shows an observation point R_x positioned in the middle of the subgrid, inside the Heart tissue, at $(x_a, y_a, z_a) = (36, 42, 244)$. The line $(y_a, z_a) = (42, 244)$ crosses the human torso and the human heart. Figure 6.26a presents an overall human torso environment setting in 1D. The entire simulation domain is shown in Figure 6.26a. Figures 6.26b and 6.26c provide a magnified view of Figure 6.26a and concentrate only on the human body tissues in between the defibrillator pads. Figure 6.26c gives the most precise representation of the radio environment.

Parameter	HSG	Fine
ni	$-13 \sim 67$	$-53 \sim 319$
nj	$-3 \sim 102$	$-3 \sim 494$
nk	$160 \sim 341$	$820 \sim 1691$
t_{max}	1000	5000
r	5	
OL	22, 27, 232	
IL	25, 30, 235	
IR	47, 54, 254	
OR	50, 57, 257	
$zone_b$	15	
n_{pml_a}	4	
n_{pml_b}	6	
source type	soft	soft
Δs_a	5 mm	–
Δs_b	1 mm	1 mm
Δt_a	8.955 ps	–
Δt_b	1.791 ps	1.791 ps
N_{CFL}	0.93	0.93
χ_a	10	–
χ_b	50	50

Table 6.5: Simulation settings, human torso

(a)   (b)
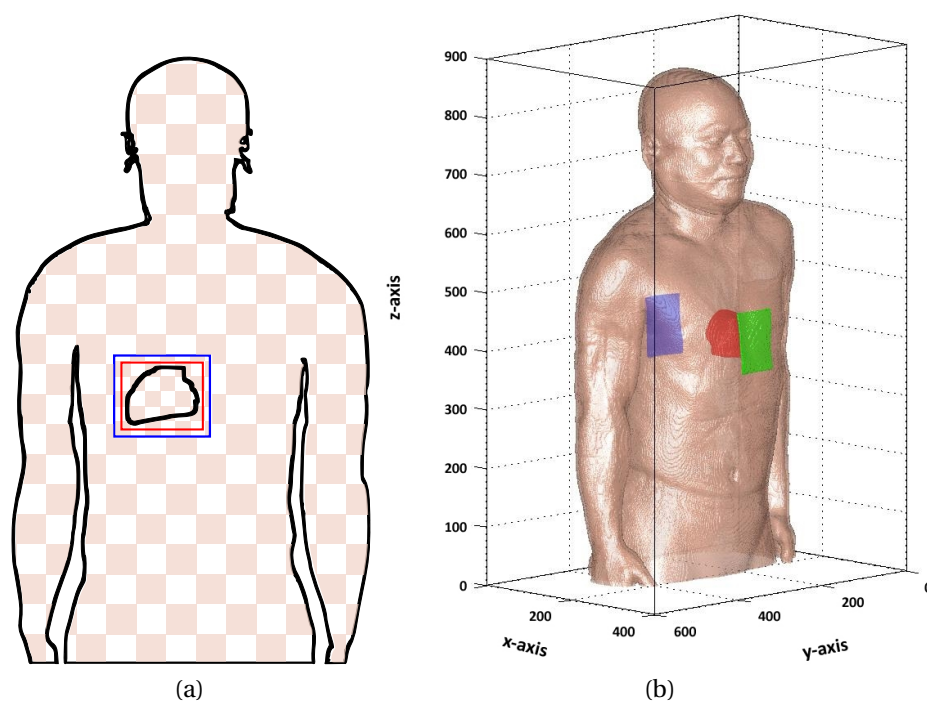
Figure 6.25: Human torso propagation environment.

(a) Human torso in main grid (large squares) with heart in subgrid (small squares). Outer Surface (blue) and Inner Surface (red) bound the subgrid region.

(b) Human torso with heart (red) and two defibrillator pads (green, purple) placed anteroposteriorly.
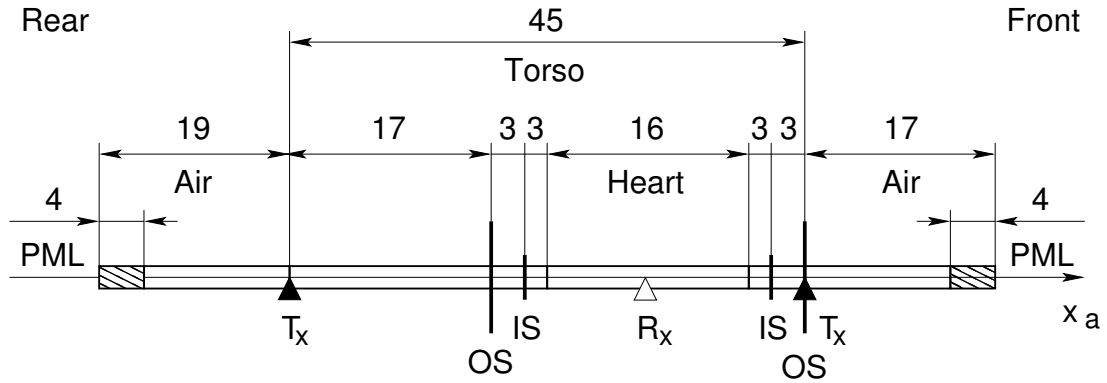
(a) Human torso with defibrillator pads placed anteroposteriorly. Scenario of human torso, setting in 1D, x_a. Observation point R_x is in the middle of the Heart. Four and six points thick PML terminate the main and subgrids respectively. Rectangular pads, where present, coincide with locations of the Skin. Numerical values are given in main grid points.
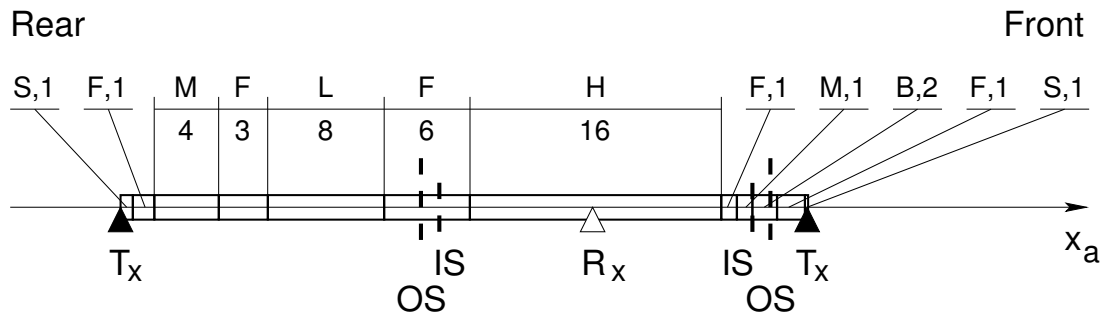
(b) Human body tissues between defibrillator pads on the line crossing the Heart at $x_a \in (5, 51)$, $y_a = 42$, $z_a = 244$. Following abbreviations are used: S—Skin, F—Fat, M—Muscle, L—Lung, H—Heart and B—Bone. Numbers specify tissue thickness in main grid points.
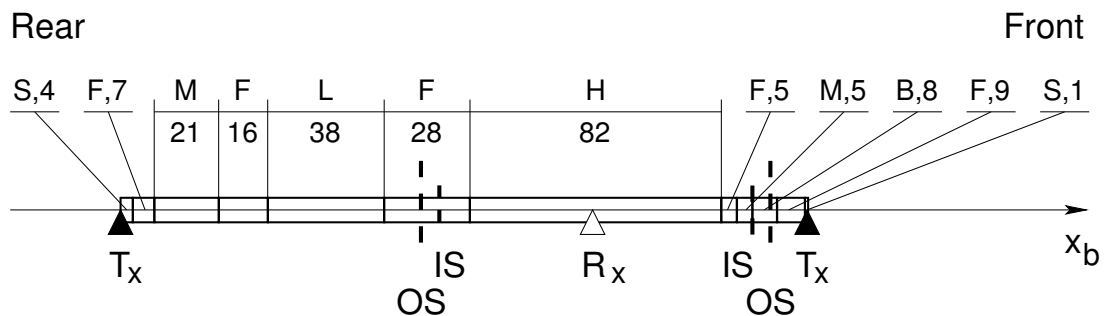
(c) Human body tissues between defibrillator pads on the line crossing the Heart at $x_b \in (26, 251)$, $y_b = 211$, $z_b = 1223$. Following abbreviations are used: S—Skin, F—Fat, M—Muscle, L—Lung, H—Heart and B—Bone. Numbers specify tissue thickness in subgrid points.

Figure 6.26: Scenario of human torso, setting

Figure 6.26b shows the Scenario of human torso as it is viewed by the main grid. In the simulation the media in the main grid is set by choosing the fine grid coordinate values that are multiples of the subgridding ratio $r = 5$. Although, the Skin thickness in the fine grid is less than 5 points, there is Skin tissue in the main grid, i.e. Skin thickness in the main grid is 1, as shown in Figure 6.26b. The Skin range on the rear of the torso is $x_b \in [27, 30]$, therefore $x_a = 30/r = 6$ is set in the main grid.

6.13.2   Defibrillator Pads Modelling

Two types of excitation sources were used for the verification tests: (i) single point source and (ii) two defibrillator pad sources. Anterior (front) and posterior (rear) defibrillator pads consist of 70 excitation point sources each. These sources are placed on top of the human body skin. There is no distance between the Skin and the pad. The pad coordinate locations, where present, coincide with locations of the Skin. Since defibrillator pads are positioned in the main grid, they are only approximations of the original pads, each occupying 75×100 fine grid points.

The expected amount of main grid points N to model a defibrillator pad is expressed by the following formula:

$$N = \big((j_{max} - j_{min})\%r + 1\big) \cdot \big((k_{max} - k_{min})\%r + 1\big), \qquad (6.11)$$

where symbols j_{min}, j_{max} and k_{min}, k_{max} denote the minimum and maximum values of y and z defibrillator pad coordinate ranges in the fine grid. Operator % signifies the integer division and r stands for the subgridding ratio. According to (6.11) the expected amount of main grid points to model a 75×100 fine grid points defibrillator pad is 300. The number 70 used in the simulation was obtained in the following manner:

(a) Skin surface under the 75×100 defibrillator pad location was extracted from the RIKEN digital human phantom using the utility program `xsurf`. The skin surface projection on y-axis for both anterior and posterior pads occupied the coordinate ranges of $y_b \in [174, 248]$ and $z_b \in [1173, 1272]$.

(b) Every main grid point coinciding with the fine grid point in the pad location data was taken out with an `awk` script `downsample-src`. Because of the particular pad location and the natural human body curvature there were less coinciding points than expected. Anterior pad resulted in 84 and posterior in 72 main grid

point approximations compared to 300 obtained with (6.11) by substitution of anterior and posterior pads coordinate ranges.

(c) Finally, the points in dense regions of anterior and posterior pads were removed manually. The x, y, z main grid locations data was sorted in a descending order along the z coordinated value. The z coordinate value span for an anterior pad was $z \in [235, 254]$. Then the total number of points for each z value were identified, e.g. 8 points for $z = 235$, 7 points for $z = 245$ and so on. A dense region was defined as the set of location points for a particular z coordinate value, where the total number of points was larger or equal to $r = 5$. The excessive points in dense regions were removed by hand to keep the total points number for a particular z coordinate equal or less than 5. Points were removed in a non-successive order to achieve a uniform points distribution. Consider the first lines of the excitation source file `anterior_a` shown in Listing 6.1. The file columns correspond to x, y, z coordinate values. Each row of the file represents an excitation source point in the main grid. Lines 2, 4 and 6 were removed manually to achieve a uniform point distribution.

```
1       51      38      235
2       51      39      235
3       51      40      235
4       51      41      235
5       51      42      235
6       51      43      235
7       51      44      235
8       51      45      235
```

Listing 6.1: Excitation sources file "anterior_a"

This manual averaging operation allowed to obtain two defibrillator pads modelled with 70 main grid excitation points.

Both pads excite anti-phase. Posterior (rear) pad injects the current density J_z, the same in magnitude, but different in sign as the anterior (front) pad.

6.13.3 Correct Modelling of Skin

The HSG main grid is incapable of representing the Skin thickness of 1, 2, 3 and 4 fine grid cells. This can be observed by comparing scenario setting in the main grid (Figure 6.26b) and the subgrid (Figure 6.26c). Also the approximation of 1, 2,

3 and 4 fine grid thickness with a single main grid cell would lead to a very strong Skin conductivity. Therefore, the electric conductivity of Skin σ was divided by the subgridding ratio of 5 in both the HSG main grid and the coarse grid FDTD methods. Conductivity σ was decreased by the subgridding ratio regardless of the Skin thickness $1 \sim 4$ in the fine grid.

Reducing the electric conductivity by the subgridding ratio is not ideal, but a reasonable approach. The high value of Skin conductivity left unchanged would absorb most of the excitation signal and result in erroneous signal amplitudes at observation locations. Precise estimation of conductivity values is possible with the Thin Slab method [146], but it was not implemented in this work due to time constraints.

6.13.4   Point Source Excitation

The first batch of verification results was produced with a single point source located 10 coarse grid points away from the skin at the back of the torso. This preliminary test was conducted in preparation for the defibrillation pads excitation.

Figure 6.27a shows the signal propagation in time domain. The observation point is placed in the centre of the Heart discretised with a subgrid at $R_{xa} = 36$. Due to high conductivity values of Skin and Muscle tissues in the main grid the signal amplitude is reduced by 10^{-6}.

Figure 6.27b illustrates the signal propagation in frequency domain. In the middle of the subgrid the HSG curve is in between the coarse and fine grid signals.

6.13.5   Defibrillator Pads Excitation

Figure 6.28a presents the HSG signal propagation in time domain at the observation location $R_{xa} = 36$. Compared to the single point source (Figure 6.27a) the signal amplitude reduction in case of defibrillator pads excitation is 1000 times lower. This is due to the stronger initial signal, where 70 points excite in one pad compared to one point in the point source excitation scenario. Also defibrillator pad is placed on top of the Skin layer, whereas in the single point source excitation scenario it lies 10 points away from the Skin.

Figure 6.28b depicts the HSG signal in frequency domain. The HSG curve lies in parallel with the fine grid curve. The difference between two signal curves is minor. Compared to the single point excitation (Figure 6.27b) the HSG–fine grid curve matching is better. Figure 6.28b shows the precision advantage of the HSG over the

(a) Time domain signal, $R_{xa} = 36$

(b) Frequency domain signal, $R_{xa} = 36$

Figure 6.27: Scenario of human torso. Point source excitation. Highly conductive Skin and Muscle tissues reduce the signal amplitudes.

main grid more clearly than Figure 6.27b. In case of the single point excitation the majority of the signal is absorbed and the visible remainder is probably mixed with a strong portion of numerical noise. Compare Figure 6.27b with Figure 6.28b. The frequency spectrum range for the single point source lies within $10^{-18} \sim 10^{-15}$ and with the defibrillator pad sources it is $10^{-16} \sim 10^{-12}$
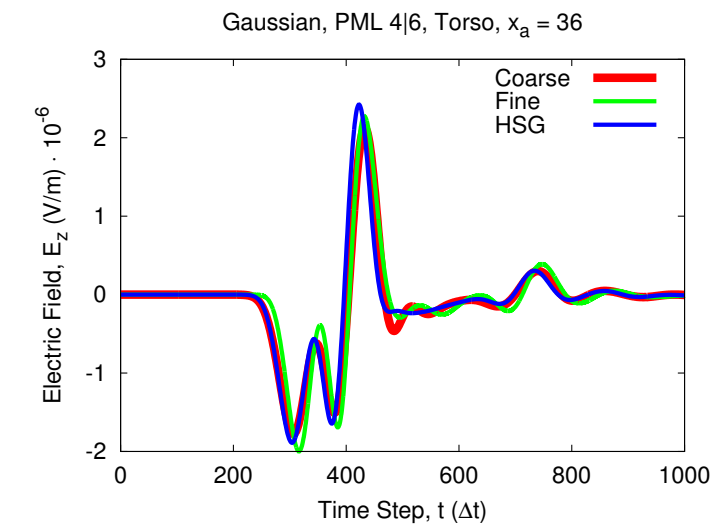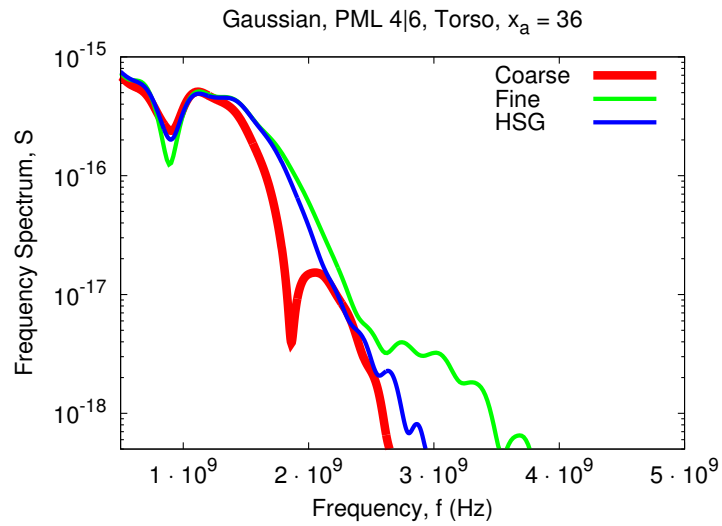

(a) Time domain signal, $R_{xa} = 36$

(b) Frequency domain signal, $R_{xa} = 36$
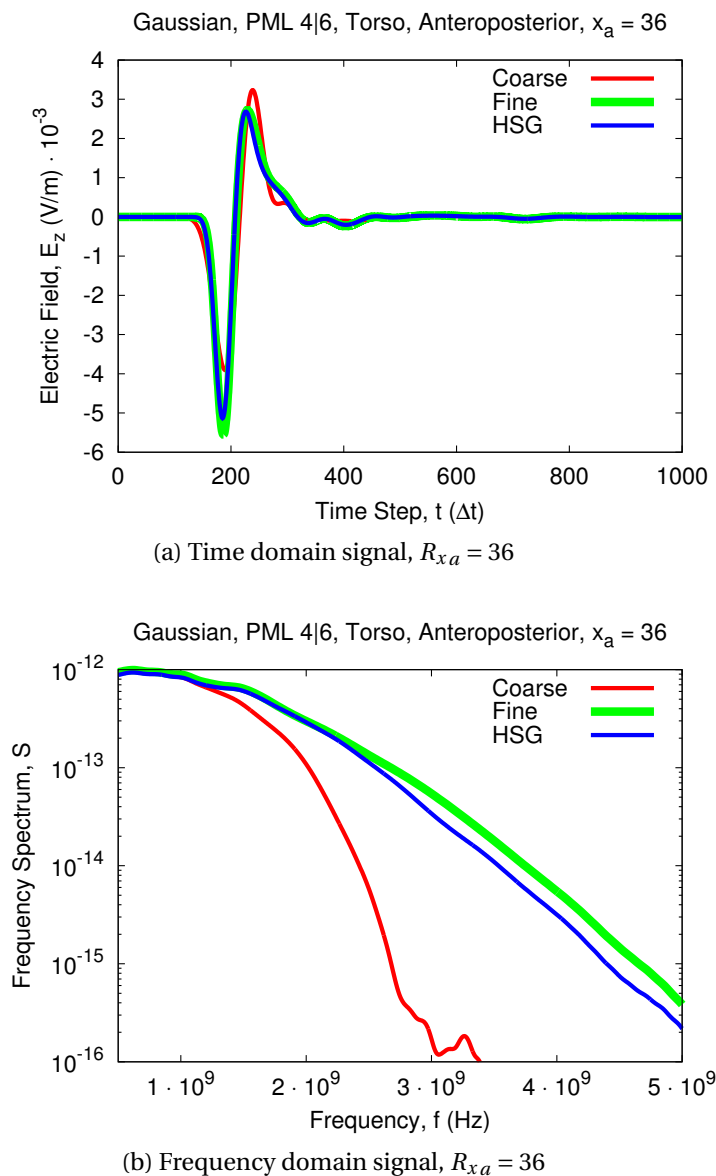
Figure 6.28: Scenario of human torso. Defibrillator pads excitation. Strong initial signal from the pad allows to preserve high signal amplitudes.

6.14 HSG Computational Requirements

A special scenario was developed to test the HSG method's computational requirements. HSG with the main grid size of 80^3 and variable subgrid sizes of 75^3, 100^3, 125^3, 150^3, 175^3 and 200^3 were run for 100 main grid time steps. Each subgrid edge is comprised of 2 PML, 2 buffering zones, 2 OS–IS separations and 1 effective subgrid size (the volume bound by IS), e.g. the subgrid edge of 75 is obtained as $(2 \times 5) + (2 \times 5) + (2 \times 15) + 25$. PML thickness of 5 was used for both main and subgrids. Buffering zone of 5 subgrid points separated the PML from the OS–IS interface. OS–IS interface thickness equalled to 15 subgrid points. The effective subgrid size changed from 25 to 150 with a stepping of 25 subgrid points. Subgridding ratio remained constant at $r = 5$. Spatial and temporal increments were set to $\Delta s_a = 10$ mm, $\Delta s_b = 2$ mm and $\Delta t_a = 0.179$ ps, $\Delta t_b = 3.582$ ps with the CFL number of $N_{CFL} = 0.93$.

The HSG computational requirements tests were executed on a high specification system with 32 processing units (8 CPU with 4 cores each) and 96 GB of memory. Further details of the testing system are given in Table 6.6.

Parameter	Value
Operating System	Scientific Linux SL 5.5 (Boron)
Kernel	2.6.18-194.26.1el5
CPU Specification	Intel Xeon E5620 @ 2.4 GHz
Cache	12 MB
Cores	4
Address sizes	40 bits physical
	48 bits virtual
CPU Total	8
Memory Total	96 GB

Table 6.6: Testing system specification

Table 6.7 presents the CPU time and memory requirements of the HSG method. Efficiency data for the coarse grid only and the fine grid only FDTD cases is given for comparison purposes. First column entitled "Case" contains the test case description, where the word "Coarse", "Fine" or "HSG" specifies the simulation method and the number defines the domain edge size, e.g. "Coarse, 80" refers to the all coarse grid test case with an edge size of 80 coarse grid points and "HSG, 75" refers to the HSG test case with a subgrid edge size of 75. Memory usage data in MB and percent

(%) is given in columns two and three, where percent data shows the memory usage in percent relative to the all fine grid reference "Fine, 400". Percent data is calculated according to (6.12):

$$M_\% = \frac{M_{HSG}}{M_{Fine}} \cdot 100\%, \tag{6.12}$$

where M_{HSG} and M_{Fine} stand for the HSG and all fine grid memory use in MB, and the HSG case includes both the main and the subgrid of the HSG. The memory use data was obtained with the UNIX command line utility `top` as the resident size non-swapped physical memory a task has used, listed under column `RES` in the `top` program interface.

Case	Memory		CPU Time			Subgrid Size	
	MB	%	min:s	s	%	points	%
Coarse, 80	128	2.08	0:14	14	0.16	0	0.00
HSG, 75	142	2.31	1:48	108	1.25	75^3	18.75
HSG, 100	213	3.46	5:32	332	3.83	100^3	25.00
HSG, 125	322	5.23	15:11	911	10.51	125^3	31.25
HSG, 150	476	7.73	28:33	1713	19.77	150^3	37.50
HSG, 175	683	11.09	47:29	2849	32.88	175^3	43.75
HSG, 200	952	15.46	80:06	4806	55.46	200^3	50.00
Fine, 400	6159	100.00	144:26	8666	100.00	400^3	100.00

Table 6.7: CPU time and memory requirements of HSG

The next three columns in Table 6.7 present the total execution time used by the test case. The time is shown in minutes and seconds, seconds only, and percent. Time in percent is given relative to the all fine grid case and is calculated using (6.13):

$$T_\% = \frac{T_{HSG}}{T_{Fine}} \cdot 100\%, \tag{6.13}$$

where T_{HSG} and T_{Fine} denote the HSG and all fine grid execution time is seconds. Execution time data was measured with the UNIX command line utility `time`. The time data presented in Table 6.7 is a sum of the user and system time as given by the `time` utility. Here user time is the CPU time the process has spent in user mode (outside of the kernel) and the system time is the CPU time the process has spent in the kernel mode. Each CPU time measurement includes the time elapsed for the entire simulation, i.e. the input parameter reading, simulation initialisation, setting of radio environment, material coefficients calculation, Gaussian pulse generation,

FDTD field updates in the main and the subgrid for the duration of the simulation and the simulation finalisation.

Last two columns to the right in Table 6.7 show the HSG subgrid size in fine grid points and in percent relative to the all fine grid case "Fine, 400". Subgrid size in percent is calculated according to (6.14):

$$S_{\%} = \frac{S_{HSG}}{S_{Fine}} \cdot 100\%, \tag{6.14}$$

where S_{HSG} and S_{Fine} signify the subgrid size in the HSG and total domain size in the all fine grid case.

According to Table 6.7 the HSG relative memory and time consumption grow with the increase of the subgrid size. However, the increase in memory use is subtle in comparison with the time increase, e.g. for the case "HSG, 125" time consumption of 10.51% is double the memory consumption of 5.23%. Another important remark is that the computation time depends on the subgridding ratio. The time will increase even faster for higher ratios. This is due to growth of the subgrid time loop iterations relative to one main grid iteration. Intuition supported by the computational requirements data in Table 6.7 suggests that the HSG method is most efficient when the subgrid occupies only a small fraction of the entire computation domain and the subgridding ratio is kept relatively low.[7] For 3D applications Bérenger [102] recommends using the ratios in the order of 30. Accurate results with the ratios of $r = 5, 11, 15$ were published in [100, 102]. Unfortunately, the CPU time and memory requirements of the HSG implementation with these ratios have not been reported. More experiments with various subgridding ratios are required to identify (i) whether the dependency of the CPU time on the subgridding ratio is linear or exponential and (ii) the subgridding ratio influences the HSG time and memory efficiency.

Figure 6.29 illustrates the HSG memory consumption depending on the subgrid size. Abscissa shows the subgrid size relative to the main grid size and ordinate— the HSG memory usage relative to the all fine grid memory usage. For example, in case of HSG, 75 the x-axis value is calculated as $(75/5/80)^3$, where 75 is the subgrid size in subgrid points S_{HSG}, 5 is the subgridding ratio r and 80 is the main grid size in main grid points. The y-axis value is calculated as $142/6159$, where 142 is

---

[7]Subgridding ratio in 3D should be relatively low with respect to the ratios of 2D and 1D cases. In 2D the HSG method was successfully applied with $r = 11, 33, 99$ [98, 101] and in 1D with $r = 99$ [99].

the memory use of the HSG M_{HSG} (main and subgrid together) in MB, and 6159 is the memory consumption of the all fine grid M_{Fine} in MB. Crosses in Figure 6.29 highlight the data values obtained experimentally, while the continuous lines represent the fitted curves. Curves were fitted by means of the `fit` command of the `gnuplot` interactive plotting utility. The `fit` command implements the Non-Linear Least-Squares (NLLS) Levenberg–Marquardt algorithm [147, pp. 58–64]. Three fitting functions were used to fit the memory requirements data: exponential, linear and power. The functions with their final coefficient values are given in Table 6.8.

Exponential	**Linear**	**Power**
$\Omega_1(l) = a \cdot \exp(b \cdot l)$	$\Omega_2(l) = d \cdot l + e$	$\Omega_3(l) = g \cdot l^h$
$a = 0.0353759$	$d = 1.10634$	$g = 0.704369$
$b = 12.1382$	$e = 0.0175081$	$h = 0.737731$

Table 6.8: Fitting functions and final coefficient values for HSG memory requirements data fitting

The exponential fitting function $\Omega_1(l)$ with the initial coefficient values of $a_0 = 0.1$, $b_0 = 0.2$ converged after 7 iterations, the linear fitting function $\Omega_2(l)$ with the initial coefficient values of $d_0 = 0.1$, $e_0 = 0.2$ converged after 5 iterations and the power fitting function $\Omega_3(l)$ with the initial coefficient values of $g_0 = 0.1$, $h_0 = 0.2$ converged after 7 iterations.

Three fitting functions were applied to the memory consumption data to provide the best possible curve fit. The fitting functions are denoted as `exp()`, `lin()` and `pow()` in Figure 6.29. Due to relatively small amount of experimental data it is hard to identify the memory consumption dependency over the grid size. According to the `gnuplot` utility the linear function had the smallest standard deviation of the fit $S_{dev} = 1.43465 \cdot 10^{-3}$ compared with $3.84815 \cdot 10^{-3}$ for the power function and $1.24786 \cdot 10^{-2}$ for the exponential function. The standard deviation of the fit is the Root Mean Square (RMS) of residuals and is calculated as:

$$S_{dev} = \sqrt{\frac{WSSR}{ndf}}, \qquad (6.15)$$

where $WSSR$ is the Weighted Sum-of-Squares Residual and ndf is the number of degrees of freedom. Parameter ndf is the number of data points minus the number of fitted parameters [147, p. 61].

Careful analysis of the lower part of Figure 6.29 shows that the dependency is

linear, but it is unlikely that the dependency will stay linear for larger relative subgrid sizes. Therefore, it was decided to choose the most restrictive exponential function for the relative HSG memory requirements estimation. Using the subgridding ratio of 5 the HSG memory consumption will reach the all fine grid when the HSG subgrid size is approximately 0.27 of the main grid. It is beneficial to apply the HSG with the subgridding ratio of 5 when the subgrid region occupies less than 27% of the main grid.
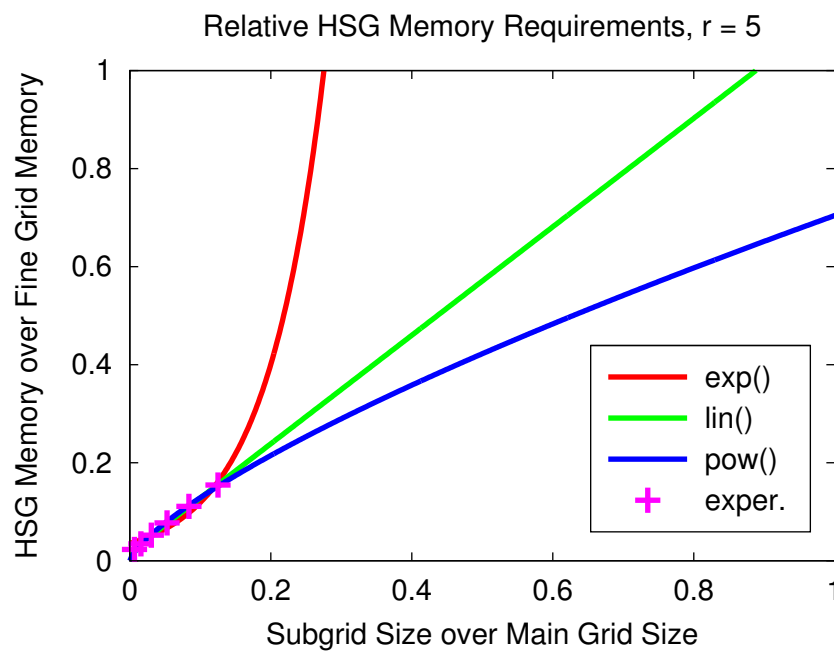
Figure 6.29: HSG memory consumption relative to all fine grid case

Figure 6.30 presents the HSG execution time depending on the subgrid size. Abscissa shows the HSG subgrid size relative to the main grid size and ordinate—the HSG CPU time usage relative to the all fine grid CPU time usage. For example, in case of HSG, 75 the x-axis value is calculated as $(75/5/80)^3$ where 75 is the subgrid size given in subgrid points S_{HSG}, 5 is the subgridding ratio r and 80 is the main grid size in main grid points. The y-axis value is derived as 108/8666, where 108 is the CPU time usage of HSG in seconds T_{HSG} and 8666 is the CPU time consumption of the all fine grid in seconds T_{Fine}. Crosses in Figure 6.30 illustrate the data values obtained experimentally and the continuous lines represent the fitted curves.

Curve fitting was conducted by means of the `fit` command of the `gnuplot` utility [147, pp. 58–64] using similar fitting functions as in the memory requirements

test case. The exponential, linear and power data fitting functions are listed in Table 6.9. Exponential function in Table 6.9 differs from the exponential function in Table 6.8, since the function $a^l + b$ provided a better fit for the CPU time requirements than the function $a \cdot \exp(b \cdot l)$.

Exponential	Linear	Power
$\Omega_1(l) = a^l + b$	$\Omega_2(l) = c \cdot l + d$	$\Omega_3(l) = e \cdot l^g$
$a = 36.1352$	$c = 4.55588$	$e = 6.99934$
$b = -1.01414$	$d = -0.0324328$	$g = 1.22191$

Table 6.9: Fitting functions and final coefficient values for HSG CPU time requirements data fitting

The exponential fitting function $\Omega_1(l)$ with the initial coefficients $a_0 = 0.1$, $b_0 = 0.2$ converged after 9 iterations, the linear fitting function $\Omega_2(l)$ with the initial coefficients $c_0 = 0.1$, $d_0 = 0.2$ converged after 5 iterations and the power fitting function $\Omega_3(l)$ with the initial coefficients $e_0 = 0.1$, $g_0 = 0.2$ converged after 17 iterations. Three fitting functions produced similar results. The exponential function had the smallest standard deviation of the fit $S_{dev} = 5.57501 \cdot 10^{-3}$ The second-best fit was obtained with the power function $S_{dev} = 7.14865 \cdot 10^{-3}$ Linear function resulted in the worst fit with $S_{dev} = 1.61753 \cdot 10^{-2}$

Careful analysis of the experimental data in Figure 6.30 shows that the exponential and power functions provide better curve fits. Selecting the most restrictive exponential function, the HSG CPU time use will reach the all fine grid time consumption when the subgrid size occupies approximately 20% of the main grid.

The HSG time requirements are higher than the memory requirements. The time requirements exponential curve exhibits a steeper growth, which is explained by the HSG algorithm. To synchronise the EM-field calculation in both grids the HSG has to execute r subgrid iterations for each main grid step. Field update in the subgrid requires more computational effort for a larger subgrid. Figure 6.30 shows that it is beneficial to use the HSG method with a subgridding ratio of 5 up to the subgrid sizes occupying less than 20% of the main grid.

For the subgrid sizes covering below 7.5% of the main grid the HSG computation time will constitute approximately 1/5 of the all fine grid time, i.e. the time requirements will be proportional to the subgridding ratio $r = 5$. The HSG time usage for the subgrid sizes over 7.5% of the main grid exhibits a steep exponential growth. It is still beneficial to use HSG for large subgrid sizes ranging from 7.5–20% of the main

grid size, but the benefit will constitute a fraction of rather than the full subgridding ratio.
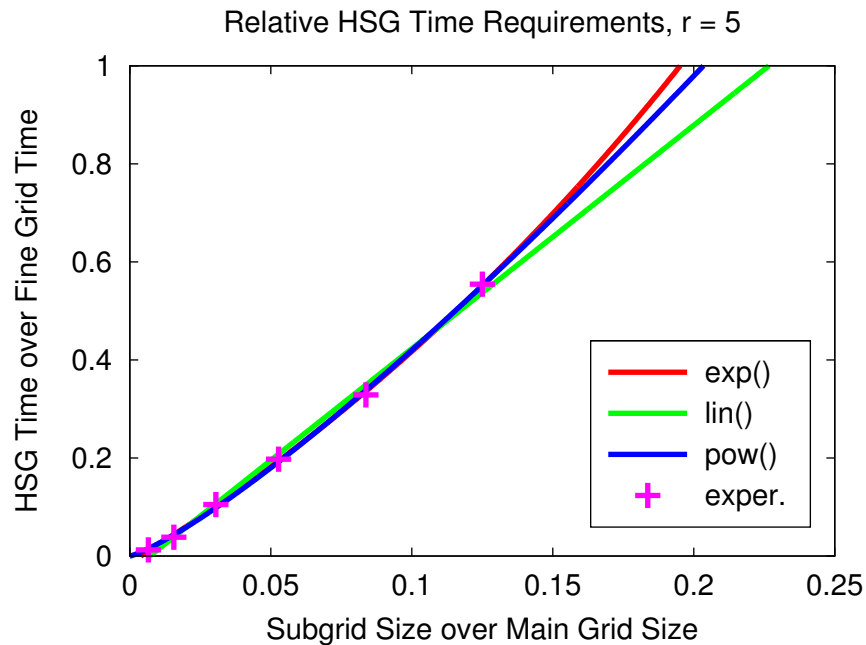
Figure 6.30: HSG time consumption relative to all fine grid case

6.15 Conclusion

Numerical results presented in this chapter verify the expected HSG performance: due to high spatio-temporal resolution in the subgrid and low in the main grid the HSG outperforms the coarse grid case in accuracy and the fine grid case in computation speed. The HSG method increases transferable frequency range compared with the all coarse grid case. Dispersive materials covering the OS–IS interface contribute to a delay in the visibility of HSG instability. No instability was visible in any of the test cases where Debye medium crossed the subgridding interface. Realistic test case with the human torso shows a possible HSG application area as an efficient tool for defibrillation parameter optimisation. HSG efficiency tests show that memory usage exhibits linear and the CPU time usage exponential growth relative to the increase of the subgrid size. However, more practical experiments are required to verify the linear or exponential memory use dependency of the HSG. The HSG memory and time efficiency tests identified the computation time to be

a more critical performance factor than the memory usage. The HSG method with $r = 5$ outperforms the all fine grid case in terms of CPU time for the subgrid sizes constituting less than 20% of the main grid.

Chapter 7

Conclusion

This chapter highlights the major and minor contributions of the research project described in this dissertation.

Subgridding approaches decompose the simulation domain into a number of subdomains with the coarse and fine spatio-temporal resolutions. The computational efficiency of the FDTD method is increased, because the CFL criterion is maintained independently in each grid. This work adopted a very promising subgridding technique called the Huygens Subgridding (HSG).

The main contribution of this research project is the extension of the frequency-dependent HSG method from one dimension (1D) to three dimensions (3D). The new algorithm, in short termed the dispersive HSG, enables an efficient simulation of electromagnetic wave propagation inside the frequency-dependent materials. The frequency dependency was implemented via the Auxiliary Differential Equation (ADE) approach using the one pole Debye relaxation model. The dispersive HSG program was written using an existing Fortran code containing the classical HSG method.

Minor contributions of this work included: (i) the implementation of the radio environment setting functionality using the PGM-files, (ii) the development of an application test case, simulating the wave propagation from the defibrillator pads through the human torso and (iii) the analysis of computational requirements of the dispersive HSG code with the subgridding ratio of 5. Numerical experiments show that the dispersive HSG program with the subgridding ratio of 5 outperforms the all fine grid FDTD program, when the subgrid size occupies less than 20% of the main grid.

The future research directions that can be pursued on the basis of this project

are described in Chapter 8.

Chapter 8

Future Work

This chapter discusses the potential directions for future work that can be undertaken on the dispersive HSG method.

The frequency dispersive HSG project offers a solid base for investigation of the following research questions. The problems for future work are grouped into three categories addressing the HSG method's stability, realistic simulation of defibrillation current and efficiency.

8.1 Stability

The instability remains the major hurdle limiting the general acceptance of the HSG method for a broad range of numerical simulations. Future research ideas presented below can help to reduce or eliminate the native HSG instability:

Decoupling of spatial and temporal interfaces in the HSG approach to decrease and potentially eliminate the late-time instability. As suggested by [41, 78, 79, 89, 90] separation of the spatial and temporal interfaces with a subsequent nesting of temporal interface inside of the spatial solves the problem of instability.

Use of an artificial constant loss with a dispersive gain [105, 106] also can have a positive effect on the HSG stability.

The effect of relative permittivity ε_r on general stability of the HSG method. Although, tested in Section 6.12 the hypothesis of ε_r suppressing the late-time instability requires an in depth testing approach.

Application of an implicit FDTD scheme in the subgrid region can possibly remove
the HSG instability.

8.2   Defibrillation

Application of the dispersive HSG method to calculate the defibrillation current
density and current flow distribution in the human heart. The human torso
simulation scenario should be taken further to investigate the defibrillation
current behaviour for different defibrillator settings.

Implementation and exploration of realistic defibrillator waveforms for the human
torso simulation scenario. To achieve practical results of the defibrillation cur-
rent simulation the Gaussian pulse excitation waveform used in Section 6.13
should be replaced with monophasic and biphasic ascending exponential, as-
cending ramp, rectangular and descending exponential waveshapes [148].

Thin Slab method similar to [146] can be implemented for a correct calculation
of Debye relaxation media parameters in the main grid cells larger than the
medium size. Division of the main grid media parameters by the subgridding
ratio described in Section 6.13.3 is only a temporary measure.

8.3   Efficiency

Parallelisation of the dispersive HSG approach might be undertaken to further
improve the FDTD efficiency. It would be interesting to compare the CPU
and memory performance of the HSG method parallelised with conventional
MPI [149] approach, CUDA [150] or OpenCL [151] and novel truly parallel lan-
guage as Fortress [152] or Chapel [153].

Appendix A

Introduction to Defibrillation

This chapter gives a brief introduction to defibrillation. It explains the general steps of the cardiac cycle and highlights the most important types of heart fibrillation in Appendix A.1. Main part of this work is dedicated to defibrillation phenomenon discussed in Appendix A.2.1. Devices used for defibrillation and their characteristics are described in Appendix A.2.2. Finally, Appendix A.3 of this chapter presents the approaches to study defibrillation with numerical simulation.

A.1 Basic Cardiography

Cells of cardiac conducting system and myocardium[1] are polarised at rest. Between the inside of the cell and the extracellular space exists a potential difference of 90 mV. Rapid shift of calcium and sodium ions across the cell membrane causes cell depolarisation.[2] The cell property to depolarise spontaneously and regularly is called *automaticity*. This depolarisation generates an electrical signal in the heart. The electrical impulse passes through the conducting system of the heart. The contraction of myocardial cells is a mechanical reaction to an electric impulse.

Different parts of heart's conducting system depolarise at different rates (Figure A.1). Fastest 'pacemaker' cells set the cardiac rhythm.

---

[1]"Myocardium—the middle of the three layers forming the wall of the heart (endocardium, myocardium, epicardium). It is composed of cardiac muscle and forms the greater part of the heart wall, being thicker in the ventricles than in the atria." [154]

[2]"Depolarisation—a change in the value of the resting membrane potential towards zero. The inside of the cell becomes less negative compared to the outside. This is due to a change in permeability and migration of sodium ions into the interior of the cell. Depolarisation is excitatory because the membrane potential shifts towards the neuron's threshold at which an action potential occurs." [155]
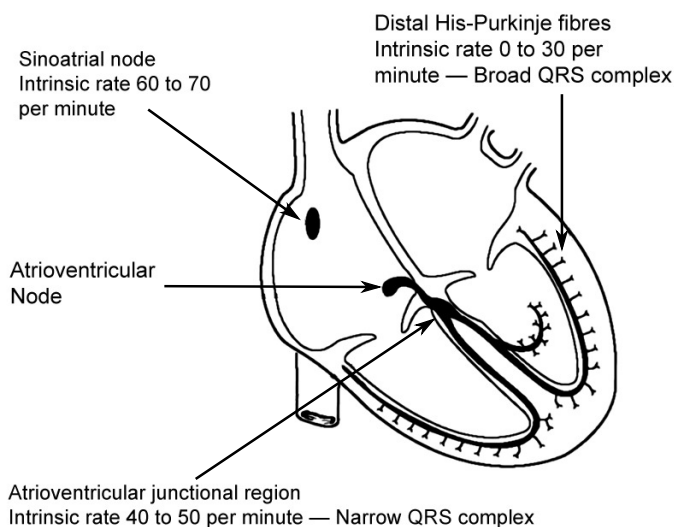
Figure A.1: Cardiac conducting system and rates of spontaneous depolarisation [156]

In a normal sinus rhythm the 'pacemaker' cells in the sinoatrial (SA) node[3] (Figure A.2) start the process of depolarisation.

Then depolarisation spreads through the atrial myocardium and stimulates the atrial contraction. Special tissue called Purkinje fibres conducts the electrical signal to the ventricles. First the impulse is slowly conducted in the atrioventricular (AV) node,[4] followed by a rapid conduction in ventricular myocardium.

Then bundle of His[5] (denoted as "Bundle branches" in Figure A.2) divides the impulse and via the Purkinje fibres passes it to the right and left bundles and ventricles. This rapid electric conduction ensures a well co-ordinated ventricle contraction.

---

[3]"Sinoatrial (SA) node—the pacemaker of the heart: a microscopic area of specialised cardiac muscle located in the upper wall of the right atrium near the entry of the vena cava. Fibres of the SA node are self-excitatory, contracting rhythmically at around 70 times per minute. Following each contraction, the impulse spreads throughout the atrial muscle and into fibres connecting the SA node with the atrioventricular node. The SA node is supplied by fibres of the autonomic nervous system; impulses arriving at the node accelerate or decrease the heart rate." [154]

[4]"Atrioventricular (AV) node—a mass of modified heart muscle situated in the lower middle part of the right atrium. It receives the impulse to contract from the sinoatrial node, via the atria, and transmits it through the atrioventricular bundle to the ventricles." [154]

[5]"Bundle of His (atrioventricular bundle, AV bundle)—a bundle of modified heart muscle fibres (Purkinje fibres) passing from the atrioventricular (AV) node forward to the septum between the ventricles, where it divides into right and left bundles, one for each ventricle. The fibres transmit contraction waves from the atria, via the AV node, to the ventricles." [154]

SA node

STEP 1:
SA node activity and atrial activation begin.

Time = 0

STEP 2:
Stimulus spreads across the atrial surfaces and reaches the AV node.

Elapsed time = 50 msec

AV node

STEP 3:
There is a 100-msec delay at the AV node. Atrial contraction begins.

Elapsed time = 150 msec

Bundle branches

AV bundle

Moderator band

STEP 4:
The impulse travels along the interventricular septum within the AV bundle and the bundle branches to the Purkinje fibers and, via the moderator band, to the papillary muscles of the right ventricle.

Elapsed time = 175 msec

STEP 5:
The impulse is distributed by Purkinje fibers and relayed throughout the ventricular myocardium. Atrial contraction is completed, and ventricular contraction begins.

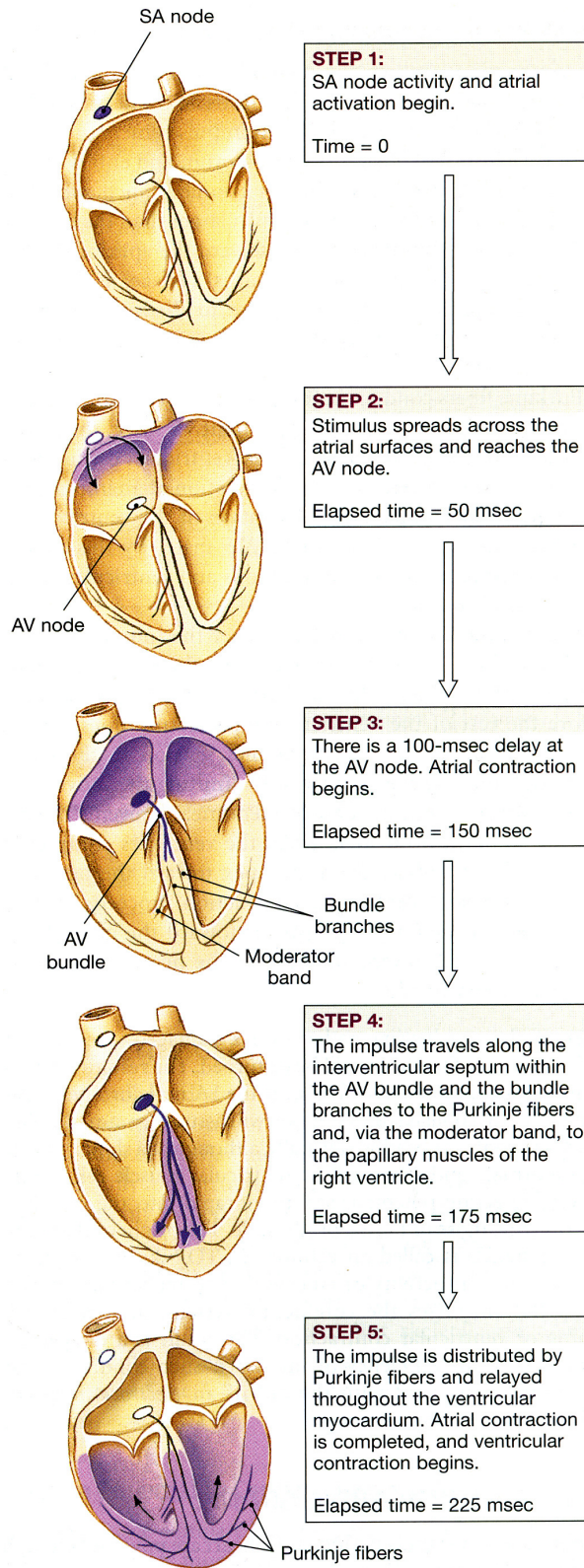Elapsed time = 225 msec

Purkinje fibers

Figure A.2: Electric impulse conduction through heart [157]

Figure A.3 shows one period of the electrocardiogram (ECG) for a normal sinus rhythm (Figure A.4a). Atrial contraction is indicated as a P wave. The peaks of the QRS complex are the depolarisation of bundle of His, left and right branches and the ventricular myocardium. T wave peak illustrates the potential recovery in the cells of conducting system and ventricular myocardium. Normal QRS complex lasts for 0.12 s.
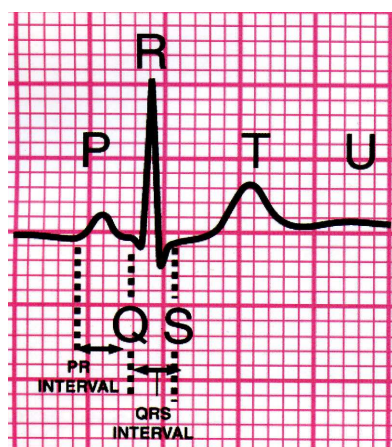

Figure A.3: Normal ECG signal components [156]. Abscissa shows the time and ordinate—the voltage.

Cardiac arrest rhythms include Ventricular Fibrillation (VF)[6] (Figures A.4b and A.4c), some cases of Ventricular Tachycardia (VT)[7] (Figures A.4d to A.4f), asystole and Pulseless Electrical Activity (PEA). AF (Figure A.4g) is the most common form of arrhythmia. *All of these cardiac arrest rhythms are treated with defibrillation.*

---

[6]"Fibrillation—chaotic electrical and mechanical activity of a heart chamber, which results in loss of synchronous contraction. The affected part of the heart then ceases to pump blood. Fibrillation may affect the atria or ventricles independently. In atrial fibrillation (a common type of arrhythmia), the chaotic electrical activity of the atria is conducted to the ventricles in a random manner resulting in a rapid and irregular pulse rate. When ventricular fibrillation occurs the ventricles stop beating. It is most commonly the result of myocardial infarction." [154]

[7]"Ventricular Tachycardia (VT)—a dangerously fast beating of the heart stemming from an abnormal focus of electrical activity in the ventricles. The electricity does not pass through the heart along the usual channels and as a result the contraction of the heart muscle is often not as efficient as normal, which can result in a sudden drop in blood pressure or even cardiac arrest." [154]
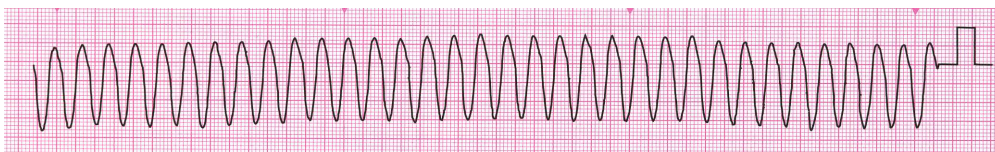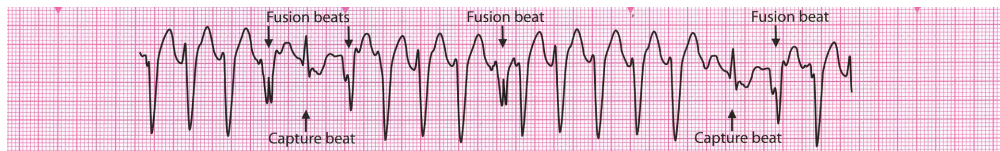
(a) Normal Sinus Rhythm
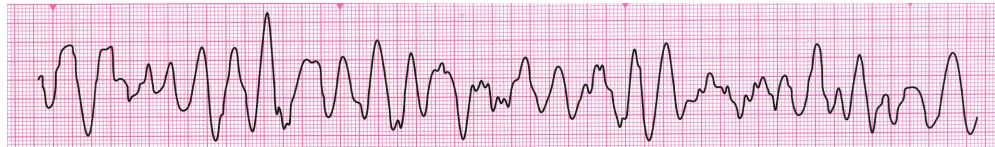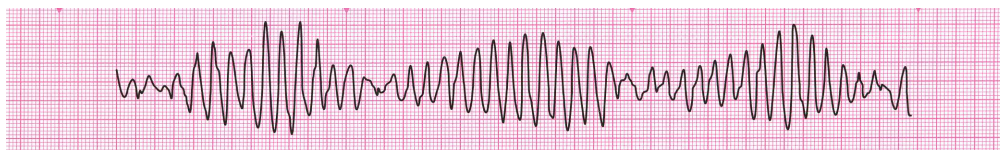
(b) Coarse Ventricular Fibrillation

(c) Fine Ventricular Fibrillation

(d) Monomorphic Ventricular Tachycardia

(e) Ventricular Tachycardia with Capture and Fusion Beats

(f) Ventricular Tachycardia Torsade de Pointes

(g) Atrial Fibrillation

Figure A.4: Important ECG Rhythms [156]. Abscissa shows the time and ordinate—the voltage.

A.2   Defibrillation

A.2.1   General Knowledge

In Europe approximately 700000 deaths a year are accredited to a sudden cardiac arrest [158]. The only effective therapy for a cardiac arrest caused by VF or VT is electrical *defibrillation.* No drugs have similar positive effect on restoration of the cardiac function.

With the onset of ventricular fibrillation or pulseless ventricular tachycardia the cardiac output ceases. Within 3 min begins the cerebral hypoxic injury. Conduction of an early successful defibrillation is vital to achieve complete neurological recovery.

"Defibrillation is the passage of an electrical current of sufficient magnitude to depolarise a critical mass of myocardium and enable restoration of coordinated electrical activity." [159] Defibrillation success rate decreases by 7–10% (without Cardiopulmonary Resuscitation (CPR)[8]) and by 3–4% (with CPR: 30 compressions, 2 ventilations) for every minute passing after the collapse. Figure A.5 shows the effect of time delay on the success of defibrillation. Figure A.6 illustrates a drastic decrease of amplitude strength with time in VF. Defibrillation is successful if no VF or VT exists 5 s after the shock delivery. But ultimately the return of spontaneous circulation (ROSC) is required.

Success of defibrillation is proportional to the the amount of current transferred to myocardium. The necessary amount of current is difficult to identify. It depends on a number of factors: the transthoracic impedance (TTI), electrode position, patient's metabolic state, extent of myocardial ishaemia and the previous drug therapy. TTI is defined as the human body resistance to electric current [161]. TTI is influenced by an electrode-to-skin contact, body size, electrode or paddle size, paddle–skin coupling material, paddle force and the phase of ventilation [156, 160]. For a normal adult TTI varies between 70 and 80 Ω. But using an incorrect technique for

---

[8]"Cardiopulmonary Resuscitation (CPR)—an emergency procedure for life support, consisting of artificial respiration and manual external cardiac massage. It is used in cases of cardiac arrest or apparent sudden death resulting from electric shock, drowning, respiratory arrest, or other causes, to establish effective circulation and ventilation in order to prevent irreversible brain damage. External cardiac massage compresses the heart, forcing blood into the systemic and pulmonary circulation; venous blood refills the heart when the compression is released. Mouth-to-mouth resuscitation or a mechanical form of ventilation oxygenates the blood being pumped through the circulatory system." [154]
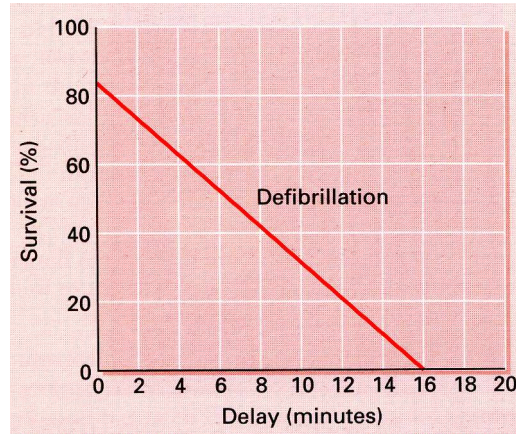
Figure A.5: Effect of time on defibrillation success [160]

(a) Onset

(b) 5 min

(c) 10 min
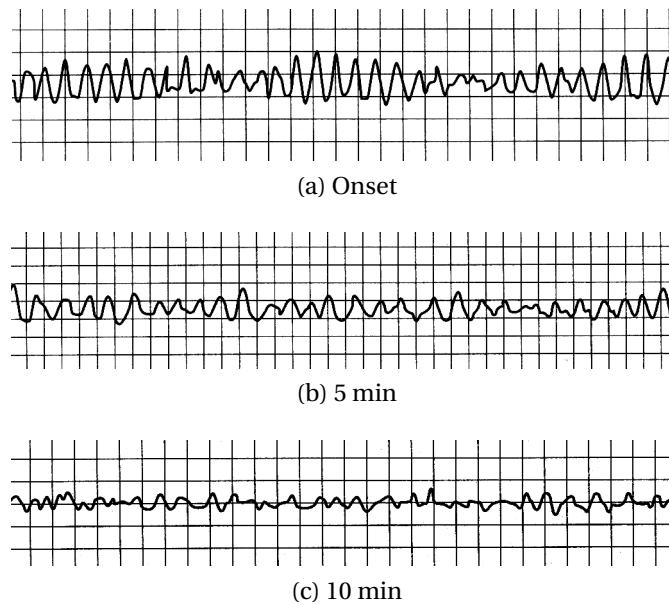
Figure A.6: Amplitude deterioration with time in VF [160]. Abscissa shows the time and ordinate—the voltage.

defibrillation might cause TTI increase up to 150 Ω. Some modern defibrillators have an impedance compensation functionality. They can measure the TTI and automatically adjust the current required for defibrillation.

(a) Manual Defibrillator   (b) Automated External Defibrillator
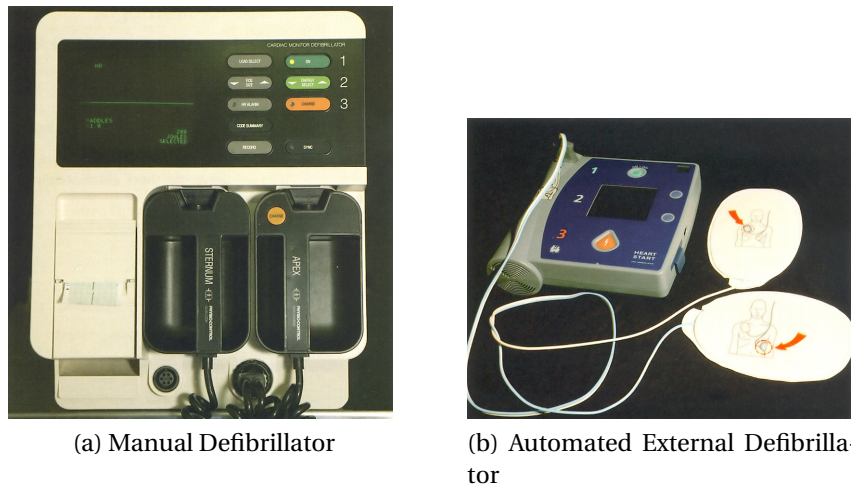
Figure A.7: Defibrillator Types [156]

A.2.2   Defibrillator Devices

Manual and Automated Defibrillators

All defibrillators consist of three major parts: (i) power source to provide direct current (DC), (ii) capacitor to contain the electric energy and (iii) electrodes, that conduct current through the patient's chest at capacitor's discharge. Two types of defibrillators—manual defibrillator (MD) and automated external defibrillator (AED) are shown in Figure A.7. Operating manual defibrillators requires high level of medical expertise, while use of automated external defibrillators is relatively simple and intended for lay users. Most AED models are equipped with audio and visual guides and will direct the user during the defibrillation process. AED can analyse victim's rhythm, determine a need for shock and deliver the shock [158]. AED is safer to use, since the self-adhesive paddles allow the operator to discharge the current from a distance. While operating an MD the user has to lean over the patient. Self-adhesive paddles of AED also enable quicker delivery of the electric shock [156].

Electrode Shape

There is no clear recommendation on the optimal electrode shape. Most industrial defibrillators have electrodes of a rectangular form with one direction longer than another and rounded corners [156, 161–163].

Electrode Size

Electrode size is inversely proportional to the transthoracic impedance. Larger electrodes can successfully defibrillate a patient with higher TTI value. On the other hand a size balance is important, since larger electrodes might overdose a patient with lower TTI value [161, 164]. Sum of both defibrillator electrode areas should be larger than 150 cm^2. Diameter of handheld and self-adhesive electrodes used in practice is in the range of 8 to 12 cm [156, 162, 165, 166].

Electrode Placement

Only 4% of the discharged current will reach the heart, the rest will be diverted by other body parts [156]. Therefore electrodes should be positioned to maximise the current flow through the heart. Fibrillating area of the heart (ventricles in VF, atria in Atrial Fibrillation (AF)) should lie directly beneath the electrodes.

VF or VT, Sterno-apical: sternal electrode should be placed to the upper right part of the sternum and apical electrode should be centred over the 5th left intercostal space in the mid-axillary line, corresponding to the cardiac apex, approximately level with the V6 ECG electrode or the female breast. To reduce impedance the long side of the latter electrode should lie parallel to the mid-axillary axis [156, 159, 160]. Figure A.8 illustrates the standard electrode placement.

AF, Anteroposterior: one electrode is placed anteriorly, over the left precordium, and the other on the back, behind the heart, inferior to the left scapula [156, 167–169].

Alternatively: bi-axillary electrode placement can be used. Electrodes are situated on the left and right sides of lateral chest walls.

Figure A.8: Standard electrode positions for defibrillation [156]

A.2.3   Defibrillator Waveforms

There exist two main resuscitation strategies: first utilises single defibrillation shock followed by CPR and the second three-shock defibrillation with CPR. Modern defibrillators use two types of current waveforms: *monophasic*, with direct current flowing in only one direction and *biphasic* with current flowing in positive and then negative direction.

No published research exists comparing the single- versus three-shock sequence of defibrillation. But the first-shock efficacy of biphasic defibrillators for a long duration VF or VT is 86–98%, compared with 54–91% of monophasic [156]. Therefore the latest edition of Resuscitation Guidelines [158] recommends a single-shock strategy with a biphasic defibrillator. Monophasic devices are not manufactured anymore, but are still being used in various places.

Suggested current and energy levels for monophasic defibrillator are 30–40 A, 360 J and 15–20 A, 120–150 J for biphasic [156].

Monophasic defibrillators use damped sinusoidal waveform (Figure A.9a). Biphasic defibrillators apply Biphasic Truncated Exponential (BTE) (Figure A.9b) or Rectilinear Biphasic (RLB) (Figure A.9c) waveform. Minimum levels for the initial biphasic shock energy should be 150 J for BTE and 120 J for RLB. Usually a default value of 200 J is pre-set in modern defibrillators. There is no clear evidence supporting the fixed or escalating energy protocol for every consecutive shock [158].

Current and energy are the important parameters for defibrillation. Previously more emphasis was placed on the energy setting. Resuscitation guidelines [158] identify the need to shift from the energy-based to current-based defibrillation, since
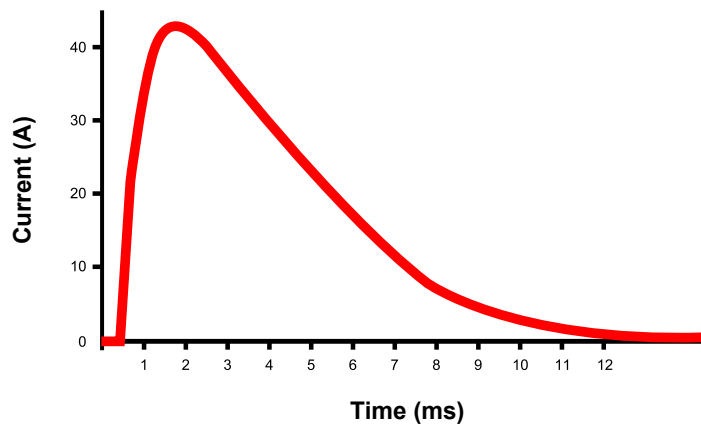
(a) Monophasic Damped Sinusoidal
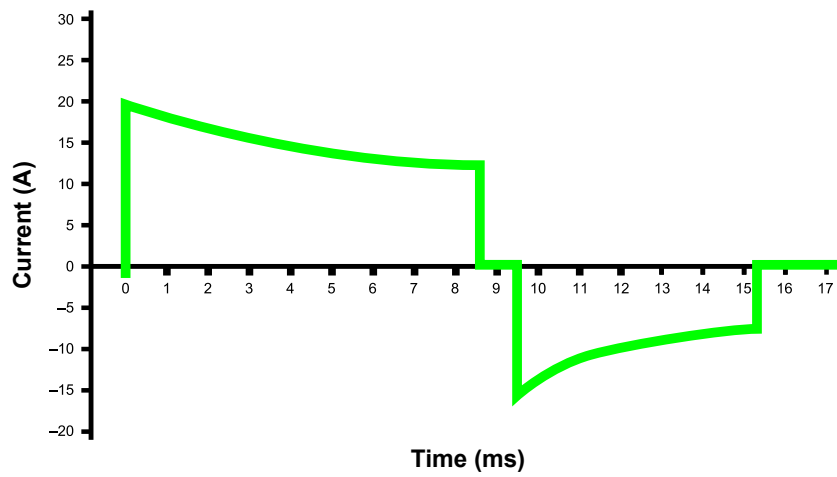
(b) Biphasic Truncated Exponential (BTE)
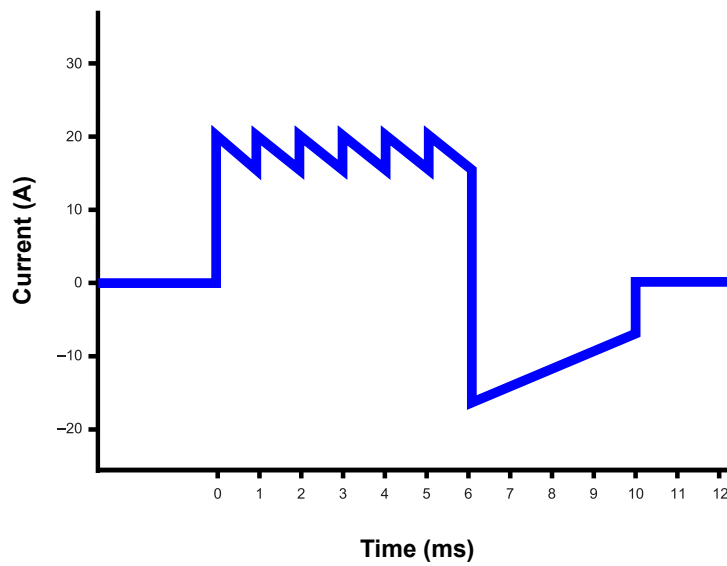
(c) Rectilinear Biphasic (RLB)

Figure A.9: Modern waveforms [156]

it is the current that achieves the actual defibrillation. Peak current amplitude, average current and the phase duration are the parameters that should be studied.

Modern research on optimal waveforms for defibrillators should consider such factors as the amount of energy delivered to the patient, peak current, energy to be stored in the capacitor and the maximum voltage of operation. To improve defibrillator efficacy a waveform should be of low energy and low peak current [164]. Biphasic waveform is more effective at cardioversion of atrial and ventricular arrhythmias at lower energy levels [159]. Work conducted by Schönegg and Bolz [164] suggests that modern waveforms are not definitely superior to historic waveforms. Gurvich waveform [170] provides the best defined simulation with different impedances. BTE was found to be less sufficient with high TTI and capable of overdosing a patient with low TTI. Moreover, the electric impulse durations in modern waveforms are longer than needed.
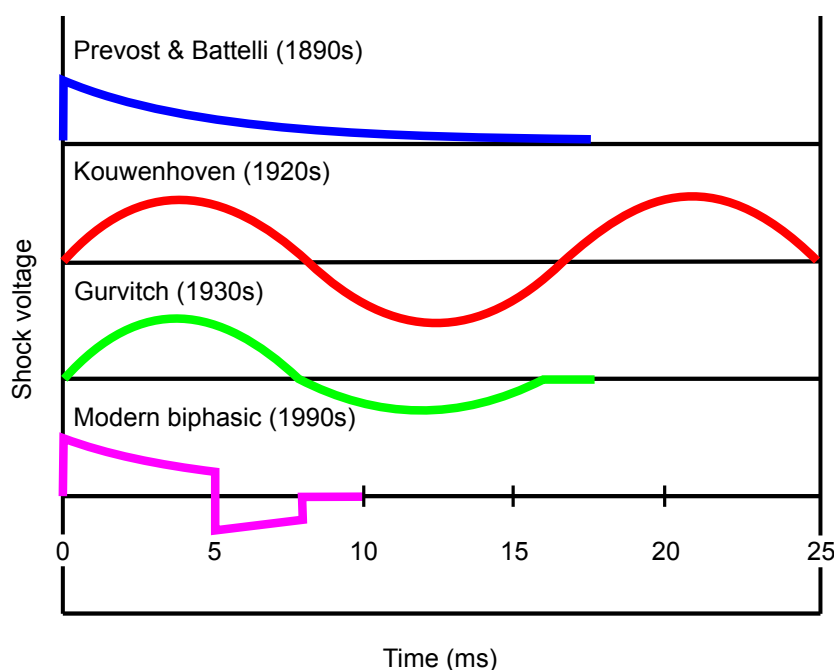
Figure A.10: Waveform evolution [170, 171]

Figure A.10 illustrates evolution of the defibrillator waveform. Naum Gurvich worked in the USSR and first published a biphasic defibrillator waveform in 1939. Due to the Iron Curtain there was little scientific communication between the USSR and other countries. Biphasic waveform was independently discovered by Bernard Lown in the USA in the 1960s. The term Lown waveform is more common in the Western literature, than the Gurvich waveform, but both terms refer to the biphasic

defibrillator waveform [170, 171].

A.3 Numerical Simulation of Defibrillation

A.3.1 Application of Computational Electromagnetics

In general two Computational Electromagnetics (CEM) methods are used to solve Maxwell's equations inside the human body—Finite-Difference Time-Domain (FDTD) and Transmission Line Matrix (TLM) Cell Method [172–175]. In these methods the simulation space is modelled with a three-dimensional (3D) Cartesian grid, where material properties are specified at each grid point. Typical grid resolutions used in FDTD and TLM are 2 mm for the entire human body simulation and 0.8–1.0 mm for the human heart only [172, 174–176].

Strategy to study human body response to defibrillation could consist of the following steps:

1. Calculate peak current densities $J(i, j, k)$ at each point inside and outside of the heart:

$$J(i, j, k) = \sigma(i, j, k) \cdot \sqrt{E_x^2(i, j, k) + E_y^2(i, j, k) + E_z^2(i, j, k)}. \qquad \text{(A.1)}$$

2. Calculate current distribution $I(i, j, k)$ at each point in the heart:

$$I(i, j, k) = J(i, j, k) \cdot S_p. \qquad \text{(A.2)}$$

3. Calculate total current I_{tot} flowing through the heart:

$$I_{tot} = \sum_{p=1}^{P} I(i, j, k), \qquad \text{(A.3)}$$

where

i, j, k grid point coordinates in x, y, z-axes,

σ electric conductivity [S/m],

I electric current [A],

J electric current density $[\text{A/m}^2]$,

E electric field [V/m],

S_p surface area of grid point p,

P total number of surface grid points.

4. Plot energy gradient curves in different areas around the heart.

5. Compare current flow in different areas of the heart for various defibrillation settings.

A.3.2   Explanation of Defibrillation Phenomenon

Knowledge about the restoration of heart function through defibrillation is incomplete. This is due to a complex pattern of current distribution inside ventricles during and after the electric shock. Usually defibrillation is presented as a two step process: (i) shock current is applied to myocardium initiating complex polarisation changes in transmembrane potential distribution, and (ii) potential distribution invokes active membrane reactions that terminate fibrillation wave fronts.

   Two major hypotheses exist, that explain the defibrillation mechanism: Critical Mass (CM) and the Upper Limit of Vulnerability (ULV) [177]. CM states that a critical amount of tissue sustains fibrillation. On the contrary ULV poses that VF must be extinguished everywhere throughout the heart. To achieve complete defibrillation a certain electric potential gradient has to be established everywhere inside the heart. Electric potential is calculated using the FEM applied to the variational formulation of potential field distribution based on the experimental data. Electric potential gradients in x, y, z directions are also calculated with help of FEM and the brick element mesh. Frazier et al. in the Appendix of [178] explain the calculation of electric potential and electric potential gradients in detail.

A.3.3   Approaches to Study Fibrillation

Major approaches to study fibrillation in the human heart are (i) electric current distribution around the heart and (ii) myocardial cell potential method.

Electric current distribution methods such as an electrical computer model [179] and a rheographic model[9] [180] determine the amount of current that will arrive to myocardium cells. Computational electromagnetic methods such as FDTD and TLM can be employed to obtain the electric current distribution.

Myocardial cell potential approach mainly based on bidomain model [181] gave birth to a multitude of schemes: reentry drift [181–184], ventricular anatomy comparison [185], dynamics of scroll wave filaments [185] and Virtual Electrode Pattern (VEP) analysis [177]. Compared to current distribution approach the cell potential approach is better, since it simulates the real behaviour of myocardium cells.

But the most benefit could be achieved combining two approaches [186]. Calculating the electric current distribution with a CEM software first and then using the distribution results in a myocardial cell potential scheme. Applying both approaches will enable an effective study of an optimal defibrillator electrode placement. Important criteria that should be studied are: the amount of energy delivered to the myocardium, electric current density around the heart, energy losses in human body tissues and impedance along the current paths. Each electrode placement can be evaluated according to the highest possible potential difference through the myocardium, homogeneity of current distribution in the heart and the ratio of energy reaching the heart to the total energy delivered [186].

A.3.4 Modelling Defibrillator Waveforms

In CEM software biphasic defibrillator waveforms could be modelled using the generalised Charge-Burping theory. This theory predicts the time course of the cell membrane potential during a biphasic shock pulse. Charge-Burping theory originated in the work of Mark Kroll [187]. Detailed explanation of Charge-Burping equations is given in the appendices to publications of Yoshio Yamanouchi [188, 189].

---

[9]Rheographic model consists of the cross-sections of the thorax at the level of the heart. Each tissue is characterised with electric conductivity values at the elementary cubes of the model. Every elementary cube is represented by six connected resistors. Connected resistor network enables the simulation of anisotropic, nonlinear or capacitor tissue behaviour. The resulting voltage applied between any two or more points of the model can be calculated on a computer. Different potentials of the resistor network nodes are identified with the Kirchhoff's law. Finally, the equipotential lines can be drawn on a thorax cross-section [180].

Appendix B

List of Publications

Refereed Journal Publications

[B1] M. Abaļenkovs, F. Costen, J.-P. Bérenger, R. Himeno and M. Fujii, "Huygens subgridding for 3D frequency-dependent Finite-Difference Time-Domain method," *IEEE Trans. Antennas Propag.*, 2011, accepted with major revisions, to be re-submitted in Nov. 2011.

Refereed Conference Proceedings

[B2] M. Abaļenkovs, F. Costen*, J.-P. Bérenger, R. Himeno and M. Fujii, "Defibrillation optimisation via Huygens subgridding for Finite-Difference Time-Domain method," in *IEEE Antennas Propag. Soc. Intern. Symp.*, Spokane, WA, USA, Jul. 6, 2011.

[B3] M. Abaļenkovs*, F. Costen and J.-P. Bérenger, "Huygens subgridding for Auxiliary Differential Equation–Finite Difference Time Domain," in *IEEE Antennas Propag. Soc. Intern. Symp.*, Charleston, SC, USA, Jun 1–5, 2009.

[B4] M. Abaļenkovs, F. Costen*, J.-P. Bérenger and A. K. Brown, "Application of Huygens subgridding technique to human body modelling," in *IEEE Antennas Propag. Soc. Intern. Symp.*, Jul. 2008.

[B5] M. Abaļenkovs, F. Costen*, C. Lucas and A. K. Brown, "Data format selection for an I/O-intensive large-scale FDTD," in *IEEE Antennas Propag. Soc. Intern.*

Symbol "*" indicates the presenter.

Symp., Jul. 2008.

[B6] M. Abaļenkovs*, F. Costen and A. K. Brown, "Adaptation of HDF5 for FD–FDTD data manipulation tasks," in *IX International PhD Workshop, OWD'2007,* Oct 20–23, 2007.

Posters

[B7] M. Abaļenkovs*, F. Costen, J.-P. Bérenger, R. Himeno and M. Fujii, "Application of Huygens subgridding to study defibrillation in human body," in *3rd Post-graduate Conference of Engineering and Physical Sciences Faculty,* The University of Manchester, UK, Nov. 24, 2010, poster presentation.

[B8] M. Abaļenkovs*, F. Costen and J.-P. Bérenger, "Huygens subgridding with filtering for Finite-Difference Time-Domain method," in *2nd Postgraduate Conference of Engineering and Physical Sciences Faculty,* The University of Manchester, UK, Nov. 25, 2009, poster presentation.

Short Talks

[B9] M. Abaļenkovs*, F. Costen and J.-P. Bérenger, "Huygens subgridding for Frequency-Dependent Finite-Difference Time-Domain method," Jul. 1, 2010, Computational Electromagnetics Meeting, The University of Manchester, UK, short talk.

[B10] M. Abaļenkovs*, L. Cebamanos and F. Costen, "Simulation of electromagnetic wave propagation from an antenna element," Jan. 25, 2008, Manchester SKADS meeting, short talk.

Technical Reports

[B11] Y. D. Zhang and M. Abaļenkovs, C. Argyropoulos, F. Costen and A. K. Brown, "Design study annual report," Microwave and Communication Systems Group, The University of Manchester, UK, Tech. Rep. EU DS4-T6, Sep 5, 2007, SKADS progress report.

Bibliography

[1] D. B. Davidson, *Computational Electromagnetics for RF and Microwave Engineering*. The Edinburgh Building, Cambridge CB2 2RU, UK: Cambridge University Press, 2005.

[2] The FEKO website. Accessed: Mar. 24, 2011. [Online]. Available: http://www.feko.info/

[3] The SuperNEC website. Accessed: Mar. 24, 2011. [Online]. Available: http://www.supernec.com/

[4] The IE3D website. Accessed: Mar. 24, 2011. [Online]. Available: http://www.mentor.com/electromagnetic-simulation/

[5] The GEMACS website. Accessed: Mar. 24, 2011. [Online]. Available: http://www.ara.com/products/GEMACS.htm

[6] The CST Microwave Studio® website. Accessed: Mar. 24, 2011. [Online]. Available: http://www.cst.com/content/products/mws/overview.aspx/

[7] The XFDTD website. Accessed: Mar. 24, 2011. [Online]. Available: http://www.remcom.com/xf7/

[8] T. Namiki, "A new FDTD algorithm based on Alternating-Direction Implicit method," *IEEE Trans. Microw. Theory Tech.*, vol. 47, no. 10, pp. 2003–2007, 1999.

[9] S. Garcia, T. Lee, and S. Hagness, "On the accuracy of the ADI–FDTD method," *IEEE Antennas Wireless Propag. Lett.*, vol. 1, pp. 31–34, 2002.

[10] C. Hafner, *Post-Modern Electromagnetics: Using Intelligent Maxwell Solvers*, 1st ed. Baffins Lane, Chichester, West Sussex, PO19 1UD, England: John Wiley & Sons Ltd, 1999.

[11] The HFSS website. Accessed: Mar. 24, 2011. [Online]. Available: http://www.ansoft.com/products/hf/hfss/

[12] The COMSOL Multiphysics® website. Accessed: Mar. 24, 2011. [Online]. Available: http://www.comsol.com/products/multiphysics/

[13] The MICROSTRIPES™ website. Accessed: Mar. 24, 2011. [Online]. Available: http://www.cst.com/content/products/mst/overview.aspx/

[14] W. Yu, R. Mittra, T. Su, Y. Liu, and X. Yang, *Parallel Finite-Difference Time-Domain Method*. 685 Canton Street, Norwood, MA 02062: Artech House, 2006.

[15] A. F. Peterson, S. L. Ray, and R. Mittra, *Computational Methods for Electromagnetics*, ser. The IEEE/OUP Series on Electromagnetic Wave Theory, D. G. Dudley, Ed. 445 Hoes Lane, P.O. Box 1331, Piscataway, NJ 08855-1331: IEEE Press, Oxford University Press, 1998.

[16] A. Taflove and S. C. Hagness, *Computational Electrodynamics: The Finite-Difference Time-Domain Method*, 3rd ed. 685 Canton Street, Norwood, MA 02062: Artech House, 2005.

[17] J. Hadamard, "Sur les problèmes aux dérivées partielles et leur signification physique," *Princeton Uni. Bull.*, vol. 13, pp. 49–52, 1902.

[18] A. Ribés and F. Schmitt, "Linear inverse problems in imaging," *IEEE Signal Process. Mag.*, vol. 25, no. 4, pp. 84–99, Jul. 2008.

[19] G. Smith, *Numerical Solution of Partial Differential Equations: Finite Difference Methods*, 3rd ed. Great Clarendon Street, Oxford OX2 6DP: Oxford University Press, 1985.

[20] C. O'Brien, M. Hyman, and S. Kaplan, "A study of the numerical solution of partial differential equations," *J. Math. Phys.*, vol. 29, pp. 223–251, 1951.

[21] P. Lax and L. Nirenberg, "On stability for difference schemes: A sharp form of Gårding's inequality," *Comm. Pure Appl. Math.*, vol. 19, pp. 473–492, 1966.

[22] R. Richtmyer and K. Morton, *Difference Methods for Initial-Value Problems*, 2nd ed. New York: Wiley-Interscience, 1967.

[23] K. S. Yee, "Numerical solution of initial boundary value problems involving Maxwell's equations in isotropic media," *IEEE Trans. Antennas Propag.*, vol. 14, no. 3, pp. 302–307, May 1966.

[24] T. Kashiwa and I. Fukai, "A treatment by the FD–TD method of the dispersive characteristics associated with electronic polarization," *Microwave Optical Tech. Lett.*, vol. 3, no. 6, pp. 203–205, 1990.

[25] R. Luebbers, F. Hunsberger, K. Kunz, R. Standler, and M. Schneider, "A frequency-dependent Finite-Difference Time-Domain formulation for dispersive materials," *IEEE Trans. Electromagn. Compat.*, vol. 32, no. 3, pp. 222–227, 1990.

[26] R. Joseph, S. Hagness, and A. Taflove, "Direct time integration of Maxwell's equations in linear dispersive media with absorption for scattering and propagation of femtosecond electromagnetic pulses," *Optics Lett.*, vol. 16, no. 18, pp. 1412–1414, 1991.

[27] J.-P. Bérenger, "A Perfectly Matched Layer for the absorption of electromagnetic waves," *J. Comp. Phys.*, vol. 114, no. 2, pp. 185–200, 1994.

[28] D. Katz, E. Thiele, and A. Taflove, "Validation and extension to three dimensions of the Berenger PML absorbing boundary condition for FD–TD meshes," *IEEE Microw. Guided Wave Lett.*, vol. 4, no. 8, pp. 268–270, 1994.

[29] J. A. Roden and S. D. Gedney, "Convolution PML (CPML): An efficient FDTD implementation of the CFS–PML for arbitrary media," *Microwave Optical Tech. Lett.*, vol. 27, no. 5, pp. 334–339, Oct. 2000.

[30] "Revision of part 15 of the commission's rules regarding Ultra-Wideband transmission systems," Federal Communications Commission, Washington, D.C. 20554, Tech. Rep. FCC 02–48, ET Docket 98–153, Apr. 22, 2002.

[31] A. Thiry, "Efficient FDTD for broadband systems," Ph.D. dissertation, The University of Manchester, School of Electrical and Electronic Engineering, 2006.

[32] H. K. Rouf, "Unconditionally stable Finite-Difference Time-Domain methods for frequency dependent media," Ph.D. dissertation, The University of Manchester, School of Electrical and Electronic Engineering, 2010.

[33] C. Gabriel and S. Gabriel, "Compilation of the dielectric properties of body tissues at RF and microwave frequencies," Physics Dept., King's College London, WC2R 2LS, UK, Tech. Rep. AFB DC 20332–0001, Jun. 1996. [Online]. Available: http://niremf.ifac.cnr.it/docs/DIELECTRIC/Report.html

[34] F. Torres, P. Vaudon, and B. Jecko, "Application of fractional derivatives to the FDTD modeling of pulse propagation in a Cole–Cole dispersive medium," *Microwave Optical Tech. Lett.*, vol. 13, no. 5, pp. 300–304, 1996.

[35] S. Benkler, N. Chavannes, and N. Kuster, "Novel FDTD Huygens source enables highly complex simulation scenarios on ordinary PCs," in *IEEE Antennas Propag. Soc. Intern. Symp.*, 2009.

[36] M. Feliziani and F. Maradei, "Mixed Finite-Difference / Whitney-Elements Time Domain (FD/WE-TD) method," *IEEE Trans. Magn.*, vol. 34, no. 5, pp. 3222–3227, Sep. 1998.

[37] M. W. Chevalier, R. J. Luebbers, and V. P. Cable, "FDTD local grid with material traverse," *IEEE Trans. Antennas Propag.*, vol. 45, no. 3, pp. 411–421, 1997.

[38] I. S. Kim and W. J. Hoefer, "A local mesh refinement algorithm for the Time Domain-Finite Difference method using Maxwell's curl equations," *IEEE Trans. Microw. Theory Tech.*, vol. 38, no. 6, pp. 812–815, Jun. 1990.

[39] S. S. Zivanovic, K. S. Yee, and K. K. Mei, "A subgridding method for the Time-Domain Finite-Difference method to solve Maxwell's equations," *IEEE Trans. Microw. Theory Tech.*, vol. 39, no. 3, pp. 471–479, Mar. 1991.

[40] M. Okoniewski, E. Okoniewska, and M. A. Stuchly, "Three-dimensional sub-gridding algorithm for FDTD," *IEEE Trans. Antennas Propag.*, vol. 45, no. 3, pp. 422–429, Mar. 1997.

[41] K. Xiao, D. J. Pommerenke, and J. L. Drewniak, "A three-dimensional FDTD subgridding method with separate spatial and temporal subgridding interfaces," in *International Symposium on Electromagnetic Compatibility (EMC)*, vol. 2. IEEE, 2005, pp. 578–583.

[42] S. Wang, F. L. Teixeira, R. Lee, and J.-F. Lee, "Optimization of subgridding schemes for FDTD," *IEEE Microw. Wireless Compon. Lett.*, vol. 12, no. 6, pp. 223–225, Jun. 2002.

[43] K. Xiao, D. J. Pommerenke, and J. L. Drewniak, "A three-dimensional FDTD subgridding algorithm based on interpolation of current density," in *International Symposium on Electromagnetic Compatibility (EMC)*, vol. 1.   IEEE, 2004, pp. 118–123.

[44] M. Celuch-Marcysiak and J. Rudnicki, "On the effect of total reflection on subgridded FDTD meshes," in *IEEE Antennas Propag. Soc. Intern. Symp.*, vol. 1, 2004, pp. 65–68.

[45] P. Thoma and T. Weiland, "Numerical stability of Finite Difference Time Domain methods," *IEEE Trans. Magn.*, vol. 34, no. 5, pp. 2740–2743, Sep. 1998.

[46] H. E. Abd-El-Raouf, R. Mittra, and J.-F. Ma, "A new domain decomposition Finite-Difference Time-Domain for solving large electromagnetic problems," *Microwave and Optical Technology Letters*, vol. 48, no. 12, pp. 2399–2405, 2006.

[47] C. Manry, S. Broschat, and J. Schneider, "Higher-order FDTD methods for large problems," *Appl. Comput. Electromagn. Soc. J*, vol. 10, no. 2, pp. 17–29, 1995.

[48] H. E. Abd-El-Raouf, E. El-Diwani, E. Ammar, and F. El-Hefnaw, "A modified 3D fourth order FDTD algorithm M3d$_{24}$ for improving phase accuracy with low resolution," in *IEEE Antennas Propag. Soc. Intern. Symp.*, vol. 1, 1999, pp. 196–199.

[49] H. E. Abd-El-Raouf, E. El-Diwani, A. Ammar, and F. El-Hefnawi, "A low-dispersion 3-D second-order in time fourth-order in space FDTD scheme (M3d$_{24}$)," *IEEE Trans. Antennas Propag.*, vol. 52, no. 7, pp. 1638–1646, 2004.

[50] J. Young, D. Gaitonde, and J. Shang, "Toward the construction of a fourth-order difference scheme for transient EM wave simulation: Staggered grid approach," *IEEE Trans. Antennas Propag.*, vol. 45, no. 11, pp. 1573–1580, 1997.

[51] W. Press, S. Teukolsky, W. Vetterling, and B. Flannery, *Numerical Recipes in C: The Art of Scientific Computing*, 2nd ed.   Cambridge University Press, 1992.

[52] P. Monk, "Sub-gridding FDTD schemes," *Appl. Computat. Electromagn. Soc. J.*, vol. 11, pp. 37–46, 1996.

[53] W. Yu and R. Mittra, "A new subgridding method for the Finite-Difference Time-Domain (FDTD) algorithm," *Microwave and Optical Technology Letters*, vol. 21, no. 5, pp. 330–333, Jun. 5, 1999.

[54] V. Douvalis, Y. Hao, and C. Parini, "Reduction of late time instabilities of the Finite-Difference Time-Domain method in curvilinear co-ordinates," in *Proc. Science, Measurement and Technology*, vol. 149, no. 5. IET, 2002, pp. 267–271.

[55] Y. Hao, V. Douvalis, and C. Parini, "Reduction of late time instabilities of the Finite-Difference Time-Domain method in curvilinear co-ordinates," in *Proc. Science, Measurement and Technology*, vol. 149, no. 5. IET, Sep. 2002, pp. 267–271.

[56] C.-C. Chang and S.-K. Jeng, "Modified subgridding algorithm with multilevel scheme for two-dimensional Finite-Difference Time-Domain method," in *Proc. of Microwave Conference, APMC, Asia-Pacific*, vol. 2. Taipei, Taiwan, R.O.C: IEEE, 2001, pp. 831–834.

[57] Z. Meglicki, S. K. Gray, and B. Norris, "Multigrid FDTD with Chombo," *Computer Physics Communications*, vol. 176, no. 2, pp. 109–120, 2006.

[58] Y. Zhang, A. A. Kishk, A. B. Yakovlev, and A. W. Glisson, "Analysis of wideband dielectric resonator antenna arrays for waveguide-based spatial power combining," *IEEE Trans. Microw. Theory Tech.*, vol. 55, no. 6, pp. 1332–1340, Jun. 2007.

[59] P. Chow, T. Yamagajo, T. Kubota, and T. Namiki, "A novel HE-coupling for explicit multigrid-FDTD," in *Wireless Communications and Applied Computational Electromagnetics*. IEEE, 2005, pp. 269–272.

[60] L. Kulas and M. Mrozowski, "Low-reflection subgridding," *IEEE Trans. Microw. Theory Tech.*, vol. 53, no. 5, pp. 1587–1592, May 2005.

[61] P. Park, D. Lee, S. Choi, S. Lee, S. Lim, and J. Choi, "A novel 3D sub-gridding method with odd interpolation ratio and magic location scheme," in *IEEE Antennas Propag. Soc. Intern. Symp.*, 2007, pp. 3061–3064.

[62] Y. Zhang, A. A. Kishk, A. B. Yakovlev, and A. W. Glisson, "DRA analysis using simple and flexible FDTD subgridding scheme," in *IEEE Antennas Propag. Soc. Intern. Symp.*, 2006, pp. 2767–2770.

[63] C.-C. Chang and S.-K. Jeng, "A multilevel subgridding scheme for two-dimensional Finite-Difference Time-Domain method," in *IEEE Antennas Propag. Soc. Intern. Symp.*, vol. 1, 2001, pp. 36–39.

[64] P. Chow, R. Nobes, T. Kubota, and T. Namiki, "Advanced methods for electromagnetic simulation," *FUJITSU Sci. Tech. J.*, vol. 43, no. 4, pp. 524–531, Oct. 2007.

[65] J. Ritter and F. Arndt, "A generalized 3D subgrid technique for the Finite-Difference Time Domain method," in *MTT-S International Microwave Symposium Digest*, vol. 3.   IEEE, 1997, pp. 1563–1566.

[66] A. Zakharian, M. Brio, C. Dineen, and J. Moloney, "Second-order accurate FDTD space and time grid refinement method in three space dimensions," *IEEE Photon. Technol. Lett.*, vol. 18, no. 11, pp. 1237–1239, Jun. 1, 2006.

[67] D. Prescott and N. Shuley, "A method for incorporating different sized cells into the Finite-Difference Time-Domain analysis technique," *IEEE Microw. Guided Wave Lett.*, vol. 2, no. 11, pp. 434–436, Nov. 1992.

[68] X. Xiaoli and W. Wenbing, "FDTD simulation of interstitial antenna for bone cancer microwave hyperthermic therapy," in *IEEE Antennas Propag. Soc. Intern. Symp.*, vol. 2, 2004, pp. 1855–1858.

[69] K. Krishnaiah and C. Railton, "Passive equivalent circuit of FDTD: An application to subgridding," *Electronics Letters*, vol. 33, no. 15, pp. 1277–1278, Jul. 17, 1997.

[70] ——, "A stable subgridding algorithm and its application to eigenvalue problems," *IEEE Trans. Microw. Theory Tech.*, vol. 47, no. 5, pp. 620–628, May 1999.

[71] J. M. Johnson and Y. Rahmat-Samii, "MR/FDTD: A multiple-region Finite-Difference–Time-Domain method," *Microwave and Optical Technology Letters*, vol. 14, no. 2, pp. 101–105, Feb. 1997.

[72] M. J. White and M. F. Iskander, "A new 3D FDTD multi-grid technique with dielectric-traverse capabilities," in *IEEE Antennas Propag. Soc. Intern. Symp.*, Jul. 1997, pp. 2160–2163.

[73] H. Ding and Q.-X. Chu, "An improved subgridding method with the second-order accurate FDTD technique at the dielectric interface," in *Asia-Pacific Symposium on Electromagnetic Compatibility and 19th International Zurich Symposium.* IEEE, 2008, pp. 52–55.

[74] H. E. Abd-El-Raouf, "A class of Finite Difference Time Domain (FDTD) techniques for solving large electromagnetic structures," in *RF and Microwave Conference, RFM. International.* IEEE, 2006, pp. 301–305.

[75] H. E. Abd-El-Raouf and E. A. El-Diwani, "Application of the FDTD hybrid "M3d$_{24}$-Yee" for simulating EM scattering from two objects separated by long distances," in *IEEE Antennas Propag. Soc. Intern. Symp.*, 2007, pp. 2325–2328.

[76] L. Kulas and M. Mrozowski, "A technique of stabilizing FDTD-subgridding algorithm using reciprocity principle," in *17th International Conference on Microwaves, Radar and Wireless Communications.* IEEE, 2008.

[77] K. Ramli, R. Abd-Alhameed, C. See, D. Zhou, E. Elkhazmi, and P. Excell, "Precise computation of the induced fields inside biological cell tissue using Floquet boundary and subgridding quasi-static FDTD method," in *Asia Pacific Microwave Conference (APMC).* IEEE, 2009, pp. 1533–1536.

[78] Y. Wang, S. Langdon, and C. Penney, "Analysis of accuracy and stability of FDTD subgridding schemes," in *Proc. 40th European Microwave Conference*, Paris, France, Sep. 28–30, 2010, pp. 1297–1300.

[79] K. Xiao, D. J. Pommerenke, and J. L. Drewniak, "A three-dimensional FDTD subgridding algorithm with separated temporal and spatial interfaces and related stability analysis," *IEEE Trans. Antennas Propag.*, vol. 55, no. 7, pp. 1981–1990, 2007.

[80] X. Xiaoli and W. Wenbing, "Modeling of interstitial applicators used for microwave hyperthermia of bone cancer based on subgridding FDTD method," in *Proc. The 6th International Symposium on Antennas*, vol. 10, 2003, pp. 645–648.

[81] W. Yu and R. Mittra, "A new higher-order subgridding method for Finite Difference Time Domain (FDTD) algorithm," in *IEEE Antennas Propag. Soc. Intern. Symp.*, vol. 1, 1998, pp. 608–611.

[82] R. Kopecký and M. Persson, "Subgridding method for FDTD modeling in the inner ear," in *Proc. of SPIE*, vol. 5445, 2003, pp. 398–401.

[83] M. J. White, M. F. Iskander, and Z. Huang, "Development of a multigrid FDTD code for three-dimensional applications," *IEEE Trans. Antennas Propag.*, vol. 45, no. 10, pp. 1512–1517, Oct. 1997.

[84] A. Vaccari, R. Pontalti, C. Malacarne, and L. Cristoforetti, "A robust and efficient subgridding algorithm for Finite-Difference Time-Domain simulations of Maxwell's equations," *Journal of Computational Physics*, vol. 194, no. 1, pp. 117–139, 2004.

[85] S.-H. Sun and C. T. Choi, "A new subgridding scheme for two-dimensional FDTD and FDTD (2, 4) methods," *IEEE Trans. Magn.*, vol. 40, no. 2, pp. 1041–1044, Mar. 2004.

[86] B. Donderici and F. L. Teixeira, "Subgridding with domain overriding for FDTD," in *IEEE Antennas Propag. Soc. Intern. Symp.*, vol. 1, 2004, pp. 61–64.

[87] ——, "Improved FDTD subgridding algorithms via digital filtering and domain overriding," *IEEE Trans. Antennas Propag.*, vol. 53, no. 9, pp. 2938–2951, Sep. 2005.

[88] ——, "Domain-overriding and digital filtering for 3-D FDTD subgridded simulations," *IEEE Microw. Wireless Compon. Lett.*, vol. 16, no. 1, pp. 10–12, Jan. 2006.

[89] P. Chow, T. Kubota, and T. Namiki, "A stable FDTD subgridding method for both spatial and temporal spaces," in *IEEE Antennas Propag. Soc. Intern. Symp.*, 2008.

[90] ——, "A stable three-dimensional subgridding method for both spatial and temporal spaces," in *Proc. Loughborough Antennas and Propagation Conference.* Loughborough, UK: IEEE, Nov. 8–9, 2010, pp. 213–216.

[91] S. V. Georgakopoulos, R. A. Renaut, C. A. Balanis, C. R. Birtcher, and A. H. Panaretos, "A hybrid method of FDTD (2, 4) and subgrid FDTD (2, 2) for modeling of coupling," in *IEEE Antennas Propag. Soc. Intern. Symp.*, vol. 2, 2002, pp. 694–697.

[92] Y. Liu and C. D. Sarris, "AMR-FDTD: A dynamically adaptive mesh refinement scheme for the Finite-Difference Time-Domain technique," in *IEEE Antennas Propag. Soc. Intern. Symp.*, vol. 1, 2005, pp. 134–137.

[93] ——, "Efficient modeling of microwave integrated-circuit geometries via a dynamically adaptive mesh refinement—FDTD technique," *IEEE Trans. Microw. Theory Tech.*, vol. 54, no. 2, pp. 689–703, Feb. 2006.

[94] J. Gazave, A. Reineix, and J. Seaux, "3D space-time subgridding algorithm for FDTD," in *IEEE Antennas Propag. Soc. Intern. Symp.*, 2007, pp. 3065–3068.

[95] B. Donderici and F. L. Teixeira, "Accurate interfacing of heterogeneous structured FDTD grid components," *IEEE Trans. Antennas Propag.*, vol. 54, no. 6, pp. 1826–1835, Jun. 2006.

[96] A. Barchanski, M. Clemens, H. D. Gersem, T. Steiner, and T. Weiland, "Using domain decomposition techniques for the calculation of low-frequency electric current densities in high-resolution 3D human anatomy models," *COMPEL: The International Journal for Computation and Mathematics in Electrical and Electronic Engineering*, vol. 24, no. 2, pp. 458–467, 2005.

[97] L. Catarinucci, P. Palazzari, and L. Tarricone, "A parallel variable-mesh FDTD algorithm for the solution of large electromagnetic problems," in *Proc. of the 19th IEEE International Parallel and Distributed Processing Symposium (IPDPS)*.   IEEE Computer Society, 2005.

[98] J.-P. Bérenger, "A FDTD subgridding based on Huygens surfaces," in *IEEE Antennas Propag. Soc. Intern. Symp.*, vol. 2A, Washington D.C., USA, Jul. 3–8, 2005, pp. 98–101.

[99] ——, "A Huygens subgridding for the FDTD method," *IEEE Trans. Antennas Propag.*, vol. 54, no. 12, pp. 3797–3804, Dec. 2006.

[100] ——, "Three dimensional Huygens subgridding for FDTD," in *IEEE Antennas Propag. Soc. Intern. Symp.*, 2009.

[101] ——, "Extension of the FDTD Huygens subgridding algorithm to two dimensions," *IEEE Trans. Antennas Propag.*, vol. 57, no. 12, pp. 3860–3867, Dec. 2009.

[102] ——, "The Huygens subgridding for the numerical solution of the Maxwell equations," *J. Comp. Phys.*, vol. 230, pp. 5635–5659, 2011.

[103] G. Gradoni, V. Primiani, and F. Moglie, "Accuracy evaluation of the Huygens subgridding method," in *Proc. Progress In Electromagnetics Research Symposium (PIERS)*, Moscow, Russia, Aug. 18–21, 2009, pp. 1338–1343.

[104] J. Xie, Y. Yang, S. Liu, and R. Chen, "Huygens subgrid technique for FDTD analysis of plasma problems," in *International Conference on Microwave and Millimeter Wave Technology (ICMMT)*.   IEEE, 2010, pp. 929–932.

[105] L. Zhou, J. B. Schneider, and R. G. Olsen, "Using artificial loss to control the instability in the Huygens subgridding method," 2010, unpublished report.

[106] ——, "Using artificial loss to control the instability in the Huygens subgridding method," in *IEEE Antennas Propag. Soc. Intern. Symp.*, Toronto, Ontario, Canada, Jul. 11–17, 2010.

[107] J. Costa, F. Costen, J.-P. Bérenger, and A. Brown, "Inclusion of frequency dependency in the Huygens subgridding FDTD for UWB systems," in *IEEE Antennas Propag. Soc. Intern. Symp.*, 2007, pp. 3077–3080.

[108] M. Abaļenkovs, F. Costen, J.-P. Bérenger, and A. Brown, "Application of Huygens subgridding technique to human body modelling," in *IEEE Antennas Propag. Soc. Intern. Symp.*, 2008.

[109] F. Costen and J.-P. Bérenger, "Extension of the FDTD Huygens subgridding to frequency dependent media," *Annals of Telecommunications*, vol. 65, no. 3, pp. 211–217, 2010.

[110] W. Bilgic, X. Cui, I. Wolff, and D. Erni, "Subgridding capabilities of the wavelet-transformed FDTD scheme," in *Microwave Conference, APMC, Asia-Pacific*. IEEE, 2008.

[111] L. Kulas and M. Mrozowski, "Reduced order models of refined Yee's cells," *IEEE Microw. Wireless Compon. Lett.*, vol. 13, no. 4, pp. 164–166, Apr. 2003.

[112] G. Carat, R. Gillard, J. Citerne, and J. Wiart, "An efficient analysis of planar microwave circuits using a DWT-based HAAR MRTD scheme," *IEEE Trans. Microw. Theory Tech.*, vol. 48, no. 12, pp. 2261–2270, 2000.

[113] R. A. Chilton and R. Lee, "Conservative and provably stable FDTD subgridding," *IEEE Trans. Antennas Propag.*, vol. 55, no. 9, pp. 2537–2549, 2007.

[114] ——, "Explicit 3D FDTD subgridding with provable stability and conservative properties," in *IEEE Antennas Propag. Soc. Intern. Symp.*, 2007, pp. 3069–3072.

[115] ——, "Conservative subgridding for Lobatto cell FDTD method," in *IEEE Antennas Propag. Soc. Intern. Symp.*, 2008.

[116] L. Kulas and M. Mrozowski, "A fast high-resolution 3-D Finite-Difference Time-Domain scheme with macromodels," *IEEE Trans. Microw. Theory Tech.*, vol. 52, no. 9, pp. 2330–2335, Sep. 2004.

[117] L. Kulas, P. Sypek, J. Podwalski, and M. Mrozowski, "Model order reduction for subgridding in FDTD scheme," in *17th International Zurich Symposium on Electromagnetic Compatibility*. IEEE, 2006, pp. 18–21.

[118] M. Marrone and R. Mittra, "A theoretical study of the stability criteria for hybridized FDTD algorithms for multiscale analysis," *IEEE Trans. Antennas Propag.*, vol. 52, no. 8, pp. 2158–2167, Aug. 2004.

[119] ——, "A new stable hybrid three-dimensional generalized Finite Difference Time Domain algorithm for analyzing complex structures," *IEEE Trans. Antennas Propag.*, vol. 53, no. 5, pp. 1729–1737, May 2005.

[120] N. V. Venkatarayalu, R. Lee, Y.-B. Gan, and L.-W. Li, "A stable FDTD subgridding method based on Finite Element formulation with hanging variables," *IEEE Trans. Antennas Propag.*, vol. 55, no. 3, pp. 907–915, Mar. 2007.

[121] L. Kulas and M. Mrozowski, "A simple high-accuracy subgridding scheme," in *33rd European Microwave Conference*. Munich, Germany: IEEE, 2003, pp. 347–350.

[122] M. Bonilla, M. F. Wong, J. Wiart, G. Alquié, and V. F. Hanna, "3D-FDTD subgridding technique applied to radiating structures," in *Microwave Symposium Digest, MTT-S International*, vol. 3. IEEE, 2001, pp. 2035–2038.

[123] A. Monorchio and R. Mittra, "A novel subgridding scheme based on a combination of the Finite-Element and Finite-Difference Time-Domain methods," *IEEE Trans. Antennas Propag.*, vol. 46, no. 9, pp. 1391–1393, Sep. 1998.

[124] B.-Z. Wang, Y. Wang, W. Yu, and R. Mittra, "A hybrid 2-D ADI-FDTD subgridding scheme for modeling on-chip interconnects," *IEEE Trans. Adv. Packag.*, vol. 24, no. 4, pp. 528–533, 2001.

[125] Z. D. Chen and I. Ahmed, "3D hybrid ADI-FDTD/FDTD subgridding scheme applied to RF/Microwave and optical structures," in *National Radio Science Meeting*, 2004, pp. 1684–1687.

[126] W. Pernice, F. Payne, and D. Gallagher, "Simulation of metallic nano-structures by using a hybrid FDTD-ADI subgridding method," in *Proc. International Conference on Electromagnetics in Advanced Applications, ICEAA*. IEEE, 2007, pp. 633–636.

[127] Z. Huang and G. Pan, "A novel subgridding technique for unconditionally stable Time Domain method," in *IEEE Antennas Propag. Soc. Intern. Symp.*, 2010.

[128] F. Mayer, R. Schuhmann, and T. Weiland, "Flexible subgrids in FDTD calculations," in *IEEE Antennas Propag. Soc. Intern. Symp.*, vol. 3, 2002, pp. 252–255.

[129] O. Poděbrad, M. Clemens, and T. Weiland, "New flexible subgridding scheme for the Finite Integration Technique," *IEEE Trans. Magn.*, vol. 39, no. 3, pp. 1662–1665, May 2003.

[130] P. Thoma and T. Weiland, "A consistent subgridding scheme for the Finite Difference Time Domain method," *International Journal of Numerical Modelling: Electronic Networks, Devices and Fields*, vol. 9, no. 5, pp. 359–374, 1996.

[131] K. S. Kunz and L. Simpson, "A technique for increasing the resolution of finite-difference solutions of the Maxwell equation," *IEEE Trans. Electromagn. Compat.*, no. 4, pp. 419–422, Nov. 1981.

[132] R. Pascaud, R. Gillard, R. Loison, J. Wiart, and M. Wong, "Dual-grid Finite-Difference Time-Domain scheme for the fast simulation of surrounded antennas," *Microwaves, Antennas & Propagation*, vol. 1, no. 3, pp. 700–706, 2007.

[133] ——, "Multiresolution FDTD with switchable grid," in *First European Conference on Antennas and Propagation, EuCAP*.   Nice, France: IEEE, Nov. 6–10, 2006, pp. 1–5.

[134] G. Marrocco, M. Sabbadini, and F. Bardati, "FDTD improvement by dielectric subgrid resolution," *IEEE Trans. Microw. Theory Tech.*, vol. 46, no. 12, pp. 2166–2169, Dec. 2002.

[135] R. Holland, "Finite-difference solution of Maxwell's equations in generalized nonorthogonal coordinates," *IEEE Trans. Nucl. Sci.*, vol. 30, no. 6, pp. 4589–4591, Dec. 1983.

[136] K. S. Yee, J. S. Chen, and A. H. Chang, "Conformal Finite-Difference Time-Domain (FDTD) with overlapping grids," *IEEE Trans. Antennas Propag.*, vol. 40, no. 9, pp. 1068–1075, Sep. 1992.

[137] H. Ding and Q.-X. Chu, "Enlarged cell technique in FDTD method at the dielectric curved surface," in *Asia-Pacific Microwave Conference, APMC*. IEEE, 2008.

[138] M. W. Chevalier and R. J. Luebbers, "FDTD local grid with material traverse," in *IEEE Antennas Propag. Soc. Intern. Symp. Digest*, vol. 1, Baltimore, MD, Jul. 21–26, 1996, pp. 116–119.

[139] G. Mur, "Absorbing boundary conditions for the finite-difference approximation of the time-domain electromagnetic-field equations," *IEEE Trans. Electromagn. Compat.*, vol. 23, no. 4, pp. 377–382, Nov. 1981.

[140] K. R. Umashankar and A. Taflove, "A novel method to analyze electromagnetic scattering of complex objects," *IEEE Trans. Electromagn. Compat.*, vol. 24, pp. 397–405, 1982.

[141] J.-P. Bérenger, "Three-dimensional Perfectly Matched Layer for the absorption of electromagnetic waves," *J. Comp. Phys.*, vol. 127, no. 2, pp. 363–379, 1996.

[142] ——, *Perfectly Matched Layer (PML) for Computational Electromagnetics*, 1st ed., ser. Synthesis Lectures on Computational Electromagnetics, C. A. Balanis, Ed. Morgan & Claypool Publishers, Mar. 1, 2007, Lecture #8.

[143] F. Costen, J.-P. Bérenger, and A. Brown, "Comparison of FDTD hard source with FDTD soft source and accuracy assessment in Debye media," *IEEE Trans. Antennas Propag.*, vol. 57, no. 7, pp. 2014–2022, 2009.

[144] T. Wuren, T. Takai, M. Fujii, and I. Sakagami, "Effective 2-Debye-pole FDTD model of electromagnetic interaction between whole human body and UWB radiation," *IEEE Microw. Wireless Compon. Lett.*, vol. 17, no. 7, pp. 483–485, Jul. 2007.

[145] The Fastest Fourier Transform in the West (FFTW) website. Accessed: Apr. 5, 2011. [Online]. Available: http://www.fftw.org/

[146] J.-P. Bérenger, "Plaques minces aux différences finies," in *6éme Colloque International et Exposition sur la Compatibilité Electromagnétique, CEM'92*, Jun. 1992, pp. 298–303, (in French).

[147] T. Williams, C. Kelley *et al.*, *Gnuplot 4.4 Manual*, gnuplot.pdf, GNU, Mar. 5, 2010, accessed: Jun. 10, 2011. [Online]. Available: http://www.gnuplot.info/docs_4.4/

[148] M. G. Fishler, "Theoretical predictions of the optimal monophasic and biphasic defibrillation waveshapes," *IEEE Trans. Biomed. Eng.*, vol. 47, no. 1, pp. 59–67, Jan. 2000.

[149] MPI website. Accessed: Jun. 6, 2011. [Online]. Available: http://www.mcs.anl.gov/research/projects/mpi/

[150] CUDA website. Accessed: May 11, 2011. [Online]. Available: http://www.nvidia.com/object/cuda_home_new.html

[151] OpenCL website. Accessed: May 11, 2011. [Online]. Available: http://www.khronos.org/opencl/

[152] Fortress website. Accessed: May 13, 2011. [Online]. Available: http://java.net/projects/projectfortress/pages/Home

[153] Chapel website. Accessed: May 13, 2011. [Online]. Available: http://chapel.cray.com/

[154] E. Martin, Ed., *Concise Medical Dictionary*, 10th ed. Market House Books Ltd, 2010, ISBN 9780199557141.

[155] M. Millodot, *Dictionary of Optometry and Visual Science*, 7th ed. Butterworth-Heinemann, 2009, Accessed: Jul. 19, 2011. [Online]. Available: http://medical-dictionary.thefreedictionary.com/depolarization

[156] J. Nolan, J. Soar, A. Lockey, D. Pitcher, D. Gabbott, G. Perkins, M. Scott, and S. Mitchell, Eds., *Advanced Life Support*, 5th ed. 5th Floor, Tavistock House North, Tavistock Square, London, WC1H 9JR: Resuscitation Council (UK), Jun. 2008, ISBN 1-903812-11-9.

[157] F. H. Martini, *Fundamentals of Anatomy & Physiology*, 6th ed. Benjamin Cummings, 1301 Sansome Street, San Francisco, CA 94111: Pearson Education International, 2004, ISBN 0-13-120346-0.

[158] A. J. Handley, Ed., *Resuscitation Guidelines 2005*. 5th Floor, Tavistock House North, Tavistock Square, London, WC1H 9JR: Resuscitation Council (UK), Dec. 2005, ISBN 1-903812-10-0.

[159] H. H. Gray, K. D. Dawkins, J. M. Morgan, and I. A. Simpson, *Lecture notes. Cardiology*, 5th ed. 350 Main Street, Malden, Massachusetts 02148-5020: Blackwell Publishing Inc., 2008, ISBN 978-1-4051-5708-7.

[160] M. Colquhoun, A. J. Handley, and T. Evans, Eds., *ABC of Resuscitation*, 4th ed. BMJ Publishing Group, BMA House, Tavistock Square, London, WC1H 9JR: BMJ Books, 1999, ISBN 0-7279-1190-2.

[161] G. W. N. Dalzell, "Determinants of successful defibrillation," *British Heart Journal*, vol. 80, pp. 405–407, 1998.

[162] M. Zimmermann, "Elective cardioversion of atrial fibrillation," in *Swiss-rhythm 2005*, Luzern, 2005.

[163] T. P. DeMonte, P. D. Gadsby, P. F. Meyer, and M. L. Joy, "Measurement of edge effects in automatic external defibrillation electrodes using current density imaging," in *13th Annual ISMRM International Conference, Miami Beach*, 2005.

[164] M. Schönegg and A. Bolz, "There is more than biphasic truncated exponential in defibrillation," in *4th European Conference of the International Federation for Medical and Biological Engineering*, ser. IFMBE Proceedings, vol. 22. Springer Berlin Heidelberg, Feb. 2009, pp. 2524–2527.

[165] E. J. Topol, R. M. Califf, E. N. Prystowsky, J. D. Thomas, and P. D. Thompson, *Textbook of Cardiovascular Medicine*. Lippincott Williams & Wilkins, 2006.

[166] P. R. Kowey and G. V. Naccarelli, *Atrial Fibrillation*.   Informa Health Care, 2005.

[167] I. A. Vogiatzis, V. Sachpekidis, I. M. Vogiatzis, and E. Kambitsi, "External cardioversion of atrial fibrillation: The role of electrode position on cardioversion success," *International Journal of Cardiology*, vol. 10, Mar. 2008.

[168] T. M. Muñoz, S. A. Martínez, C. L. Vinuesa, and Y. H. Poveda, "Comparación de dos posiciones de electrodos en la cardioversión eléctrica de la fibrilación auricular," Unidad de Cuidados Intensivos. Hospital Txagorritxu. Vitoria-Gasteiz. Spain, Tech. Rep., 2006.

[169] T. P. Mathew, A. Moore, M. McIntyre, M. T. Harbinson, N. P. S. Campbell, A. J. Adgey, and G. W. N. Dalzell, "Randomised comparison of electrode positions for cardioversion of atrial fibrillation," *British Heart Journal*, vol. 81, pp. 576–579, 1999.

[170] H. Akselrod, M. W. Kroll, and M. V. Orlov, "History of defibrillation," in *Cardiac Bioelectric Therapy*, I. R. Efimov, M. W. Kroll, and P. J. Tchou, Eds. Tufts University, School of Medicine, Caritas St. Elizabeth's Medical Center of Boston, Boston, MA, USA: Springer US, 2009, pp. 15–40, Accessed: Jul. 20, 2011. [Online]. Available: http://dx.doi.org/10.1007/978-0-387-79403-7_2

[171] M. W. Kroll, K. Kroll, and B. Gilman, "Idiot-proofing the defibrillator," *IEEE Spectr.*, Nov. 2008, Accessed: Jul. 19, 2011. [Online]. Available: http://spectrum.ieee.org/biomedical/devices/idiotproofing-the-defibrillator/0

[172] S. J. Holden, R. D. Sheridan, T. J. Coffey, R. A. Scaramuzza, and P. Diamantopoulos, "Electromagnetic modelling of current flow in the heart from TASER devices and the risk of cardiac dysrhythmias," *Physics in Medicine and Biology*, vol. 52, pp. 7193–7209, Nov. 23, 2007.

[173] B. Lenaerts and R. Puers, *Omnidirectional Inductive Powering for Biomedical Implants*.   Springer Science and Business Media B.V., 2009.

[174] H. Sun, "Models of ventricular fibrillation probability and neuromuscular stimulation after taser use in humans," Ph.D. dissertation, University of Wisconsin at Madison, School of Electrical Engineering, 2007.

[175] L. Xia, C. He, F. Liu, and H. Zhao, "Study of heart stimulation caused by induced eddy-currents in fast-switched MRI," Department of Biomedical Engineering, Zhejiang University, Hangzhou 310027, China; Centre for Magnetic Resonance, University of Queensland, St. Lucia, Brisbane, Queensland 4072, Australia, Tech. Rep., 1998.

[176] O. Ferhanoglu, T. O. Tasci, A. M. El-Sharkawy, A. Altintas, and E. Atalar, "Investigating RF heating of pacemakers in MRI using a safety index," in *International Society of Magnetic Resonance in Medicine, 12th Scientific Meeting, Kyoto*, 2004, pp. 662–662.

[177] I. R. Efimov, Y. Cheng, D. R. Van Wagoner, T. Mazgalev, and P. J. Tchou, "Virtual electrode induced phase singularity: A basic mechanism of defibrillation failure," *American Heart Association*, vol. 82, pp. 918–925, 1998.

[178] D. Frazier, W. Krassowska, P. Chen, P. Wolf, E. Dixon, W. Smith, and R. Ideker, "Extracellular field required for excitation in three-dimensional anisotropic canine myocardium," *Circulation Research*, vol. 63, no. 1, p. 147, 1988.

[179] D. Mocanu, J. Kettenbach, M. Sweeney, B. KenKnight, R. Kikinis, and S. Esinberg, "Patient-specific simulation of internal defibrillation," *Med. Image Comput. Comput. Assist. Interv. MICCAI*, vol. 4, pp. 983–990, 2001.

[180] A. Cansell, P. H. Lechat, G. Fontaine, Y. Grosgogeat, and K. Meyer-Waardent, "Transvenous and subcutaneous electrode system for an implantable defibrillator improved on large pigs," *Pacing and Clinical Electrophysiology (PACE)*, vol. 11, pp. 2008–2014, 1988.

[181] S. Morgan, G. Plank, I. Biktasheva, and V. N. Biktashev, "Low energy defibrillation in human cardiac tissue: A simulation study," *Biophysical Journal*, vol. 96, pp. 1364–1373, 2009.

[182] I. V. Biktasheva, S. W. Morgan, G. Plank, and V. N. Biktashev, "Feedback control of resonant drift as a tool for low voltage defibrillation," *Computers in Cardiology*, vol. 35, pp. 501–504, 2008.

[183] Simula Research Laboratory, "Simulations of low-volt defibrillation of the atria," Simula Research Laboratory, Tech. Rep., Jul. 2007.

[184] K. Skouibine, N. Trayanova, and P. Moore, "Success and failure of the defib-
rillation shock: Insights from a simulation study," *Journal of Cardiovascular
Electrophysiology*, vol. 11, pp. 785–796, 2000.

[185] N. Trayanova, "Defibrillation of the heart: Insights into mechanisms from
modelling studies," *Experimental Physiology*, vol. 91, no. 2, pp. 323–337, 2006.

[186] D. M. Martinez, "Right towards successful defibrillation via electric shock,"
2009, school of Electrical and Electronic Engineering, The University of
Manchester, United Kingdom, Unpublished Report.

[187] M. W. Kroll, "A minimal model of the single capacitor biphasic defibrillation
waveform," *Pacing and Clinical Electrophysiology*, vol. 17, no. 11, pp. 1782–
1792, 1994.

[188] Y. Yamanouchi, J. E. Brewer, K. A. Mowrey, M. W. Kroll, A. Donohoo, B. L.
Wilkoff, and P. J. Tchou, "Sawtooth first phase biphasic defibrillation wave-
form," *Journal of Cardiovascular Electrophysiology*, vol. 8, no. 5, pp. 517–528,
1997.

[189] Y. Yamanouchi, J. E. Brewer, K. A. Mowrey, A. M. Donohoo, B. L. Wilkoff, and
P. J. Tchou, "Optimal small-capacitor biphasic waveform for external defib-
rillation: Influence of phase-1 tilt and phase-2 voltage," *Circulation*, vol. 98,
no. 22, p. 2487, 1998.